

In Silico Investigations of Mechanophore Activation in Polymers

Dissertation

to obtain the doctoral degree in natural sciences

Dr. rer. nat.

Submitted to the doctoral committee
of Faculty 02 (Biology / Chemistry)
at the University of Bremen



**University
of Bremen**

from

Sourabh Kumar

Institute for Physical and Theoretical Chemistry

University of Bremen, Germany

Bremen, May 2023

This work was carried out in the working group of Prof. Dr. Tim Neudecker (former Stauch) at the “Institute for Physical and Theoretical Chemistry” at the University of Bremen from January 2020 to May 2023.

Assessment of the written part:

1. Reviewer: Prof. Dr. Jan Meisner, Heinrich-Heine-Universität Düsseldorf

2. Reviewer: Prof. Dr. Tim Neudecker, Universität Bremen

Date of Defense: 12th July, 2023

In Silico Investigations of Mechanophore Activation in Polymers

Dissertation

zur Erlangung des Doktorgrades der Naturwissenschaften

Dr. rer. nat.

Vorgelegt dem Promotionsausschuss
des Fachbereichs 02 (Biologie/Chemie)
der Universität Bremen



**Universität
Bremen**

von

Sourabh Kumar

Institut für Physikalische und Theoretische Chemie

Universität Bremen, Germany

Bremen, im May 2023

Diese Arbeiten wurden in der Arbeitsgruppe von Prof. Dr. Tim Neudecker (former Stauch) am “Institut für Physikalische und Theoretische Chemie” der Universität Bremen von Januar 2020 bis Mai 2023 durchgeführt.

Begutachtung des schriftlichen Teils:

- 1. Gutachter:** Prof. Dr. Jan Meisner, Heinrich-Heine-Universität Düsseldorf
- 2. Gutachter:** Prof. Dr. Tim Neudecker, Universität Bremen

Datum der Verteidigung: 12th Juli, 2023

Acknowledgement

I would like to express my sincere gratitude to Prof. Dr. Tim Neudecker for giving me the incredible opportunity to conduct my doctoral research as a first PhD student in his research group at the University of Bremen. It gives me immense pleasure to thank him for his continuous support, guidance, and meaningful scientific discussions.

Further, I would like to extend my gratitude to Prof. Jan Meisner from Heinrich-Heine-Universität Düsseldorf for graciously accepting to co-referee my dissertation. I am deeply thankful to him for generously devoting his valuable time.

I would like to thank Prof. Dr. Anne Staubitz and Prof. Dr. Petra Swiderek, my doctoral committee members, for generously giving their valuable time and expertise.

I am deeply grateful to our esteemed collaborators, Prof. Dr. Lucio Colombi Ciacchi and Dr. Baris Demir, for their invaluable expertise and fruitful scientific discussions.

I also want to thank my fellow PhD colleague, Tarek Scheele for providing technical expertise. Special thanks to Felix Zeller for proofreading part of my thesis. I am very thankful to all the present and past group members: Tarek Scheele, Felix Zeller, Julius Werthschütz, Chieh-Min Hsieh, Rahel Weiß, Jonas Bentrup, Alexander Dellwisch, Henry Wang, Gheorghe Adam, Phil Hepke, Philipp Diephaus and Dr. Mausumi Chatthopadyaya for the wonderful and unforgettable moments.

I am grateful to University of Bremen for providing the computational facilities.

I would like to express my sincere appreciation to Souvik Ghosh and Kowshik Ghosh for being like a family to me. I am thankful to Meenu Upadhyay for her unconditional support and encouragement throughout my PhD journey.

Finally, I wish to express my deepest gratitude to my incredible family. Their unwavering love, support, and constant encouragement have been a driving force in all aspects of my life. Their patience and support have been invaluable and essential in the completion of this thesis.

*This thesis is dedicated to my mother, Mrs. Jaya Devi and my father, Mr.
Sanjeevaan Kumar.*

Erklärungen zur elektronischen Version und zur Überprüfung einer Dissertation

Hiermit betätige ich gemäß §7, Abs. 7, Punkt 4, dass die zu Prüfungszwecken beigelegte elektronische Version meiner Dissertation identisch ist mit der abgegebenen gedruckten Version.

Ich bin mit der Überprüfung meiner Dissertation gemäß §6 Abs. 2, Punkt 5 mit qualifizierter Software im Rahmen der Untersuchung von Plagiatsvorwürfen einverstanden.

Unterschrift:

Ort, Datum: Bremen, 23.05.2023

Declaration

I hereby declare that this submission is my own work under guidance of Prof. Dr. Tim Neudecker and that, to the best of my knowledge and belief, it contains no material previously published or written by another person nor material which to a substantial extent has been accepted for the award of any other degree or diploma of the university or other institute of higher learning, except where due acknowledgment has been made in the text.

Signature:

Place, Date: Bremen, 23.05.2023

Declaration

Versicherung an Eides Statt

Hiermit versichere ich, Sourabh Kumar,

an Eides statt durch meine Unterschrift, dass ich die vorstehende Arbeit mit dem Titel "In Silico Investigations of Mechanophore Activation in Polymers" selbständig und ohne fremde Hilfe angefertigt und alle Stellen, die ich wörtlich dem Sinne nach aus Veröffentlichungen entnommen habe, als solche kenntlich gemacht habe, mich auch keiner anderen als der angegebenen Literatur oder sonstiger Hilfsmittel bedient habe.

Ich versichere an Eides statt, dass ich die vorgenannten Angaben nach bestem Wissen und Gewissen gemacht habe und dass die Angaben der Wahrheit entsprechen und ich nichts verschwiegen habe.

Die Strafbarkeit einer falschen eidesstattlichen Versicherung ist mir bekannt, namentlich die Strafandrohung gemäß § 156 StGB bis zu drei Jahren Freiheitsstrafe oder Geldstrafe bei vorsätzlicher Begehung der Tat bzw. gemäß § 161 Abs. 1 StGB bis zu einem Jahr Freiheitsstrafe oder Geldstrafe bei fahrlässiger Begehung.

Signature:

Ort, Datum: Bremen, 23.05.2023

**Declaration on the contribution of the candidate to a multi-author
article/manuscript/chapter which is included as a chapter in the
submitted doctoral thesis**

Chapter 3.2, 3.3 :

Contribution of the candidate in total workload (in order of lead, equal, support and none for each of the following categories):

Scientific concept and design:	support
Computational modeling and/or implementation:	support
Computational analysis and interpretation of data:	support
Preparation of Figures and Tables:	support
Drafting of the manuscript:	support

Chapter 4.2, 4.3 :

Contribution of the candidate in total workload (in order of lead, equal, support and none for each of the following categories):

Scientific concept and design:	lead
Computational modeling and/or implementation:	lead
Computational analysis and interpretation of data:	lead
Preparation of Figures and Tables:	lead
Drafting of the manuscript:	lead

Chapter 4.4, 4.5 :

Contribution of the candidate in total workload (in order of lead, equal, support and none for each of the following categories):

Scientific concept and design:	lead
Computational modeling and/or implementation:	lead
Computational analysis and interpretation of data:	lead
Preparation of Figures and Tables:	lead
Drafting of the manuscript:	lead

Chapter 5:

Contribution of the candidate in total workload (in order of lead, equal, support and none for each of the following categories):

Scientific concept and design:	equal
Computational modeling and/or implementation:	lead
Computational analysis and interpretation of data:	lead
Preparation of Figures and Tables:	lead
Drafting of the manuscript:	lead

Signature:

Place, Date: Bremen, 23.05.2023

Abstract

The study of chemical reactions induced by mechanical forces, termed Mechanochemistry, has emerged as a promising field for developing new materials and processes. The advancements in the last two decades in this field have shown that significant deformations in materials can induce mechanochemical reactions which allows for a broad range of applications. Mechanochromism, the response to deformations in terms of changes in color or luminescent behavior, is a key feature that is contributing to numerous applications. In the field of polymer mechanochemistry, this behaviour is governed by small molecular subunits called *mechanophores*. Specifically, when a bulk material is deformed, its internal stress and strain distribution change, which can create local variations in the forces experienced by specific regions within the material. These local forces lead to the activation of mechanophores and contribute to the overall mechanical behavior of the material. This thesis explores the such complex interplay between mechanical forces and chemical reactions in polymer materials, shedding light on the fundamental mechanisms underlying mechanophore activation processes.

Most mechanophores developed to date are activated by stretching forces, that pull the mechanophore from two opposite directions and break a labile bond in it. However, in some cases the bond present in the polymer itself or some other bonds of the mechanophore rupture, which limits the mechanophore activation efficiency. The third Chapter of the thesis focuses on this issue, where the activation of mechanophores as a result of stretching forces is discussed in detail. This chapter is divided into two parts. The first part discusses the activation mechanism of flex-activated mechanophores under tension. A combination of quantum chemical static and dynamic calculations is used to compare three different mechanical deformation modes to identify the most efficient method. The results provide detailed insights into the activation of flex-activated mechanophores in polymers. The second part of the chapter addresses the adjustable threshold parameter by identifying eleven

different linkers to fine-tune the activation rates of three different mechanophores. The linkers allow for the adjustment of the threshold barrier, and the results show applicability in the context of the gating mechanochemical process, tuning it from one-step to two-step gating.

Another way to apply forces to the mechanophores is by compressing them. Generally, there are mechanophores which activate based on compressive forces, but here we are showing that the activated form of a mechanophore can be reversed using hydrostatic pressure. For this purpose, a spiropyran (SP) mechanophore is activated under stretching forces through linkers. Under hydrostatic pressure the activated form (i.e. merocyanine (MC)) is deactivated back to SP form. By subjecting the SP-MC system to static and dynamic calculations, we established a two-step baro-mechanical cycle for repeated activation and deactivation of the mechanophores, achieved by alternating mechanical stretching forces and hydrostatic pressure. As SP-MC show the mechanochromism behaviour, a time-resolved UV/Vis absorption spectrum is provided to show the interconversion and true mapping of the stress type over the material.

The second part of Chapter 4 is dedicated to explore the effect of hydrostatic pressure on a [2,3]-sigmatropic rearrangement. In this study, we demonstrate that under hydrostatic pressure the transition state of a rearrangement can be transformed into a minimum on the potential energy surface. Our simulations, conducted using Born-Oppenheimer molecular dynamics (BOMD) methodology, revealed that a gradual increase in hydrostatic pressure up to 120 GPa results in the formation of the transition state (i.e., the five-membered ring). Conversely, a step-wise reduction in pressure led to the formation of a 70:30 mixture of the product and educt of the sigmatropic rearrangement. To facilitate experimental studies, we have included reference data in the form of simulated IR, Raman, and time-resolved UV/Vis absorption spectra.

Lastly, a multiscale mechanochemical model was developed to simulate the SP mechanophore activation inside linear poly(methyl methacrylate) (PMMA) polymers. To achieve this, we parameterize the force fields of SP and MC molecules

in molecular mechanics (MM) to obtain a SP-MC isomerization force-modified potential energy surface (PES) as reference Quantum mechanics (QM) energies. During bulk deformations, such as uniaxial tensile and shear deformation of the system, mechanophores activation is captured at $5 \cdot 10^7$ and $5 \cdot 10^8 \text{ s}^{-1}$ strain rates. The molecular rearrangement of the chains as a function of the applied strain provided the insight that the force transduction behaviour from the macroscopic level to the local environment of the mechanophore is a result of direct chain elongation. Interestingly, we also found that there is a strong influence of the stress type on the stress-strain behaviour and resulting mechanochemical activity. Overall, our results provide a detailed understanding of the force transduction behaviour of bulk scale deformation to govern the mechanophore activation.

Zusammenfassung

Die Erforschung chemischer Reaktionen, die durch mechanische Kräfte ausgelöst werden, die so genannte Mechanochemie, hat sich zu einem vielversprechenden Gebiet für die Entwicklung neuer Materialien und Verfahren entwickelt. Die Fortschritte der letzten zwei Jahrzehnte auf diesem Gebiet haben gezeigt, dass erhebliche Verformungen in Materialien mechanochemische Reaktionen auslösen können, die ein breites Spektrum von Anwendungen bieten. Mechanochromie, die Reaktion auf Verformungen in Form von Farbänderungen oder lumineszierendem Verhalten, sind Schlüsselmerkmale, welche eine Vielzahl von Anwendungen ermöglichen. Im Bereich der Mechanochemie von Polymeren wird dieses Verhalten von kleinen molekularen Untereinheiten, den so genannten Mechanophoren, gesteuert. Wenn ein bulk polymere verformt wird, ändert sich seine innere Spannungs- und Dehnungsverteilung, was zu lokalen Schwankungen der Kräfte in bestimmten Regionen des Materials führen kann. Diese lokalen Kräfte führen zur Aktivierung von Mechanophoren und tragen zum mechanischen Gesamtverhalten des Materials bei. In dieser Arbeit wird das komplexe Zusammenspiel zwischen mechanischen Kräften und chemischen Reaktionen in Polymerwerkstoffen untersucht, um die grundlegenden Mechanismen zu beleuchten, die den Mechanophor-Aktivierungsprozessen zugrunde liegen.

Die meisten bisher entwickelten Mechanophore werden durch Streckkräfte aktiviert, d. h. durch Kräfte, die das Mechanophor aus zwei entgegengesetzten Richtungen ziehen und eine darin vorhandene labile Bindung aufbrechen. In einigen Fällen reißt jedoch entweder eine Bindung im Polymer selbst oder einige andere Bindungen des Mechanophors, was die Effizienz der Mechanophoraktivierung einschränkt. Das dritte Kapitel der Dissertation befasst sich mit diesem Problem, in welchem die Aktivierung von Mechanophoren infolge von Streckkräften im Detail diskutiert wird. Dieses Kapitel ist in zwei Teile gegliedert. Der erste Teil des Kapitels befasst sich mit dem Aktivierungsmechanismus von flex-aktivierten Mechanophoren unter Spannung.

Mit einer Kombination aus quantenchemischen statischen und dynamischen Berechnungen werden drei verschiedene mechanische Verformungsmodi verglichen, um die effizienteste Methode zu ermitteln. Die Ergebnisse liefern detaillierte Einblicke in die Aktivierung von flex-aktivierten Mechanophoren in Polymeren. Der zweite Teil des Kapitels befasst sich mit dem einstellbaren Schwellenparameter, indem elf verschiedene Linker zur Feinabstimmung der Aktivierungsraten von drei verschiedenen Mechanophoren identifiziert werden. Die Linker ermöglichen die Einstellung der Schwellenwertbarriere, und die Ergebnisse zeigen die Anwendbarkeit im Kontext des mechanochemischen Gating-Prozesses, indem sie diesen von einem einstufigen zu einem zweistufigen Gating-Prozess abstimmen.

Eine weitere Möglichkeit, Kräfte auf Mechanophoren auszuüben, besteht darin, sie zu komprimieren. Im Allgemeinen gibt es Mechanophore, die durch Druckkräfte aktiviert werden, aber hier zeigen wir, dass die aktivierte Form eines Mechanophors durch hydrostatischen Druck umgekehrt werden kann. Zu diesem Zweck wird ein Spiropyran (SP)-Mechanophor unter Streckkräften durch die Linker aktiviert, unter hydrostatischem Druck wird die aktivierte Form (d.h. Merocyanin (MC)) wieder zur SP-Form deaktiviert. Indem wir das SP-MC-System statischen und dynamischen Berechnungen unterzogen, stellten wir einen zweistufigen baro-mechanischen Zyklus für die wiederholte Aktivierung und Deaktivierung der Mechanophore fest, der durch den Wechsel von mechanischen Streckkräften und hydrostatischem Druck erreicht wird. Da SP-MC ein mechanochromes Verhalten zeigen, wird ein zeitaufgelöstes UV/Vis-Absorptionsspektrum zur Verfügung gestellt, um die Umwandlung und die genaue Zuordnung der Belastungsart zum Material zu zeigen.

Der zweite Teil von Kapitel 4 ist der Erforschung der hydrostatischen Druckanwendung auf eine [2,3]-sigmatrope Umlagerung gewidmet. In dieser Studie zeigen wir, dass unter hydrostatischem Druck der Übergangszustand einer Umlagerung in ein Minimum auf der potentiellen Energieoberfläche (PES) umgewandelt werden kann. Unsere Simulationen, die mit der Born-Oppenheimer-Molekulardynamik (BOMD)-Methode durchgeführt wurden, ergaben, dass ein gradueller Anstieg des hydrostatischen Drucks bis zu 120 GPa zur Bildung des Übergangszustands (d. h.

des fünfgliedrigen Rings) führt. Umgekehrt führte eine schrittweise Verringerung des Drucks zur Bildung einer 70:30-Mischung aus dem Produkt und dem Edukt der sigmatropen Umlagerung. Um experimentelle Studien zu erleichtern, haben wir Referenzdaten in Form von simulierten IR-, Raman- und zeitaufgelösten UV/vis-Absorptionsspektren beigefügt.

Schlussendlich wurde ein multiskaliges mechanochemisches Modell entwickelt, um die SP Mechanophoraktivierung in linearen Poly(methylmethacrylat)-Polymeren (PMMA) zu simulieren. Um dies zu erreichen, parametrisieren wir die Kraftfelder von SP- und MC-Molekülen in der Molekularmechanik (MM), um eine SP-MC Isomerisierungs kraft-modifizierte potenzielle Energieoberfläche (PES) als Referenz-Quantenmechanik (QM) Energien zu erhalten. Während Massendeformationen, wie einachsige Zug- und Scherverformung des Systems, wird die Aktivierung der Mechanophore bei $5 \cdot 10^7$ und $5 \cdot 10^8$ s⁻¹ Dehnungsraten erfasst. Die molekulare Umlagerung der Ketten in Abhängigkeit von der angewandten Dehnung lieferte die Erkenntnis, dass die Kraftübertragung von der makroskopischen Ebene auf die lokale Umgebung des Mechanophors auf eine direkte Kettendehnung zurückzuführen ist. Interessanterweise haben wir auch festgestellt, dass die Art der Belastung einen starken Einfluss auf das Spannungs-Dehnungsverhalten und die daraus resultierende mechanochemische Aktivität hat. Insgesamt liefern unsere Ergebnisse ein detailliertes Verständnis des Kraftübertragungsverhaltens bei der Verformung im Massenmaßstab, das die Aktivierung des Mechanophors bestimmt.

Contents

Abstract	ix
Abbreviations and symbols	xxii
1 Introduction	1
1.1 Mechanochemistry	1
1.2 Polymer mechanochemistry	3
2 Theoretical background	11
2.1 Theoretical models incorporating external forces	11
2.2 Force-modified potential energy surface	12
2.3 Modeling external forces for single molecules	14
2.3.1 COGEF	14
2.3.2 EFEI	16
2.3.3 X-HCFF	17
2.4 Stress on bulk scale	19
2.5 JEDI analysis	22
2.6 QTAIM basin analysis	24
2.7 Quantum mechanical methods	26
2.7.1 Density functional theory	29
2.8 Molecular mechanics methods	33
2.8.1 Force field	33
2.9 Molecular dynamics simulations	37
2.10 Statistical ensemble in molecular dynamic simulations	39
2.11 Periodic boundary conditions	41
3 Mechanophores Response to Stretching Forces	43
3.1 Scope of the project	43
3.2 Publication: The mechanism of flex-activation in mechanophores revealed by quantum chemistry	45
3.3 Additional information	55
3.3.1 Computational details	55
3.3.2 Electron density for deformation modes 1 and 2	57
3.3.3 Normal mode analysis	57
3.4 Publication: The activation efficiency of mechanophores can be modulated by adjacent polymer composition.	59
3.5 Additional information	71
3.5.1 Computational Details	71
3.5.2 Dependence of rupture force on the length of the alkyl chain	72

3.5.3	Influence of the linker on the rupture force	73
3.5.4	Rupture forces using combinations of different linkers	74
3.5.5	JEDI analysis	74
3.5.6	Electron density at the bond critical points	76
3.5.7	Bond angles in the linkers	77
4	Stress induced from pressure	83
4.1	Scope of the project	83
4.2	Publication: A two-step baromechanical cycle for repeated activation and deactivation of mechanophores.	85
4.3	Additional information	95
4.3.1	Computational Details	95
4.3.2	Propagation of electron density in the BOMD trajectories	97
4.3.3	Baro-mechanical data for the BOMD trajectories	98
4.4	Publication: Trapping the transition state in a [2,3]-sigmatropic rearrangement by applying pressure.	99
4.5	Additional information	111
4.5.1	Influence of functionals on the "trapping" pressure	111
4.5.2	Structural parameters of the five-membered ring	112
4.5.3	Number of imaginary frequencies as a function of pressure	112
4.5.4	Propagation of bond angles in the BOMD trajectories	113
4.5.5	Time evolution of the RMSD	114
4.5.6	Barochemical and structural data for the BOMD trajectories	115
4.5.7	Time-resolved UV/Vis spectra	116
4.5.8	Propagation of electron densities in the BOMD simulations	117
4.5.9	IR and Raman spectra	119
5	A multiscale mechanochemical model	121
5.1	Introduction	123
5.2	Methodology	125
5.2.1	Parameterization of SP-MC isomerization	125
5.2.2	Simulation details	127
5.2.3	End-to-end distance distribution	128
5.2.4	Thermal properties	129
5.2.5	Bulk deformation	130
5.3	Results	131
5.3.1	Energy distribution	137
5.3.2	Effect of temperature	138
5.4	Conclusion	139
5.5	Additional information	141
6	Summary and outlook	149
	Bibliography	155
	Appendices	196
	List of Publications	215

Abbreviations

AFM	Atomic Force Microscopy
BOMD	Born-Oppenheimer Molecular Dynamics
COGEF	COstrained Geometries simulate External Force
DFT	Density Functional Theory
FMPEs	Force-Modified Potential Energy Surface
gDCC	<i>gem</i> -Dichlorocyclopropane
JEDI	Judgement of Energy DIstribution
LDA	Local Density Approximation
MD	Molecular Dynamics
MC	Merocyanine
PBC	Periodic Boundary Conditions
PES	Potential Energy Surface
PMMA	Poly(methyl methacrylate)
PS	Polystyrene
PVP	Poly(vinyl pyrrolidone)
EFEI	External Force is Explicitely Included
QTAIM	Quantum Theory of Atoms in Molecules
SMFS	Single Molecule Force Spectroscopy
SP	Spiropyran
TS	Transition State
X-HCFF	eXtended Hydrostatic Compression Force Field
XP-PCM	eXtreme Pressure Polarizable Continuum Model

Chapter 1

Introduction

1.1 Mechanochemistry

Thermal activation is a conventional method for initiating chemical reactions. This method involves a straightforward application of heat to a chemical system, which supplies the desired thermal perturbation to overcome the activation energy barrier of the reaction. In addition to heat, activation energy can also be supplied by other sources such as light or electricity. Moreover, mechanical forces have the capacity to transfer energy to bonds thus facilitate chemical reactions. The use of mechanical forces to initiate a chemical reaction is known as "mechanochemistry".

It is challenging to trace the historical origins of mechanochemistry. The field has been present since ancient times, where reactions were unintentionally initiated through grinding and rubbing techniques.^[1] In the 1800s, mechanochemistry was subject to formal academic research for the first time when Faraday^[2] and Carey Lea^[3] discovered the reduction of silver halides in a mortar.

The origins of the term "mechanochemistry" can be traced back to Wilhelm Ostwald, who first coined it in the early 20th century in his *Handbuch der Allgemeinen Chemie*.^[4] In this work, Ostwald identified mechanochemistry as a distinct

subfield of chemistry, alongside more established areas such as thermochemistry, electrochemistry, and photochemistry.

In its most basic form, mechanochemistry can be understood as a chemical process that serves to release stress, imposed from outside sources. Per definition, stress refers to the magnitude of force or pressure applied per unit area of a material. At the molecular level, stress can be understood in terms of mechanical forces, which can be applied at both the molecular and bulk scales.

The present state of the field of mechanochemistry is characterized into three partially overlapping subfields: biomechanochemistry,^[5] polymer mechanochemistry,^[6] and powder mechanochemistry.^[7]

Biomechanochemistry, also known as mechanobiochemistry, focuses on the application of mechanical forces to biological molecules and materials, such as proteins,^[8,9] DNA,^[10] and cells,^[11] in order to understand their chemical and physical properties and how they respond to mechanical stimuli. Polymer mechanochemistry involves the use of stretching,^[12] shearing,^[13] or compressing^[12,14] forces to induce the scission of covalent bonds to manipulate the structural properties of polymers. Polymer mechanochemistry has a broad range of applications integrated with both other subfields.^[15] The third subfield, powder mechanochemistry, focuses on applying the mechanical energy to contacting crystalline surfaces via relative motion or other tribochemical ways to initiate chemical changes.^[16] This approach involves the formation and rupture of both covalent and non-covalent bonds.

This thesis focuses on the field of polymer mechanochemistry, specifically on the external stress response of bulk polymers and small molecular subunits embedded within the polymers. In the following section, a brief introduction to polymer mechanochemistry will be provided to contextualize the research work and highlight its significance.

1.2 Polymer mechanochemistry

The origins of polymer mechanochemistry can be traced back to the 1930s, when Staudinger first time reported the reduction in molecular weight of polystyrene (PS) upon mastication using high speed ball milling.^[17-19] This discovery inspired further studies to explore the mechanical properties of polymers and the relationship to their chemical structure. Kauzmann and Eyring in 1940, suggested that the shear forces developed due to the mastication give rise to bond rupture events and lead to the formation of radical species at the newly broken chain ends.^[20] Later under the investigation of electron spin resonance (ESR) Tabata et al. confirmed that the PS and poly(methyl methacrylate) (PMMA) cleavage is a result of the homolytic scission of C–C bonds.^[21]

One of early key developments in the field was in 1980, when Encina et al. found that the incorporation of weak peroxide linkages into the polymer backbone increased the rate of degradation of the poly(vinyl pyrrolidone) (PVP) polymer under ultrasonication, which is tenfold faster than for neat PVP.^[22] These findings suggest that the molecular structure can be utilized to program the location and outcome of a mechanochemical reaction, paving the way for the development of site specific mechanochemical activation.

In 2005, Moore and colleagues showcased the ability to modify the properties of polymer chains by selectively targeting relatively weak covalent bonds.^[23] For this purpose, single azo linkage was incorporated into the center of the backbone of a poly(ethylene glycol) (PEG) polymer. The mechanical forces that arose from ultrasonication caused a specific cleavage of the weak homolytic C-N bond, leading to the formation of a single type of chain end and resulted in fragments of low polydispersity. These results gave polymer mechanochemistry a new direction and led to the birth of the "mechanophore" concept.

A remarkable study "Biasing reaction pathways with mechanical force"^[24] of 2007 helped to launch the concept of mechanophores on its fascinating journey, which led to the discovery, that mechanochemical activation can be used to govern chemical reactions that are not allowed via other stimuli (such as heat or light). In this study Hickenboth et al. have showed that the cis and trans form of 1,2-disubstituted benzocyclobutene (BCB) mechanophore produce identical products when subjected to external forces, thereby contravening the principles of orbital symmetry. This finding suggests that the mechanical forces can be used to alter the reaction coordinates irrespective of orbital symmetry.

Mechanophores are small molecular units that undergo structural rearrangements (via bond scission or conformational rearrangement), in response to the applied mechanical forces. The resulted rearrangement generates a range of responses, from physical signals (like changes in color or light emission) to chemical signals (formation of reactive radicals, or the release of small molecules).

Mechanophores showing changes in the absorption spectra as a result of structural rearrangement are known as mechanochromophores or mechanochromic materials. Under deformation, if a material exhibits a significant bathochromic shift in its visible absorption spectrum, it becomes easy to detect stress or damage in the material, making such materials attractive for use in stress-sensing and/or damage-detection applications.

A heavily researched bathochromic mechanophore is Spiropyran^[25,26] (SP) in which indoline and benzopyran moieties are connected through the spiro form. Under a specific amount of force the labile C-O bond present near the spiro junction ruptures and leads to a 6π electrocyclic ring opening reaction. This mechanical activity turns colorless/yellow SP to the blue/red/purple colored activated Merocyanine (MC) form.

In 2009, Moore et al. developed a novel approach to activate SP inside the solid polymeric materials poly(methyl acrylate) (PMA) and PMMA, by applying mechanical forces.^[12] This marked the first time that a SP molecule had been utilized as a mechanochromic mechanophore. When subjected to tensile stress, the initially colorless SP molecules transformed into a vividly colored MC form, inducing a dramatic shift in the color of the PMA material from yellow to purple. The activation of SP inside the PMMA is quite challenging under tensile stress. Therefore PMMA bead samples were introduced to the compression deformation, which caused a change in color at the center of the bead when the strain level exceeded the yield point.^[12] Under loading tests, the monofunctional SP units (only one side of spiro junction attached from polymer) had shown no detectable change in color or significant fluorescence, which confirmed that SP molecules were activated only through external forces transduced through the spiro form. It was found that the SP molecule only undergoes activation when the applied pulling forces provide enough force to break the C-O bond. For this purpose, the opposite points of the spiro junction serve as the anchor to apply stretching and transduce the force efficiently.

Polymer mechanochemistry is a rapidly growing area of research that focuses on the development of smart force induced materials.^[27] The mechanophore concept has played a key role in advancing this field and thereby led to the development of hundreds of new mechanophores for specific polymer systems.^[28] To achieve mechanophore activation in different systems, forces can be generated through a variety of means, including Single-Molecule Force Spectroscopy^[29,30] (SMFS), sonication,^[31,32] ball mill grinding (BMG),^[33,34] extrusion,^[35] tensile,^[36] and compression.^[5,15,37,38]

Atomic Force Microscopy (AFM) is a widely used tool for conducting SMFS experiments on single polymer chains.^[39–42] This technique involves bringing a

sharp tip (probe) attached to a cantilever onto the molecular substrate. The forces exerted through the tip are then recorded using a detector based on the motion of the cantilever. By applying Hooke's law, the electrical signal obtained from the detector is converted into the force acting on the sample. The AFM technique is sensitive up to the piconewton regime. For example, SMFS experiments performed by Wang et al. in 2014 showed that the activation force for the *E*-alkene-substituted *gem*-dichlorocyclopropane (gDCC) mechanophore was 0.4 nN lower than the force required for the activation of *Z*-alkene isomer mechanophore.^[43]

The majority of studies in polymer mechanochemistry are typically conducted in a solution phase.^[15] The most common method for producing mechanochemical reactions in dilute solutions is through the use of ultrasonication.^[44,45] This process involves utilizing a sonication (sound energy) probe, which produces sonic waves responsible for the cavitation (formation of microscopic vacuum bubbles) and pressure fluctuations in the medium. These pressure fluctuations and bubble collapses generate shear forces that act on the polymer chains located near the cavitation sites.^[46] As a result, the polymer chains gain high velocity from the elongational shear forces and induce the mechanochemical activation.

A common approach to apply mechanical forces on powdered materials is ball-mill grinding (BMG).^[34,47–49] The Grinding technique is utilized for exploring the activation of small molecules through mechanical stimulation, without the need to integrate the mechanophore into a polymer matrix.

Extrusion,^[50] on the other hand, is a technique used to force the materials through a specific cross-section. In polymer mechanochemistry, extrusion is used to derive the mechanochemical processes within the polymer melt.^[51–53] While performing the extrusion, sudden acceleration near at the contraction site generates a continuous flow of high strain rate, thereby stretching forces through the polymer chains are responsible to initiate the mechanophores activation.^[35]

In addition to ball-milling and extrusion, tensile^[54–57] and compression^[58,59] are two different techniques commonly used to examine the bulk deformations of a material, involving direct stretching or compression respectively. The forces generated from both techniques distribute throughout the system, depending upon the polymer architecture and material properties. The tensile deformation leads to monotonic tension in the material. Depending upon the magnitude of the tensile stress on the polymers they exhibit elastic or plastic behaviour.^[60] The mechanophores present in linear polymer chains activate upon full elongation of the chains, after the critical force is delivered. For instance, the SP-PMA polymer system requires high stress on material for mechanoactivation just before the ultimate failure of the system. In the compression approach, the areas experiencing the highest stress levels are typically the first to exhibit activation. For example, the highest level of activation in a compressed SP-PMMA bead occurs at its center.^[12] This is due to the Poisson effect, which generates the greatest tensile stresses perpendicular to the applied compressive load at this location.

Apart from experimental techniques, severe progress has been achieved in the field of quantum mechanochemistry.^[61] In the last two decades, a wide range of quantum mechanochemical computational tools,^[62–64] based on electronic structure methods have been developed (see Section 2.3) to study the mechanical response in terms of molecular rearrangements. For instance a combination of experimental and computational approaches has resulted in the development of newly designed materials, such as ladder-type cyclobutane mechanophores^[29] and mechanophores with the gating functionality.^[65] However, at larger length scales, polymers exhibit complex behavior such as viscoelasticity,^[66] crazing,^[67] yielding and fracture,^[68] which are difficult to predict based solely on molecular-level properties. Multiscale modeling approaches^[69–71] aim to bridge the gap between these different length

and time scales, by integrating information from quantum chemical dynamics,^[61] molecular simulations,^[72] mesoscale simulations^[73] and continuum-level models.^[74]

In 2014, Silberstein et al. developed a model framework that describe the SP mechanophores response to mechanical loading within the PMA elastomeric matrix.^[75] This model combines the results from *ab initio* steered molecular dynamics (AISMD) simulations^[64] of the mechanophore with rubber elasticity theory. The predicted activation from this model is in reasonable agreement with experimental data. However, over the plastic region, the activation model performs relatively poorly compared to the experimental results.

Later, in 2016 Koo and coworkers developed an atomistic modeling framework to simulate the cyclobutane-based mechanophores within the epoxy-based thermoset polymer.^[76] To consider the mechanophore activation, a hybrid molecular dynamics (MD) simulation framework was developed by combining the Merck Molecular Force Field^[77] (MMFF) and Reactive Force Field^[78] (ReaxFF). To address mechanophore activation events a local work approach was adopted to calculate the work done (i.e. $\int \vec{F} \cdot d\vec{L}$) by a local applied force, which resulted a accurate description of mechanical deformation and mechanophore activation. The local work approach yielded better results and provided a more accurate understanding of the mechanisms involved in mechanophore activation.^[76]

Outline of the thesis

The primary focus of this thesis is to investigate the effect of external stretching and compression forces on mechanophores. To achieve this goal, a combination of quantum mechanical and classical methodologies are utilized to develop a comprehensive understanding of the molecular response at both the single molecule and bulk levels.

The theoretical background of the quantum mechanochemical computational tools are described in Chapter 2. This includes an introduction to the force-modified

PES and force-analysis tools. The theoretical concepts of classical dynamics such as the concept of stress tensors (a possible way to consider stress over the bulk scale in classical dynamics simulations), molecular mechanics methods, force-fields, statistical ensembles, and periodic boundary conditions are discussed in this chapter. Additionally, the chapter covers the topology analysis method i.e. atoms in molecules (AIM) analysis^[79] and a general introduction to quantum mechanical methods.

Chapter 3, 4 and 5 are dedicated to specific projects and therefore each begin with a detailed outline of the projects scope and aims. Chapter 3 is dedicated to explore the role of stretching forces over different pulling coordinates and linker compositions to enhance the efficiency of mechanophores.

In Chapter 4 the role of external forces resulting from pressure is examined. Theoretical investigations under hydrostatic pressure led to the prediction of a baro-mechanochemical cycle for the SP mechanophore, which is elaborated in the first section of the Chapter. The second section involves the simulation of a pressure-induced [2,3]-sigmatropic rearrangement, in which the trapping of a five-membered cyclic transition state is proposed.

Chapter 5 is dedicated to a multi-scale model, which is developed to consider the SP mechanophore activation in PMMA polymer chains. This chapter provides a detailed analysis of the mechanophore activation process under tensile and shear deformations over a range of temperatures.

Chapter 6 provides a brief summary of the research conducted and its implications. This chapter also includes an outlook for future research in the field of polymer mechanochemistry.

Chapter 2

Theoretical background

2.1 Theoretical models incorporating external forces

In the realm of theoretical models, the incorporation of external forces has been a topic of active research for several decades. Shortly after the introduction of their transition state theory, Eyring et. al. developed a force dependent extension to the model.^[20] This approach allowed for the inclusion of external forces in the calculation of transition state rates, providing a more accurate depiction of the underlying physical processes.^[80,81] Later Zhurkov proposed a general rate relation (between lifetime, stress, and temperature) based on the Arrhenius equation^[82], which served as a critical precursor to the subsequent development of Bell type models.^[83,84] These models, named after George Bell, who proposed a theoretical framework to estimate the reaction rates on the basis of cell adhesion forces.^[83] Bell's model postulates that the activation energy required for a reaction can be reduced by a linear term that is depending on the force exerted along the reaction coordinate. The relationship between the applied force and the activation energy of a chemical reaction is expressed using equation 2.1

$$\Delta G^\ddagger(F_0) = \Delta G^\ddagger(0) - F_0 \Delta q \quad (2.1)$$

where $\Delta G^\ddagger(0)$ represents the activation energy of the reaction in the absence of any external force F_0 , and Δq is a structural parameter that characterizes the change in the reaction coordinate due to the applied force.

$$k(F_0, T) = A \cdot \exp\left(\frac{\Delta G^\ddagger(0) - F_0 \Delta q}{RT}\right) \quad (2.2)$$

Equation 2.2, relates the force required to break a bond to the rate (k) at which the bond is ruptured, where A is the Arrhenius pre-exponential factor. Further approximations to the model led to more accurate depiction of the system under constant forces.^[84] Readers who seek a comprehensive understanding of the models are referred to relevant review articles^[61,84–86] and the corresponding references cited therein.

2.2 Force-modified potential energy surface

When a molecule is exposed to external forces, it can lead to various effects on its properties and behavior. The effect of the external forces can vary based on the type,^[12] magnitude,^[87] and duration of the forces,^[88] as well as the molecular structure^[24,89,90] and environment.^[91,92] For instance, mechanical forces can alter the conformation of the molecule,^[12,30,93] initiate chemical reactions,^[94,95] modify mechanical properties^[96,97] and influence the potential energy surface of the molecule.^[64,98]

Insight into the interaction between external forces and potential energy surfaces helps to better understand the underlying chemical and physical principles that govern the molecular behavior.^[99] A simple method to model the potential energy

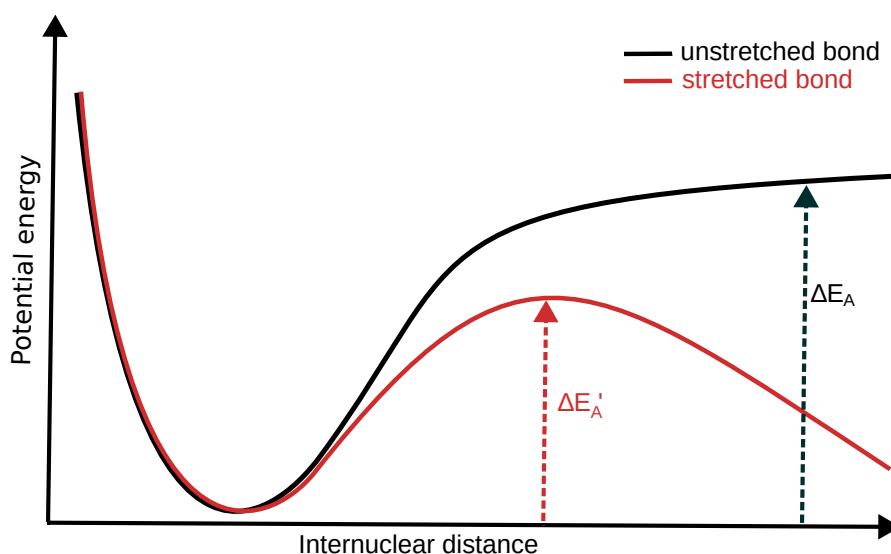


Figure 2.1: Schematic representation of dissociation of a covalent bond under various potentials. The black curve corresponds to the relaxed Morse PES, while the red curve shows the tilted Morse PES, which shows the changes occurred as a response to the external applied force. ΔE_A and $\Delta E_A'$ corresponds to different energy barriers at zero force and under constant force respectively.

function of a bond is the Morse potential. The Morse-type potential as a function of inter-nuclear distance r is given by

$$V(r) = D_e[1 - e^{-\beta(r-r_e)}]^2, \quad (2.3)$$

where D_e is the dissociation energy, r_e is the equilibrium bond distance, β is the stretching constant, which describes the slope of potential energy as a function of distance between the atoms. The potential $V(r)$ for a unstretched covalent bond is expressed in Figure 2.1.

The effect of force on the potential energy is significant. For instance, under the exposure of a constant external stretching force F_0 along the coordinate r , the potential $V(r)$ undergoes a distortion from its equilibrium shape (see Figure 2.1).

$$V_F(r) = D_e[1 - e^{-\beta(r-r_e)}]^2 - F_0(r - r_e) \quad (2.4)$$

A potential energy surface modified this way, i.e. $V_F(\mathbf{r})$, is commonly known as a force modified potential energy surface (FMPES), and can be expressed using a Morse potential as equation 2.4. The additional term, i.e. $F_0(\mathbf{r} - \mathbf{r}_e)$ is a straightforward product of the restoring force F_0 and the change in spring length, i.e. $\mathbf{r} - \mathbf{r}_e$, using the Hook's law.

2.3 Modeling external forces for single molecules

When a molecule is subjected to external mechanical forces, its nuclear structure undergoes a significant change. There are two different approaches (i.e. isometric and isotensional) to consider the effect of external forces on molecules. In the isometric approach the deformation is considered in such a way that the distance between two atoms is fixated. On the other hand, in the isotensional approach the explicit mechanical force is applied as an additional term to the gradient or as potential energy that maintains a constant tension. In the following subsections the examples for both approaches are discussed in detail.

2.3.1 COGEF

In 2000, Martin Beyer introduced the term **COGEF** as an abbreviation for **CO**nstrained **G**eometries simulate **E**xternal **F**orce^[63]. This methodology involves a specialized protocol where a specified internal coordinate is fixed at a particular value, and a relaxed PES scan of the strained molecule is carried out. Throughout this process, the entire system, with the exception of the specific fixed internal coordinate, is permitted to relax locally. To acquire the COGEF potential, the constraint value is increased incrementally and a constrained geometry optimization performed for each step.

The COGEF potential can be expressed using following equation

$$V_{\text{COGEF}}(\mathbf{x}, q_0) = V_{\text{BO}}(\mathbf{x}) - \lambda(q(\mathbf{x}) - q_0) \quad (2.5)$$

where q_0 is the geometrical constraint or control parameter. V_{BO} denoted the Born-Oppenheimer PES and depends on the nuclear Cartesian coordinates \mathbf{x} and λ is a Lagrange multiplier.

As all degrees of freedom are optimized locally along the constrained coordinate, the only remaining non-zero component of the PES gradient is the force that acts along the fixed, or strained, coordinate. Consequently, the required mechanical force to induce this change or assessment of a bond breaking point during the COGEF scheme can be obtained by the first derivative or the point of inflection of the potential. This makes the COGEF method a versatile methodology that can be used in conjunction with DFT or wave function based approaches and has been implemented in many quantum chemical packages.

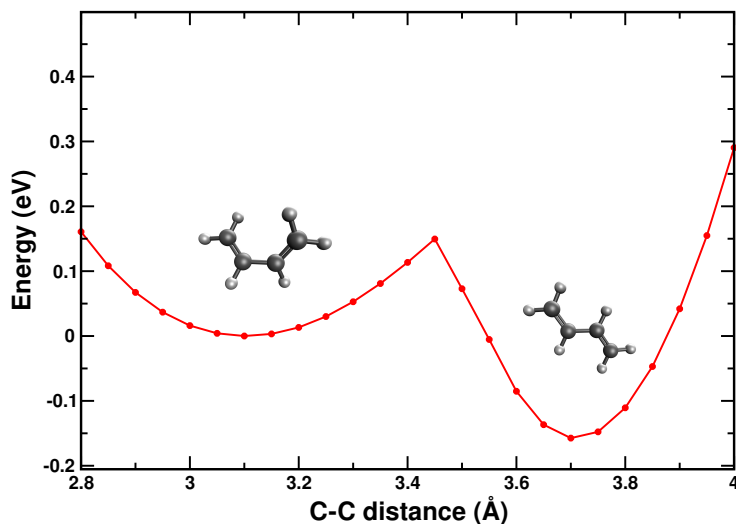


Figure 2.2: 2D-PES of a 1,3-butadiene molecule. The end-to-end carbon atom's distance is varied using the COGEF scheme. The PES scan is carried out from 2.8 Å to 4 Å with a step size of 0.05 Å at B3LYP^[100–102]/cc-pVDZ^[103] level of theory.

Figure 2.2 presents the utilization of a 1,3-butadiene molecule in the COGEF scheme, where the constraint is applied along the end-to-end carbon atoms. The drop in energy is observed at 3.45 Å in the Figure 2.2 corresponds to the change from cis to trans confirmation of the molecule. This observation indicates that the constraints applied along the anchor atoms caused rearrangements in the molecular geometry, while the other degrees of freedom were locally optimized on the PES.

For the past two decades, COGEF has served as a valuable tool for predicting the precise maximum amount of force required to break a covalent bond. Recently this method has been employed to over a hundred of different mechanophores to investigate its efficiency^[28]. At the B3LYP/6-31G* level of DFT, the investigation revealed excellent agreement with experimentally determined reactivity, and highlighted the reliability of COGEF as a method for predicting mechanochemical information.

As the COGEF method is solely based on constrained geometry optimizations, its applicability is limited in molecular dynamics simulations that involve constraints. Therefore, it is not an appropriate tool for studying the impact of constraints under thermal oscillations. The limitations of the isomeric approach can be resolved by utilizing the isotensional approach.

2.3.2 EFEI

Another way to consider the direct influence of mechanical force on the PES rather than structural constraints is via the **External Force is Explicitly Included** method (**EFEI**), which was introduced by Marx and coworkers in 2009^[62]. The forces considered in this method are based on the isotensional approach, which explicitly considers the distortion of the equilibrium geometry by mechanical force.

In the EFEI method, the force-modified PES is obtained by applying a distortion potential, defined by a constant force F_0 acting on respective atoms of a geometry x , as in the following equation

$$V_{EFEI}(\mathbf{x}, F_0) = V_{BO}(\mathbf{x}) - F_0 \cdot \mathbf{q}(\mathbf{x}), \quad (2.6)$$

where $V_{BO}(\mathbf{x})$ is the Born-Oppenheimer PES and $\mathbf{q}(\mathbf{x})$ is a structural parameter. The geometry of the distorted molecule is then obtained by optimizing the EFEI potential. The convergence of a geometry optimization under external force occurs when the external force F_0 acting on the molecule is canceled by the internal restoring force of the molecule.

The practical implementation of a geometry optimization for a system under the influence of an external force is carried out by adding a constant force to the gradient along the vector joining two atoms. This joining vector takes care of the overall translations and rotations of the molecule. The direction of the joining force vector is updated at every iterative cycle of the optimization.

The EFEI method yields the exact distortion of the molecular structure with force, as with the control parameters. Moreover, at a stationary point, the EFEI potential ($V_{EFEI}(F_0)$) and COGEF potential ($V_{COGEF}(q_0)$) are related through the Legendre transformation, with q_0 and F_0 being conjugate variables. Hence, both methodologies will produce identical distorted geometries under similar conditions.

Compared with the COGEF method, the EFEI method offers the advantage of performing the calculation at a precisely defined magnitude of external force. However, to accomplish this using the COGEF method, a specific number of calculations are necessary along the COGEF potential. Thus it makes the computational requirements of each approach dependent upon the nature of the problem at hand.

2.3.3 X-HCFF

The mechanochemical methods (COGEF and EFEI) discussed above are based on the implementation of external stretching forces on molecules, causing them to either

elongate or to be compressed by allowing the force vectors to act along a specific coordinate. However, in more complex situations, for example when a molecule is distorted by pressure, many different external forces act on the molecule, allow the system to include bending and torsion distortions as a primary mechanism for mechanochemical activation.^[104,105]

At the single-molecule level, various models have been developed to simulate the behavior of molecules under pressure.^[106] One prominent example is the eXtreme Pressure Polarizable Continuum Model (XP-PCM), which is an extension of the Conductor-like PCM (CPCM) implicit solvent model. Here, pressure is applied by decreasing the cavity size of the molecule to stronger Pauli and coulomb repulsion interactions with the solvent. Alternatively there are mechanochemical pressure models such as Generalized Force-Modified Potential Energy Surface (G-FMPES) in which pressure dependent external forces are added to the molecular gradient. The Hydrostatic Compression Force Field (HCFF)^[107] pressure model was introduced as an advancement of the G-FMPES method, in which the pressure is calculated from molecular van der Waals (vdW) surface area using the equation 2.7.

$$P_{HP} = \frac{\langle \|f\| \rangle}{A_{vdW}} \quad (2.7)$$

However, the pressure applied in G-FMPES and HCFF compresses the molecule towards its mass center, which leads to unrealistic results for non-spherical molecules.^[108] Moreover, the previously discussed models share the common limitation, that the applied pressure is not possible to be determined beforehand.

To circumvent previous pressure models limitations, the eXtended **H**ydrostatic **C**ompression **F**orce **F**ield (**X-HCFF**)^[108] method was introduced by Tim Neudecker (former Stauch), in 2020. The X-HCFF pressure model is an extension of the HCFF model that was developed to overcome the previously introduced mechanochemical models drawbacks by allowing full control over the applied pressure and simulating

hydrostatic compression of extended molecules realistically. Therefore in X-HCFF, the vdW surface of a molecule is discretized and then for each surface element a force vector is projected onto the closest atom.

In the X-HCFF pressure scheme, the vdW surface is discretized using a lebedev grid algorithm, which after neglecting overlapping regions results a tessellated surface. Each surface tessera j corresponds to an area element A_j . The force $f_{i,j}$ acting from each tessera to the corresponding atom i can be expressed using equation 2.8

$$f_{i,j} = -P \cdot A_j \cdot \frac{r_i - r_j}{|r_i - r_j|}, \quad (2.8)$$

where r_i and r_j are the positions of atom i and tessera j respectively.

As a result, the net force f_i acting on an atom i , can be calculated as a sum of $f_{i,j}$ (see equation 2.9)

$$f_i = \sum_j^{N_{Tess,i}} f_{i,j} \quad (2.9)$$

where $N_{Tess,i}$ denotes all tessera closest to atom i . The overall effect of forces acting on the atoms within a molecule push the atoms closer together, causing the molecule to compress. For the convergence of the molecule while performing the geometry optimization under pressure, the net resulting forces f_i on each atom are added to the nuclear gradient and an updated tessellated surface is constructed at each optimization step. The convergence of the molecule is considered when the external pressure force is canceled by the restoring force of the molecule.

2.4 Stress on bulk scale

When considering materials at a bulk scale, stress refers to the set of internal forces acting within a material. As per definition *Stress* is defined as applied load divided

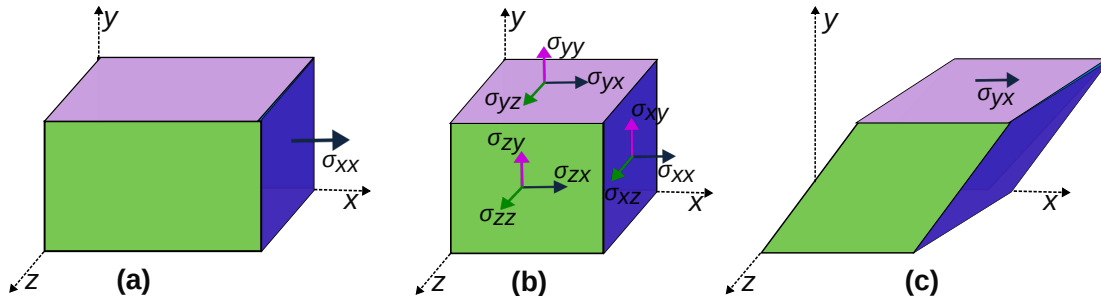


Figure 2.3: An illustration diagram of the stress tensor in the i and j principal direction (b), where σ_{ii} express the uniaxial stress tensor components (a), while σ_{ij} (i.e. $i \neq j$) shows the shear stress components (c). The symbols i and j can represent any of the three principal axes.

by the cross-sectional area over which the load is distributed. Stress in a material is not uniform and varies across space, with its distribution being defined by a tensor known as the stress tensor σ . The mathematical expression for stress acting over the cross-sectional area \vec{A}_i can be expressed using the following equations

$$\vec{F}_i = \vec{\sigma}_{ij} \vec{A}_{ij} \quad (2.10)$$

$$\begin{bmatrix} F_x \\ F_y \\ F_z \end{bmatrix} = \begin{bmatrix} \sigma_{xx} & \sigma_{xy} & \sigma_{xz} \\ \sigma_{yx} & \sigma_{yy} & \sigma_{yz} \\ \sigma_{zx} & \sigma_{zy} & \sigma_{zz} \end{bmatrix} \begin{bmatrix} A_x \\ A_y \\ A_z \end{bmatrix} \quad (2.11)$$

Here the stress component (i.e. σ_{ij}) is generated due to the force F_i applied over the material. The stress component's indices i.e. i and j expressed in equation 2.10 can be any of the principal axes (x , y or z), where i denotes the direction of the stress and j is the orientation of the respective surface, i.e. A , on which the stress is applied. In the vector notation \vec{F}_i , the index i represents the direction of the force component. As per definition the units of the stress are expressed as force per unit area i.e. N/m^2 or measured in Pascals (Pa).

Based on the type of external forces exerted over the material, stress can be divided into different forms. If the load is applied to the material is uniaxial extensional, then

the stress is called tensile stress. Tensile stress can be understood as a stress caused by the material being pulled apart along its length. If the material is compressed along its length, it is defined as a compressive stress. A third type of stress is shear stress, where the external force acting on the material is set parallel to the plane in which the material is situated. This causes the material to deform by sliding along a plane parallel to the applied forces.

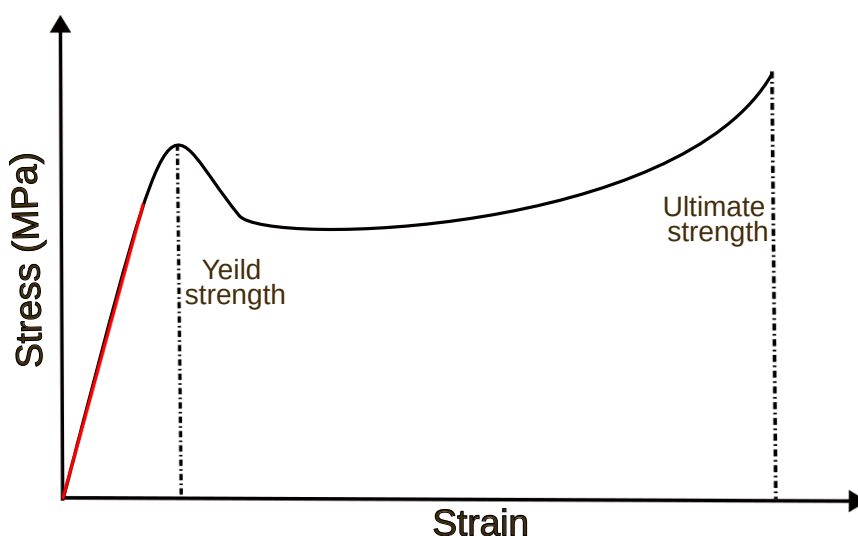


Figure 2.4: Illustration of a stress-strain curve for the behavior of an amorphous polymer, with the brittle yield stress region indicated by the red linear line. The curve also depicts the material’s yield strength, which represents the stress level at which permanent deformation occurs, and ultimate strength, which is the maximum stress level the material can sustain before experiencing failure or fracture.

The capacity of a material to withstand under stress without undergoing significant deformation, fracture, or other forms of permanent damage is termed as *strength* of the material. The strength of the material specially for polymers under stress can be influenced by a range of factors, including molecular weight,^[109] crystallinity,^[110] cross-linking,^[111] temperature,^[112] and loading conditions.^[113]

As other materials, polymers exhibit elongation when subjected to stress. The resulting elongation, or deformation, is known as strain, and is defined as the change in length of a material divided by its original length. Strain is a dimensionless

quantity that can be expressed as a percentage. The correlation between the level of deformation (strain) and the magnitude of force or stress exerted on a material is explored using a strain-stress curve (SSC) (cf. Figure 2.4).

2.5 JEDI analysis

The prior discussion was focused on the techniques that model the distorted geometries under an external force. The resulting distortions on the molecular level are helpful to understand how the molecules respond under external forces. Moreover, the precise explanation for why only certain regions of a molecule respond to such forces while others remain unaffected still is a subject of interest.

In the last decade, several tools were developed to capture the force-bearing scaffold present in the mechanically deformed molecule.^[114] Some of these tools are focused on quantifying forces, while others are designed to analyze the distribution of stress energy within molecules. The approaches based on quantifying forces will not be comprehensively discussed in this thesis, however further details can be found in the literature.^[114]

In 2016, a quantum chemical analysis tool known as **JEDI** (**J**udgement of **E**nergy **D**istribution)^[115–117] analysis was introduced by Tim Neudecker et al.. JEDI is used to evaluate the distribution of mechanochemical stress energy within a deformed molecule.

The JEDI analysis is based on the idea that mechanical energy is stored in internal coordinates and can be calculated in a more simplified way by directly analyzing the energy present in the internal coordinates of the molecule. This stress energy contribution from all the internal coordinates (bond lengths, bond angles and torsions) provides a comprehensive picture of the energy distribution in a mechanically deformed molecule. In the field of mechanochemistry, JEDI analysis

has been found to be effective for describing changes in bond lengths, bond angles, and dihedral angles^[118].

JEDI analysis relies on the harmonic approximation, which assumes that the potential around the equilibrium structure of a molecule can be approximated as a Taylor series truncated at second order. This assumption allows for a simplified, yet effective, method of analyzing the internal mechanics of the molecule, which is a key component of the JEDI analysis method. It should be noted that the JEDI analysis approach does not take anharmonic effects into account, thus when using JEDI, it is important to consider the limitations of the harmonic approximation and any potential implications for the interpretation of the results of a JEDI analysis.

To calculate the energy present in each internal coordinate (i) of a mechanically deformed molecule, the JEDI analysis uses the following expression

$$\Delta E_i = \frac{1}{2} \sum_j^M \frac{\partial^2 V(\vec{q})}{\partial q_i \partial q_j} \Big|_{\vec{q}=\vec{q}_0} \Delta q_i \Delta q_j \quad (2.12)$$

the first term, $\frac{\partial^2 V(\vec{q})}{\partial q_i \partial q_j} \Big|_{\vec{q}=\vec{q}_0}$ is the Hessian of the equilibrium geometry \vec{q}_0 , in redundant internal coordinates (q). As a result of distortions in the internal coordinate (i), the change is expressed as Δq_i .

Finally, the harmonic stress energy E_{harm} is calculated by summing up the energy contributions of all internal coordinates i , i.e. E_i and expressed using the equation 2.13

$$E_{harm} = \sum_i E_i = \frac{1}{2} \sum_{i,j}^M \frac{\partial^2 V(\vec{q})}{\partial q_i \partial q_j} \Big|_{\vec{q}=\vec{q}_0} \Delta q_i \Delta q_j \quad (2.13)$$

Neudecker et al. tested different coordinate systems (i.e., normal modes, delocalized internal, redundant internal, and Z-matrix coordinates) to get chemically intuitive results for mechanochemical force analysis.^[117] Based on the results on

different tested molecules, the redundant internal coordinates provide the most reliable and meaningful results.

The JEDI analysis has a wide range of applications.^[119] It can be carried out in combination with Born-Oppenheimer molecular dynamics (BOMD) simulations.^[116,118] The results from BOMD simulations can be interpreted as a real-time monitoring of the stress distribution in a deformed molecule. Moreover JEDI analysis can be used to study the strain distribution in electronically excited molecules, via energy released by each internal coordinate as it relaxes on the excited state PES.^[116]

2.6 QTAIM basin analysis

In quantum mechanics, it is postulated that all information about a system can be defined in terms of a state function denoted as ψ . By applying the corresponding operator on this state function ψ , the values of physical quantities can be obtained. These values, along with the equations that predict them, collectively define the total state of the system.

To accurately predict the behavior of atoms in a molecule, a unique partitioning of the molecule into subsystems is necessary in order to provide a comprehensive description of these subsystems. Schwinger's principle of stationary action^[120] is used to achieve this task, as it directly determines the observables, their respective values, and the equations of motion for a quantum system that is "uniquely" partitioned into subsystems. This principle enables a systematic approach to describe the behavior of the subsystems in a quantum system.^[79]

The Quantum Theory of Atoms in Molecules (QTAIM), also referred as atoms in molecules, was developed by Prof. Richard F. W. Bader in the 1980s.^[79] In this approach the electron density gradient $\nabla\rho$ of the molecule is used as a criteria to partition the electronic volumes, known as topological basins. By partitioning the

electron density of a molecule into individual atoms and analyzing their interactions, QTAIM analysis provides insights into chemical bonding and the distribution of electrons within a molecule.

The locations where the gradient of the density field is zero (i.e. $\nabla\rho = 0$) are interpreted as Critical Points (CP). Based on the second derivatives of the gradient density there are four types of CP:

- *Nuclear Critical Points* (NCPs): The NCPs are situated at the position of a nucleus and correspond to a region of high electron density, where the second derivatives with respect to all three directions display a negative value.
- *Bond Critical Points* (BCPs): A BCP is located between two atoms and represents the point where the electron density is at its minimum relative to the bond axis. A BCP has two negative second derivatives with respect to two directions and a positive second derivative with respect to the remaining direction. The electron density at the BCP is indicative of the strength of the chemical bond.
- *Ring Critical Points* (RCPs): The RCPs are characterized by one negative and two positive second derivatives with respect to the three directions. A RCP is an indication of the presence of a ring structure, which is formed by other covalent bonds. Consequently, a RCP is typically surrounded by adjacent BCPs.
- *Cage Critical Points* (CCPs): CCPs are surrounded by adjacent RCPs. A CCP has three positive second derivatives with respect to the three spatial directions.

2.7 Quantum mechanical methods

Molecules can be described using wave functions, which are derived by solving the Schrödinger equation, 2.14. The wave functions provide a direct link to the molecular structure and energetics.

$$\hat{H}\Psi(r, R) = E\Psi(r, R) \quad (2.14)$$

$$\left[-\frac{1}{2}\nabla^2 - \frac{Z}{r} \right] \Psi(r, R) = E\Psi(r, R) \quad (2.15)$$

The Schrödinger equation for a single-electron systems such as the Hydrogen atom (equation 2.15) can be solved exactly. However, the Hamiltonian for multi-electron systems is much more complex, making the multi-electron Schrödinger equation (equation 2.16) analytically unsolvable. As a result, approximations are required to solve the Schrödinger equation for systems with more than one electron.

$$\left[-\frac{1}{2M_N} \sum_N \nabla_N^2 - \frac{1}{2} \sum_e \nabla_e^2 - \sum_N \sum_r \frac{Z_N}{r_{iN}} + \sum_i \sum_{j>i} \frac{1}{r_{ij}} + \sum_{N_A} \sum_{N_B>N_A} \frac{Z_{N_A} Z_{N_B}}{R_{AB}} \right] \Psi(r, R) = E\Psi(r, R) \quad (2.16)$$

Born-Oppenheimer Approximation:

The Born-Oppenheimer approximation is a technique utilized to distinguish the motion of nuclei and electrons. It is based on the assumption that the atomic mass of the nucleus is significantly greater than that of the electron, and thus, it neglects the motion of the nuclei. This approximation simplifies the multi-electron Schrödinger equation, separating it into a nuclear and an electronic part. The resulting electronic Schrödinger equation, 2.17, then can be solved considering the core coordinates

to be constant. The nuclear-nuclear coulombic interaction becomes constant for a given set of nuclear positions and can be included to the electronic energy E_{ele} for resolving the electronic Schrödinger equation.

$$\underbrace{\left[-\frac{1}{2} \sum_e \nabla_e^2 - \sum_N \sum_i \frac{Z_N}{r_{iN}} + \sum_i \sum_{j>i} \frac{1}{r_{ij}} + \sum_{N_A} \sum_{N_B>N_A} \frac{Z_{N_A} Z_{N_B}}{R_{AB}} \right]}_{H_{ele}} \Psi(r, R) = E \Psi(r, R) \quad (2.17)$$

$$\hat{H}_{ele} \Psi(r, R) = [T_e(r) + V_{eN}(r, R) + V_{ee}(r)] \Psi(r, R) = E_{ele} \Psi(r, R) \quad (2.18)$$

Hartree-Fock approximation:

The electronic Schrödinger equation 2.17, is still difficult to solve. Therefore, coordinates of the electrons need to be separable. One possible method to preserve the electron-electron coulomb interaction V_{ee} while attaining this objective is by implementing the independent particle approximation. This approximation assumes that the electrons move independently of one another. However, this only accounts for their interaction in an average manner. To achieve a more accurate representation of the many-body wavefunctions and obtain the lowest energy of the system, it is necessary to combine the single particle wavefunctions into a Slater determinant, a technique known as the Hartree-Fock (HF) approximation.

A simple way to construct the electronic wave function is by taking the product of the orthogonal wave functions of the individual electrons, which is also known as the Hartree product.

$$\Psi_{HP}(x_1, x_2, \dots, X_N) = \psi_1(x_1) \psi_2(x_2) \dots \psi_N(X_N) \quad (2.19)$$

However the Hartree product does not satisfy the Pauli antisymmetry principle, which is a fundamental requirement for a system of N electrons. According to this

principle, the wave function of a system of N electrons must change sign under the exchange of any two electrons. In order to satisfy this principle, John Slater introduced the Slater determinant as the general form of the total wave function for a system of N electrons that adhere to the Pauli exclusion principle. The Slater determinant is expressed mathematically as follows:

$$\Psi(x_1, x_2, \dots, x_N) = \frac{1}{\sqrt{N!}} \begin{vmatrix} \chi_1(x_1) & \chi_2(x_1) & \dots & \chi_N(x_1) \\ \chi_1(x_2) & \chi_2(x_2) & \dots & \chi_N(x_2) \\ \dots & \dots & \ddots & \dots \\ \chi_1(x_N) & \chi_2(x_N) & \dots & \chi_N(x_N) \end{vmatrix} \quad (2.20)$$

To consider the inter-electronic interactions in a wave function for N electrons (represented by Slater determinant, equation 2.20), minimizing the total energy (E_{ele}) through variational optimization is the most effective approach. The variational principle states that the ground state energy of a system can be obtained by minimizing the expectation value of the Hamiltonian with respect to a trial wave function.

$$E_{ele} = \frac{\int \Psi^* \hat{H}_{ele} \Psi dr}{\int \Psi^* \Psi dr} \quad (2.21)$$

When using the variational principle to minimize the total energy E_{ele} with the constraint that the orbitals remain mutually orthogonal, the following equation is obtained:

$$\hat{F}_i \phi_i = \epsilon_i \phi_i \quad (2.22)$$

In equation 2.22, the Fock operator is denoted as \hat{F}_i and the orbital energy of the i^{th} orbital is denoted as ϵ_i . For a closed-shell system of $2N$ electrons, the expression for the Fock operator is given by:

$$\hat{F}_i = h_i + \sum_{j=1}^N [2\hat{J}_j - \hat{K}_j] \quad (2.23)$$

where h_i refers to the hydrogen like single electron Hamiltonian given in equation 2.17. On the other hand, the terms \hat{J} and \hat{K} represent the Coulomb and exchange integrals, respectively, that describe the interactions between two or more electrons and are given by

$$\hat{J}_i|\phi_j(2)\rangle = \langle\phi_i(1)|\frac{1}{r_{12}}|\phi_i(1)\rangle|\phi_j(2)\rangle \quad (2.24)$$

$$\hat{K}_i|\phi_j(2)\rangle = \langle\phi_i(1)|\frac{1}{r_{12}}|\phi_j(1)\rangle|\phi_i(2)\rangle \quad (2.25)$$

To optimize the wave function, the HF method solves the Schrödinger equation for each electron self-consistently using the variational principle (i.e. by using equation 2.22). This process leads to the determination of a set of optimized one-electron orbitals that minimize the electronic energy of the system. However, for larger systems, the HF method becomes computationally demanding as it scales as N^4 (where N is the number of basis functions).

2.7.1 Density functional theory

In contrast to the HF method, which takes into account the many-body wavefunction, the Density Functional Theory (DFT) deals with the electron density that solely depends on the three spatial variables x , y , and z . The fundamental premise of DFT is that there exists a correlation between the total electron density and energy. This theory is founded upon two theorems, which were proposed and demonstrated by Hohenberg and Kohn in 1964.^[121,122]

Theorem 1: The first theorem of Hohenberg and Kohn asserts that the external potential $V_{ext}(\mathbf{r})$ is a unique functional of ground-state electron density, $\rho(\mathbf{r})$.

Theorem 2: The second theorem states that there is a unique functional of the electron density $E[\rho(\mathbf{r})]$ that corresponds to the correct ground-state energy. This implies that the ground-state energy can be computed solely from the electron density without knowing the wavefunction.

Based on the both theorems, the ground state energy of multi-electron system can be expressed as follows

$$E(\rho) = T(\rho) + V_{eN}(\rho) + J_{ee}(\rho) + E_{xc}(\rho) \quad (2.26)$$

where ρ is the electron density and expressed as $\rho = \sum_i |\psi_i(\mathbf{r})|^2$. In order to evaluate the expression for the $T(\rho)$, Kohn and Sham proposed to calculate the kinetic energy (equation 2.27) from a non-interacting reference system, which states that the same electron density is obtained as that of the interacting system, but with non-interacting electrons.

$$T_s(\rho) = -\frac{1}{2} \sum_i^N \langle \psi_i^{ks} | \nabla^2 | \psi_i^{ks} \rangle \quad (2.27)$$

where N is the total number of electrons and ψ_i^{ks} represent the Kohn-Sham orbitals. The nuclei-electron interaction V_{eN} and the electron-electron coulomb interactions J_{ee} can be expressed as

$$V_{eN}(\rho) = \int \sum_{A=1}^M \frac{Z_A \rho(\mathbf{r})}{r - R_A} d\mathbf{r} \quad (2.28)$$

$$J_{ee}(\rho) = \int \int \frac{\rho(\mathbf{r}_1)\rho(\mathbf{r}_2)}{r_1 - r_2} d\mathbf{r}_1 d\mathbf{r}_2 \quad (2.29)$$

In equation 2.26, the final term E_{xc} not only accounts for the exchange and correlation energy, but it also represents the difference between the actual kinetic energy of the interacting system $T(\rho)$ and the non-interacting kinetic energy $T_s(\rho)$

. Additionally, E_{xc} compensates for the self-interaction error by measuring the difference between the non-classical electron-electron repulsion energy $V_{ee}(\rho)$ and the Coulomb energy $J_{ee}(\rho)$. Therefore, E_{xc} can be expressed as

$$E_{xc}(\rho) = [T(\rho) - T_s(\rho)] + [V_{ee}(\rho) - J_{ee}(\rho)] \quad (2.30)$$

Finally combining all energy terms, the total energy of N electron system can be expressed as

$$E[\rho(r)] = -\frac{1}{2} \sum_i^N \langle \psi_i | \nabla^2 | \psi_i \rangle - \int \sum_{A=1}^M \frac{Z_A \rho(r)}{r - R_A} dr + \frac{1}{2} \int \int \frac{\rho(r_1) \rho(r_2)}{r_1 - r_2} dr_1 dr_2 + E_{xc}[\rho] \quad (2.31)$$

Through the application of the variational principle and considering the expression for the electron density, it is possible to derive the one-electron Kohn-Sham equation by means of minimizing the energy of the system, where the equation can be expressed as

$$\left[-\frac{1}{2} \nabla^2 - \left(\sum_{A=1}^M \frac{Z_A}{r_{1A}} + \int \frac{\rho(r_2)}{r_{12}} dr_2 + v_{xc}[r_1] \right) \right] \psi_i(r_1) = \epsilon_i \psi_i(r_1) \quad (2.32)$$

where v_{xc} denotes the exchange-correlation functional and can be expressed as

$$v_{xc}(r) = \frac{\delta E[\rho(r)]}{\delta \rho(r)} \quad (2.33)$$

Finally, the one-electron Kohn-Sham equation 2.32 is solved by using an iterative self-consistent process. The initial guess densities are used to obtain a new set of wavefunctions and electron densities, which are then used as the input for the next iteration. This iterative process continues until the wavefunctions and electron densities converge to a stable solution, indicating that the self-consistency has been achieved.

The primary issue with DFT is that the precise exchange-correlation functional is not known. The local density approximation (LDA) is the simplest form of the exchange-correlation functional and only relies on the local electron density.

$$E_{xc}^{LDA}[\rho] = \int \epsilon_{xc}[\rho(r)]\rho(r)dr \quad (2.34)$$

where ϵ_{xc} is exchange-correlation energy of a single electron, which is a function of the electron density. However, it is observed that the use of the LDA functionals is limited, as they do not accurately account for the long-range behavior of the electron density. Moreover, they exhibit poor performance when predicting physical properties, such as energetics and magnetic properties. In contrast, the generalized gradient approximation (GGA) considers not only the local electron density but also its gradient, as demonstrated by equation 2.35. The use of GGA functionals results in better prediction of the ground state energy and geometry.

$$E_{xc}^{GGA}[\rho] = \int \epsilon_{xc}[\rho(r), \nabla\rho(r)]\rho(r)dr \quad (2.35)$$

The choice of functional used in DFT is critical in determining the accuracy of predicting the physical and chemical properties of materials, as it represents the mathematical framework that is used to describe the electron density of a material. Some examples of LDA functionals include VWN5,^[123] PZ81,^[124] and PW92.^[125] A few examples of GGA functionals are PW91,^[126] PBE,^[127] LYP,^[128] P86,^[129] and regTPSS.^[130] Apart from LDA and GGA functionals, hybrid functionals that additionally take into account a portion of HF exchange were developed. One of the most commonly used hybrid functionals is the B3LYP^[100–102] (Becke, 3-parameter, Lee-Yang-Parr) functional, which has been found to perform reasonably well in predicting the geometries and thermochemistry of molecules. More examples of

hybrid-GGA functionals based on the HF contribution are PBE0,^[131,132] B97,^[133] B5050LYP^[134] and BHLYP.^[100–102]

2.8 Molecular mechanics methods

2.8.1 Force field

In silico simulations offer a powerful tool for exploring the structural and dynamic characteristics of molecular level systems based on fundamental principles of quantum mechanics. Nevertheless, the utilization of quantum mechanics in such investigations faces several obstacles due to the high computational expenses, rendering many problems unfeasible to investigate using this method. Therefore a simplified approach is required to understand the structure, dynamics, and functions of a bulk scale system.

In molecular simulations, a force field (FF) method is a mathematical ball-and-spring model used to describe the potential energy of the system. Considering atoms as balls held together with springs (bonds), bonded and non-bonded interactions are computed. In practice, a set of rules is used to calculate the forces between atoms or molecules, which determines their movements and interactions in the simulated environment. Based on the Born-Oppenheimer approximation, nuclear and electronic motions are treated separately, whereas, in the FF model only the motions of the nuclei are computed and all the electronic contributions are approximated. The potential energy of the system as a function of nuclear coordinates $V(\vec{R})$ is usually divided into bonded and non-bonded contributions.

$$V(\vec{R}) = E_{\text{bonded}} + E_{\text{non-bonded}} \quad (2.36)$$

$$V(\vec{R}) = \underbrace{E_{bond} + E_{angle} + E_{torsional} + E_{improper}}_{E_{bonded}} + \underbrace{E_{coul} + E_{vdw}}_{E_{non-bonded}} + E_{cross} \quad (2.37)$$

The bonded term, E_{bonded} , is composed of bonding energy E_{bond} , angles contributions E_{angle} , dihedrals $E_{torsional}$ and impropers $E_{improper}$ energy terms. The non-bonded $E_{non-bonded}$ energy terms includes the contribution from *Coulomb* interactions E_{coul} and *van der Waals* interactions E_{vdw} . The coupling among the bonds, angles and dihedrals are separately computed using cross energy terms E_{cross} . The FF style OPLS-AA (Optimized Potentials for Liquid Simulations-All Atom)^[135] is used in this research work.

Bond energy terms

The simplest representation of the bond energy is modeled using a harmonic potential function, according to this the energy required to stretch or compress the bond is proportional to the displacement from its equilibrium distance r_0 . The computation of the bond interaction for each bonded pair of atoms is performed using the following equation

$$E_{bond} = \sum_{bond} \frac{1}{2} K_b (r - r_0)^2 \quad (2.38)$$

where K_b and r_0 are the force constant and equilibrium distance. These empirical parameters (K_b , r_0) for each bond depend on the types of atoms bonded together, and therefore vary depending on the specific atoms involved.

The bonds based on harmonic potentials are considered rigid, and can not be formed or broken. Thus the use of the harmonic approximation is impossible for designing the chemical reactions. Moreover, the harmonic approximation works correct only in the vicinity of equilibrium distance (r_0), it completely neglects the anharmonicity required to mimic the bond breaking behaviour.

Angle energy terms

The bond bending energy term can also be computed using harmonic functions, describing oscillations about an equilibrium angle θ_0 with force constant K_θ by using the following equation

$$E_{angle} = \sum_{angle} \frac{1}{2} K_\theta (\theta - \theta_0)^2 \quad (2.39)$$

The harmonic potential for the angles also possesses certain limitations like bond potentials, such as angle energy terms also increase with deviation from equilibrium value.

Dihedral energy terms

The OPLS style force field represents the dihedral energy for a set of four atoms. The torsional energy term contribution to the inter-atomic potential follows the combination of cosine functions with varying oscillation frequencies.

$$E_{torsions} = \sum_{dihedral} \frac{1}{2} K_{\phi_1} [(1 + \cos(\phi))] + \frac{1}{2} K_{\phi_2} [(1 - \cos(2\phi))] + \frac{1}{2} K_{\phi_3} [(1 + \cos(3\phi))] + \frac{1}{2} K_{\phi_4} [(1 - \cos(4\phi))] \quad (2.40)$$

where K_{ϕ_1} , K_{ϕ_2} , K_{ϕ_3} and K_{ϕ_4} are the constant parameters and ϕ is the dihedral angle.

Improper energy terms

The improper energy terms describe the energy contribution between atoms in a molecule that are not in a linear arrangement. The improper style CVFF (Consistent-Valence Force Field) is used here to describe the torsional energy associated with

a non-linear arrangement of atoms. The CVFF improper function uses a cosine function to describe the improper energy contribution.

$$E_{improper} = \sum_{improper} K_{\omega}[1 + d\cos(n\omega)] \quad (2.41)$$

where K_{ω} is the force constant, n is the number of cosine functions. The expression 5.7 also used as a harmonic dihedral style.

Coulomb energy terms

The classical electrostatic interactions are described using the Coulomb's law, as mentioned in the following equation

$$E_{coul} = \sum_{coul} \frac{q_i q_j}{4\pi\epsilon_0 r_{ij}} \quad (2.42)$$

where q_i and q_j are the atom centered point charges and r_{ij} is the distance of separation between them. ϵ_0 is the effective dielectric constant.

Van der Waals energy terms

The *van der Waals* energy term is defined using *Lenard-Jones* (LJ) potential. The LJ potential includes repulsive and attractive terms are of 12th and 6th order, and is commonly referred to as as 12-6 potential.

$$E_{vdW} = \sum_{vdW} 4\epsilon_{ij} \left[\left(\frac{r_{0,ij}}{r_{ij}} \right)^{12} - \left(\frac{r_{0,ij}}{r_{ij}} \right)^6 \right] \quad (2.43)$$

The potential is described with well depth $\epsilon = \sqrt{\epsilon_i \epsilon_j}$ and range $r_{0,ij} = (r_{o,i} - r_{o,j})/2$, which is the distance at which the LJ potential is minimum. The first part $\left(\frac{r_{0,ij}}{r_{ij}} \right)^{12}$, describes the repulsive nature of the potential and supposed to model the repulsive forces felt by molecules due to overlapping of their electron orbitals and the second part $\left(\frac{r_{0,ij}}{r_{ij}} \right)^6$ is the van der Waals/dispersion term.

2.9 Molecular dynamics simulations

Molecular dynamics (MD) simulations are a powerful tool to provide valuable insight into the basis and structural behaviour of polymeric materials at the molecular level. MD simulations use mathematical models to simulate the interactions and movements of individual molecules, enable to observe and understand the molecular processes that govern polymeric behavior, such as chain mobility,^[136] conformational changes,^[137] and molecular interactions.^[138]

In recent years, MD simulations have predicted useful information in response to different stimuli, such as temperature changes,^[139] stress and chemical exposure,^[140] which leads to the design of new polymeric materials with specific properties. In the field of mechanochemistry, MD simulation models developed in last decade has shed light on mechanophore kinetics,^[141] activation efficiency^[76] and mechanophore alignment under stress.^[142]

In general MD simulations are a computational techniques used to study the dynamic behavior of atoms and molecules based on the classical equations of motion, also known as Newtonian dynamics. MD simulations involve the step-by-step solution of Newton's equations of motion, which generate successive configurations or trajectories of the system over time. These trajectories contain information about how the positions and velocities of the atoms change with respect to time, providing a detailed description of the dynamic behavior of the system. Newton's second law can be described by the following equations:

$$f_i = m_i a_i \tag{2.44}$$

$$f_i = m_i \frac{\partial^2 r_i}{\partial t^2} \tag{2.45}$$

$$f_i = \frac{\partial^2 r_i}{\partial t^2} = \frac{f_i}{m_i} \quad (2.46)$$

where m_i , a_i and r_i are the mass, acceleration and position (coordinates) of atom i at time t and force f_i acting on it. The force on atom i is calculated from the gradient of the potential energy $V(r^N)$, where $r^N = (r_1, r_2, r_3, \dots, r_N)$ are the $3N$ atomic coordinates.

$$f_i = -\frac{\partial V}{\partial r_i} \quad (2.47)$$

To analyze the dynamics of a molecular system, its potential energy is computed using either quantum mechanical methods or molecular mechanics (force fields). Once the potential energy has been calculated, the trajectory of the system can be obtained by solving the differential equation 2.45. In MD simulations, this is typically achieved using various numerical algorithms for integrating the equations of motion, such as the finite difference method, velocity Verlet algorithm,^[143] Leapfrog algorithm,^[144] etc. The velocity Verlet algorithm is a commonly used integration algorithm for molecular dynamics simulations. In the velocity Verlet algorithm, three stages are involved to compute the new positions and velocities of atoms after a time step δt . Let us consider a time-point t , where the positions, velocities, and accelerations of atoms are $r(t)$, $v(t)$, and $a(t)$, respectively.

$$r(t + \delta t) = r(t) + \delta t v(t) + \frac{1}{2} \delta t^2 a(t) \quad (2.48)$$

$$v(t + \delta t) = v(t) + \frac{1}{2} \delta t [a(t) + a(t + \delta t)] \quad (2.49)$$

In order to calculate $v(t + \delta t)$, it is necessary to determine the acceleration at both time points t and $t + \delta t$. To achieve this, the position of the atoms at time $t + \delta t$ is

first computed using equation 2.48. Subsequently, the velocities at time $t + \frac{1}{2}\delta t$ were determined by

$$v(t + \frac{1}{2}\delta t) = v(t) + \frac{1}{2}\delta t a(t) \quad (2.50)$$

Then the forces were calculated for the updated positions, which gives the new accelerations $a(t + \delta t)$. Finally the velocities $v(t + \delta t)$ were obtained by computing the following relationship

$$v(t + \delta t) = v(t + \frac{1}{2}\delta t) + \frac{1}{2}\delta t a(t + \delta t) \quad (2.51)$$

2.10 Statistical ensemble in molecular dynamic simulations

In the previous section we have learnt that MD simulations give a detailed information about the behavior of the atoms/molecules. This includes their positions, velocities, and the forces that are acting on them at the microscopic level. In order to derive macroscopic observables from the simulations, statistical mechanics is used. The macroscopic properties of the system are specified by using the thermodynamic conditions under which the MD simulation is carried out. These conditions are commonly known as thermodynamic ensemble. Based on the requirement of the conditions in a MD simulation, the thermodynamic ensemble provides its own set of constraints and variables that determine the macroscopic properties of the system.

These thermodynamic ensembles are characterized by using the specific variables (such as number of particles, temperature, pressure, and energy) that are held constant. During the equilibration and deformation simulations (tensile and shear

stress) of bulk polymer systems different thermodynamic ensembles are used, which are discussed as follows

Microcanonical Ensemble

The thermodynamic statistical ensemble in which the system maintains a collection of particles or molecules that are isolated from their environment and are not allowed to exchange energy or matter with the surroundings is known as microcanonical ensemble. In the microcanonical ensemble, the number of particles (N), volume (V), and total energy (E) of the system are held constant. So the microcanonical ensemble is typically abbreviated as NVE ensemble.

Generally, the standard MD is performed in the microcanonical (NVE) ensemble. However, experiments performed at a specific temperature are dealt with other ensembles, modified using velocity scaling algorithms.

Canonical ensemble

The canonical ensemble is a statistical thermodynamic ensemble which is used to describe a collection of particles or molecules in contact with a heat bath at a fixed temperature, T . In this ensemble, the number of particles (N), volume (V), and temperature (T) are held constant, while the system is allowed to exchange energy with the heat bath. Thus the ensemble commonly known as NVT ensemble.

Isothermal-Isobaric ensemble

The isothermal-isobaric ensemble is a thermodynamic ensemble in which the system is governed by a collection of particles or molecules in contact with a heat bath at a fixed temperature and pressure. This ensemble is also known as NPT ensemble, as the number of particles (N), pressure(P), and temperature (T) are held constant. The NPT ensemble, is very useful while performing equilibration and deformation

simulations as the system is allowed to exchange energy with the heat bath and undergo volume changes at constant pressure.

2.11 Periodic boundary conditions

MD simulations provide a platform to consider atomistic system sizes up to a certain range (up to a maximum of approximately 10^6 molecules). This could lead to unnecessary surface effects or negligence of long-range interactions, such as electrostatic forces. Thus resulting the requirement of an unfeasible amount of computational resources, since the interactions would need to be calculated between every pair of particles in the system.

Periodic boundary condition (PBC) resolve such problems by replicating the simulation cell in all three dimensions, creating an infinite system environment. The basic idea is that any particle that leaves the simulation cell through one side will re-enter the cell from the opposite side.

PBC conditions or the shape of the simulation box can also be modified by using constant pressure boundary conditions.

Chapter 3

Mechanophores Response to Stretching Forces

3.1 Scope of the project

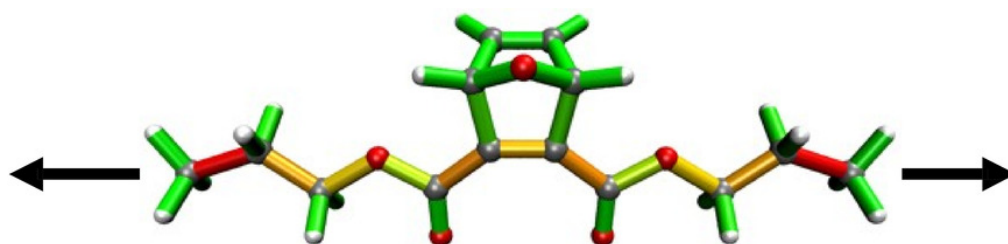
Mechanophores exhibit the property that at specific critical force, will rupture the labile bond and lead to further molecular rearrangements. However, mechanophore's stereo and regiochemistry and the position of the mechanophore in polymers has a big influence on the critical force required to break the bond, which is limiting the activation efficiency for specific mechanophores. The polymers itself play a crucial role on the mechanophores activation. The polymer composition, stereochemistry and the architecture regulate the force transduction to the mechanophores. As a result, it has been seen that while applying load to a system, some other bonds of the polymer may break, whereas the mechanophore remains intact. Moreover, in some cases it is desirable to strengthen the mechanophore below an adjustable threshold.

By the aim to overcome the two problems of low activation efficiency and the need of an adjustable threshold parameter, this chapter covers two different studies

related to the mechanophore activation. The first part of the chapter is related to the activation mechanism involved for mechanophores with low activation efficiency. Specifically, a flex-activated mechanophore under tension has been investigated. The computational approach is used to provide detailed insights by comparing the three different mechanical deformation modes (end-to-end pulling, direct pulling of critical bonds and constraining the bond angle joining to the polymer composition) to identify the most efficient method to activate flex-activated mechanophores in polymers.

The second part of the chapter shows how to adjust the threshold barrier to regulate the force transduction behavior towards the mechanophores. For this purpose eleven different linkers, which are joining the mechanophore with the polymer's backbone, were identified. For three different mechanophores, it has been found that these linkers are useful to enhance or reduce the activation rates by adjusting the threshold barrier of the mechanophores activation. The results allow the fine tuning of mechanophores activation with adjustable threshold parameter. The applicability of the an adjustable threshold parameter of mechanophores has been examined in the context of the gating mechanochemical process. The linkers tuned the one-step gating process into a two-step gating process.

3.2 Publication: The mechanism of flex-activation in mechanophores revealed by quantum chemistry



The results presented in this chapter have been previously published:

ChemPhysChem, **2020**, 21, 2402–2406.

Lennart J. Mier and Gheorghe Adam from the University of Bremen contributed to this work as first and second author.

Abstract

Flex-activated mechanophores can be used for small-molecule release in polymers under tension by rupture of covalent bonds that are orthogonal to the polymer main chain. Using static and dynamic quantum chemical methods, we here juxtapose three different mechanical deformation modes in flex-activated mechanophores (end-to-end stretching, direct pulling of the scissile bonds, bond angle bendings) with the aim of proposing ways to optimize the efficiency of flex-activation in experiments. It is found that end-to-end stretching, which is a traditional approach to activate mechanophores in polymers, does not trigger flex-activation, whereas direct pulling of the scissile bonds or displacement of adjacent bond angles are efficient methods to achieve this goal. Based on the structural, energetic and electronic effects responsible for these observations, we propose ways of weakening the scissile bonds experimentally to increase the efficiency of flex-activation.

Introduction

During recent years, the field of polymer mechanochemistry^[51,145–149] has matured to a point where a plethora of useful applications are available. Examples include the optical sensing of stress and strain using mechanochromic materials,^[12,87,150–158] the self-healing of polymers,^[159–161] and the force-induced activation of latent catalysts.^[162–164] Many of today’s functional polymers incorporate mechanophores, which are small subunits of the polymer that respond to mechanical deformation by significant structural changes and fulfil diverse tasks upon activation. One particularly intriguing class of these subunits, so-called flex-activated mechanophores,^[165,166] display the unique feature that bonds that are orthogonal to the polymer main chain are ruptured upon mechanical deformation. With this approach, small molecules can be released well before material failure occurs,^[59] which is helpful in the development of stress-sensing and self-healing materials.

However, the mechanism of flex-activation has hitherto not been understood in detail. Considering that the efficiency of flex-activation commonly lies below 10%,^[165,166] detailed insights into the activation mechanism are direly needed, since this knowledge would allow the optimization of this process. In this study, the mechanism of flex-activation in mechanophores is elucidated using quantum mechanochemical methods,^[61,167,168] which have been used successfully in the past to, e.g., study the debated cycloreversion of triazoles,^[169–171] develop novel molecular subunits for stress-sensing in polymers,^[30,116,172–174] and investigate the impact of topological effects on mechanical properties and the reactivity of molecules.^[119,175,176]

The model system considered in this study (Scheme 3.1) is similar to the one examined in ref. 165, however, it includes longer alkyl chains to simulate the influence of the polymer surrounding more realistically. Successful activation of the mechanophore leads to the release of furan *via* a retro-[4+2] cycloaddition. To the best of the authors’ knowledge, successful flex-activation in experiments has only been described for systems that are very closely related to the model system considered here. Three different modes of deformation are applied, in particular end-to-end pulling (mode 1), direct pulling of the “critical” bonds that rupture upon successful activation of the mechanophore (mode 2) and displacements of the bond angles adjacent to the functional subunit (mode 3). Deformation modes 1 and 2 are attained *via* the External Force is Explicitly Included (EFEI) approach,^[62,177,178] which is a quantum chemical geometry optimization under constant external force, whereas the COstrained Geometries simulate External Forces (COGEF) approach,^[63,179] a geometry optimization with geometric constraints, is used for deformation mode 3. Each of the three deformation modes was applied progressively until rupture of a carbon-carbon bond occurred. Density Functional Theory (DFT)^[121,122] at the PBE^[127]/cc-pVDZ^[103] level of theory is applied throughout. The full set of computational details is given in the Supporting Information.

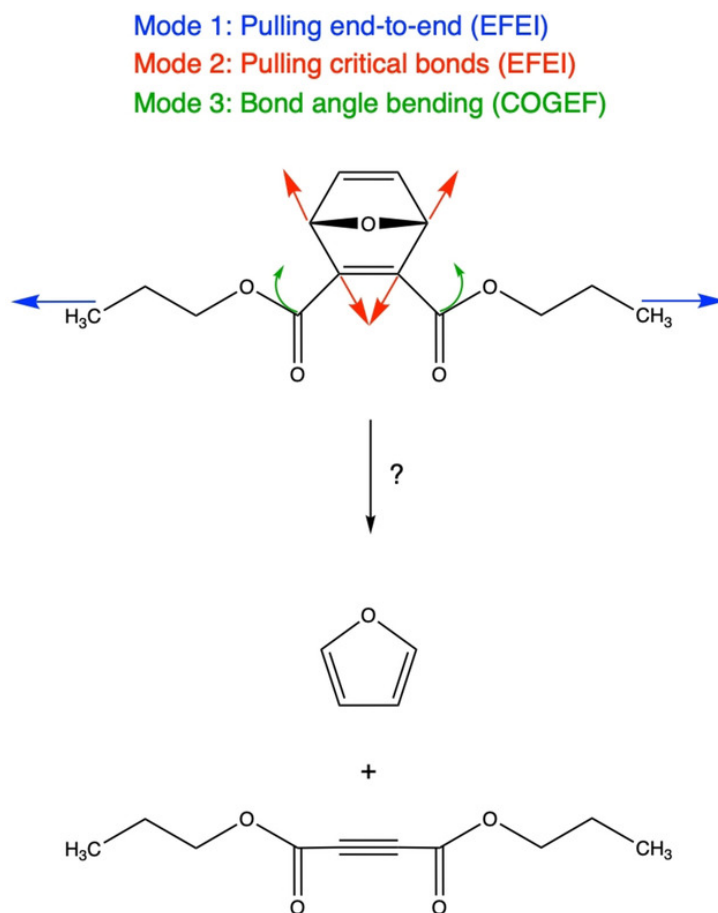


Figure 3.1: Deformation schemes of the model system considered in this work that might lead to the release of furan *via* a retro-[4+2] cycloaddition.

Mechanical stretching of a polymer is intuitively viewed as an end-to-end stretching of the polymer chains. Applying this deformation to the model system (mode 1) leads to a rupture force of 5.9 nN, but, surprisingly, rupture occurs in the terminal methyl groups of the polymer main chain and not in the “critical bonds” that must be broken for a successful retro-[4+2] cycloaddition. The reason for this effect is revealed by the Judgement of Energy DIstribution (JEDI) analysis,^[115–117] which is a quantum chemical tool to analyze the distribution of strain energy among the various bonds, bendings and torsions of a mechanically deformed molecule (Figure 3.2). The critical bonds are hardly elongated and therefore do not store significant amounts of strain energy. Instead, the terminal carbon-carbon bonds

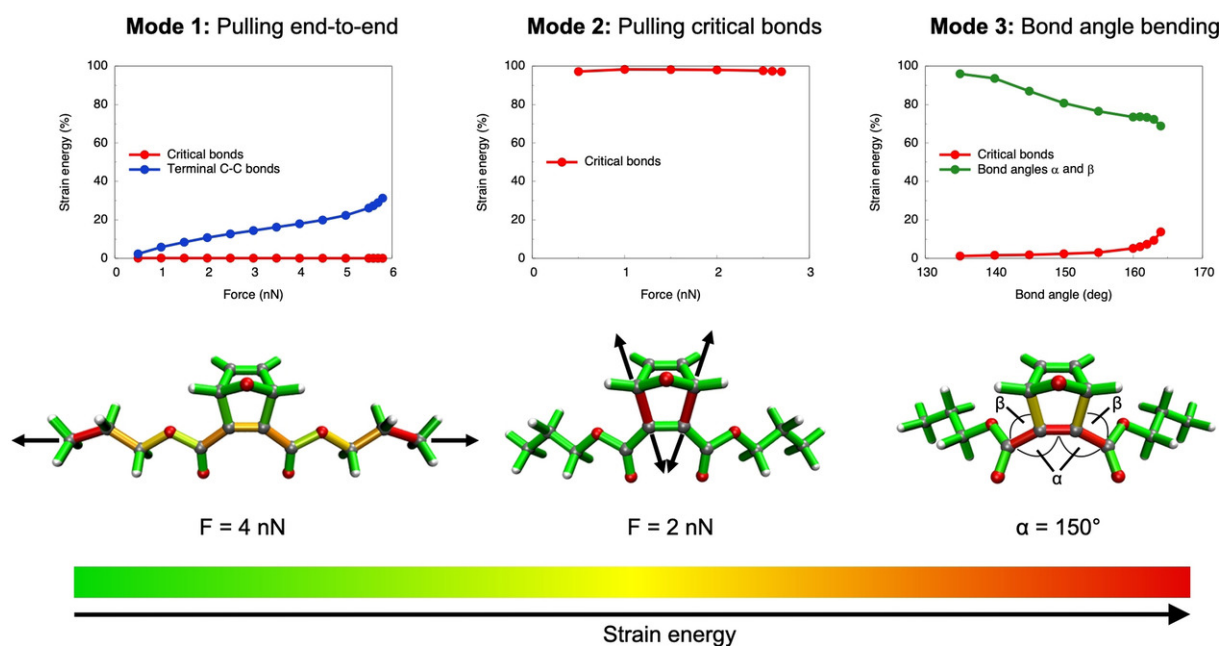


Figure 3.2: Distribution of strain energy among selected internal coordinates of a flex-activated mechanophore that is mechanically deformed *via* three different modes, as calculated with the JEDI analysis.^[115,117,180] “Critical bonds” denote the carbon-carbon bonds that need to be ruptured for a successful retro-[4+2] cycloaddition. Color-coded representations of strain energy at selected forces (modes 1 and 2) or bond angles α (mode 3) were derived by mapping strain values in bonds, bendings and torsions onto the involved covalent bonds.

that connect the methyl groups to the rest of the polymer linker store increasing amounts of strain energy with increasing pulling forces. While several other bonds and bendings in the polymer chain are also being strained during elongation of the molecule (cf. the color-coded structures in Figure 3.2), bond scission ultimately occurs in the terminal carbon-carbon bonds of the polymer chain. Hence, a simple stretching of the polymer main chain, e.g. in mechanical pulling experiments, is insufficient to trigger small-molecule release in this flex-activated mechanophore.

Mode 2, on the other hand, constitutes a very efficient way of achieving flex-activation, which agrees with chemical intuition. Throughout the entire stretching coordinate, the critical bonds store almost 100% of the strain energy in the system

and the retro-[4+2] cycloaddition occurs efficiently if both bonds are being pulled with a force of 2.8 nN, since no strain is wasted on other parts of the molecule.

In a mechanical pulling experiment, however, it is far from straightforward to trigger flex-activation *via* mode 2, since the critical bonds need to be stretched in an isolated manner. A more realistic scenario is the bending of the bond angles in the main polymer chain that are adjacent to the critical bonds (mode 3). If the bond angles α (cf. Figure 3.2) are displaced from their initial values of 131.7° to 164.1° , the critical bonds rupture and the retro-[4+2] cycloaddition occurs. The bond angle bendings store most strain energy throughout the entire deformation coordinate and pass on some of it to the critical bonds, leading to efficient rupture of the latter at 164.1° . Hence, the bond angles in the polymer main chain that are adjacent to the critical bonds act as work funnels that localize the strain energy in the region of the scissile bonds. An analogous effect was found for torsions, which facilitate the rupture of knotted polymer chains.^[119] Interestingly, immediately before bond rupture the strain energies stored by the critical bonds are very similar in mode 2 (15.2 kcal/mol) and mode 3 (17.9 kcal/mol), signifying the same degree of weakening of these bonds in both modes.

The unsuitability of mode 1 for flex-activation is emphasized when combining it with mode 2 (Figure 3.3, top panel). The rupture force of the critical bonds when pulling them directly decreases only slightly when simultaneously stretching the molecule end-to-end: It decreases from 2.8 nN in the absence of end-to-end stretching to 2.3 nN shortly before the terminal carbon-carbon bonds are ruptured. Since a significant amount of force is still required to achieve the retro-[4+2] cycloaddition, end-to-end stretching barely diminishes the strength of the critical bonds. When combining mode 2 and mode 3, on the contrary, the rupture forces of the critical bonds decrease monotonously (Figure 3.3, bottom panel). This again demonstrates the weakening of the critical bonds by adjacent bond angle bendings. Decreasing the

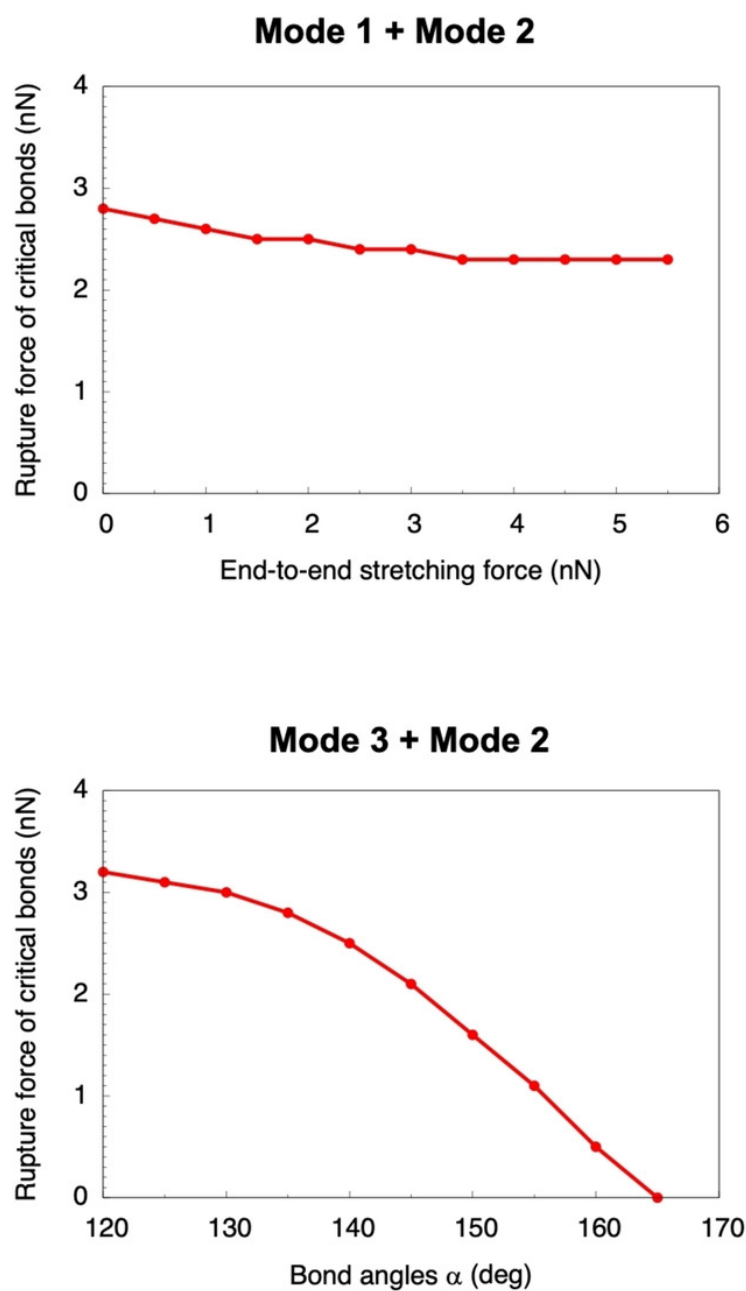


Figure 3.3: Rupture forces of the critical bonds *via* mode 2 when simultaneously stretching the molecule end-to-end (mode 1, top panel) or constraining the bond angles α (mode 3, bottom panel).

bond angles α form their optimal value (131.7°) leads to an increase in the rupture force of the critical bonds.

In an effort to identify the reason why adjacent bond angle bendings weaken the critical bonds, the Quantum Theory of Atoms in Molecules (QTAIM) was

applied.^[79] Increasing the adjacent bond angles leads to a decrease of electron density in the critical bonds (Figure 3.4). Conversely, the electron density in other covalent bonds in the molecule increases, two of which are singled out in Figure 3.4 as well. The mechanism by which adjacent bond angle displacements weaken the critical bonds and thus facilitate flex-activation is therefore a complex phenomenon that involves the rearrangement of electron density within the furan ring that is being created by the retro-[4+2] cycloaddition as well as in certain parts of the polymer chain. Interestingly, the electron density in the critical bonds hardly changes during deformation *via* modes 1 and 2 (cf. Supporting Information, Figure 3.5), showing that the rearrangement of electron density is a unique feature of deformation mode 3.

The results presented here demonstrate that the retro-[4+2] cycloaddition in the investigated flex-activated mechanophore cannot be triggered by mere end-to-end pulling of the main polymer chain. This limits the applicability of flex-activated mechanophores in mechanochemical pulling experiments, especially in ultrasound baths. The question remains how the activation efficiency in such experiments can be increased. Since deformation modes 2 and 3 have been identified as efficient ways of triggering flex-activation, we propose using an infrared laser to excite certain normal modes that either lead to a stretching of the critical bonds or to a bending of the bond angles adjacent to them in the polymer chain. Although normal modes are typically delocalized, using the JEDI analysis examples of promising normal modes have been identified (cf. Supporting Information, Figure 3.6). We hypothesize that tuning an infrared laser to the wavelengths that are necessary to excite these modes during mechanical deformation of polymers including flex-activated mechanophores will lead to an increase in the rate of flex-activation and the more efficient release of small molecules. However, it must be noted that the bond angles α and β need to be displaced significantly to achieve flex-activation and that it is unknown whether the vibration of a single normal mode is enough to achieve this deformation. Rather,

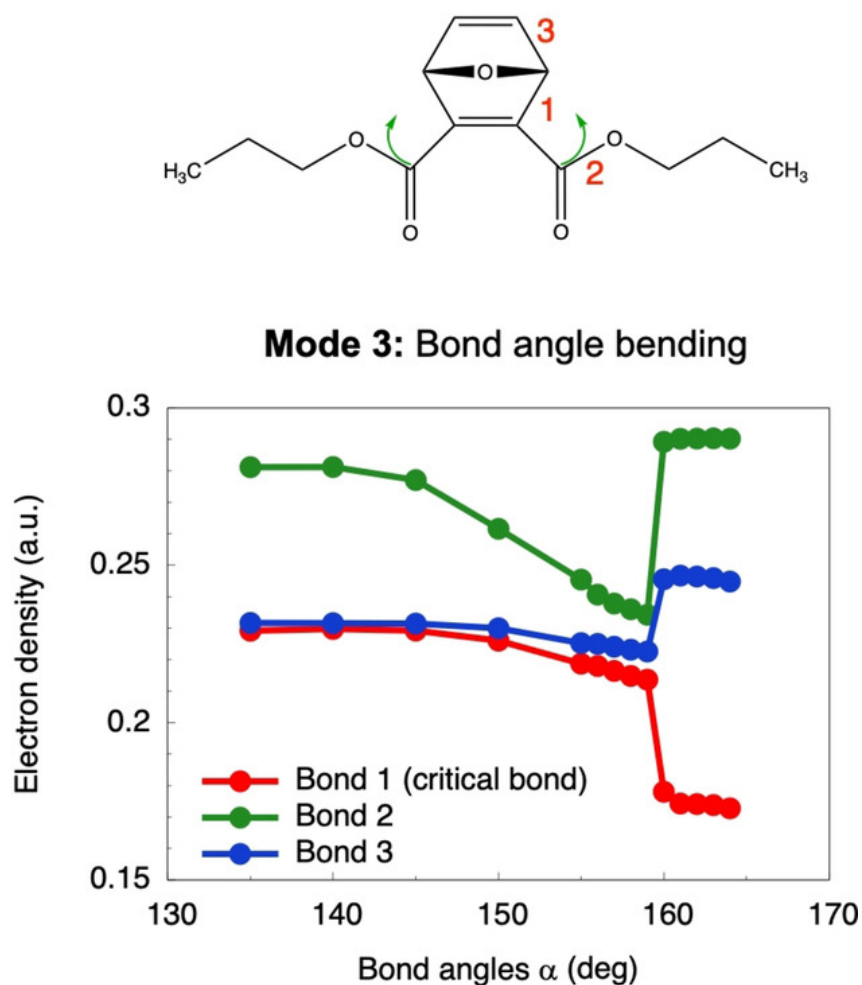


Figure 3.4: Progression of electron density in selected bonds (1–3) when constraining the bond angles α to different values.

the combination of several normal modes that involve bond angle bendings as well as the stretching of the critical bonds is the most promising approach.

In the future we plan to apply our methodology to a recently proposed mechanophore based on anthracene,^[58] for which flex-activation was tested but remained unsuccessful, with the aim of determining the optimal conditions (e.g. the pulling/deformation setup) for successful flex-activation. Moreover, we plan to apply quantum mechanochemical models of pressure^[107,108,181] to test the efficiency of flex-activation in polymers, since experiments on flex-activated mechanophores were performed under compression.^[59,165,166] It will be insightful to juxtapose the influences of me-

chanical compression, hydrostatic pressure and mechanical forces deforming the systems, which can all be assumed to play a role in the process of flex-activation.

3.3 Additional information

3.3.1 Computational details

All calculations using the External Force is Explicitly Included (EFEI)^[62,177,178] and the COstrained Geometries simulate External Forces (COGEF)^[63,179] approaches were carried out with the Q-Chem 5.2.1 program package.^[182] Since mechanical forces can be applied to a molecule directly in the EFEI method, this approach has some clear technical advantages over COGEF for deformation modes 1 and 2.^[61,168] However, the use of COGEF is necessary for mode 3, since isolated bond angle bending can only be achieved with COGEF. Rupture forces of the C_s-symmetric model system in deformation modes 1 and 2 were determined iteratively with a resolution of 100 pN. Similarly, the bond angles α that are displaced for flex-activation (deformation mode 3) were determined with a resolution of 0.1°. Density Functional Theory (DFT)^[121,122] at the PBE^[131]/cc-pVDZ^[103] level of theory was used in all calculations. This choice was made due to the lack of experimental data against which to benchmark and because the results calculated with PBE/cc-pVDZ fall within the range of other established computational methods (cf. Table 3.1).

The Judgement of Energy DIstribution (JEDI) analysis^[115–117] was applied to determine the distribution of strain energy among the internal coordinates of the molecule, based on the deformed geometries generated *via* EFEI and COGEF. Color-coded representations were created with VMD 1.9.3^[183] by mapping the strain energies in the bond lengths, bond angles and dihedral angles onto the covalent bonds involved in the particular internal coordinate.

The electron densities in the bond critical points were calculated based on the Quantum Theory of Atoms In Molecules (QTAIM)^[79] using the Multiwfn 3.7 program

package.^[184] The wavefunctions required for these calculations were generated with Q-Chem.

Steered Born-Oppenheimer Molecular Dynamics (BOMD) simulations were carried out with Q-Chem 5.2. A time step of 10 a.u. (0.242 fs) was adjusted. The end-to-end stretching force was increased by 250 pN each 413 time steps, i.e. roughly each 0.1 ps. Temperatures of 300K, 600K, 900K and 1200K were adjusted and ten simulations were carried out for each temperature. Initial velocities were sampled randomly from a Maxwell-Boltzmann distribution. The trajectories were run until bond rupture occurred which was accompanied by SCF convergence failure. PBE/cc-pVDZ was used as the electronic structure method.

Functional	cc-pVDZ	cc-pVTZ
BP86 ^[100,129]	163.4	161.2
B97 ^[133]	165.5	164.2
PBE ^[131]	164.1	162.7
BLYP ^[100,185]	161.0	160.0
B3LYP ^[100-102]	164.3	162.7
BHHLYP ^[100-102]	167.5	166.5
PBE0 ^[131,132]	167.2	166.1

Table 3.1: Bond angles α that lead to flex-activation in the model system, calculated with the COGEF approach at different levels of theory.

3.3.2 Electron density for deformation modes 1 and 2

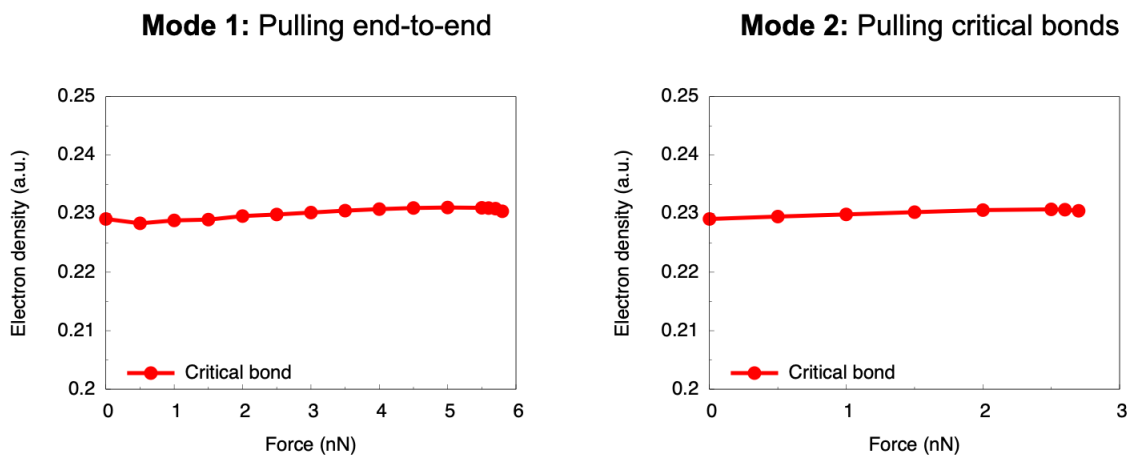


Figure 3.5: Progression of electron density in each critical bond when applying pulling forces to the flex-activated mechanophore *via* deformation modes 1 and 2.

3.3.3 Normal mode analysis

For deformation modes 2 and 3, which lead to a successful retro-[4+2] cycloaddition reaction of the flex-activated mechanophore considered in this work, the JEDI analysis in normal modes^[116,117] was carried out to determine normal modes that precondition the critical bonds for rupture. Pulling the critical bonds apart directly (mode 2) of course leads to an elongation of these bonds. Using the JEDI analysis it was found that a plethora of normal modes involve an elongation of the critical bonds and therefore store strain energy, two of which are shown in Figure 3.6. At a stretching force of 2 nN, e.g., normal modes A and B store 11% and 10% of the strain energy, respectively. Applying infrared radiation with the energies appropriate to excite these (and other) normal modes might weaken the critical bonds and thus lead to an increase in the rate of the retro-[4+2] cycloaddition reaction.

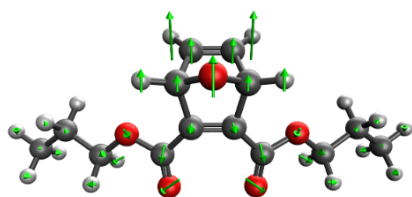
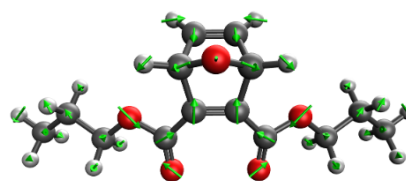
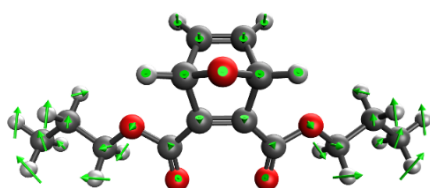
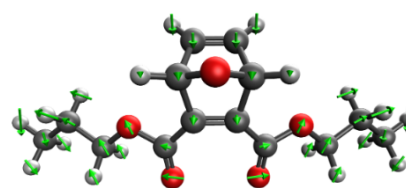
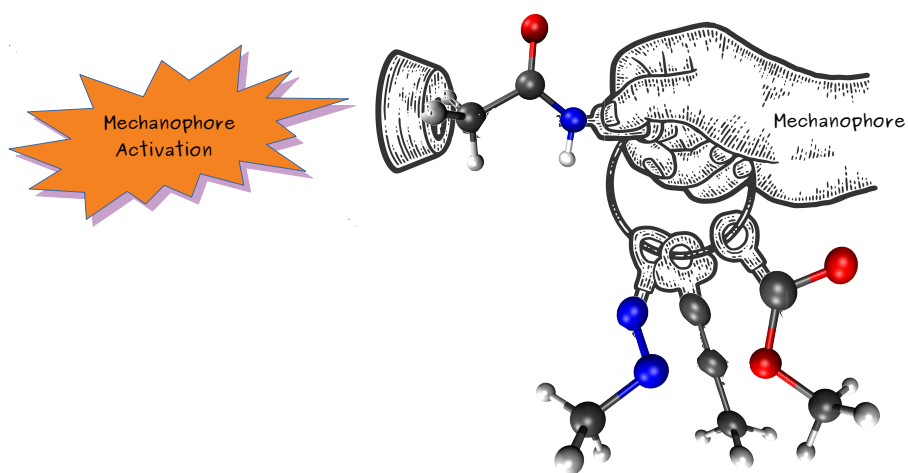
Deformation mode 2 (Pulling critical bonds):Normal mode A
 $\tilde{\nu} = 386 \text{ cm}^{-1}$ Normal mode B
 $\tilde{\nu} = 778 \text{ cm}^{-1}$ **Deformation mode 3 (Bond angle bendings):**Normal mode C
 $\tilde{\nu} = 48 \text{ cm}^{-1}$ Normal mode D
 $\tilde{\nu} = 153 \text{ cm}^{-1}$

Figure 3.6: Two selected normal modes for deformation modes 2 and 3, respectively, that either lead to an elongation of the critical bonds (mode 2) or a displacement of the bond angles α (mode 3).

Since normal modes are rectilinear, they describe inherently curvilinear motions like bond angle bendings only poorly.^[117] As a result, the error of the harmonic approximation in the JEDI analysis becomes quite large, so that, in the case of deformation mode 3, only minor displacements of the bond angle α were considered. If α is constrained to 135° , the error of the harmonic approximation is only 12%. Normal modes C and D store 21% and 28% of the harmonic strain energy in this case, signifying that a vibration of these modes is beneficial for the retro-[4+2] cycloaddition reaction.

3.4 Publication: The activation efficiency of mechanophores can be modulated by adjacent polymer composition.



Reproduced from

RSC Adv., **2021**, 11, 7391–7396.

with permission from the Royal Society of Chemistry.

Abstract

The activation efficiency of mechanophores in stress-responsive polymers is generally limited by the competing process of unspecific scission in other parts of the polymer chain. Here it is shown that the linker between the mechanophore and the polymer backbone determines the force required to activate the mechanophore. Using quantum chemical methods, it is demonstrated that the activation forces of three mechanophores (Dewar benzene, benzocyclobutene and *gem*-dichlorocyclopropane) can be adjusted over a range of almost 300% by modifying the chemical composition of the linker. The results are discussed in terms of changes in electron density, strain distribution and structural parameters during the rupture process. Using these findings it is straightforward to either significantly enhance or reduce the activation rate of mechanophores in stress-responsive materials, depending on the desired use case. The methodology is applied to switch a one-step “gating” of a mechanochemical transformation to a two-step process.

Introduction

The interest in polymer mechanochemistry has been increasing steadily throughout the past two decades,^[146–149] which is due to fascinating applications of the field, such as force-induced activation of latent catalysts,^[163] the development of self-healing polymers,^[159] and optical sensing of stress and strain using mechanochromic materials.^[152] Many of these applications are enabled by mechanophores, which are small molecular subunits embedded in the polymer that respond to external forces *via* significant changes in their geometries. Experimentally, mechanophores in stress-responsive polymers can be activated by single-molecule force spectroscopy,^[186] sonochemistry,^[187] nozzle flow setups^[45] or direct mechanical manipulation.^[12] However, in many cases the activation efficiency of mechanophores in stress-responsive materials is limited and bond rupture in other parts of the polymer backbone is

predominant,^[114] thus limiting the efficiency of such functional materials. On the contrary, in other application scenarios, it would be desirable to strengthen the polymer and prevent mechanophore activation below an adjustable threshold force. Therefore, a better control over the force required to activate mechanophores is highly desirable.

In computational investigations of the activation of mechanophores embedded in polymer backbones it was found that the pulling vector as well as local distortions in the linking units connecting the mechanophore to the rest of the polymer backbone (the “linkers”) have an influence on the activation efficiency of the mechanophores.^[91,188–190] The chemical composition of these linkers, on the other hand, has not been considered in detail in computational studies on polymer mechanochemistry, since, for simplicity, the immediate vicinity of a mechanophore is often modeled as an alkyl chain.^[114] While, experimentally, the chemical composition of the linkers is usually dictated by the synthetic route, it was shown that a stiffer polymer chain with a higher T_g transmits mechanical load more efficiently to the mechanophore.^[146,163] However, a comprehensive understanding of the influence of the chemical composition of the linkers between the polymer chain and the mechanophore on the activation of the latter remains elusive.

Using quantum mechanochemical methods,^[114] we here provide such an understanding by demonstrating that the activation force of three different mechanophores, i.e. Dewar benzene,^[172] benzocyclobutene^[189] and *gem*-dichlorocyclopropane,^[91] can be adjusted over a range of almost 300% by modifying the linkers that connect the mechanophore to the rest of the polymer backbone. The investigated linkers are chemically diverse and include saturated and unsaturated alkyl chains, amides, esters, an ether, a secondary amine, an imine and an azo group (Figure 3.7). We use the External Force is Explicitly Included (EFEI) approach,^[62,177,178] which allows quantum chemical geometry optimizations under constant external stretching forces,

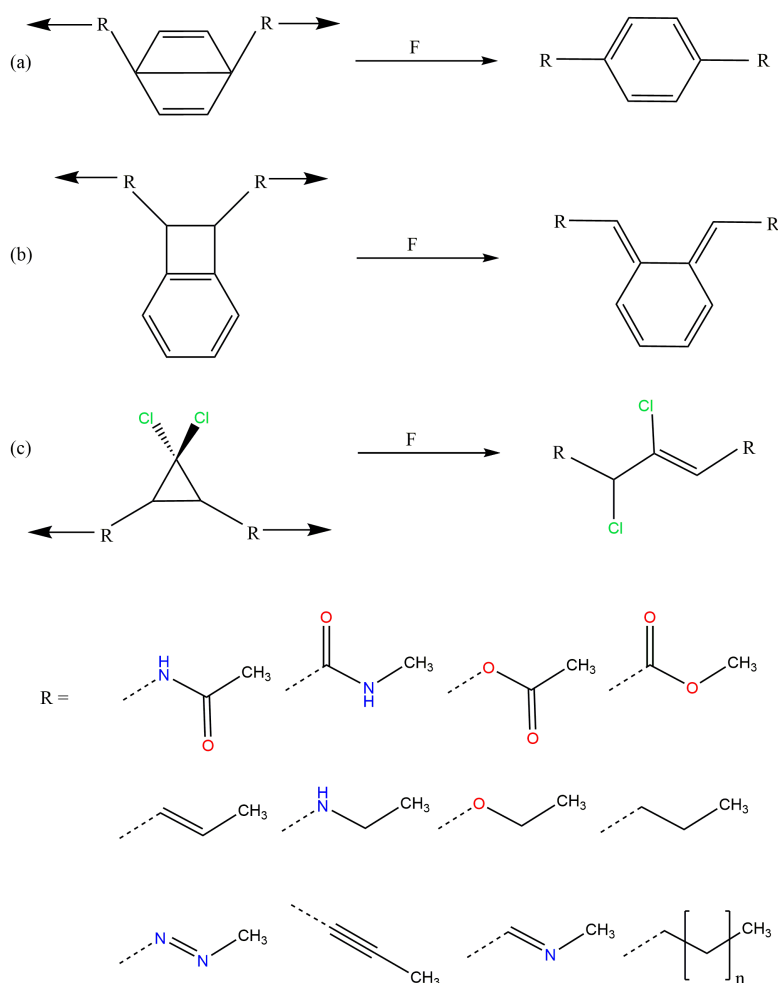


Figure 3.7: Mechanical activation pathways of the investigated mechanophores (a: Dewar benzene, b: benzocyclobutene, c: *gem*-dichlorocyclopropane) and investigated linkers.

as implemented in the Q-Chem 5.2.1 program package^[182] and apply Density Functional Theory (DFT)^[121,122] at the PBE^[131]/cc-pVDZ^[103] level of theory throughout. Further computational details can be found in the Supporting Information.

By comparing alkyl linkers of different lengths for the three investigated mechanophores (cf. the Supporting Information, Figure 3.12), it becomes apparent that the forces required to activate the mechanophores generally show an odd-even behavior with the chain length, which has been described before.^[189] Moreover, in a three-membered alkyl chain the rupture force is close to the converged value at higher chain lengths.

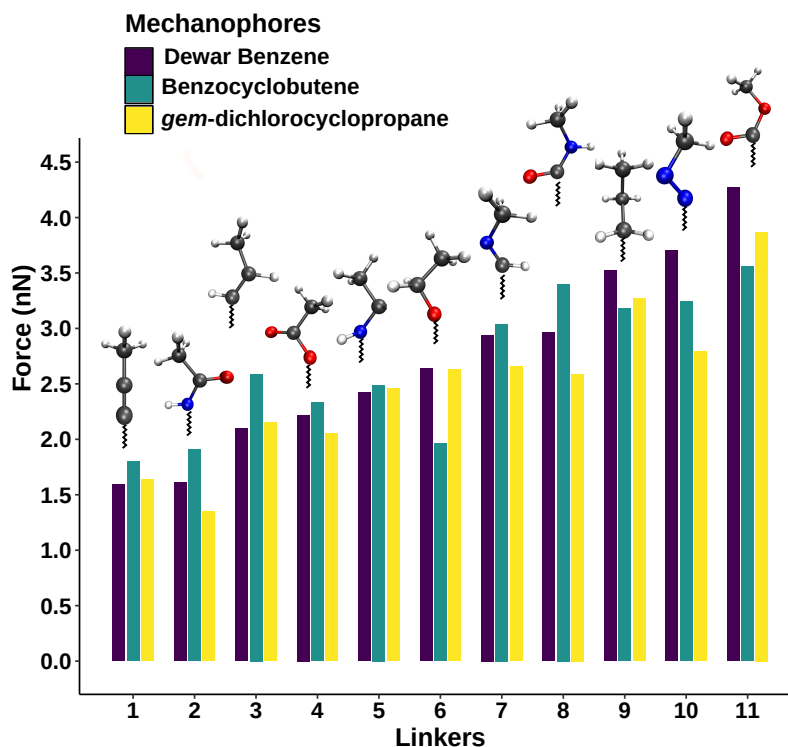


Figure 3.8: Rupture forces for the mechanical activation of Dewar Benzene, benzocyclobutene and *gem*-dichlorocyclopropane using different linkers that connect the mechanophores to the rest of the polymer backbone. Color code: gray: carbon; red: oxygen; blue: nitrogen; white: hydrogen

Hence, in this study the focus lies on three-membered chains that model the polymer linkers.

To investigate the influence of linker composition on mechanophore activation, stretching forces were applied to the terminal carbon atoms of the linkers attached to each mechanophore. The calculated rupture forces for the three mechanophores connected with the investigated linkers are given in Figure 3.8 (cf. also Table 4.1). Although the three tested mechanophores are chemically diverse and display completely different activation mechanisms, the order of linkers when organizing them according to the rupture forces is similar: The lowest rupture forces are yielded by the linker that involves an alkynyl group as well as the amide linker in which the nitrogen atom is attached to the mechanophore. In *gem*-dichlorocyclopropane,

for example, the amide and the alkynyl linkers lead to activation forces of only 1.35 nN and 1.64 nN, respectively, which is significantly lower than the value for the saturated alkyl linker (3.27 nN). This finding demonstrates that the computational modeling of the activation of a mechanophore in which the stretching force is transduced *via* the simplest alkyl chain yields rather high rupture forces, which might contribute to the well-known overestimation of experimental rupture forces by quantum chemistry.^[114] Experimentally, if the aim is to maximize the activation rate of mechanophores in polymers, it is recommended to place a carbon-carbon triple bond or an amide group directly next to the mechanophore.

Linkers that yield a high rupture force include the ester and the amide that are attached to the mechanophore *via* their carbonyl groups as well as the azo linker. Connecting these species to the mechanophores in experiments would make the polymer mechanically more resilient. All in all, Figure 3.8 provides a toolbox for fine-tuning the activation force of mechanophores in polymers, depending on the desired use case, simply by changing the chemical composition of the immediate vicinity of the mechanophore. The wide functionality of mechanophores (e.g. force-induced color-changes, fluorescence or luminescence or the release of small-molecules) would be retained.

Interestingly, using different linkers on each side of the molecule leads to intermediate rupture forces, as suggested by chemical intuition (cf. Supporting Information, Table 3.3): Taking Dewar benzene as an example, the use of the linker that yields the lowest rupture force (the alkynyl linker) on one side of the molecule and the one yielding the highest rupture force (the ester) leads to a rupture force of 2.65 nN, which is in the middle of the region spanned by the explored space of linkers. Changing one of the linkers further allows a fine-tuning of the rupture force, which is consistent among the tested mechanophores. The data presented in Table 3.3

therefore suggests that application of different linkers on each side of the molecule leads to a “mixing” of their mechanical properties.

To elucidate the reason for the significant differences in rupture forces when varying the linkers, we applied the Judgement of Energy DIstribution (JEDI) analysis,^[115–117] which is a quantum chemical tool for the analysis of strain distribution in distorted molecules. However, the strain energies stored by the scissile bonds in the stretched mechanophores do not follow an easily interpretable trend that would explain the observed differences in rupture forces (cf. Supporting Information, Tables 3.14–3.16). Instead, the distribution of strain energy is complex, signifying a more complicated rupture mechanism. Similarly, the electron densities at the bond critical points of the scissile bonds of the mechanophores, calculated with the Quantum Theory of Atoms In Molecules (QTAIM)^[79] approach, do not contribute to our understanding of the observed discrepancies in the activation forces (cf. Supporting Information Figure 3.13). While the electron densities generally decrease with increasing force, hinting towards a weakening of these bonds, these trends are similar for all mechanophores and linkers and the absolute values of the electron densities do not correlate with the rupture order.

Instead, it was found that structural parameters in the linker determine the force required for mechanophore activation. Taking Dewar benzene as an example (Figure 3.9), the angle between the scissile transannular carbon-carbon bond and the first atom in the linker (β_0), the angle between the mechanophore and the first two atoms in the linker (β_1) and the angle between the three atoms in the chain of the linker (β_2) are considered. Upon application of end-to-end stretching forces, β_0 and β_2 exhibit a steady increase in the case of most linkers. Conversely, the initial and final angles of β_1 are almost identical in most cases, signifying that β_1 is a rather stiff bond angle. A notable exception is the alkynyl linker, in which β_1 initially displays a sharp decrease. Upon close inspection it becomes apparent that

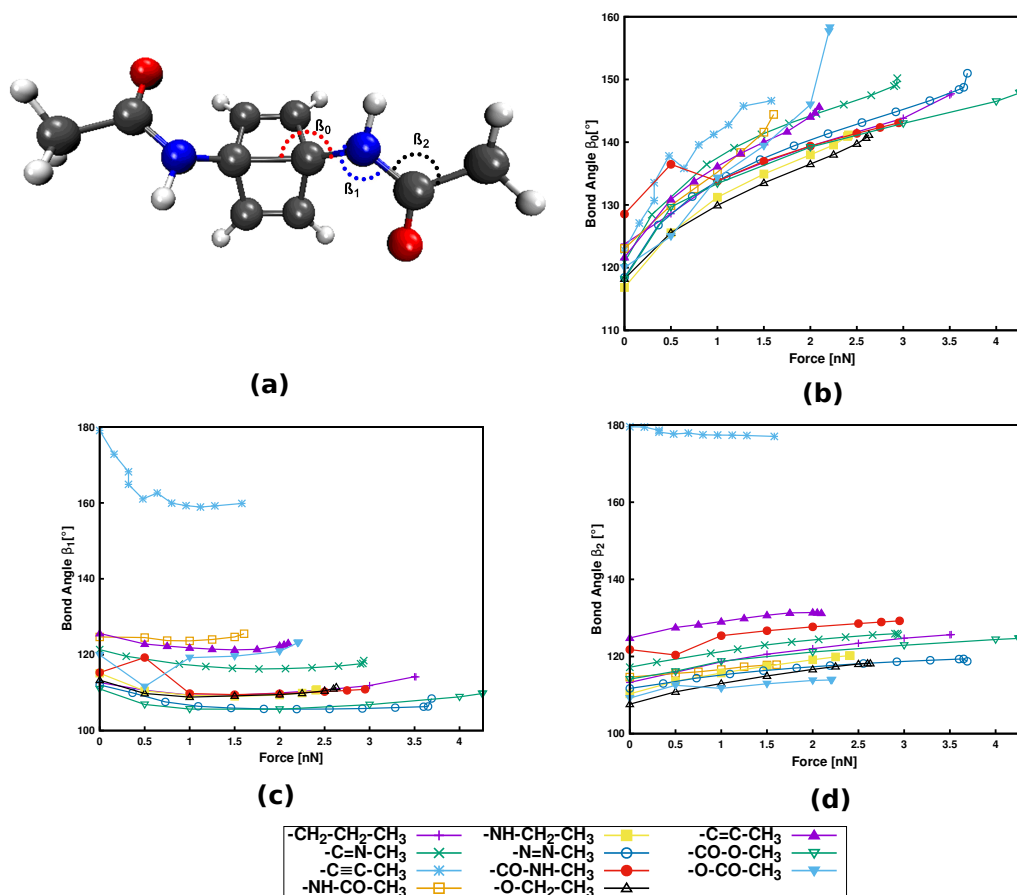


Figure 3.9: Dewar benzene with an amide linker with bond angle nomenclature (a). Progression of bond angles β_0 (b), β_1 (c) and β_2 (d) with external stretching force.

the initial value of β_1 in a specific linker is closely related to the position of this linker in Figure 3.8, with higher β_1 corresponding to lower rupture force. Hence, despite the stiffness of β_1 , this angle plays an important role in transmitting the mechanical load to the mechanophore, and that this transmission proceeds more efficiently the more linear β_1 is. Analogous results were found for benzocyclobutene and *gem*-dichlorocyclopropane (cf. Supporting Information, Figures 3.15 and 3.16 and Tables 3.9–3.12), hinting at a general validity of these results. In a previous investigation that focused on an alkyl chain connected to benzocyclobutene,^[189] out-of-plane distortions were found to influence mechanophore activation, whereas β_1 was

not considered. Thus, the findings presented here contribute to our understanding of force transduction through polymer chains from a structural point of view.

The important role of the angle β_1 is emphasized by end-to-end stretching simulations of the three mechanophores with the propyl linker in which β_1 is simultaneously constrained to different values (Figure 3.10). In these calculations, higher values of β_1 lead to lower rupture forces, which is in accordance with the aforementioned notion that a more linear angle β_1 leads to a lower rupture force. Increasing β_1 to 160° , for example, leads to a reduction of the rupture force to almost a third of the initial value. Therefore, β_1 is found to be the most critical coordinate for an efficient transmission of force to the mechanophore.

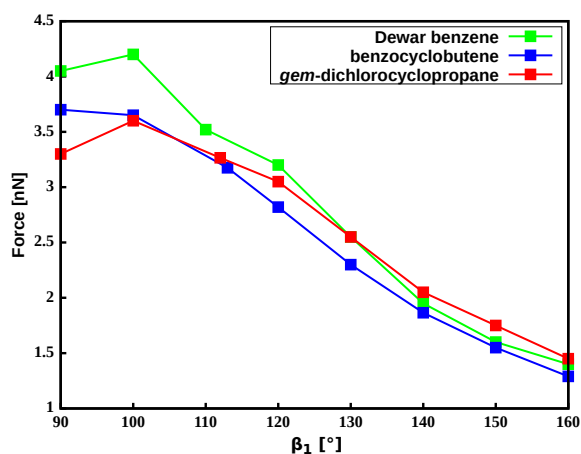


Figure 3.10: Amount of force required to activate the mechanophores using a propyl liker while constraining the angle β_1 .

The usefulness of the possibility to modulate the rupture forces of mechanophores by modifications of the linkers is demonstrated by considering the gating of a mechanochemical process, which has been reported recently.^[65] In the gating approach, a “weaker” mechanophore, i.e. *gem*-dichlorocyclopropane, is protected mechanically by the “stronger” cyclobutane (Figure 3.11a). At the PBE/cc-pVDZ level of theory, a stretching force of 4.7 nN is required to initiate the rupture of cy-

clobutane, which is followed immediately by the rupture of *gem*-dichlorocyclopropane. Hence, this mechanochemical reaction can be considered as a one-step process.

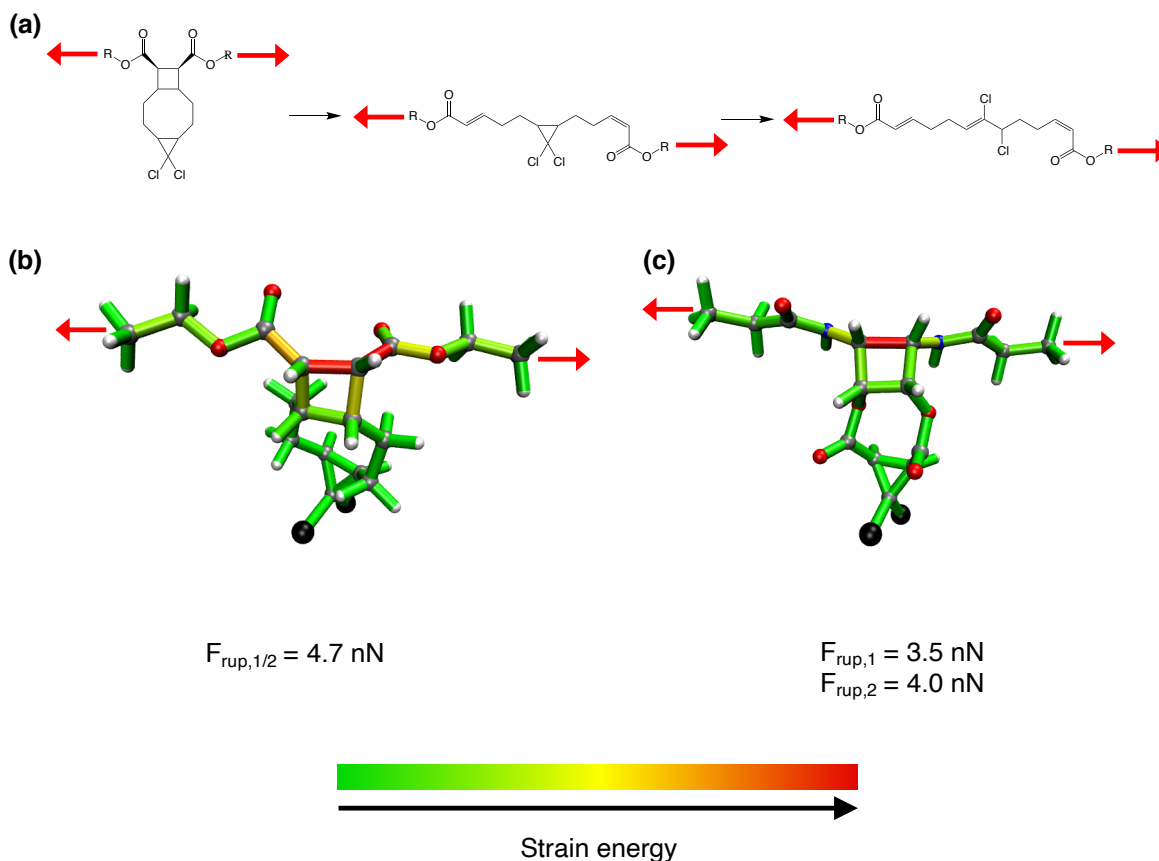


Figure 3.11: (a) Original gating approach presented in ref. 65. Red arrows signify mechanical stretching forces. (b) Distribution of strain energy^[115–117] in the bonds, bendings and torsions of a gating model system, in which both mechanophores (cyclobutane and *gem*-dichlorocyclopropane) are ruptured by a force of $F_{rup} = 4.7 \text{ nN}$. (c) Distribution of strain energy in a modified system with amide linkers attached to cyclobutane ($F_{rup} = 3.5 \text{ nN}$) and ester linkers attached to *gem*-dichlorocyclopropane ($F_{rup} = 4.0 \text{ nN}$). Color code for the atoms: white: hydrogen; gray: carbon; red: oxygen; black: chlorine; blue: nitrogen.

We aim at a transformation of the one-step gating to a two-step process, which lends itself for incorporating a hidden length in a polymer.^[191] In the original gating approach, an ester linker is used to transmit the mechanical stretching force to cyclobutane and a simple alkyl chain connects cyclobutane to *gem*-dichlorocyclopropane

(Figure 3.11b). According to Figure 3.8, in all investigated mechanophores the ester linker yields the highest rupture forces. By changing the linkers that transmit the stretching force to cyclobutane to amides and connecting cyclobutane to *gem*-dichlorocyclopropane *via* esters, the rupture force of cyclobutane was decreased to 3.5 nN. This force is insufficient to rupture *gem*-dichlorocyclopropane, for which 4.0 nN are required. Hence, by a simple modification of the linkers, the original one-step gating was switched to a two-step process. Since cyclobutane was not incorporated in the set of mechanophores investigated in Figure 3.8, these findings lend further credibility to the general validity of the presented results.

Using the JEDI analysis,^[115–117] the reason for the reduction of rupture force in the investigated system when changing the ester linker next to cyclobutane to an amide linker are elucidated. In the original system featuring an ester linker, several bonds, bendings and torsions within the cyclobutane ring and in its vicinity are significantly strained (Figure 3.11b). By contrast, the amide linker leads to an accumulation of strain almost exclusively in the scissile bond of cyclobutane (Figure 3.11c), thus facilitating the rupture of this bond.

Conclusion

In conclusion, the calculations presented here demonstrate that the force required for the activation of a mechanophore can be tuned over a range of almost 300% simply by changing the chemical composition of the linkers between the mechanophore and the rest of the polymer chain. This paves the way for a fine-tuning of the activation rate of mechanophores in polymers when exposed to mechanical deformation or ultrasound, with the possibility to either maximize mechanophore activation or to suppress it below a threshold force. In the future, we plan to apply our findings to maximize the efficiency of flex-activation of mechanophores in polymers,^[108,165,166] which can be used for the release of small molecules. Moreover, it is planned to

apply quantum chemical models of pressure^[106,181,192–197] to test the role of the linkers in experiments in which mechanophore activation is achieved by compression. Finally, our future studies will focus on a more realistic modeling of the polymer environment by using a multiscale model of mechanophores embedded in a polymer matrix.

3.5 Additional information

3.5.1 Computational Details

The External Force is Explicitly Included (EFEI)^[62,177,178] method was used to optimize the molecular geometries under a constant external stretching force. In the EFEI method, external mechanical forces are applied to a molecule during a quantum chemical geometry optimization by adding a constant to the nuclear gradient of a pair of atoms that drives these atoms apart. The geometry optimization converges when the external stretching force and the internal restoring force of the molecule cancel. Rupture forces were calculated iteratively. The COstrained Geometries simulate External Forces (COGEF)^[63,179] method was used to constrain the bond angle β_1 to different values while simultaneously stretching the molecules apart with the EFEI method. In COGEF, geometrical constraints are applied during a geometry optimization, which is equivalent to the application of mechanical stress. Both EFEI and COGEF were carried out with the Q-Chem 5.2.1^[182] program package using Density Functional Theory (DFT)^[121,122] at the PBE^[131]/cc-pVDZ^[103] level of theory based on geometries optimized at zero force. The lack of imaginary frequencies at zero force confirmed that the obtained structures are indeed true minima. The Cartesian coordinates of all structures (the three investigated mechanophores with all tested linkers) are available online as part of the Supporting Information.

The analysis of strain distribution in the mechanically distorted molecules was achieved with the Judgement of Energy DIstribution (JEDI)^[115–117] analysis. Based on the harmonic approximation, the JEDI analysis quantifies the strain energies within each bond, bending and torsion of a mechanically deformed molecule. Color-coded structures of molecules under tensile stress were created with VMD 1.9.3,^[183] where the strain in each bond, bending and torsion was mapped onto the bonds.

To study the role of electron density at the bond critical points, topology analysis was carried out with the Quantum Theory of Atoms In Molecules (QTAIM)^[79] approach using the Multiwfn 3.7 program package.^[184] The wavefunctions required for these calculations were generated with Q-Chem.

3.5.2 Dependence of rupture force on the length of the alkyl chain

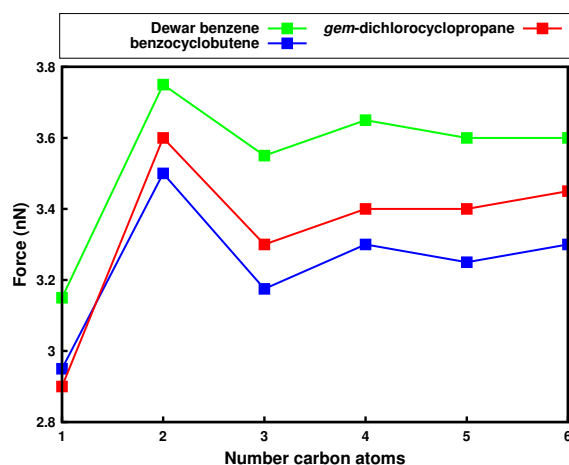


Figure 3.12: Amount of force required to activate the investigated mechanophores when changing the number of carbon atoms in the alkyl linker. Lines were included to guide the eye.

3.5.3 Influence of the linker on the rupture force


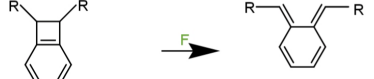

					
Substitution	Rupture force (nN)	Substitution	Rupture force (nN)	Substitution	Rupture force (nN)
-C≡C-CH ₃	1.59	-C≡C-CH ₃	1.80	-NH-CO-CH ₃	1.35
-NH-CO-CH ₃	1.61	-NH-CO-CH ₃	1.91	-C≡C-CH ₃	1.64
-C=C-CH ₃	2.10	-O-CH ₂ -CH ₃	1.96	-O-CO-CH ₃	2.05
-O-CO-CH ₃	2.22	-O-CO-CH ₃	2.33	-C=C-CH ₃	2.15
-NH-CH ₂ -CH ₃	2.42	-NH-CH ₂ -CH ₃	2.49	-NH-CH ₂ -CH ₃	2.46
-O-CH ₂ -CH ₃	2.64	-C=C-CH ₃	2.59	-CO-NH-CH ₃	2.59
-C=N-CH ₃	2.94	-C=N-CH ₃	3.04	-O-CH ₂ -CH ₃	2.63
-CO-NH-CH ₃	2.96	-CH ₂ -CH ₂ -CH ₃	3.18	-C=N-CH ₃	2.66
-CH ₂ -CH ₂ -CH ₃	3.52	-N=N-CH ₃	3.24	-N=N-CH ₃	2.79
-N=N-CH ₃	3.70	-CO-NH-CH ₃	3.40	-CH ₂ -CH ₂ -CH ₃	3.27
-CO-O-CH ₃	4.27	-CO-O-CH ₃	3.56	-CO-O-CH ₃	3.87

Table 3.2: Rupture forces for the mechanical activation of Dewar Benzene, benzocyclobutene and *gem*-dichlorocyclopropane using different linkers that connect the mechanophores to the rest of the polymer backbone.

3.5.4 Rupture forces using combinations of different linkers

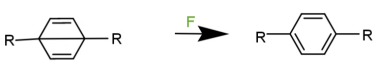


					
Substitution (Linker1, Linker2)	Rupture force (nN)	Substitution (Linker1, Linker2)	Rupture force (nN)	Substitution (Linker1, Linker2)	Rupture force (nN)
-C≡C-CH ₃ , -O-CH ₂ -CH ₃	2.05	-C≡C-CH ₃ -C=C-CH ₃	2.15	-NH-CO-CH ₃ -CO-NH-CH ₃	1.6
-C≡C-CH ₃ -CO-O-CH ₃	2.65	-C≡C-CH ₃ -CO-O-CH ₃	2.65	-NH-CO-CH ₃ -CO-O-CH ₃	1.9
-CO-O-CH ₃ -O-CH ₂ -CH ₃	3.3	-O-CH ₂ -CH ₃ -C=C-CH ₃	3.15	-CO-NH-CH ₃ -CO-O-CH ₃	3.0

Table 3.3: Rupture forces for the mechanical activation of Dewar Benzene, benzocyclobutene and *gem*-dichlorocyclopropane using combinations of different linkers.

3.5.5 JEDI analysis

Dewar Benzene

Substitution	Strain percentage			Absolute energy (a.u.)
	Bond lengths	Bond angles	Dihedral angles	
-NH-CO-CH ₃	27.55	18.03	54.42	0.0134181807
-C=C-CH ₃	24.09	22.55	53.36	0.0109785290
-CO-O-CH ₃	39.17	20.34	40.49	0.033472350

Table 3.4: Percentage of total strain stored in the bond lengths, bond angles and dihedral angles of Dewar benzene with different linkers as well as strain energy in the scissile C-C bond at a stretching force that is 0.01 nN lower than the rupture force.

Benzocyclobutene

Substitution	Strain percentage			Absolute energy (a.u.)
	Bond lengths	Bond angles	Dihedral angles	
-NH-CO-CH ₃	12.41	19.14	68.45	0.02943622
-C=C-CH ₃	35.09	27.78	37.13	0.0288327
-CO-O-CH ₃	21.11	20.24	58.66	0.0295591

Table 3.5: Percentage of total strain stored in the bond lengths, bond angles and dihedral angles of benzocyclobutene with different linkers as well as strain energy in the scissile C–C bond at a stretching force that is 0.01 nN lower than the rupture force.

***gem*-dichlorocyclopropane**

Substitution	Strain percentage			Absolute energy (a.u.)
	Bond lengths	Bond angles	Dihedral angles	
-NH-CO-CH ₃	4.13	2.63	93.24	0.0050843
-C=C-CH ₃	22.05	25.90	52.05	0.008019
-CO-O-CH ₃	26.09	19.39	54.51	0.0277913

Table 3.6: Percentage of total strain stored in the bond lengths, bond angles and dihedral angles of *gem*-dichlorocyclopropane with different linkers as well as strain energy in the scissile C–C bond at a stretching force that is 0.01 nN lower than the rupture force.

3.5.6 Electron density at the bond critical points

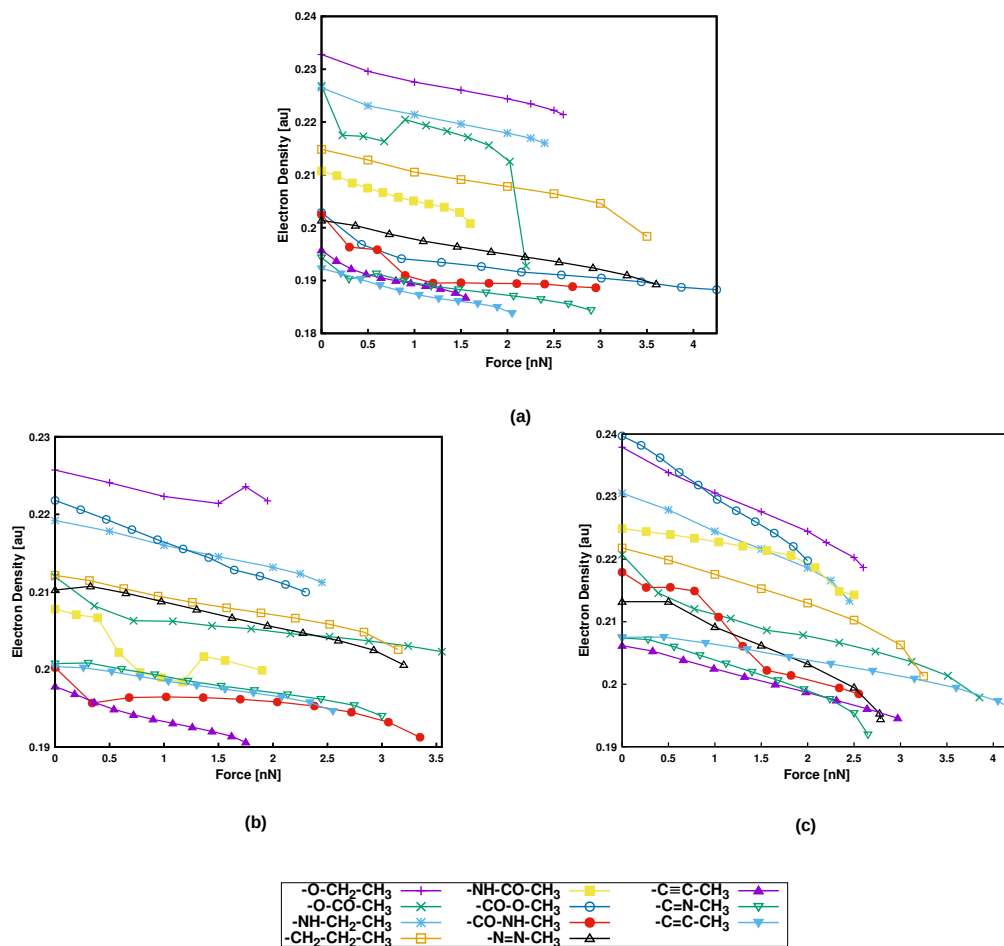


Figure 3.13: Electron densities in the scissile C–C bonds in Dewar benzene (a), benzocyclobutene (b) and *gem*-dichlorocyclopropane (c) using different linkers, as a function of external stretching force.

3.5.7 Bond angles in the linkers

Dewar Benzene

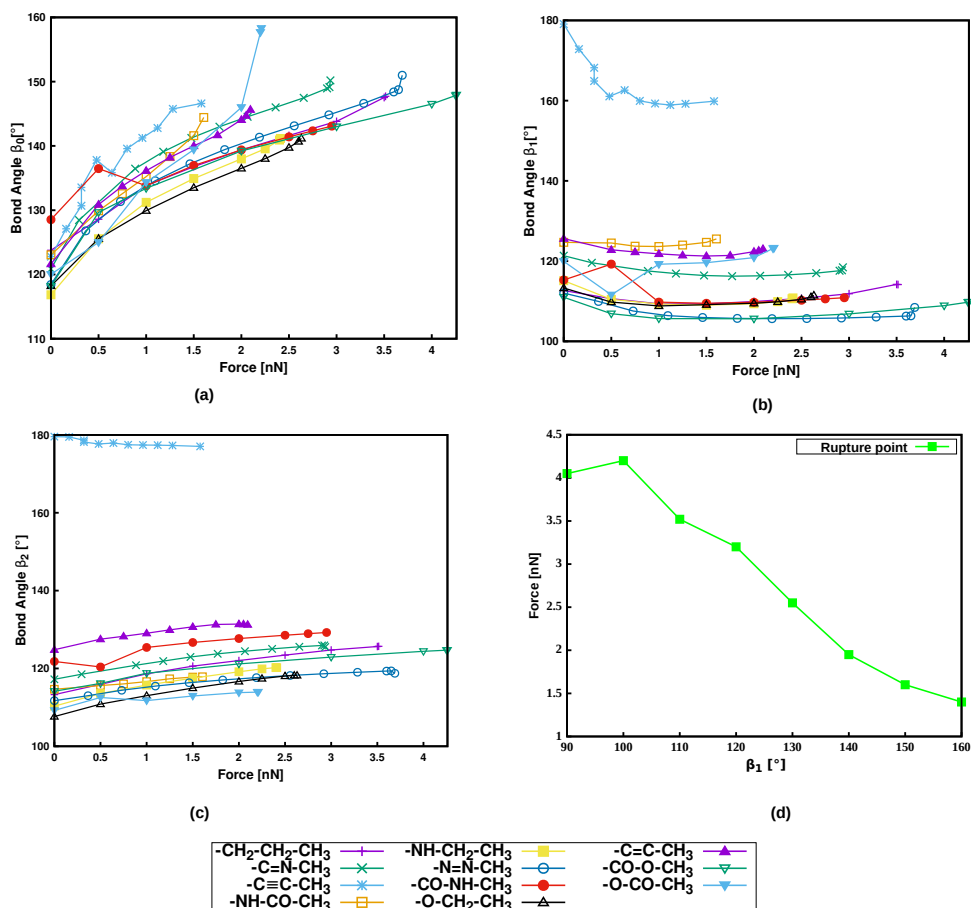


Figure 3.14: Bond angles β_0 (a), β_1 (b) and β_2 (c) as a function of external stretching force applied to the terminal methyl groups in Dewar benzene with different linkers. (d) Rupture forces as a function of the constrained angle β_1 .

Substitution	β_0 (initial)	β_0 (final)
$-\text{C}\equiv\text{C}-\text{CH}_3$	122.78	146.61
$-\text{NH}-\text{CO}-\text{CH}_3$	123.05	144.43
$-\text{C}=\text{C}-\text{CH}_3$	121.63	145.65
$-\text{O}-\text{CO}-\text{CH}_3$	120.03	158.29
$-\text{NH}-\text{CH}_2-\text{CH}_3$	116.81	141.15
$-\text{O}-\text{CH}_2-\text{CH}_3$	118.22	141.17
$-\text{C}=\text{N}-\text{CH}_3$	120.86	150.19
$-\text{CO}-\text{NH}-\text{CH}_3$	128.53	143.09
$-\text{CH}_2-\text{CH}_2-\text{CH}_3$	123.76	147.72
$-\text{N}=\text{N}-\text{CH}_3$	118.43	150.99
$-\text{CO}-\text{O}-\text{CH}_3$	118.18	147.93

Table 3.7: Initial ($F = 0$) and final (0.01 nN before bond rupture) values of the bond angle β_0 in Dewar benzene.

Substitution	β_1 (initial)	β_2 (initial)	β_1 (final)	β_2 (final)
$-\text{C}\equiv\text{C}-\text{CH}_3$	179.08	179.64	159.86	177.05
$-\text{NH}-\text{CO}-\text{CH}_3$	124.67	114.65	125.53	117.87
$-\text{C}=\text{C}-\text{CH}_3$	125.61	124.81	123.05	131.26
$-\text{O}-\text{CO}-\text{CH}_3$	119.94	109.22	123.24	113.95
$-\text{NH}-\text{CH}_2-\text{CH}_3$	115.12	110.32	110.83	120.20
$-\text{O}-\text{CH}_2-\text{CH}_3$	113.29	107.64	111.44	118.20
$-\text{C}=\text{N}-\text{CH}_3$	121.34	117.22	118.44	125.51
$-\text{CO}-\text{NH}-\text{CH}_3$	115.54	122.68	110.92	129.95
$-\text{CH}_2-\text{CH}_2-\text{CH}_3$	112.67	113.27	114.15	125.69
$-\text{N}=\text{N}-\text{CH}_3$	112.03	111.72	108.46	118.75
$-\text{CO}-\text{O}-\text{CH}_3$	110.98	114.14	109.80	124.70

Table 3.8: Initial ($F = 0$) and final (0.01 nN before bond rupture) values of the bond angles β_1 and β_2 in Dewar benzene.

Benzocyclobutene

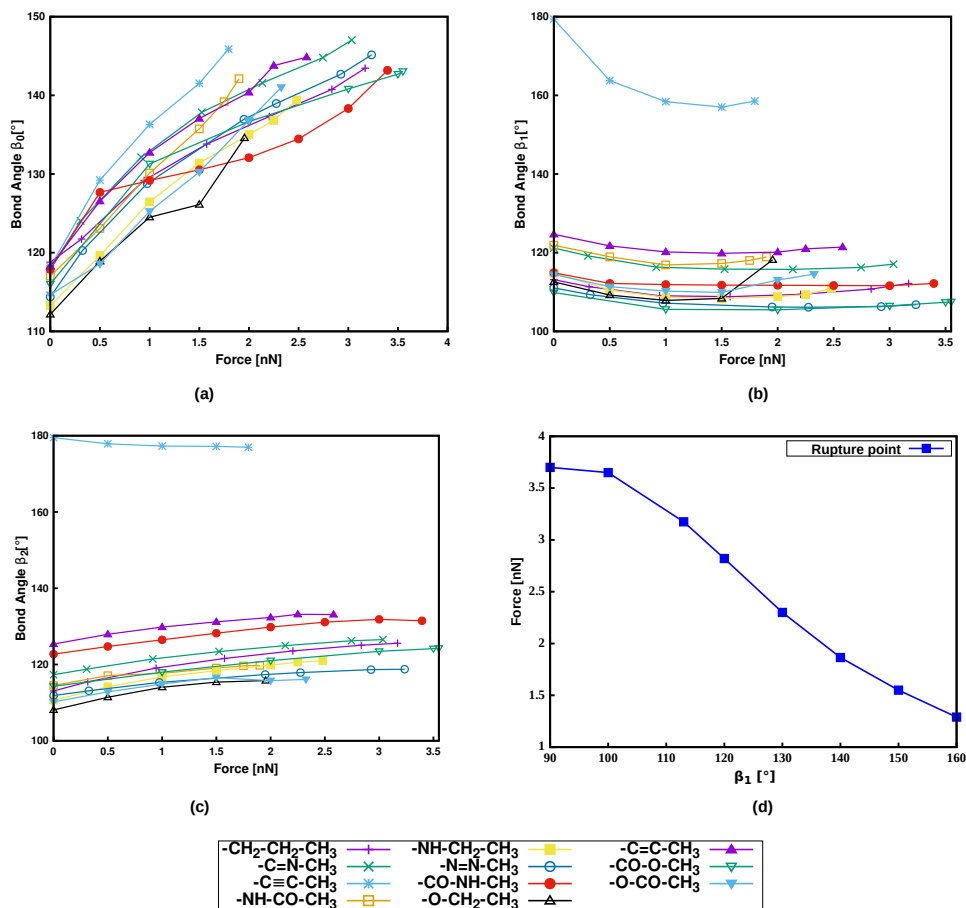


Figure 3.15: Bond angles β_0 (a), β_1 (b) and β_2 (c) as a function of external stretching force applied to the terminal methyl groups in benzocyclobutene with different linkers. (d) Rupture forces as a function of the constrained angle β_1 .

Substitution	β_0 (initial)	β_0 (final)
$-\text{C}\equiv\text{C}-\text{CH}_3$	118.171	145.894
$-\text{NH}-\text{CO}-\text{CH}_3$	120.048	140.658
$-\text{O}-\text{CH}_2-\text{CH}_3$	112.153	134.608
$-\text{O}-\text{CO}-\text{CH}_3$	113.25	141.284
$-\text{NH}-\text{CH}_2-\text{CH}_3$	111.734	138.678
$-\text{C}=\text{C}-\text{CH}_3$	118.263	144.854
$-\text{C}=\text{N}-\text{CH}_3$	117.916	147.029
$-\text{CH}_2-\text{CH}_2-\text{CH}_3$	118.802	143.453
$-\text{N}=\text{N}-\text{CH}_3$	114.382	145.159
$-\text{CO}-\text{NH}-\text{CH}_3$	117.876	143.183
$-\text{CO}-\text{O}-\text{CH}_3$	119.926	142.93

Table 3.9: Initial ($F = 0$) and final (0.01 nN before bond rupture) values of the bond angle β_0 in benzocyclobutene.

Substitution	β_1 (initial)	β_2 (initial)	β_1 (final)	β_2 (final)
$-\text{C}\equiv\text{C}-\text{CH}_3$	179.49	179.31	158.53	176.95
$-\text{NH}-\text{CO}-\text{CH}_3$	125.71	115.08	126.032	118.005
$-\text{O}-\text{CH}_2-\text{CH}_3$	112.59	108.08	118.19	115.79
$-\text{O}-\text{CO}-\text{CH}_3$	115.81	109.73	114.55	115.99
$-\text{NH}-\text{CH}_2-\text{CH}_3$	113.85	110.82	109.04	120.93
$-\text{C}=\text{C}-\text{CH}_3$	124.68	125.36	121.42	133.12
$-\text{C}=\text{N}-\text{CH}_3$	121.175	117.33	117.089	126.53
$-\text{CH}_2-\text{CH}_2-\text{CH}_3$	113.14	113.07	112.17	125.57
$-\text{N}=\text{N}-\text{CH}_3$	111.05	111.87	106.79	118.77
$-\text{CO}-\text{NH}-\text{CH}_3$	114.89	122.72	112.17	131.47
$-\text{CO}-\text{O}-\text{CH}_3$	109.87	114.30	107.51	124.29

Table 3.10: Initial ($F = 0$) and final (0.01 nN before bond rupture) values of the bond angles β_1 and β_2 in benzocyclobutene.

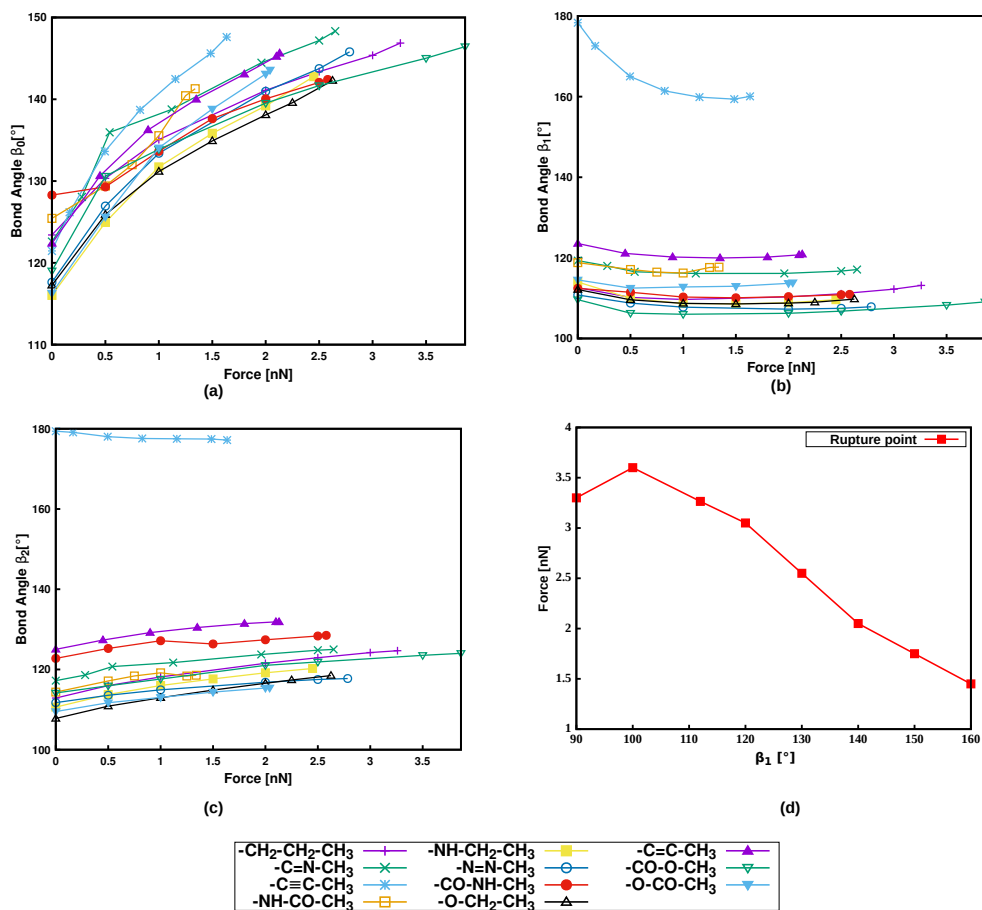
gem-Dichlorocyclopropane

Figure 3.16: Bond angles β_0 (a), β_1 (b) and β_2 (c) as a function of external stretching force applied to the terminal methyl groups in *gem*-dichlorocyclopropane with different linkers. (d) Rupture forces as a function of the constrained angle β_1 .

Substitution	β_0 (initial)	β_0 (final)
–NH–CO–CH ₃	129.373	141.233
–C≡C–CH ₃	121.469	147.619
–O–CO–CH ₃	116.307	143.588
–C=C–CH ₃	122.318	145.621
–NH–CH ₂ –CH ₃	116.030	142.323
–CO–NH–CH ₃	128.291	142.284
–O–CH ₂ –CH ₃	117.126	142.300
–C=N–CH ₃	122.61	148.311
–N=N–CH ₃	117.639	141.101
–CH ₂ –CH ₂ –CH ₃	123.419	146.877
–CO–O–CH ₃	119.029	146.292

Table 3.11: Initial ($F = 0$) and final (0.01 nN before bond rupture) values of the bond angle β_0 in *gem*-dichlorocyclopropane.

Substitution	β_1 (initial)	β_2 (initial)	β_1 (final)	β_2 (final)
–NH–CO–CH ₃	118.82	114.37	117.70	118.56
–C≡C–CH ₃	178.33	179.39	164.78	178.10
–O–CO–CH ₃	114.53	109.81	113.84	115.41
–C=C–CH ₃	123.63	124.91	120.89	131.85
–NH–CH ₂ –CH ₃	114.45	110.29	111.79	120.37
–CO–NH–CH ₃	116.98	121.20	110.97	128.45
–O–CH ₂ –CH ₃	112.14	107.78	109.76	118.48
–C=N–CH ₃	119.31	117.22	117.10	124.97
–N=N–CH ₃	110.79	111.74	107.94	117.66
–CH ₂ –CH ₂ –CH ₃	112.66	112.88	113.17	124.67
–CO–O–CH ₃	108.43	114.10	109.08	124.09

Table 3.12: Initial ($F = 0$) and final (0.01 nN before bond rupture) values of the bond angles β_1 and β_2 in *gem*-dichlorocyclopropane.

Chapter 4

Stress induced from pressure

4.1 Scope of the project

In Chapter 3 we have studied the role of stretching forces on molecules, and gained insights on the mechanism involved in mechanophore activation under external stretching forces. The force-induced structural changes in such mechanochemical reactions are usually permanent, thereby the applicability of functional materials is restricted. Although reversible mechanophores exist, they are limited in number.

However, forces can also be implemented by applying compression on the mechanophores. Experimentally, under compression fluorescence in polymers,^[58] distinct luminescent responses,^[198] [4+4] retrocycloaddition,^[105] hydrostatic-pressure-driven redox reactions^[199] have been achieved mechanochemically.

The recently developed X-HCFF method (cf. Section 2.3.3) is a valuable tool for simulating true hydrostatic pressure at the single molecule level. The X-HCFF method offers more flexibility than previous models by enabling users to define the pressure during the geometry optimization process.

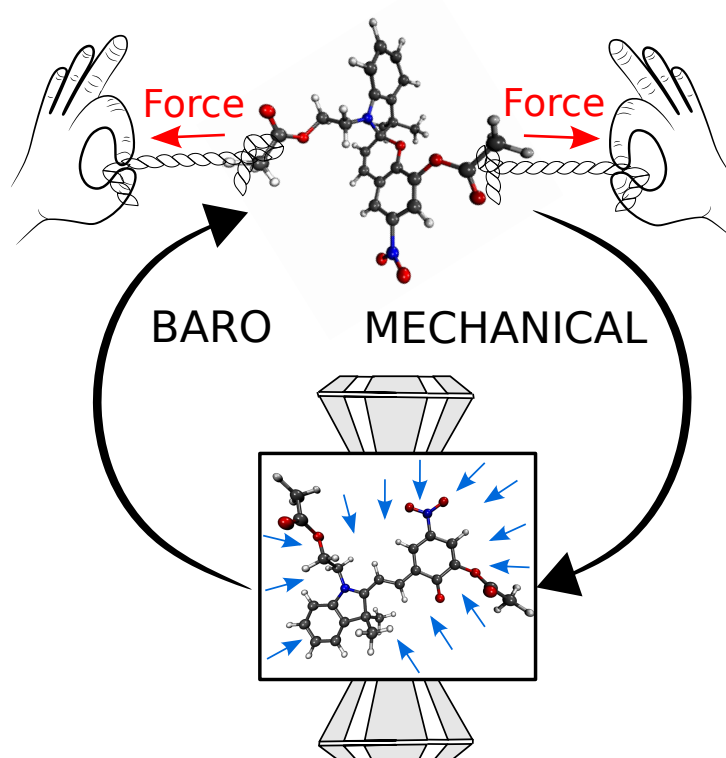
By using the X-HCFF approach we have studied a SP-MC isomerization reaction and shown that the activated form i.e. MC can be reversed back to the SP under

hydrostatic pressure, which allows the repeated activation of the SP mechanophore. The findings indicate that, when the activated form has a larger volume than the deactivated form, it can be reversed back to the deactivated form under pressure. The occurrence of repeated isomerization was monitored by the real-time UV/vis absorption spectrum.

It is well known that successful reactions under high pressure conditions possess a transition state with a volume close to or less than the products.^[200,201] But due to the lack of specific computational models it was challenging to obtain more knowledge about the phenomenon and precisely show what is happening at molecular level. The second part of this chapter is focused on addressing this challenge and demonstrating that by applying hydrostatic pressure, it is possible to trap the transition state that occurs in a [2,3]-sigmatropic rearrangement. The step-wise increase in the hydrostatic pressure during the BOMD simulations has shown the formation of a five membered ring (i.e. the transition state), and further step-wise decompression leads to the 70:30 mix of the product and the educt of the sigmatropic rearrangement.

Furthermore, the findings were evaluated based on the Mayer bond order and electron density at bond-critical points. To aid in experimental studies, simulated IR, Raman, and time-resolved UV/vis absorption spectra were included as reference data.

4.2 Publication: A two-step baromechanical cycle for repeated activation and deactivation of mechanophores.



Reprinted with permission from

J. Phys. Chem. Lett., **2021**, 12, 9470–9474.

Copyright 2021 American Chemical Society.

Felix Zeller from the University of Bremen contributed to this work as a second author.

Abstract

Mechanophores that are embedded in a polymer backbone respond to the application of mechanical stretching forces by geometric changes such as bond rupture. Typically, these structural changes are irreversible, which limits the applicability of functional materials that incorporate mechanophores. Using computational methods, we here present a general method of restoring a force-activated mechanophore to its deactivated form by using hydrostatic pressure. We use the well-known spiropyran-merocyanine (SP-MC) interconversion to show that repeated activation and deactivation of the SP mechanophore can be achieved by alternating application of mechanical stretching forces and hydrostatic compression. In the baro-mechanical cycle, MC plays the role of a “barophore” that responds to hydrostatic pressure by bond formation. The activation and deactivation pathways of SP and MC are understood in terms of strain and electronic effects. Beneficially, this two-step baro-mechanical cycle can be observed in real time by using UV/Vis spectroscopy. Our calculations pave the way for massively improving the applicability and reusability of force-responsive materials.

Introduction

Within the past two decades, mechanical force has emerged as a sustainable alternative to more traditional means of activating chemical reactions.^[202,203] At the focal point of many experimental and computational mechanochemical studies are mechanophores, i.e., small molecular units that are typically incorporated into the backbones of polymers.^[28,204,205] Mechanochemical deformation triggers profound structural rearrangements in the mechanophore, e.g. bond rupture. This effect has been used in the development of force-responsive and stress-sensing materials^[152,206] as well as for triggering reaction cascades^[94,207] and the release of small molecules.^[208,209] However, force-induced structural changes in mechanophores are typically permanent. While some reversible mechanophores have been reported,^[172] the fact that most mechanophores cannot easily be reverted back to their deactivated form limits the applicability of force-responsive materials in everyday applications due to their limited recyclability.

Here we present a general approach to restore activated mechanophores to their original, deactivated form by applying hydrostatic pressure. Our proposed two-step baro-mechanical cycle is based on alternating application of mechanical stretching forces and hydrostatic pressure to switch between the activated and deactivated forms of mechanophores. In this computational study we focus on the well-known spiropyran (SP) mechanophore, which can be transformed to merocyanine (MC) by application of mechanical stretching forces.^[12,206] (Figure 4.1). While the reverse reaction of MC to SP has been initiated by using light,^[210,211] heat,^[212] guest molecules^[213] and redox reactions,^[214] we suggest that our method of restoring a mechanophore to its deactivated form by applying hydrostatic pressure is generally applicable to mechanophores that experience an increase in volume upon activation. Beneficially, the interconversion of SP and MC can be tracked by changes in the visible part of the UV/Vis absorption spectrum.

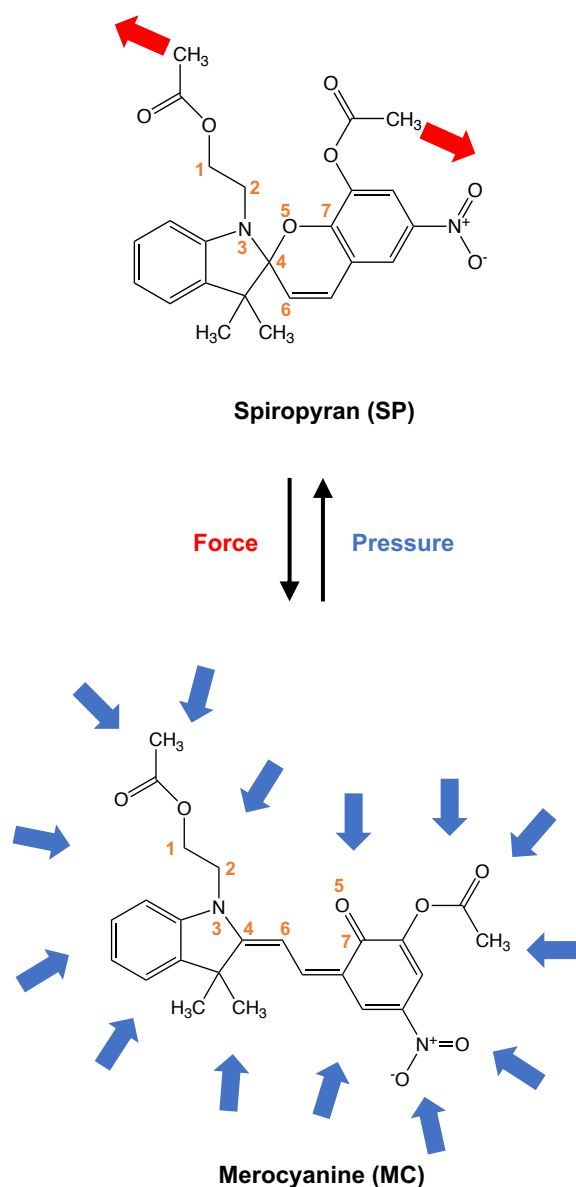


Figure 4.1: Schematic illustration of the two-step baro-mechanical cycle, in which the isomerization of spiropyran (SP) to merocyanine (MC) is triggered by mechanical stretching forces, whereas the opposite transformation is initiated by hydrostatic pressure.

In this study, we focus on molecular model systems of SP and MC, in which the polymer surrounding is largely ignored, except for short linkers between the SP/MC and the polymer (Figure 4.1). To demonstrate the gist of the baro-mechanical cycle, stretching forces were applied to the ends of linkers of the SP model system with the *External Force is Explicitly Included* (EFEI)^[62,177,178] method. EFEI allows quantum

chemical geometry optimizations in which a pair of atoms is pulled apart by a user-defined force. At the B3LYP^[100,102,215]/6-31G(d)^[216] level of theory, a force of 2.7 nN is required to initiate the isomerization from SP to MC. Conversely, application of a hydrostatic pressure of 5 GPa *via* the *eXtended Hydrostatic Compression Force Field* (X-HCFF)^[108] to MC leads to the generation of SP. In X-HCFF, mechanical forces perpendicular to the molecular surface compress a molecule during a geometry optimization. In this case, MC acts as a “barophore”, in analogy to the role of SP as a mechanophore. All calculations were conducted with the Q-Chem 5.4 program package.^[217] Further computational details can be found in the Supporting Information.

While these results suggest the possibility of returning force-activated mechanophores to their deactivated state by applying hydrostatic pressure, it is crucial to note that compression is a common method of activating mechanophores^[14,58,218] and not of deactivating them. In fact, we are unaware of any experimental studies reporting the transformation of MC to SP under pressure. However, if the activated form of a mechanophore has a higher volume than the deactivated form, the application of hydrostatic pressure clearly favors the formation of the deactivated form. In the case of SP-MC isomerism, we have calculated the volume of SP to be 352.8 Å³ and that of MC to be 357.7 Å³ (both molecules without linkers), based on electron densities. Since the chemical equilibrium can be biased towards species with a lower volume by application of hydrostatic pressure,^[106,219,220] we come to the conclusion that mechanical compression in experiments is usually not hydrostatic, which has been indicated before in the case of the dianthracene mechanophore.^[105] At the single-molecule level, compression is likely anisotropic, owing, e.g., to steric effects of the (polymer) environment. If, however, truly hydrostatic compression was achieved experimentally at the single-molecule level, we expect efficient deactivation of force-activated mechanophores to be possible. Specifically, we consider the application

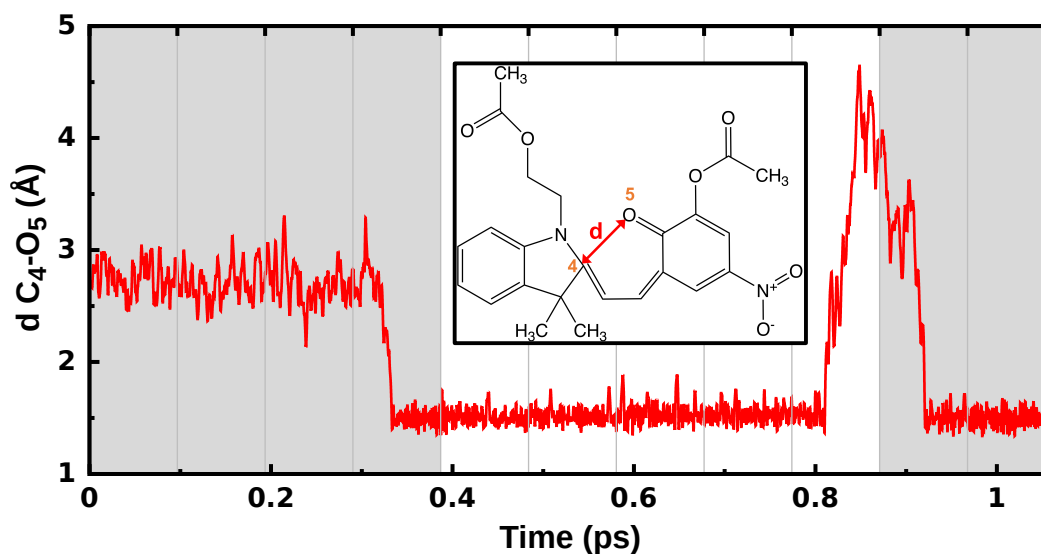


Figure 4.2: Temporal progress of the distance C_4-O_5 throughout the course of a representative Born-Oppenheimer Molecular Dynamics (BOMD) trajectory. Pressure was increased in steps of 0.5 GPa throughout the gray shaded areas. Stretching forces were increased in steps of 150 pN in the white area. Gray vertical lines signify the points in time when the pressure or the force were adjusted, respectively.

of hydrostatic pressure *via* a diamond anvil cell on isolated MC molecules as an appropriate experiment for this purpose.

To gain a dynamic picture of the repeated activation/deactivation process of the SP mechanophore, ten Born-Oppenheimer Molecular Dynamics (BOMD) simulations at a temperature of 1000 K were conducted. This temperature was adjusted to sample a considerable part of the conformational space within a reasonable computation time. Starting from MC, a step-wise increasing pressure was applied until SP was formed. In a representative BOMD trajectory (Figure 4.2), a pressure of 2 GPa was sufficient to form the C_4-O_5 bond at approx. 300 fs simulation time (cf. Figure 4.1 for the numbering scheme), leading to SP. Subsequently, pressure was switched off and an increasing force was applied. At approx. 800 fs simulation time and a stretching force of 750 pN applied to SP, the C_4-O_5 bond is ruptured and MC is formed. The interconversion between SP and MC also becomes apparent in the decrease in double bond character of the C_7-O_5 bond (Figure 4.5).

To demonstrate the reversibility of this process, pressure was subsequently applied once more. This time, a pressure of 0.5 GPa was sufficient to transform SP to MC, which is due to thermal oscillations in combination with the proximity of C₄ and O₅. In another trajectory, stretching forces applied to SP generated a fully extended, “trans” configuration of MC with a calculated volume of 358.8 Å³, which required a significantly higher pressure (3.5 GPa) to trigger the transformation to SP. Hence, the pressure required for deactivation depends heavily on the instantaneous configuration of MC. However, in all ten simulated trajectories, the interconversion between SP and MC using force and pressure, respectively, has been demonstrated, which emphasizes the robustness of the presented baro-mechanical cycle. Details on the required pressures and forces in all other BOMD trajectories are given in the Supporting Information (Table 4.1).

The force-induced activation of SP in the representative BOMD trajectory discussed above was analyzed in terms of strain energies by applying the Judgement of Energy DIstribution (JEDI) analysis.^[115–117] As shown in Figure 4.3, surprisingly, only a very small percentage of strain is stored in the scissile C₄–O₅ bond when stretching forces are applied. Instead, torsions in the vicinity of the scissile bond are significantly displaced, leading to an accumulation of strain energy in these torsions. The increase of strain energy in the torsions precedes the C₄–O₅ bond rupture process (Figure 2). A similar effect has been observed before in knotted polymer strands, where accumulation of strain in torsions facilitates bond rupture.^[119] The facilitation of bond rupture in SP by torsional motions in the vicinity of the scissile bond has, to the best of our knowledge, never been observed before. However, we assume that this effect explains the experimentally observed high mechanical yield of the SP-to-MC conversion.

The interconversion between SP and MC can be observed *via* time-resolved changes in the UV/Vis absorption spectrum (Figure 4.4). Initially, peaks in the

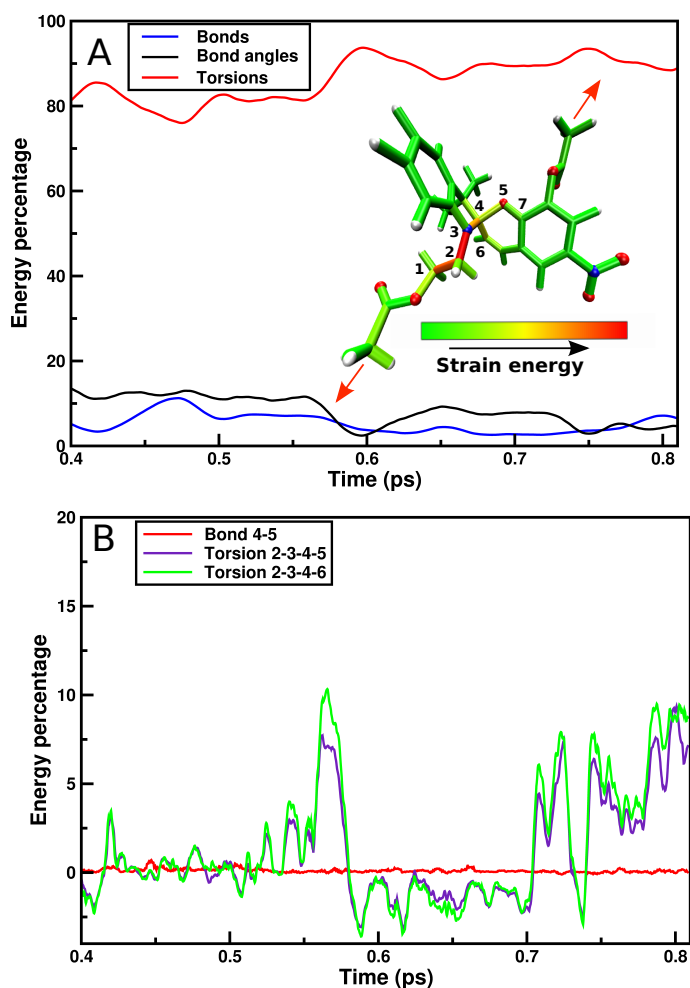


Figure 4.3: Results of the Judgement of Energy Distribution (JEDI) analysis for SP activation during a representative BOMD trajectory. A) Percentages of strain energy in the bonds, bendings and torsions of stretched SP after it is formed initially. The color-coded structure is a representation of stretched SP shortly before rupture, at an external force of 750 pN at 814 fs simulation time. Strain energies in all degrees of freedom were mapped onto the bonds. B) Percentages of strain energy in the scissile bond and in two dihedral angles.

range between 400 and 600 nm are found due to the presence of MC. Initially, the absorption spectrum remains relatively constant as pressure increases. However, as soon as SP is formed, peaks in the UV/Vis absorption spectrum are limited to the range between 300 and 350 nm, signifying the characteristic color change that is observed when switching between MC and SP. The absorption spectrum of SP is relatively insensitive to the application of stretching forces until MC is formed,

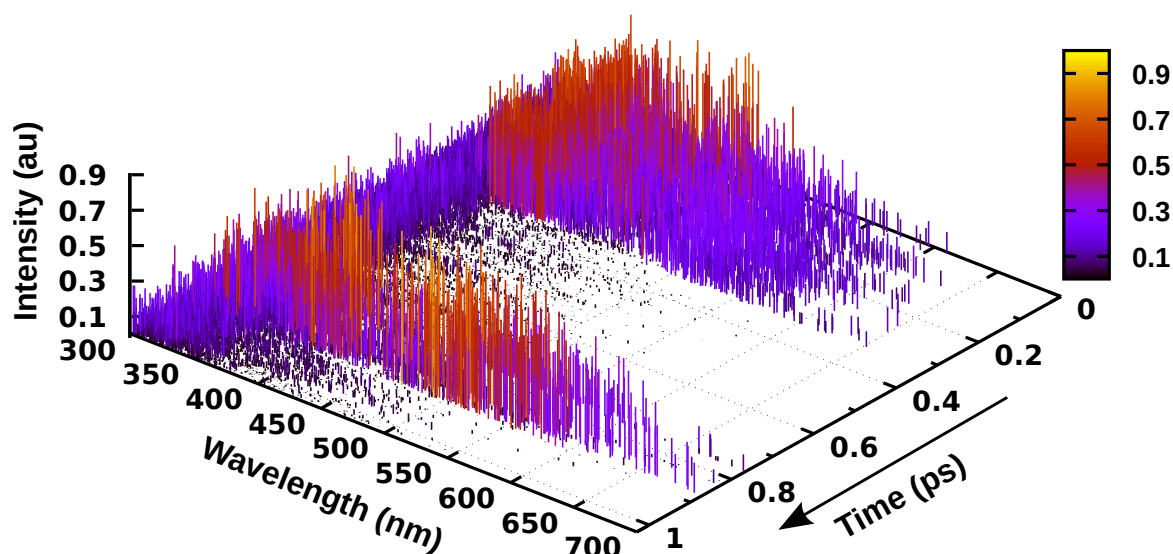


Figure 4.4: Time series plot of the UV absorption spectrum of the SP/MC system under the alternating influences of pressure and force throughout a representative BOMD trajectory. A color palette is used to highlight the intensities.

where the initial absorption spectrum is recovered. The final generation of SP by pressure is again accompanied by a marked blue shift of the absorption spectrum.

The marked changes in the absorption spectrum when switching between SP and MC are useful for experimental verification of the baro-mechanical cycle presented here, since the SP-MC interconversion can be tracked in real time either spectroscopically or with the naked eye. Quantitative optical measurements potentially even allow the estimation of the efficiency of the baro-mechanical cycle. Irrespective of the changes in UV/Vis absorption, however, we assume that force-activated mechanophores can act as barophores when their volume is higher than that of the original, deactivated mechanophore.

By using static and dynamic calculations of the spiropyran-merocyanine (SP-MC) system under alternating influences of mechanical stretching forces and hydrostatic pressure, a two-step baro-mechanical cycle for repeated activation and deactivation of mechanophores was established. The activation of SP was understood in terms of strain and it was found that SP is “twisted open” by force, which greatly

facilitates bond rupture. Conversely, MC acts as a barophore that responds to the application of pressure by bond formation. Marked changes in the visible part of the UV/Vis absorption spectrum allow the real-time tracking of the SP-MC interconversion. We hope that our proof-of-principle study triggers the interest in combined mechanochemical and barochemical experiments, using, e.g., diamond-anvil cells and ultrasound baths. The possibility to restore force-activated mechanophores to their deactivated form holds great promise for the development of reusable force-responsive materials. In addition, the color change associated with the MC-to-SP conversion paves the way for the use of MC as an internal standard in high-pressure experiments. Calculations on molecular pressure sensors are currently being conducted in our group. Moreover, we plan to model the polymer surrounding of the SP mechanophore and the MC barophore more realistically by developing a computational multiscale approach.

Acknowledgements: The authors would like to thank M. Scheurer, University of Heidelberg, for providing the python script to calculate the volume of a molecule.

4.3 Additional information

4.3.1 Computational Details

All calculations were carried out with Density Functional Theory (DFT)^[121,122] or Time-Dependent Density Functional Theory (TD-DFT),^[221] respectively, at the B3LYP^[100,102,215]/6-31G(d)^[216] level of theory. Geometry optimizations of SP and MC were performed and the lack of imaginary frequencies confirmed that the stationary points were minima on the potential energy surface. Based on these geometries, external stretching forces were applied to the terminal carbon atoms of the short linking units of SP *via* the External Force is Explicitly Included (EFEI) methodology.^[62,177,178] Hydrostatic pressure was applied to MC *via* the eXtended Hydrostatic Compression Force Field (X-HCFF) approach.^[108] A tessellation sphere scaling factor of 1.8 as well as 302 tessellation points per atom were used in the X-HCFF calculations. In the static calculations, the pressure required to form SP from MC was determined iteratively. Subsequently, stretching forces were applied to SP until MC was formed. All calculations were performed with the Q-Chem 5.4 program package.^[217]

Ten individual Born-Oppenheimer Molecular Dynamics (BOMD) simulations were conducted at a temperature of 1000 K. Initial velocities were sampled from a Maxwell-Boltzmann distribution. The integration time step amounted to 20 a.u.. The optimized *cis* form of MC was used as the initial geometry in all BOMD trajectories. Pressure was increased by 0.5 GPa each 96.8 fs until spiropyran was formed. Subsequently, pressure was switched off and mechanical stretching forces were applied to the chain ends. In analogy to pressure application, these forces were increased by 150 pN each 96.8 fs until spiropyran was formed. This process was repeated. As in the static calculations, the X-HCFF model was used to apply pressure

in the BOMD trajectories, whereas stretching forces were applied with the EFEI approach. Vertical excitation energies and oscillator strengths were calculated in each time step to generate the time-resolved UV/Vis absorption spectra throughout the BOMD trajectories.

The Judgement of Energy DIstribution (JEDI) analysis^[115–117] was performed based on input files generated by Q-Chem. Strain energies in the bonds, bendings and torsions were calculated based on the harmonic approximation and were mapped onto the bonds to generate a color-coded structure. Details on this procedure can be found elsewhere.^[119]

Electron densities at the bond critical points were calculated *via* the Quantum Theory of Atoms in Molecules (QTAIM)^[79] approach as implemented in the Multiwfn 3.7 program package.^[184] Q-Chem was used to provide the wave function files required for the analysis. Volumes of SP and MC were calculated using a previously described approach.^[197]

4.3.2 Propagation of electron density in the BOMD trajectories

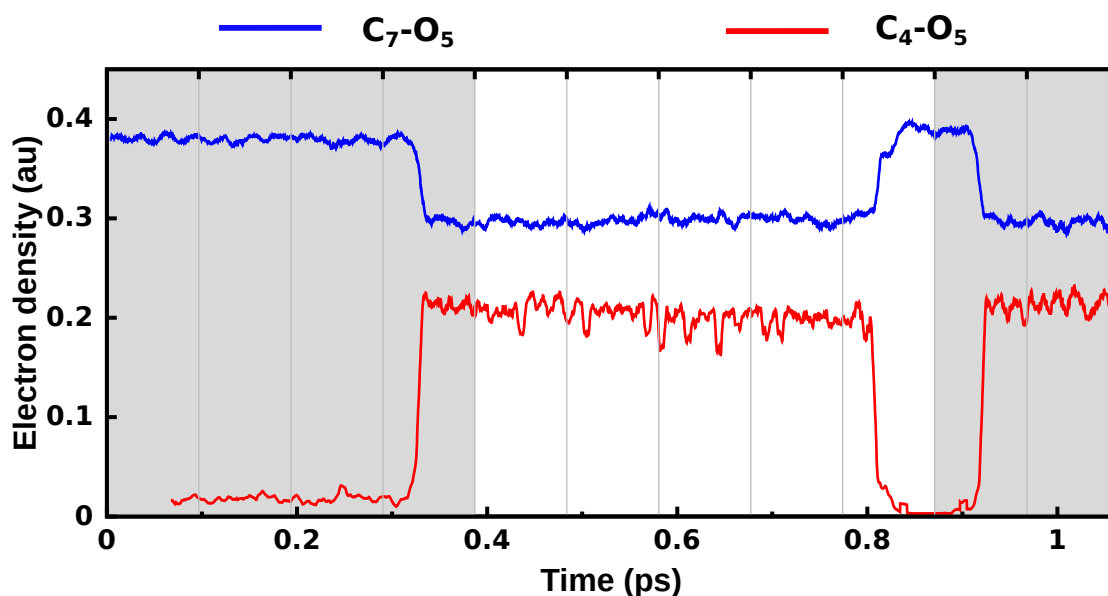


Figure 4.5: Time series plot of electron densities at the bond critical points of the C_4-O_5 and C_7-O_5 bonds throughout a representative BOMD trajectory. Pressure was increased in steps of 0.5 GPa throughout the gray shaded areas. Stretching forces were increased in steps of 300 pN in the white area. Gray vertical lines signify the points in time when the pressure or the force were adjusted, respectively.

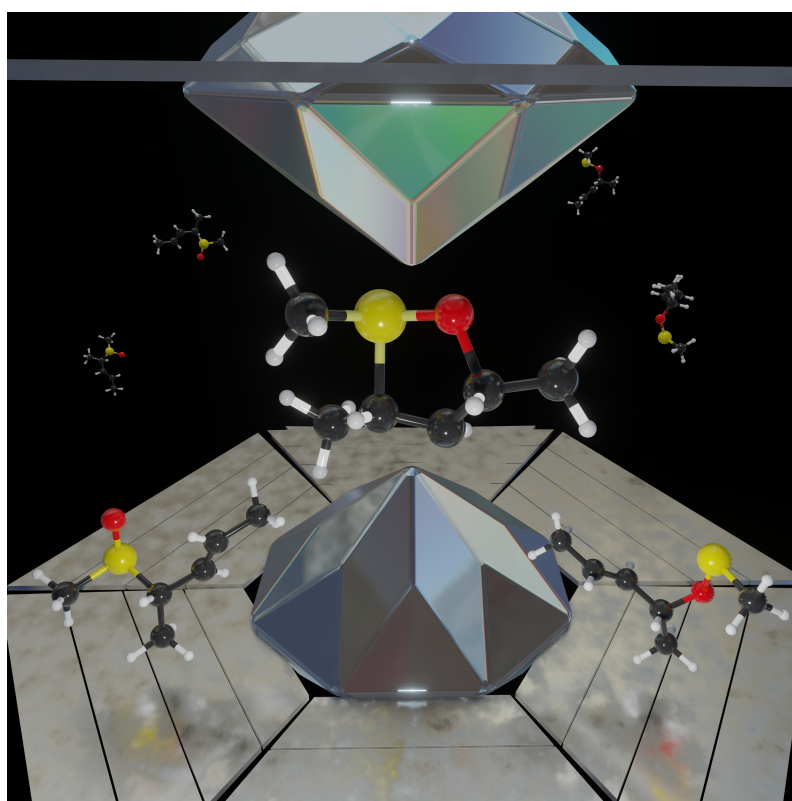
Initially, a high electron density is found in the C_7-O_5 bond of MC, which suddenly decreases as soon as SP is formed at a sufficiently high pressure (Figure 4.5). This signifies a decrease in double bond character of the C_7-O_5 bond. Simultaneously, the C_4-O_5 is created. In the further course of the trajectory, an increase in electron density in the C_7-O_5 bond and a decrease in electron density in the C_4-O_5 bond mark the creation of MC, whereas the opposite is found when SP is formed.

4.3.3 Baro-mechanical data for the BOMD trajectories

Trajectory	Pressure (GPa), Step 1	Rupture force (nN), Step 2	Pressure (GPa), Step 3
1	1.0	0.75	0.5
2	1.0	1.05	0.5
3	1.0	1.5	1.0
4	1.0	0.45	0.5
5	2.0	0.75	0.5
6	1.0	0.75	0.5
7	1.0	1.2	0.5
8	1.0	1.2	1.0
9	0.5	1.5	0.5
10	0.5	0.75	3.5

Table 4.1: Pressures and rupture force required for the interconversion between SP and MC throughout the different phases of each individual BOMD trajectory. In the final step of trajectory No. 10, a remarkably high pressure of 3.5 GPa is required to initiate MC-to-SP conversion, which is due to the *trans*-configuration of MC as a result of stretching in step 2 and the concomitant large distance between C₄ and O₅.

4.4 Publication: Trapping the transition state in a [2,3]-sigmatropic rearrangement by applying pressure.



The results presented in this chapter have been previously published:

ACS Omega, **2022**, 7, 45208–45214.

Rahel Weiß and Felix Zeller from the University of Bremen
contributed to this work as second and third author.

Abstract

Transition states are of central importance in chemistry. While they are, by definition, transient species, it has been shown before that it is possible to “trap” transition states by applying stretching forces. We here demonstrate that the task of transforming the transition state of a chemical reaction into a minimum on the potential energy surface can be achieved by using hydrostatic pressure. We apply the computational *eXtended Hydrostatic Compression Force Field* (X-HCFF) approach to the educt of a [2,3]-sigmatropic rearrangement in both static and dynamic calculations and find that the five-membered cyclic transition state of this reaction becomes a minimum at pressures in the range between 100 and 150 GPa. Born-Oppenheimer Molecular Dynamics (BOMD) simulations suggest, that slow decompression leads to a 70:30 mix of the product and the educt of the sigmatropic rearrangement. Our findings are discussed in terms of geometric parameters and electronic rearrangements throughout the reaction. To provide reference data for experimental investigations we simulated the IR, Raman and time-resolved UV/Vis absorption spectra for the educt, transition state and product to help characterize the pressure-driven reaction. We speculate that the trapping of transition states by using pressure is generally possible if the transition state of a chemical reaction has a more condensed geometry than both the educt and the product, which paves the way for new ways of initiating chemical reactions.

Introduction

The rearrangement of allylic sulfoxides to allylic sulfenate esters is a popular example of [2,3]-sigmatropic rearrangements.^[222–224] This type of reaction is also known as Mislow-Evans rearrangement^[225–232] and is widely used in asymmetric synthesis due to the possibility of chirality transfer from the carbon bearing the sulfoxide group to the alcohol resulting from a subsequent reaction with an appropriate

thiophile (Figure 4.6A). Hence, the Mislow-Evans rearrangement is a popular tool in the synthesis of bioactive substances and natural products like terpenes,^[233] vernolepin,^[234,235] amphidinol 3,^[236] and pyrenolide D.^[237]

The transition state of the Mislow-Evans rearrangement has attracted considerable attention, because it determines the stereochemistry of the reaction.^[238] It has been found that the Mislow-Evans rearrangement proceeds *via* a five-membered cyclic transition state (Figure 4.6A).^[227,232,238–240] By using quantum chemical methods, we here demonstrate that the cyclic transition state of the Mislow-Evans rearrangement becomes a minimum under pressures between 100 and 150 GPa, which is a pressure range that is accessible with modern diamond-anvil cell technology.^[241] While the “trapping” of the transition state of a chemical reaction has been achieved before with mechanical force,^[98] to the best of our knowledge this is the first time that hydrostatic pressure has been used for this purpose. Our findings present a significant advancement over previous extrapolated data that suggest that the typically unstable *cis*-conformation of 1,2-dichloroethane can be stabilized by pressure.^[242] The possibility of transforming a transition state into a minimum on the potential energy surface paves the way for isolating and characterizing this transient chemical species and will more broadly open up new possibilities in chemical synthesis.

Computational Details

Several quantum chemical methods for the application of hydrostatic pressure to molecules during geometry optimizations have been reported.^[106–108,181,193,194,197,220] In this paper, we used the *eXtended Hydrostatic Compression Force Field* (X-HCFF) approach^[108] to apply pressure during geometry optimizations and Born-Oppenheimer Molecular Dynamics (BOMD) simulations, as implemented in the Q-Chem 5.4.2 program package,^[217] since this method has been used successfully to predict structural parameters and chemical reactions in the GPa regime. BOMD

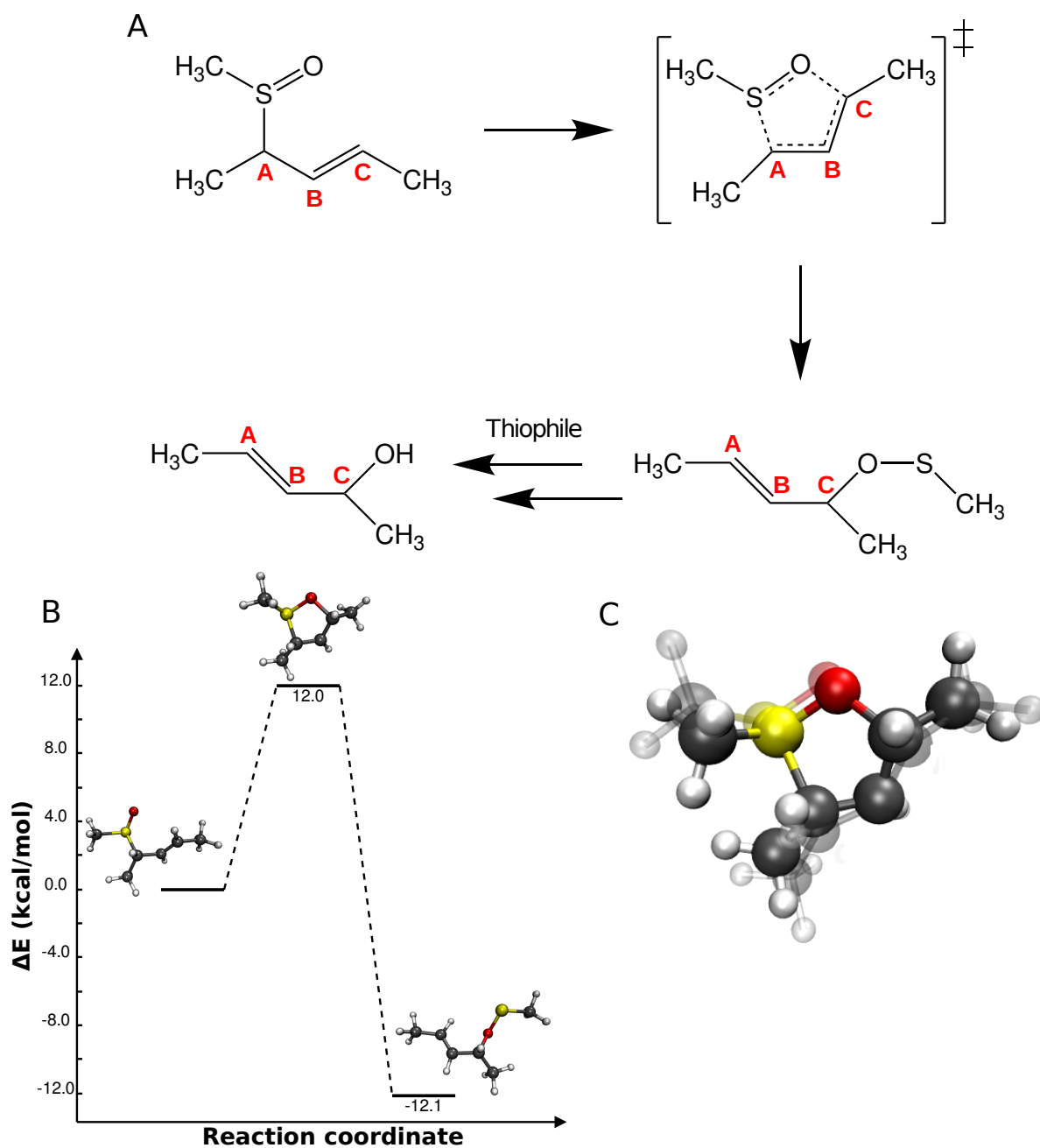


Figure 4.6: (A) Schematic representation, including labels of carbon atoms, and (B) energy profile of the Mislow-Evans rearrangement, calculated at the B3LYP/6-31G(d) level of theory. (C) Superimposed geometries of the structure found at 120 GPa (solid), calculated with X-HCFF, and the cyclic transition state of the Mislow-Evans rearrangement without pressure (transparent).

simulations can be conducted at a user-defined pressure with X-HCFF. Density Functional Theory (DFT)^[121,122] at the B3LYP^[100,102,215]/6-31G(d)^[216] level of theory was used as the electronic structure method and 302 tessellation points per atom as well as a tessellation sphere scaling factor of 1.0 were used in the X-HCFF calculations. The choice of using this set of X-HCFF parameters was motivated in the original publication.^[108] The nature of the transition state at $P = 0$ GPa was confirmed by the existence of a single imaginary frequency. Frequency analyses were carried out analytically at $P = 0$ GPa. At $P > 0$ GPa, frequency analyses of the structure found at 120 GPa were conducted by numerical differentiation (keyword `ideriv 1`) of the analytical X-HCFF gradient.

Ten individual BOMD simulations were run at a temperature of 300 K with an integration time step of 20 a.u.. The optimized geometry of the educt of the Mislow-Evans rearrangement was taken as the initial geometry of all BOMD trajectories and initial velocities were sampled randomly from a Maxwell-Boltzmann distribution. The simulations were conducted by increasing the pressure by 10 GPa every 96.8 fs until the average C_C -O distance in the current simulation window was lower than 1.5 Å, marking the formation of the five-membered ring. Depending on the trajectory, this was the case in the range between 100 and 150 GPa. Subsequently, decompression with the same rate was initiated until 0 GPa was reached.

Mayer bond orders^[243,244] and electron densities at the bond critical points^[79] were calculated with the Multiwfn 3.7 program package.^[184] Q-Chem was used to generate the wave functions for these analyses. IR and Raman spectra were plotted using the Iqmol program by applying a broadening.

Results and Discussion

While, according to our calculations, the cyclic transition state of the model Mislow-Evans reaction considered in this paper (Figure 4.6B) lies 12.0 kcal/mol above the

educt, geometry optimization with X-HCFF at a pressure of 120 GPa yields a five-membered cyclic structure (Figure 4.6C). This compressed geometry is remarkably close to the pressure-free transition state, with a mean root-mean-square deviation (RMSD) of only 0.3 Å between the ring atoms in the compressed and the pressure-free geometries (Table 4.2). While transition states have been found to disappear under pressure,^[220] leading to the formation of the product of a chemical reaction with no further energy input, our calculations demonstrate that pressure can be used to transform a transition state into a minimum on the potential energy surface. The disappearance of imaginary frequencies of the obtained cyclic structure above 110 GPa (Figure 4.11) confirms this finding from a theoretical point of view.

It must be noted that the pressure required to form the cyclic structure depends quite heavily on the chosen density functional (Figure 4.10). While B3LYP/6-31G(d) yields an average pressure, this finding will motivate a more thorough benchmark of density functionals in future calculations of high-pressure properties.

Despite the intriguing notion that a transition state can be trapped by pressure, this finding is intuitive, since the transition state of the Mislow-Evans rearrangement has a more condensed geometry than both the educt and the product. A preference of the transition state geometry is therefore expected at elevated pressures.

To investigate the formation of the five-membered ring in the model Mislow-Evans reaction under pressure more closely, we conducted ten individual BOMD simulations, in which we increased the pressure in increments of 10 GPa every 96.8 fs. Two representative distances, S–C_A and C_C–O (cf. Figure 4.6A for the labels), were averaged over all ten simulations for each 10 GPa simulation window up to the maximum applied pressure. In agreement with chemical intuition, the S–C_A bond shortens with increasing pressure (Figure 4.7A). Up to approx. 90 GPa, the S–C_A bond length decreases fairly linearly with increasing pressure, and, since

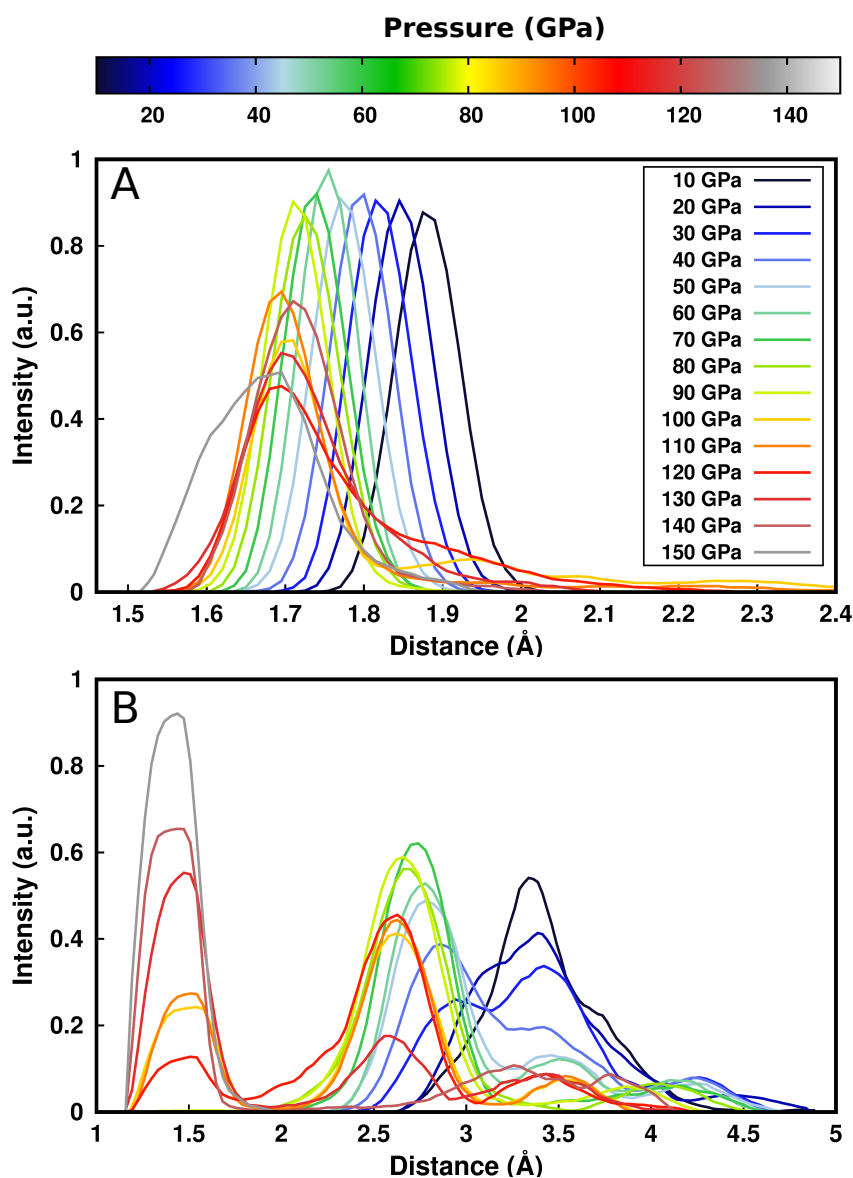


Figure 4.7: Normalized distances $S-C_A$ (A) and C_C-O (B) for each individual 10 GPa simulation window averaged over all trajectories in the pressure range between 0 and 150 GPa.

pressure is proportional to force, this observation shows that the compression of the $S-C_A$ bond is a harmonic process throughout a remarkably large pressure range.

Turning to the C_C-O distance (Figure 4.7B), the distribution initially only broadens up to a pressure of 20 GPa, since C_C and O are not bonded at first. An intermediate, slightly compressed geometry with a C_C-O distance between 2.5 and 3 Å is subsequently generated, followed by the gradual generation of cyclic species

in which C_C and O are bonded, as evidenced by the accumulation of structures with a C_C –O distance of approx. 1.5 Å at pressures above 100 GPa.

The distance C_C –O, which forms during the Mislow-Evans rearrangement, and S – C_A , which breaks, are shown in Figure 4.8 as a function of time for two representative BOMD trajectories. In the first trajectory (Figure 4.8A), formation of the five-membered ring can be observed at approx. 1.05 ps (120 GPa), marked by a sharp decrease in the C_C –O distance. Subsequently, slow decompression leads to the rupture of the S – C_A bond, yielding the reaction product. While in the second trajectory (Figure 4.8B) the formation of the five-membered ring can be observed at a pressure of 120 GPa as well, decompression in this case leads to the recovery of the educt due to the rupture of the C_C –O bond and not the S – C_A bond. Similar observations are made for other structural parameters involved in the formation of the five-membered ring (Figures 4.12 and 4.13).

The possibility to either form the product or to recover the educt is the expected behavior for a system that is held artificially at the transition state, since it can move in either direction when the constraint is lifted, depending on the instantaneous nuclear velocities that are present upon decompression. In seven out of the ten simulations, the formation of the product is observed, whereas the educt is recovered in the remaining three simulations. This observation lends further evidence that a transition state was isolated using pressure. The pressure required to form the five-membered ring ranges between 100 and 150 GPa, depending on the trajectory. Details on each individual trajectory are given in the Supporting Information (Table 4.3).

The formation of the five-membered ring and its transformation to either the product or the educt of the Mislow-Evans rearrangement upon decompression can also be understood in terms of changes in Mayer bond orders^[243,244] throughout the BOMD simulations (Figure 4.9). While the $C_B=C_C$ bond loses its double

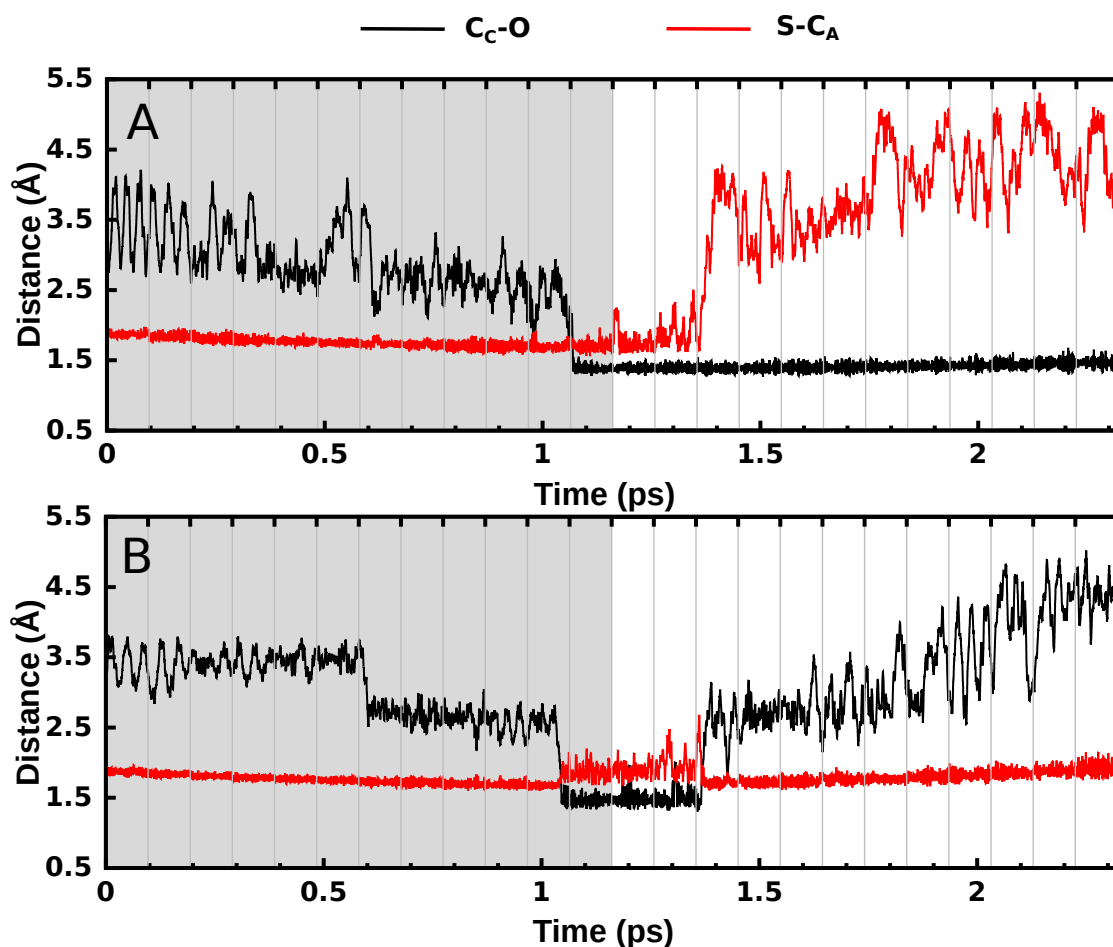


Figure 4.8: Time evolution of the distances C_C-O (black line) and $S-C_A$ (red line) for two representative BOMD simulations of the model system under hydrostatic pressure in which the formation of the product (A) or of the educt (B) of the Mislow-Evans rearrangement is observed, respectively. Gray shaded areas signify increasing compression, whereas white areas denote decompression. The pressure was changed by 10 GPa at each of the gray vertical lines.

bond character upon formation of the five-membered ring, the bond order of the C_A-C_B bond increases, signifying an increase in double-bond character. In the trajectory in which the product of the Mislow-Evans reaction is formed upon decompression (Figure 4.15A), these changes are permanent. In addition, the bond order analysis reveals the rupture of the $S-C_A$ bond and the formation of the C_C-O bond, completing the rearrangement. Contrarily, the decrease in $S-C_A$ bond order and the formation of the C_C-O bond are only transitory in the trajectory that recovers the educt upon decompression (Figure 4.15B). As soon as the five-

membered ring dissociates upon decompression and the educt forms, the bond orders return to their initial values in this trajectory.

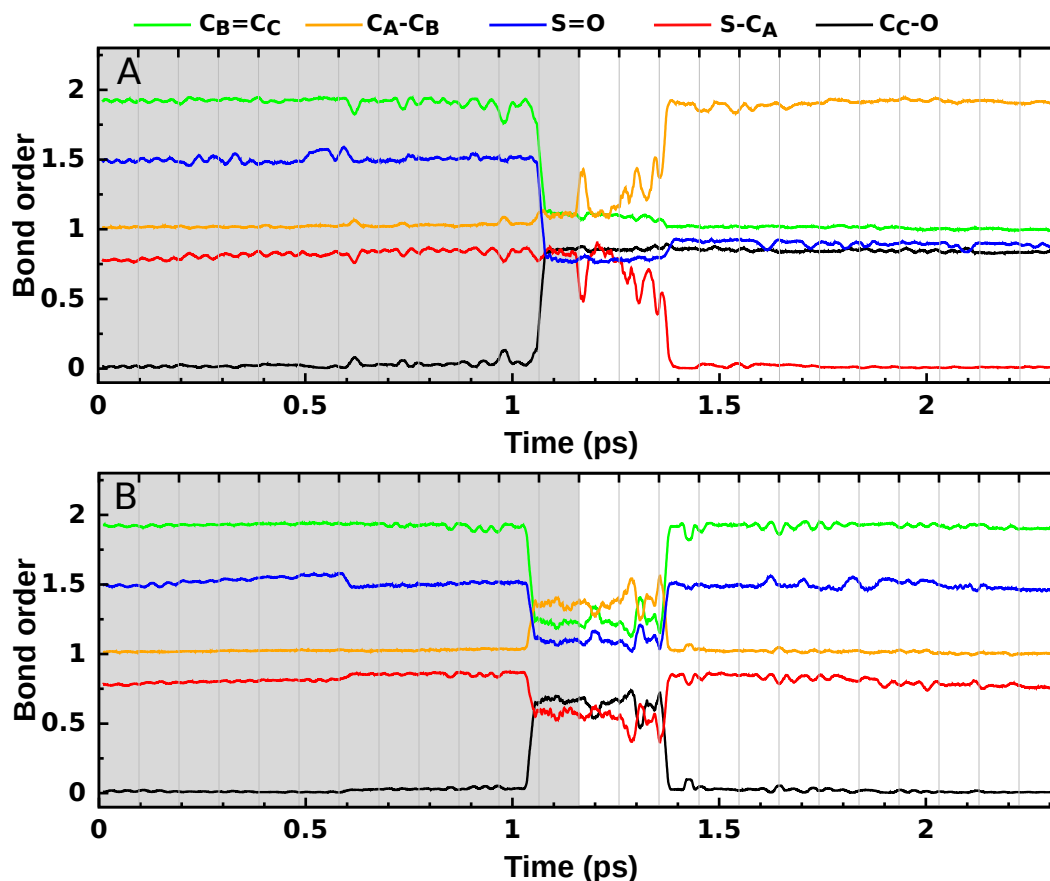


Figure 4.9: Time series plot of the Mayer bond orders of the bonds in the five-membered ring throughout two representative BOMD trajectories in which the product (A) or the educt (B) of the Mislow-Evans rearrangement is formed, respectively.

The formation of the product and the educt, respectively, after release of pressure in the BOMD trajectories can also be observed in the corresponding time-resolved UV/Vis absorption spectra (Figure 4.14). Initially, peaks in the region between 200 and 220 nm are found. With the formation of the transition state at around 1.08 ps the spectrum broadens and shifts to the visible region with peaks between 250 and 350 nm, signifying a characteristic color change when the cyclic structure is formed. When pressure is removed and the educt is formed, the peaks are shifted back to the

region between 200 and 250 nm, whereas product formation leads to peaks between 200 and 280 nm.

Analogous effects can be observed in the propagation of electron densities at the bond critical points throughout the BOMD trajectories (Figure 4.15): In addition to an overall increase in electron density with increasing pressure, which is due to the compressed nuclear scaffold and the shortened bonds, shifts in electron density mark the formation of the five-membered cyclic structure at high pressure and its transformation to either the product or the educt of the Mislow-Evans rearrangement upon decompression.

A further method for a possible experimental characterization of the trapped transition state is IR and Raman spectroscopy (Figures 4.16 and 4.17). Upon formation of the cyclic structure, the stretching modes of the methyl groups are shifted from an initial 3000-3300 cm^{-1} to 3600-3900 cm^{-1} , a process that is accompanied by a decrease in IR intensities. The final generation of the product shifts these peaks back to the region of 3000-3200 cm^{-1} .

Conclusions

The quantum chemical calculations and BOMD simulations presented in this study demonstrate that the five-membered cyclic transition state of a model Mislow-Evans rearrangement can be “trapped” by applying hydrostatic pressures in the range between 100 and 150 GPa. Decompression leads to the formation of the product of the rearrangement in seven out of ten trajectories, whereas the educt is recovered in the remaining three simulations. Our future studies will focus on the influence of environmental factors like chemical substitution^[245] or the solvent in a multiscale simulation setup. We hope that our calculations spark the interest in experimental studies on the barochemical isolation of transitory species in sigmatropic rearrangements and other chemical reactions. Calculated spectroscopic properties

of the involved species that were presented here will provide reference data for such experimental studies. We speculate that transition states can generally be isolated by using pressure if the transition state geometries are more condensed than both the educt and the product of the reaction.

Acknowledgments

The authors gratefully acknowledge the University of Bremen, the Bremen Center for Computational Materials Science (BCCMS) and the MAPEX Center for Materials and Processes for financial support and for providing computational resources.

4.5 Additional information

4.5.1 Influence of functionals on the "trapping" pressure

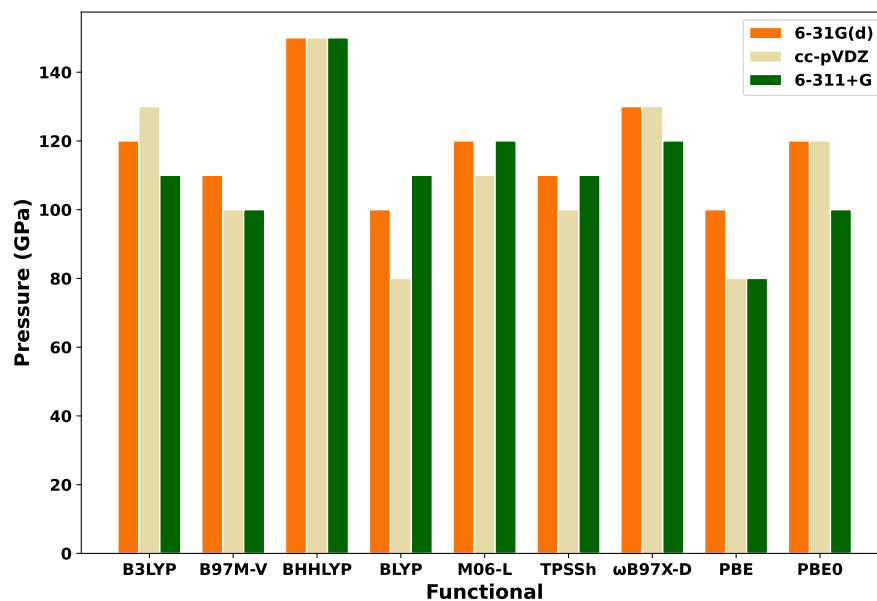


Figure 4.10: Pressure required to ‘trap’ the transition state in the investigated Mislow-Evans rearrangement, calculated with different density functionals. The evaluated functionals are B3LYP^[100,102,215], B97M-V^[246], BHHLYP^[101], BLYP^[185,247], M06-L^[248], TPSSH^[249], ω B97X-D^[250], PBE^[251] and PBE0^[252]. Basis sets used are 6-31G(d)^[216], cc-pVDZ^[253] and 6-311+G.

4.5.2 Structural parameters of the five-membered ring

Atom	RMSD (Å)
C_A	0.399
C_B	0.118
C_C	0.308
S	0.328
O	0.380
Mean	0.306

Table 4.2: RMSD (Å) of the atomic positions of the atoms in the five-membered ring between the transition state ($P = 0$ GPa) and the superimposed cyclic structure at $P = 120$ GPa.

4.5.3 Number of imaginary frequencies as a function of pressure

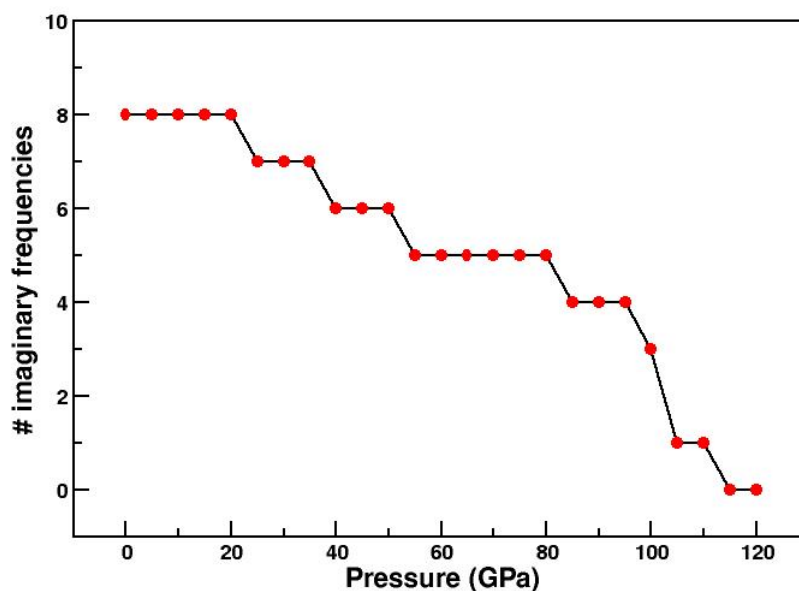


Figure 4.11: Number of imaginary frequencies found at different pressures (applied in semi-numerical frequency analyses) while trapping the transition state. Lines were included to guide the eye.

4.5.4 Propagation of bond angles in the BOMD trajectories

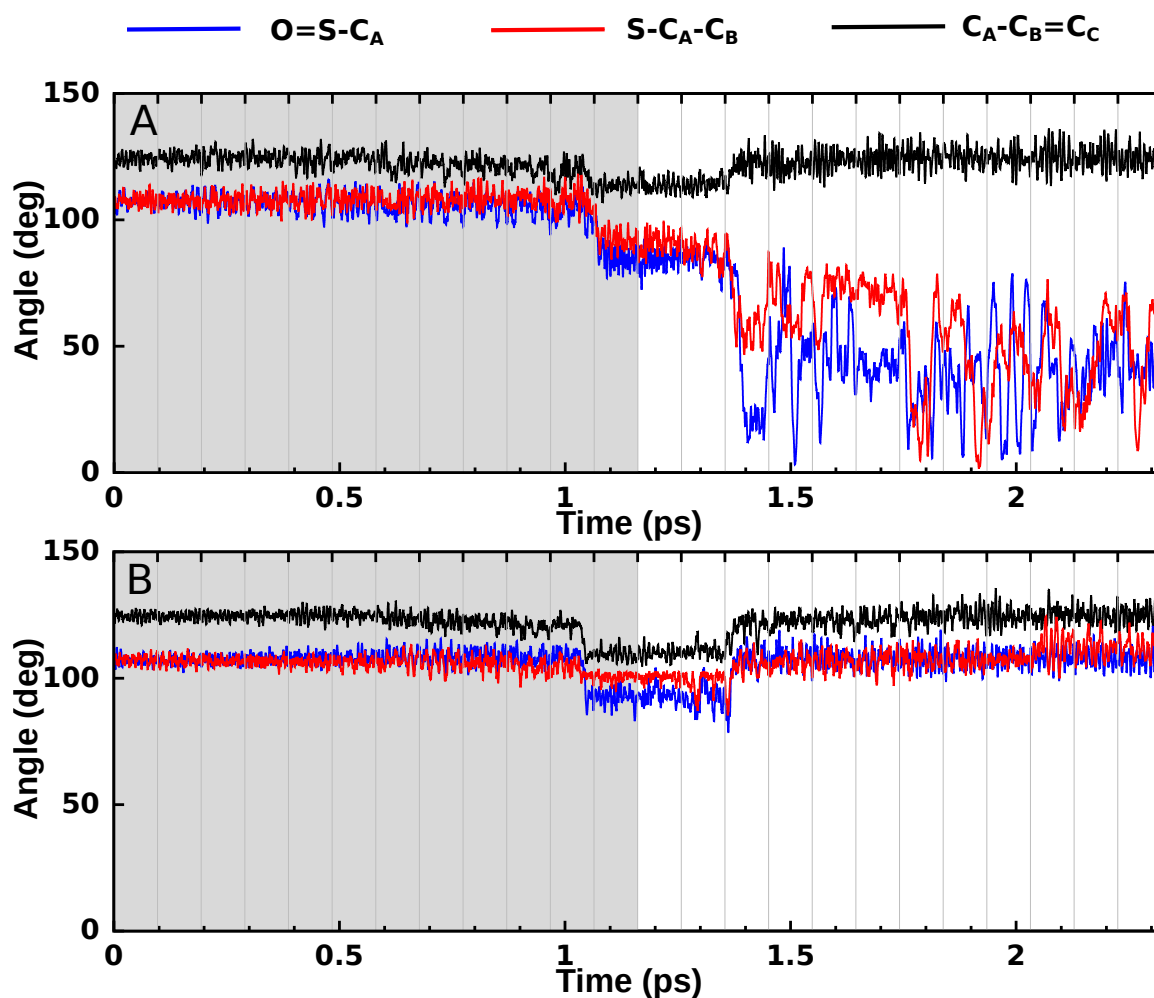


Figure 4.12: Time series plot for different angles during two representative BOMD trajectories that lead to the product (A) or the educt (B) of the Mislow-Evans rearrangement.

The formation of the product and the educt, respectively, in the two representative BOMD trajectories discussed in the main paper can be observed in the dynamic behavior of certain bond angles. While, initially, bond angles $O=S-C_A$, $S-C_A-C_B$ and $C_A-C_B=C_C$ are present and oscillate around their equilibrium value, formation of the five-membered ring leads to a decrease in all of these angles. In the trajectory leading to the formation of the product (Figure 4.12A), the marked decrease and

the heavy oscillations of the angles $O=S-C_A$ and $S-C_A-C_B$ signifies the rupture of the $S-C_A$ bond, whereas the recovery of the educt (Figure 4.12B) is demonstrated by the return of all angles to their initial values.

4.5.5 Time evolution of the RMSD

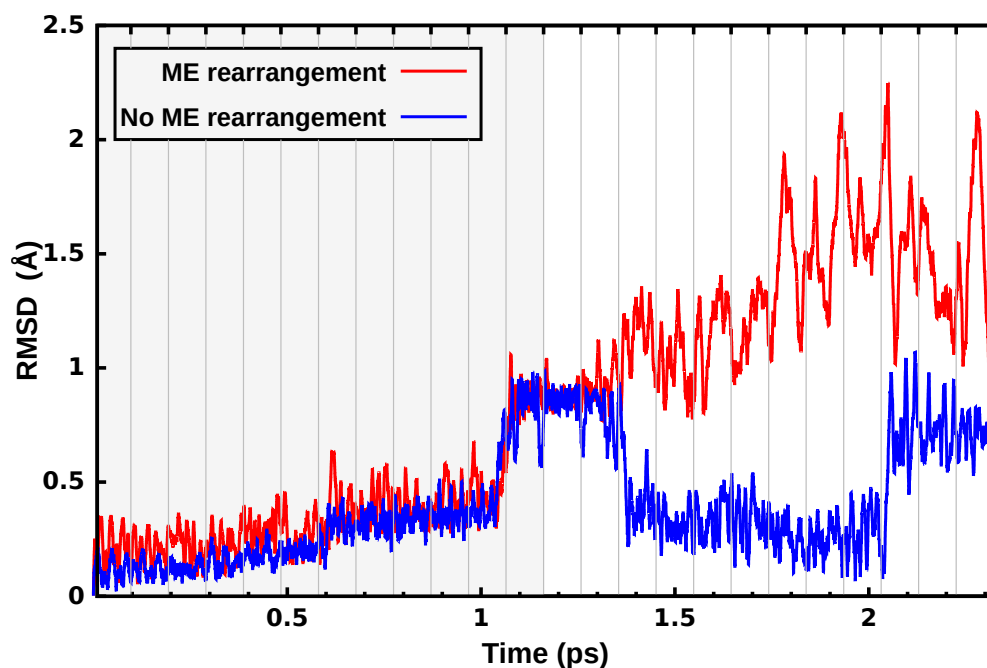


Figure 4.13: RMSD from the initial geometry for two representative trajectories that lead to the formation of the product (red curve) and the educt (blue curve), respectively. All atoms except hydrogen are included in the RMSD calculation.

4.5.6 Barochemical and structural data for the BOMD trajectories

Trajectory	Ring formation pressure (GPa)	Average C _C –O distance (Å)	Final molecule
1	120	1.38	product
2	130	1.38	product
3	100	1.46	educt
4	120	1.47	educt
5	100	1.45	product
6	130	1.48	product
7	150	1.37	educt
8	120	1.40	product
9	110	1.43	product
10	100	1.47	product

Table 4.3: Amount of pressure required for ring formation, average C_C–O distance in the simulation window with the highest pressure, and molecule found after decompression in each of the ten BOMD trajectories. In the main paper, the representative trajectories 1 and 4 are discussed.

4.5.7 Time-resolved UV/Vis spectra

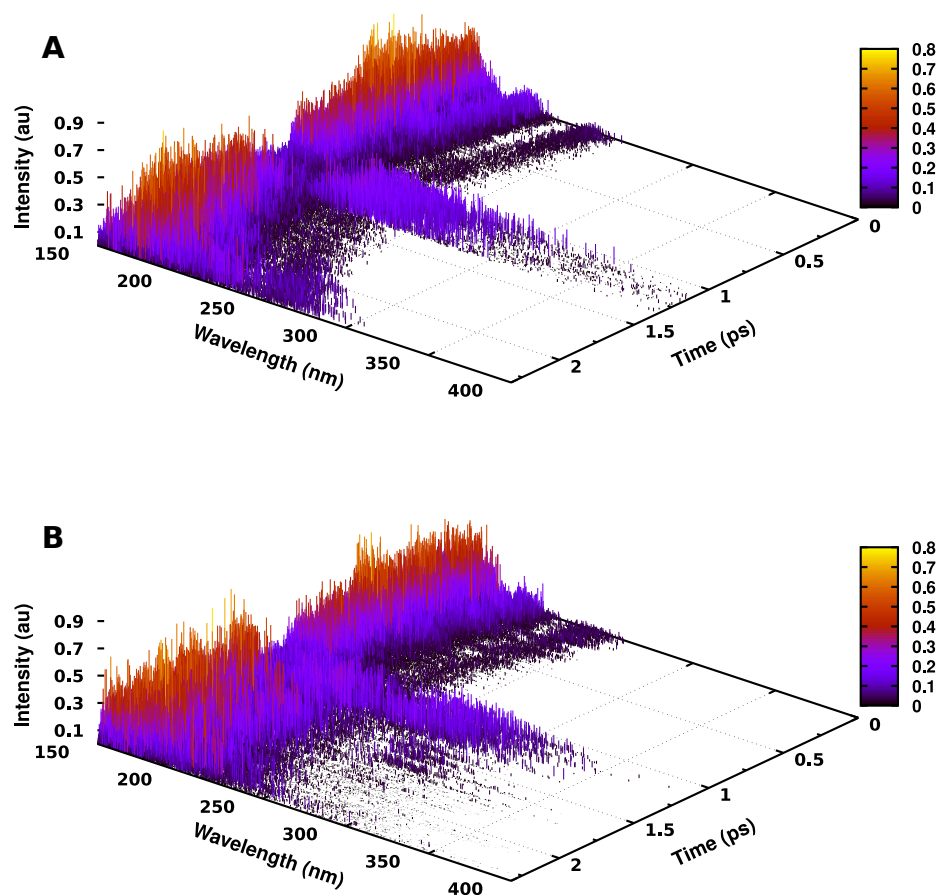


Figure 4.14: Time series plot of the UV/Vis absorption spectrum of the rearrangement process studied under the influence of pressure. Plots A and B are based on the same BOMD trajectories shown in Figure 3A and 3B of the main paper, respectively. The color palette is used to highlight the intensities.

4.5.8 Propagation of electron densities in the BOMD simulations

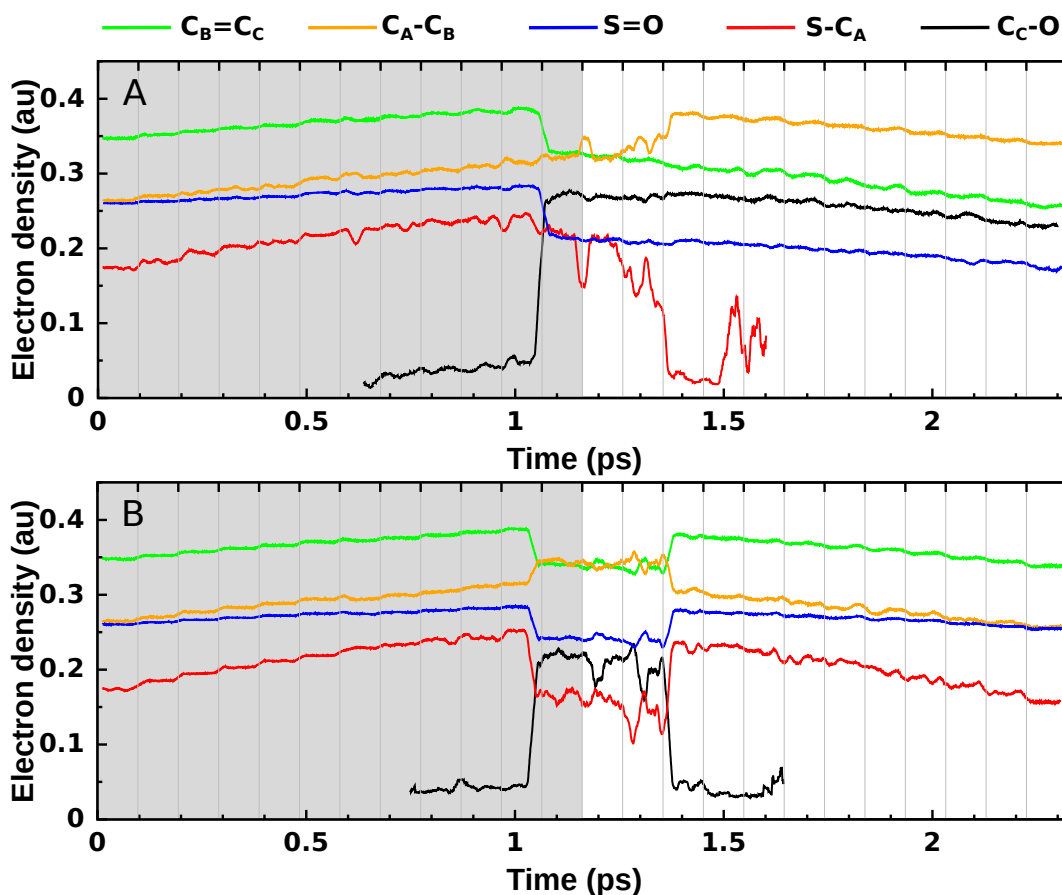


Figure 4.15: Time series plot for the electron densities at the bond critical points of the bonds in the five-membered ring throughout two representative BOMD trajectories in which the product (A) or the educt (B) is formed, respectively.

The formation of the five-membered ring and its transformation to either the product or the educt of the Mislow-Evans rearrangement upon decompression can be understood in terms of electronic rearrangements occurring throughout the BOMD simulations under pressure (Figure 4.15). Formation of the five-membered ring is accompanied by a decrease in the electron density at the bond critical points of the $C_B=C_C$ and $S=O$ bonds, signifying a decrease in double bond character, whereas, intuitively, the opposite is found for the C_A-C_B bond. In the trajectory in which

the reaction product is formed (Figure 4.15A), the S–C_A bond ceases to exist soon after decompression is initiated, whereas the C_C–O bond comes into existence, which is in good agreement with the observed geometrical changes. The changes in electron densities in the bonds between C_B and C_C as well as between C_A and C_B are permanent, signifying a shift of the double bond. In the trajectory that recovers the educt (Figure 4.15B), contrarily, soon after decompression the electron densities revert to their initial values, since no bond is broken or formed. In both trajectories, prior to the formation of the five-membered ring, increasing the pressure leads to a gradual increase in electron density in each bond, which is a result of the compressed nuclear scaffold and the shortened bonds.

4.5.9 IR and Raman spectra

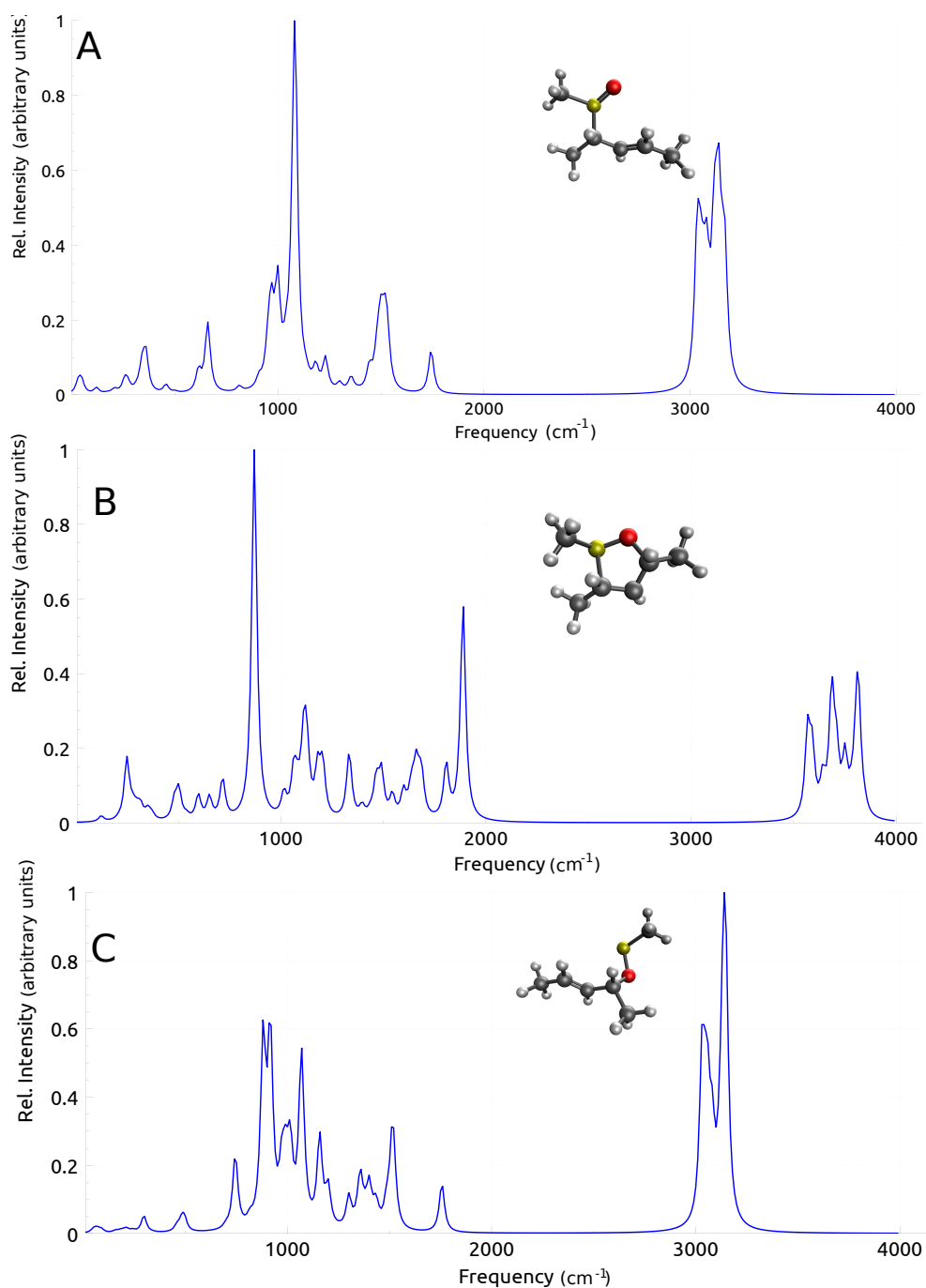


Figure 4.16: IR spectra for the (A) educt at 0 GPa, (B) cyclic structure at 120 GPa and (C) product at 0 GPa.

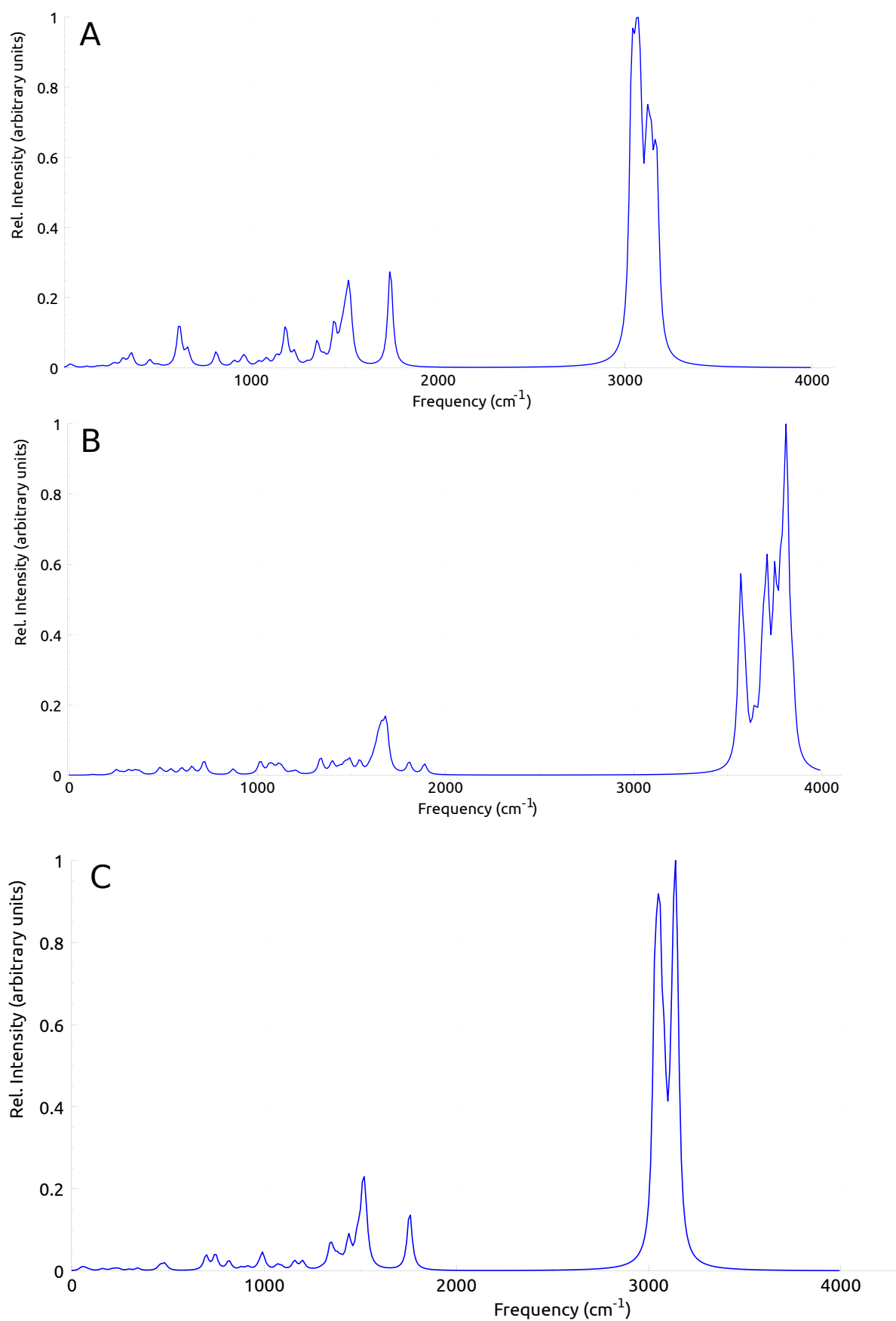


Figure 4.17: Raman spectra for the (A) educt at 0 GPa, (B) cyclic structure at 120 GPa and (C) product at 0 GPa.

Chapter 5

Multiscale mechanochemical modeling of spiropyran-merocyanine isomerization in linear PMMA polymers

Dr. Baris Demir¹ from University of Queensland and Prof. Lucio Colombi Ciacchi^{2,3,4} from University of Bremen contributed to this work.

¹ *Centre for Theoretical and Computational Molecular Science, The Australian Institute for Bioengineering and Nanotechnology, The University of Queensland, Brisbane, QLD 4072, Australia*

² *Bremen Center for Computational Materials Science, University of Bremen, Am Fallturm 1, D-28359 Bremen, Germany*

³ *MAPEX Center for Materials and Processes, University of Bremen, Bibliothekstraße 1, D-28359 Bremen, Germany*

⁴ *Hybrid Materials Interfaces Group, Faculty of Production Engineering, Center for Environmental Research and Sustainable Technology (UFT), University of Bremen, Am Fallturm 1, D-28359 Bremen, Germany*

Abstract

Mechanochemical reactions in functional polymers occur when mechanical forces cause labile bonds, e.g., in mechanophores, to break. While it is known that these reactions require a critical amount of force, the structure of the polymer network strongly affects the efficiency of force transduction. Experimentally it is challenging to track the force transmission along the polymer backbone. Despite the availability of quantum mechanochemical tools, the information on force transmission from the bulk to a local scale is still limited. Here we introduce a multiscale mechanochemical model that establishes a connection between bulk deformation and mechanophore activation. This is achieved by combining the quantum mechanical (QM) COstrained Geometries simulate External Force (COGEF) method and cost-efficient molecular mechanical (MM) simulations. Based on a new parameterization of the well-known Spiropyran-Merocyanine (SP-MC) isomerization under stretching forces, we simulate mechanophore activation inside a realistic poly(methyl methacrylate) (PMMA) network at two different strain rates ($5 \cdot 10^7$ and $5 \cdot 10^8$ s⁻¹). The results are discussed in terms of stress-strain behavior of the system and its effect on mechanochemical activity. The developed multiscale simulation model paves the way for further investigations on more complex mechanophore-doped polymer networks.

5.1 Introduction

Mechanophores are molecular subunits of polymers that are capable of converting mechanical stress into chemical energy, e.g., *via* the rupture of a covalent bond.^[254–256] Due to this effect, mechanophores are at the heart of many functional polymers, enabling mechanochemical reactions in a complex environment.^[6,51,257–260] Some mechanophores show significant changes in their UV/Vis absorption or fluorescence spectra upon isomeriation, leading to mechanochromism.^[145,151,261–265] Experimentally, mechanophores can be activated using a plethora of methods, e.g., single molecule force spectroscopy,^[29,266] ultrasonication,^[31,32] ball milling,^[33,34] as well as tensile stretching^[36] and compression.^[261,267] In each of these techniques, mechanical stress is propagated differently throughout the polymer,^[268,269] eventually leading to mechanophore activation.^[47]

The mechanochemical processes and deformations occurring at the molecular level can be simulated using quantum mechanochemical methods like COstrained Geometries simulate External Force (COGEF),^[63] Force-Modified Potential Energy Surface (FMPEs)^[64] and External Force is Explicitly Included (EFEI)^[62]. These methods deliver information on regio-^[270,271] and stereochemical^[272] effects of mechanophore activation, possible mechanistic pathways,^[64] activation energy barriers,^[28] transition states under stretching forces,^[273] and reaction rates.^[269] However, they usually fail to account for the transduction of force from the bulk to the single-molecule level. Therefore, it is generally unknown whether the forces simulated using the aforementioned quantum mechanochemical methods are representative models for a realistic polymer under mechanical stress.

For a more realistic modeling of mechanochemical processes, multiscale simulation techniques have been developed. In 2013, Silberstein *et al.* developed a multiscale simulation framework to describe the reactivity of spiropyran (SP) embedded in

a glassy poly(methyl methacrylate) (PMMA) polymer under shear stress.^[141] To predict the force-modified potential energy surface of SP activation, an *ab initio* steered molecular dynamics (SMD) simulation at the molecular level was conducted by using FMPES methodology. The molecular response in terms of local force distribution and the information on macroscopic stress was coupled with a continuum mechanical model to capture the force-dependent mechanophore activation. A similar framework was then used to investigate mechanophore activation inside a rubbery network. The multiscale simulation technique presented by Silberstein *et al.* allowed a detailed investigation of mechanophore activation based on the continuum models.^[75] In 2015, Wang *et al.* proposed a theoretical model that allows a quantitative assessment of the macroscopic load exerted on elastomers and a detailed study of how mechanical stress is transduced to the mechanophores through polymer networks with non-uniform chain lengths.^[274] A hybrid molecular dynamics (MD) simulation framework to simulate cyclobutane-based mechanophores within epoxy-based thermoset polymers was developed by Koo *et al.*^[76] The Merck Molecular Force Field (MMFF), the Reactive Force Field (ReaxFF) as well as COGEF dissociation force and energy parameters were employed to simulate mechanophore activation.

To tackle this problem, we developed a mechanochemical multiscale simulation model that captures SP mechanophore activation as a result of the deformation of bulk PMMA. The model feeds rupture forces of SP and the relevant intramolecular coordinates, generated *via* high-level quantum mechanical (QM) simulations, into classical molecular dynamics (MD) simulations of bulk scale deformations. As a result, the cost-efficient, classical MD simulations reproduce the energetic and structural parameters of SP activation accurately.

The rest of the paper is structured as follows: Section 5.2 introduces to the methodology used throughout the paper. The force-field parameterization scheme for SP-MC isomerization is discussed in Section 5.2.1. Section 5.2.2 presents the

simulation details used to perform the bulk system relaxation and equilibration. Thereafter the bulk system components such as end-to-end distance distribution, thermal properties and the bulk deformation approach is discussed in further subsections. The formulation of the multiscale model to simulate the mechanophore activation based on the critical end-to-end distance is provided in Section 5.2.5. Focusing on the mechanochemical response, we discuss the possible mechanisms behind the mechanophore activation under both tensile and shear stress types, and in Section 5.3 we show that the mechanochemical activity depends on various deformation conditions, such as stress type, rates and temperature. The concluding remarks are given in Section 5.4.

5.2 Methodology

5.2.1 Parameterization of SP-MC isomerization

When applying stretching forces to the SP mechanophore, the central C-O bond breaks and the molecule converts to a Merocyanine (MC) form *via* a 6π electrocyclic ring opening reaction (Figure 5.1 (a)). The force-modified PES of this SP-MC isomerization was calculated at the QM level by using a COGEF procedure, i.e., a constrained scan was performed for the end-to-end distance between the terminal carbon atoms (highlighted in red circles in Figure 5.1(a)). On increasing the end-to-end distance starting from the equilibrium distance (~ 10 Å), the energy of the system increases and the molecule shows C-O bond rupture at 14.6 Å, resulting in a MC form (Figure 5.1(b)). Further increase in end-to-end distance leads to a highly stretched form of MC. The quantum chemical program package Q-Chem 5.4^[217] was used to perform the COGEF calculations using Density Functional Theory (DFT)^[121,122] at the B3LYP^[100,215]/6-31G(d)^[216] level of theory.

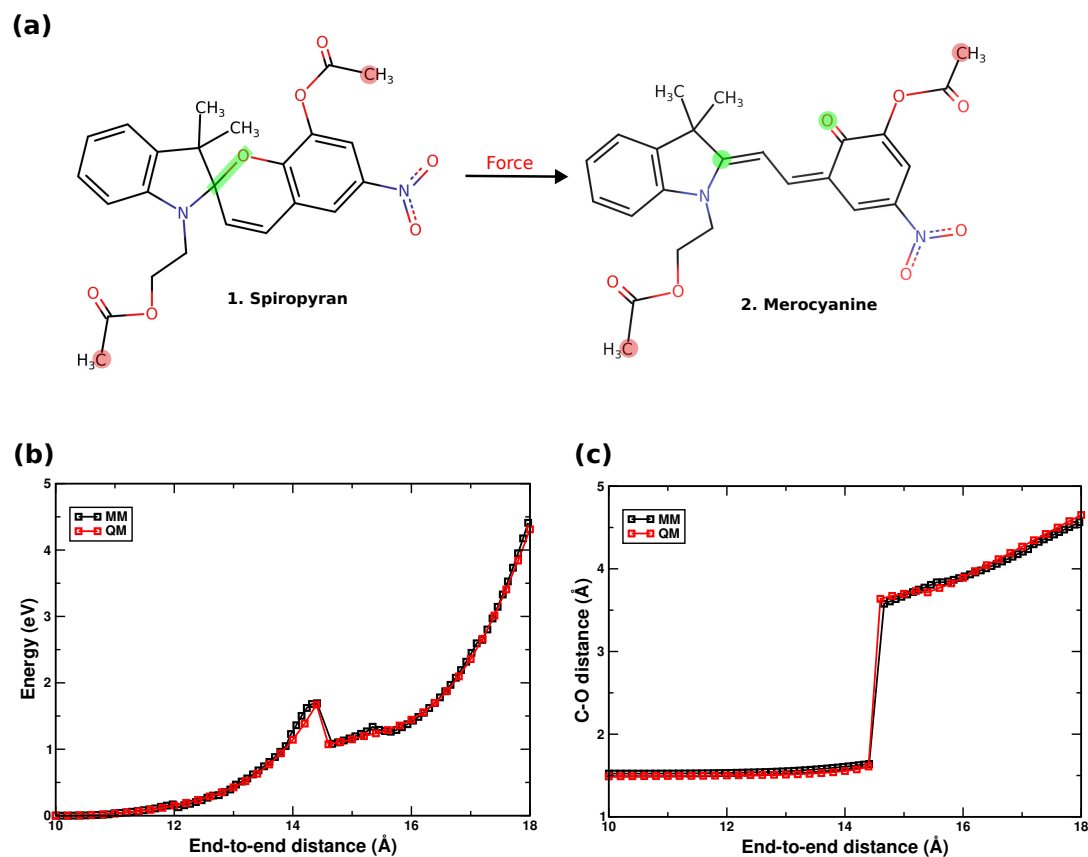


Figure 5.1: (a) SP-to-MC isomerization under stretching force. The atoms highlighted in red are the anchor atoms. The scissile bond is highlighted in green. (b) Parameterization of SP-to-MC isomerization in terms of energy versus end-to-end distance. (c) Distance between the carbon and the oxygen atom involved in the scissile bond in SP as a function of end-to-end distance.

The Optimized Potentials for Liquid Simulations (OPLS)^[135] force field (FF) for the SP and MC molecules were taken from the LigparGen website,^[275] and a parameterization was carried out separately for both molecules using reference QM energies. The parameterization procedure involved the manual updating of the parameters for specific coordinates along the force-bearing scaffold between the end-to-end carbon atoms. A step function was used to switch from SP to MC. For this purpose, the Large-scale Atomic/Molecular Massively Parallel Simulator

(LAMMPS)^[276] program was utilized and a single force-modified PES surface was generated by using a *bond_coeff* function to define different equilibrium distances between the end-to-end anchor atoms. This allowed LAMMPS to specify different constrained end-to-end distances along a *fire* minimization style procedure. The updated FF with specific topology are mentioned in the appendices (Tables S2-S6). The PPPM Ewald summation method was used to compute long-range electrostatic interactions with a neighboring list cutoff set to 13 Å. As a result, the QM and MM energy and C-O distance curves agree remarkably well with each other, as shown in Figure 5.1(c).

5.2.2 Simulation details

The bulk MD simulations were performed using the LAMMPS program, version 7 Aug 2019. The system under investigation consists of 30 linear amorphous chains comprising 93510 atoms in total. Each of the chains consists of 202 PMMA monomers and one SP molecule incorporated in the middle of each chain. The initial configurations of the regular, SP-free syndiotactic-PMMA polymer chain were generated using the CHARMM-GUI Polymer Builder tool.^[277] Moltemplate^[278] was used as a pre-processing tool to generate the SP-doped PMMA LAMMPS data files. To integrate Newton’s equations of motion, the velocity-Verlet algorithm^[143] with a 1 fs time step was employed. Periodic boundary conditions were applied in all directions. The initiation of the system involved a 0.5 ns *NVT* run (300 K) followed by a 0.5 ns *NPT* (300 K and 1 atm) simulation, followed by a 21-step equilibration process^[279] of 1.56 ns. The 21-step equilibration process simulated the initial configuration of the system *via* various compression and decompression steps within a pressure range of 1-50000 atm and a temperature range of 300-1000 K. As shown in the Supporting Information (Figures 5.9 and 5.10), the initiation and 21-step equilibration process reduced the simulation cell size, and helped achieve a

density of 1.10 g/cm^3 , which is close to the experimental value of 1.17 g/cm^3 .^[280] The equilibrated system was used as the starting point for subsequent deformation simulations.

5.2.3 End-to-end distance distribution

The initial final equilibrated system after the 21-step equilibration process, consisting of entangled linear SP-doped PMMA chains, was characterized using an end-to-end distance histogram distribution, $P(R)$. This histogram can be compared to the ideal end-to-end distance distribution generated by the freely jointed chain^[281] model (FJC) for the same mean R^2 value using the expression

$$P_{3D}(R, N)4\pi R^2 dR = \left[\frac{3}{2\pi N b^2} \right]^{\frac{3}{2}} \exp \left[-\frac{3R^2}{2N b^2} \right] 4\pi R^2 dR, \quad (5.1)$$

where $P_{3D}(R, N)$ denotes the probability of the end-to-end distance vector \vec{R} falling within a spherical shell ranging from R to $R+dR$. Here, N corresponds to the number of freely joined segments and b is the Kuhn length.

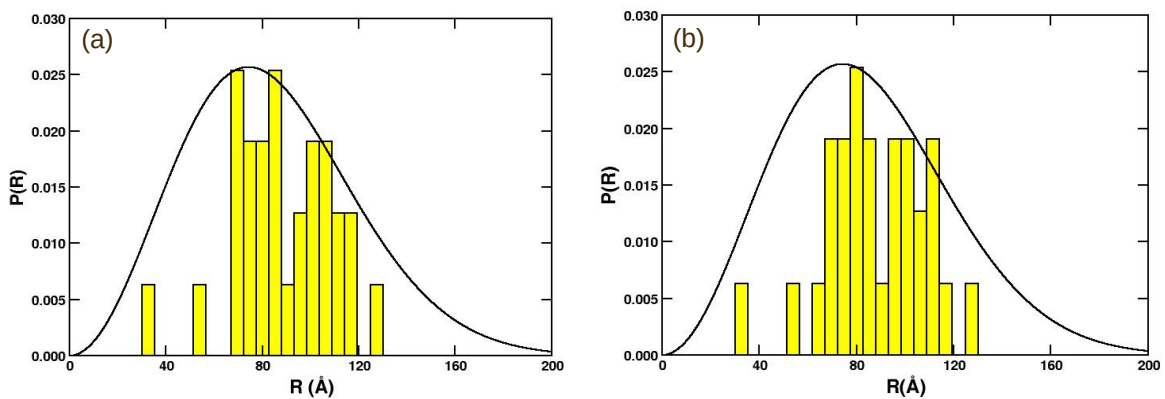


Figure 5.2: Average distribution, $P(R)$ of the end-to-end distance R for step 1 (a) and step 21 (b) of the 21-step equilibration procedure (1.53 ns). The black curves show the distributions predicted by the ideal freely joined-chain model.

Additionally, the fitting is carried out while ensuring the constraint that $N \cdot b$ be equal to the length of a completely outstretched chain, R_{max} . The number of bonds in each chain, n , is 412 (corresponding to 202 PMMA monomers and 1 SP unit) with the equilibrium length l and angle θ being 1.529 Å and 112.7°, respectively.

$$Nb = R_{max} = nl \cdot \cos(\theta/2) \quad (5.2)$$

Moreover, the average square end-to-end distance $\langle R^2 \rangle$ obtained from the fitting procedure can be utilized to calculate Flory’s characteristic ratio, C_∞ .

$$C_\infty = \langle R^2 \rangle / nl^2 \quad (5.3)$$

Table 5.1: SP-PMMA bulk system properties before (step 1) and after (step 21) the 21-step equilibration process at 300 K.

	Step 1	Step 21
R^2 (Å ²)	8291.38	8213.71
b (Å)	15.81	15.66
$\#N$	33.16	33.48
C_∞	8.60	8.52

Based on the ideal freely jointed chain model, the properties of the SP-PMMA system are given in Table 5.2. The estimated properties are in close agreement with the experimental values ($C_\infty = 8.22$ and $b = 15.3$ Å).^[282]

5.2.4 Thermal properties

The thermal properties of the system are determined by following the procedure outlined in a previous study by Laurien et al.^[140] For this purpose, a 21-step equilibration procedure was followed to generate a physically sound system at 750 K. Subsequently, the system was cooled down using an *NPT* ensemble simulation with

a step size of 10 K for 0.5 ps each until the system reached a temperature of 200 K. For each temperature simulation window, the density was calculated as the mean value obtained throughout the entire interval of 0.5 ns. Finally, as shown in Figure 5.3 (b), linear regression analyses on temperature ranges spanning 200 K both above and below the lowest and highest temperature of the density-temperature curves resulted in the glass transition temperature (T_g) of 508 K. The obtained T_g values are higher than the experimental values (403.15 K for SP-free syn-PMMA and 400.15 K SP-PMMA),^[283,284] which is due to the extremely fast cooling rate^[285] during the 21-step equilibration procedure and the short relaxation time during the T_g calculation procedure.

5.2.5 Bulk deformation

The flow diagram shown in Figure 5.4 outlines the process to simulate the SP mechanophore activation due to the mechanical stress arising from the deformation of bulk PMMA. The process begins with the application of external stress on an equilibrated system of 30 SP-doped PMMA chains, with the end-to-end distance of SP calculated every 1 fs. Based on the value of this end-to-end distance, a decision is made whether to continue the simulation. If the end-to-end distance exceeds the 14.6 Å limit in a given SP unit, the FF parameters for this specific SP are switched to the parameters of MC and the simulation loops back to the deformation process. If neither of the SP end-to-end distances exceed a limit of 14.6 Å, the simulation is continued until the deformation process reaches the target amount of strain. In the specific example shown in Figure 5.4, the deformation loop will be continued until it achieves a strain of 80%.

The *fix deform* command within an NpT ensemble (1 atm) is used to apply a constant strains of $5 \cdot 10^7$ and $5 \cdot 10^8$ s⁻¹, respectively. By using the *erate* command, tensile and shear stress are applied along the x direction and xy plane, respectively.

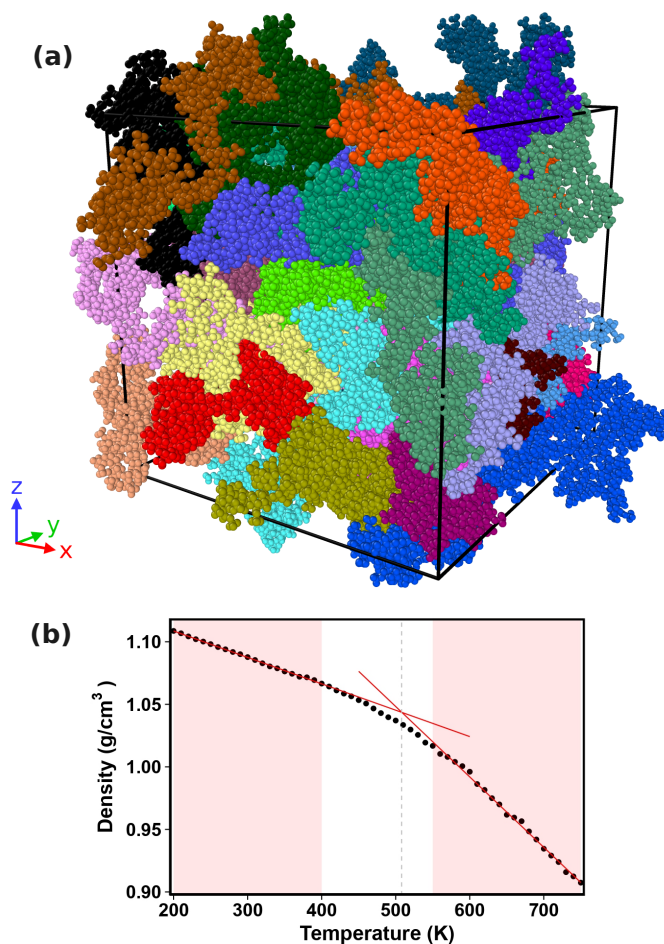


Figure 5.3: (a) Unwrapped SP-PMMA bulk simulation box and (b) density as a function of temperature. The glass transition temperature (T_g) was determined by finding the point where the linear fits of the densities within the red shaded areas intersect.

By using the *remap* command the velocities of the atoms are remapped in the applied stress direction. To facilitate relaxation of the simulation cell, a nonuniform barostat is applied, allowing relaxation specifically in the y and z directions.

5.3 Results

The equilibrated SP-doped PMMA system was subjected to tensile and shear deformations using engineering strain rates of $5 \cdot 10^7$ and $5 \cdot 10^8 \text{ s}^{-1}$, respectively. As shown in Figure 5.5, the response to the applied deformation can be analyzed using

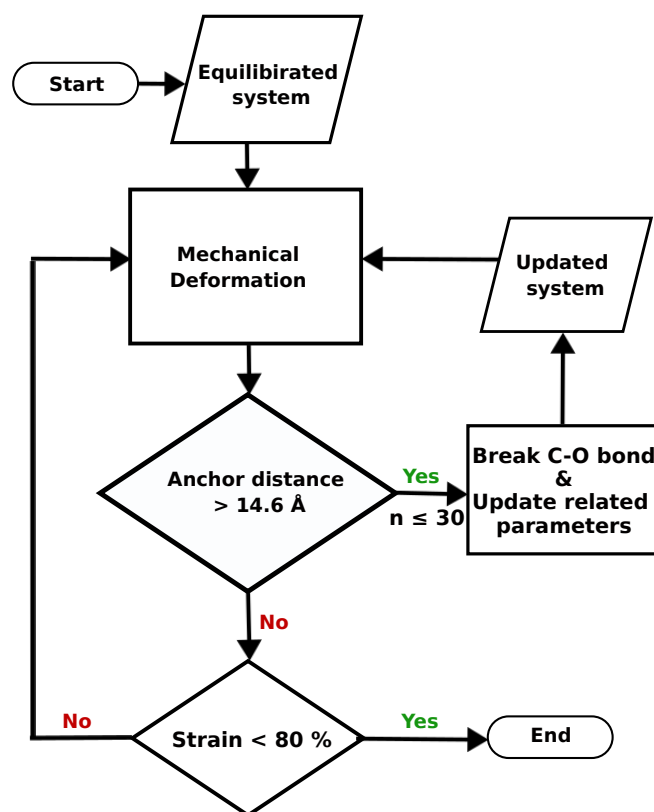


Figure 5.4: Schematic flow diagram of deformation procedure in LAMMPS for mechanochemical activation of the SP-doped PMMA system. n is the number of mechanophores.

a stress-strain curve (SSC). At low strain values, the curve shows a linear elastic region where stress is directly proportional to strain. Based on the procedure by Demir and Walsh,^[286] the elastic modulus of the system was calculated for the initial 2% of the strain (see Figure 5.5 (a), (c)). In case of tensile stress, the experimental Young's modulus for PMMA at room temperature was reported to be in a range between 2.76 GPa to 4.15 GPa,^[287] which is in close agreement with the calculated values (2.7 GPa and 4.0 GPa). Further, an increase in strain during the tensile deformation leads to the yield point of the system at 136 MPa and 161 MPa for $5 \cdot 10^7$ and $5 \cdot 10^8$ s^{-1} strain rates, respectively. In the case of shear stress, elastic deformation at low strain is defined using the shear modulus, also known as the modulus of rigidity of the material. As shown in Figure 5.5 (c), the calculated shear modulus of the material is 1.5 GPa and 1.9 GPa for strain rates of $5 \cdot 10^7$ and $5 \cdot 10^8$

s^{-1} , respectively, which are close to the experimental values (1.1 GPa to 1.7 GPa for the crosslinked system).^[288] Increasing the strain during the shear deformation leads to the yield point at 198 MPa and 175 MPa for strain rates of $5 \cdot 10^7$ and $5 \cdot 10^8$ s^{-1} , respectively.

In case of tensile deformation, following the yield point, the SSC curve initially displays strain softening, followed by strain hardening behavior. During this process, the stress first decreases and then increases gradually with increasing strain, indicating a high mobility owing to internal rearrangements of the chains. However, in the case of shear deformation, strain hardening occurs directly after the yield point. It is well-known that post-yield point stress-strain curves obtained from MD simulations are highly sensitive to the simulation conditions and the interatomic potentials employed.^[289] Therefore, in this study, we rely solely on the activation model and not on strain softening or hardening behavior to interpret our results, as we expect it to provide a more reliable measure of the mechanochemical behavior.

Both stress types (tensile and shear) and strain rates lead to mechanophore activation (marked as circles in Figure 5.5(a, b)), but at different amounts of strain. Under tensile deformation, mechanophore activation occurs at strains higher than 457% and 520% for strain rates of $5 \cdot 10^7$ and $5 \cdot 10^8$ s^{-1} , respectively. Interestingly, during shear deformation the mechanophore activation occurs around 300% and 390% of strain for strain rates of $5 \cdot 10^8$ and $5 \cdot 10^7$ s^{-1} , respectively, i.e., at significantly lower strain than in the case of tensile deformation.

Snapshots of the resulting structures of the polymer chains during tensile deformation at selected strains are shown in Figure 5.6. Additionally, the stress distribution is illustrated by per-atom stress tensors aligned along the direction of tensile stress, with highly stressed atoms colored yellow. As shown in Figure 5.6 (a), cavities become observable at a strain of 50%, and as the strain increases to 150% these cavities expand due to molecular rearrangements. Such rearrangements can be

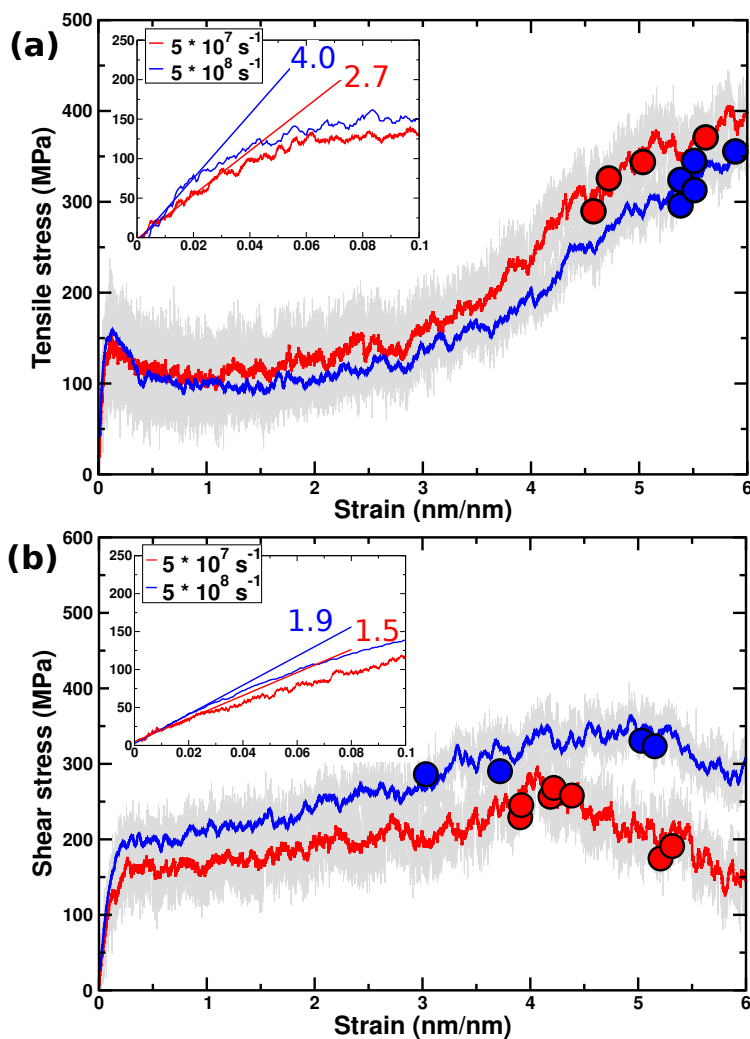


Figure 5.5: The tensile (a) and shear (b) stress-strain curves for SP-PMMA system at $5 \cdot 10^7 \text{ s}^{-1}$ (red curve) and $5 \cdot 10^8 \text{ s}^{-1}$ (blue curve) strain rates. The red and blue circle represent the mechanophore activation at strain rate of $5 \cdot 10^7$ and $5 \cdot 10^8 \text{ s}^{-1}$ respectively. The gray shaded area is representing the original data. The elastic-modulus of tensile and shear deformation at both strain rates are calculated using the linear fits for 2% of the strain, given in the respective insets.

interpreted in terms of changes in the orientation of the chains, as shown in Figure 5.6 (b), where it is demonstrated that an increase in strain from 0% to 150% causes the chain to elongate. Upon reaching strains above 150%, strain-hardening behavior is observed, characterized by a gradual increase in stress with increasing strain. At a strain of 350%, the chain starts stretching significantly and the intermolecular interactions and entanglements between the chains and within the chain itself are disrupted, allowing the chain to become more extended. Unlike in experiments, where at room temperature ultimate failure occurs at small strains (below 10%), no ultimate failure in SSC curve is reported in our results up to 800% strain. This discrepancy can be attributed to the limitations of classical force fields, which do not account for bond-breaking phenomena, unless they are specifically parameterized, as presented here, in the case of the SP mechanophore.

As the chain continues to stretch, it eventually reaches almost full linearity, causing the stress to align with the backbone carbon atoms and to be transmitted efficiently to the SP unit. The activation of the first SP mechanophore occurs at 457% strain, which is represented by the highlighted molecular unit in Figure 5.6 (b). The stress distribution snapshots indicate that the middle part of the backbone of this chain is highly stretched. As the strain is increased, mechanophore activation in other polymer chains of the system is observed until 600% strain. The behavior of the mechanophore activation in the other chains follows a similar chain elongation procedure as observed in Figure 5.6 (b), which is confirmed by the radius of gyration (R_g) plot shown in the Supporting Information (Figure 5.5). Notably, the chains that undergo mechanophore activation during tensile deformation exhibit larger R_g values.

In the case of shear stress it can be observed that mechanophore activation can occur in partially elongated chains. As shown in Figures 5.5(b) and 5.11, at a strain rate of $5 \cdot 10^7 \text{ s}^{-1}$, the first mechanophore activation occurs at 390% of strain, which

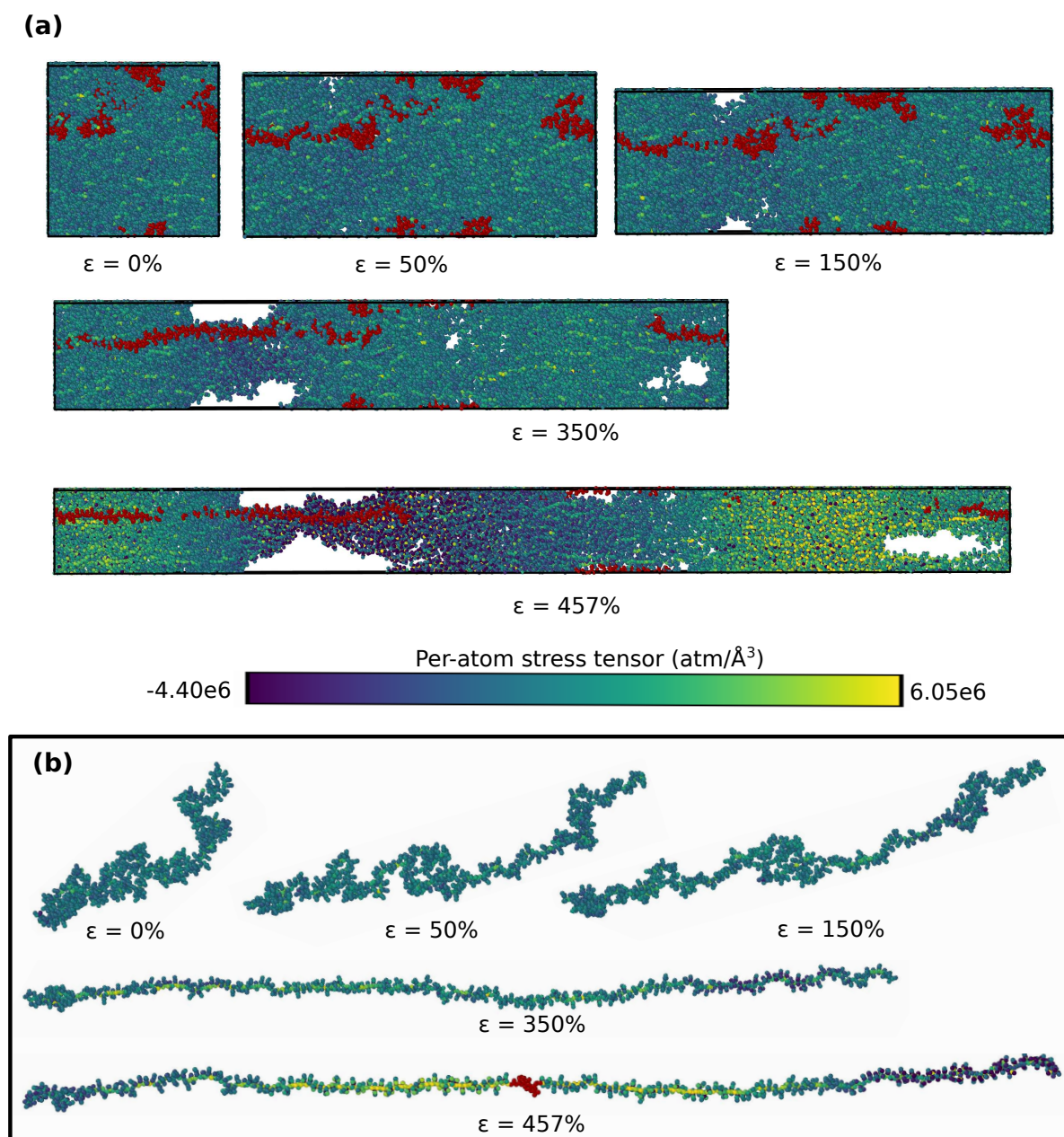


Figure 5.6: Per-atom stress tensor distribution for the tensile stress simulation along the σ_{xx} plane. (a) Snapshots of the wrapped molecular structure at selected strains. The atoms highlighted in red represent a single chain. (b) Snapshots of the unwrapped molecular structure of the chain highlighted in (a) at selected strains. The highlighted molecular unit at a strain of 457% is the first activated SP mechanophore. The hydrogen atoms are removed from the snapshots for clarity.

is below the strain required for activation upon tensile deformation (490%). The R_g for this particular chain is below 80 Å. Furthermore, it is important to note

that the activation of a mechanophore is also influenced by the specific direction and plane in which the shear stress is applied. This is supported by the observation that different chains undergo activation when stress is applied along three different planes, as shown in the Supporting Information (Figure 5.12).

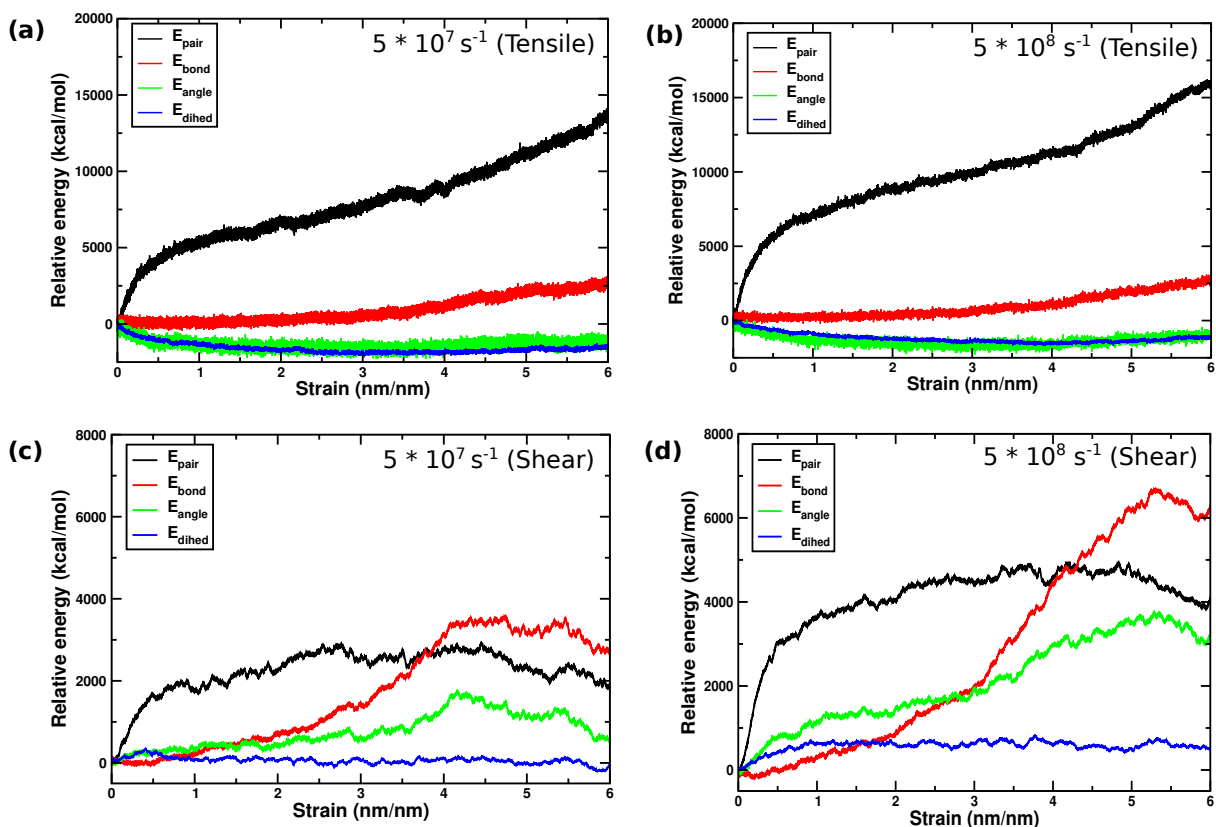


Figure 5.7: Total energy distribution under tensile (a, b) and shear (c, d) stress at $5 \cdot 10^7$ s^{-1} (a, c) and $5 \cdot 10^8$ s^{-1} (b, d) strain rates.

5.3.1 Energy distribution

The energy distribution within the simulated system during tensile and shear deformation is shown in Figure 5.7. The energy contributions from bonding (bond, angle and dihedral) and non-bonding interactions are described using equations 5.5-5.10. In both tensile and shear stress, a rapid increase in the energy of the pairwise interactions is observed. The crystallographic slip in the polymer chains is

responsible for this increase in energy at the early stage of deformation. Further increase in the strain causes the chains to orient in the applied stress direction, which attenuate the increase in the pairwise interactions. However the bonded energies show a different behavior in both types of applied stress. During the tensile loading of linear polymer chains, the polymer chains are slowly oriented along the direction of applied stress, which causes them to be stretched and pulled apart. The energy expended to stretch the bonds increases upon elongation, leading to a slow increase in the bond energies. Moreover, during the tensile deformation the energies stored in the bond angles and dihedral angles decrease in the beginning of the stretching and then remain almost constant until high strain is achieved. In shear deformation, sliding of the polymer chains occurs, which leads to a more rapid increase in bond and angle energies compared to tensile deformation. This effect could be responsible for the activation of mechanophores at lower strains during shear stress as compared to tensile deformation.

5.3.2 Effect of temperature

Experimental findings have indicated a strong correlation between polymer mobility and mechanophore activation. For SP-doped PMMA systems, the activation was observed within a specific temperature range of 90°C to 105°C^[284]. To make our simulations more realistic, we have investigated the impact of temperature on the SP-doped PMMA system. For this purpose, using the 21-step equilibration procedure a number of temperatures were adjusted in the system. The corresponding density and final volume of the simulation box are given in Table 5.2. As show in Figure 5.8, with increasing temperature, the yield strength of the system decreases upon application of both stress types, which could prevent the system from brittle fracture. Moreover, the mechanochemical activity is enhanced for temperatures between 400K and 500 K. Mechanophore activation is observed at higher strain under tensile stress

as compared to shear stress, and an overall slight decrease in strain required for mechanophore activation is observed. However, for higher temperatures between 600 K and 750 K, mechanophore activation is not observed upon application of tensile strain, due to viscous flow, whereas some mechanophores are activated under shearing.

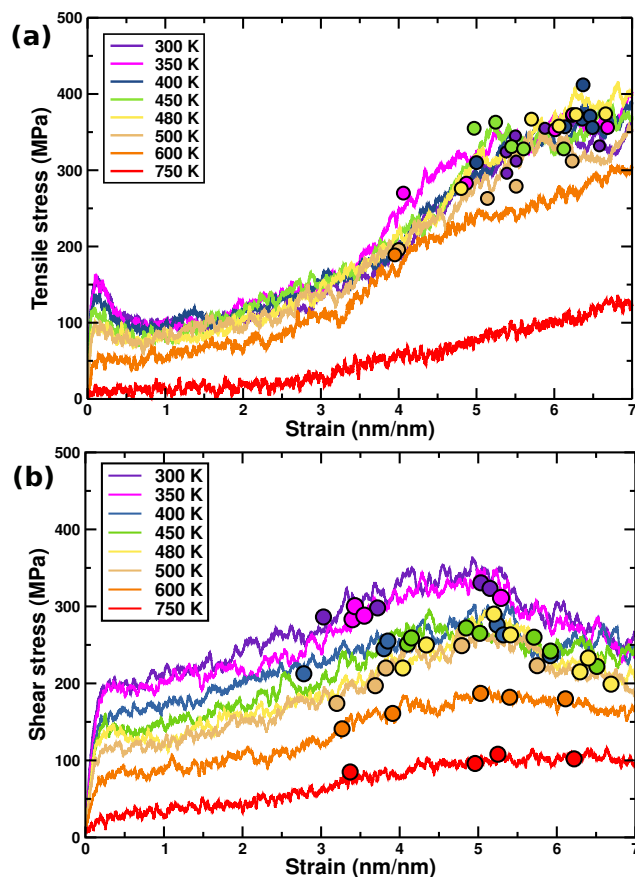


Figure 5.8: Stress-strain curves as a function of temperature at a strain rate of $5 \cdot 10^8 \text{ s}^{-1}$ for tensile (a) and shear (b) deformation. The circles represent mechanophore activation at different temperatures.

5.4 Conclusion

A multiscale mechanochemical model was developed that simulates the activation of the SP mechanophore upon deformation of bulk PMMA. To achieve this, a parameterization of SP-to-MC isomerization under stretching forces was performed

at the DFT level, which served as a reliable framework to simulate SP activation in bulk PMMA. The model revealed that mechanophore activation in linear SP-doped PMMA chains is only possible if the chain is fully extended and the backbone of a polymer chain is aligned with the stretching direction. The molecular rearrangements of the chain as a function of tensile strain are responsible for the cavitation and necking of the system, which could be responsible for the ultimate failure of the system before activation. The performance of shear stress is superior in terms of the amount of strain required for mechanophore activation. However, more possible modes of strain application, such as monotonic torsion, need to be explored to better gauge the impact of deformations on mechanochemical activation. It must also be noted that the multiscale model developed here considers SP-to-MC isomerization only if the SP meets a criterion based on the end-to-end distance. Including other degrees of freedom that play a role in the SP stretching coordinate would improve the results of the model.^[290,291] In the future, we plan to apply such a refined model to explore more complex polymer networks, featuring longer chains, increased entanglement and crosslinked systems. Moreover, the efficiency of the model in treating different mechanophores as well as different linkers^[245] will be tested.

5.5 Additional information

Force field

$$E_{Total} = E_{bond} + E_{angle} + E_{torsion} + E_{improper} + E_{coul} + E_{vdw} \quad (5.4)$$

$$E_{bond} = \sum_{bond} \frac{1}{2} K_b (r - r_o)^2 \quad (5.5)$$

$$E_{angle} = \sum_{angle} \frac{1}{2} K_\theta (\theta - \theta_o)^2 \quad (5.6)$$

$$E_{improper} = \sum_{improper} K_\omega [1 + d \cos(n\omega)] \quad (5.7)$$

$$E_{torsions} = \sum_{dihedral} \frac{1}{2} K_{\phi_1} [(1 + \cos(\phi))] + \frac{1}{2} K_{\phi_2} [(1 - \cos(2\phi))] + \frac{1}{2} K_{\phi_3} [(1 + \cos(3\phi))] + \frac{1}{2} K_{\phi_4} [(1 - \cos(4\phi))] \quad (5.8)$$

$$E_{coul} = \sum_{coul} \frac{q_i q_j}{4\pi \epsilon_0 r_{ij}} \quad (5.9)$$

$$E_{vdw} = \sum_{vdw} 4\epsilon_{ij} \left[\left(\frac{r_{0,ij}}{r_{ij}} \right)^{12} - \left(\frac{r_{0,ij}}{r_{ij}} \right)^6 \right] \quad (5.10)$$

System properties

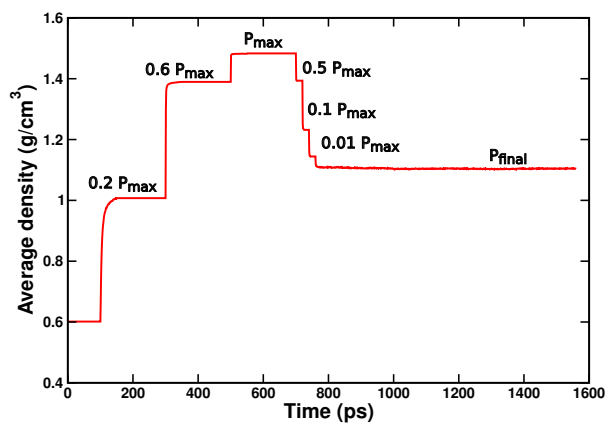


Figure 5.9: Evolution of bulk density in the SP-doped PMMA system throughout the 21-step equilibration procedure of 1.56 ns. The density fluctuations w.r.t. the pressure are marked as fractions of the maximum pressure, $P_{\max} = 50000$ atm, imposed during the NPT simulations.

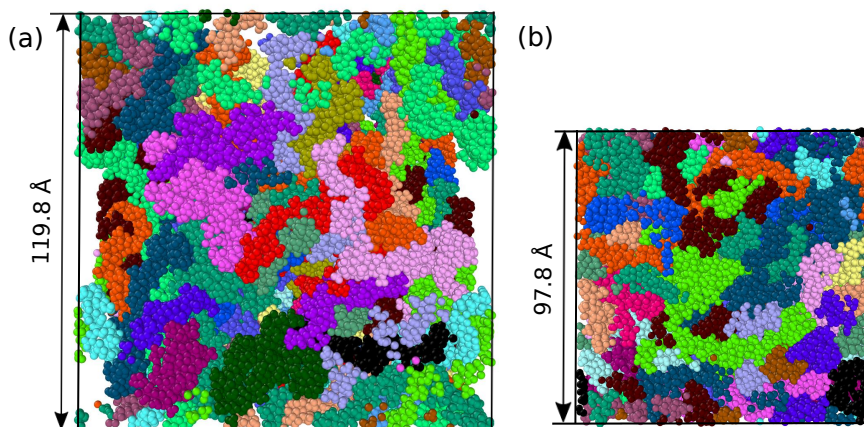


Figure 5.10: Wrapped configurations of the bulk SP-doped PMMA system (a) before and (b) after the 21-step equilibration procedure. The system consists of 30 chains where each color represents a single chain consisting of 202 PMMA monomers and one SP unit.

Shear stress snapshots

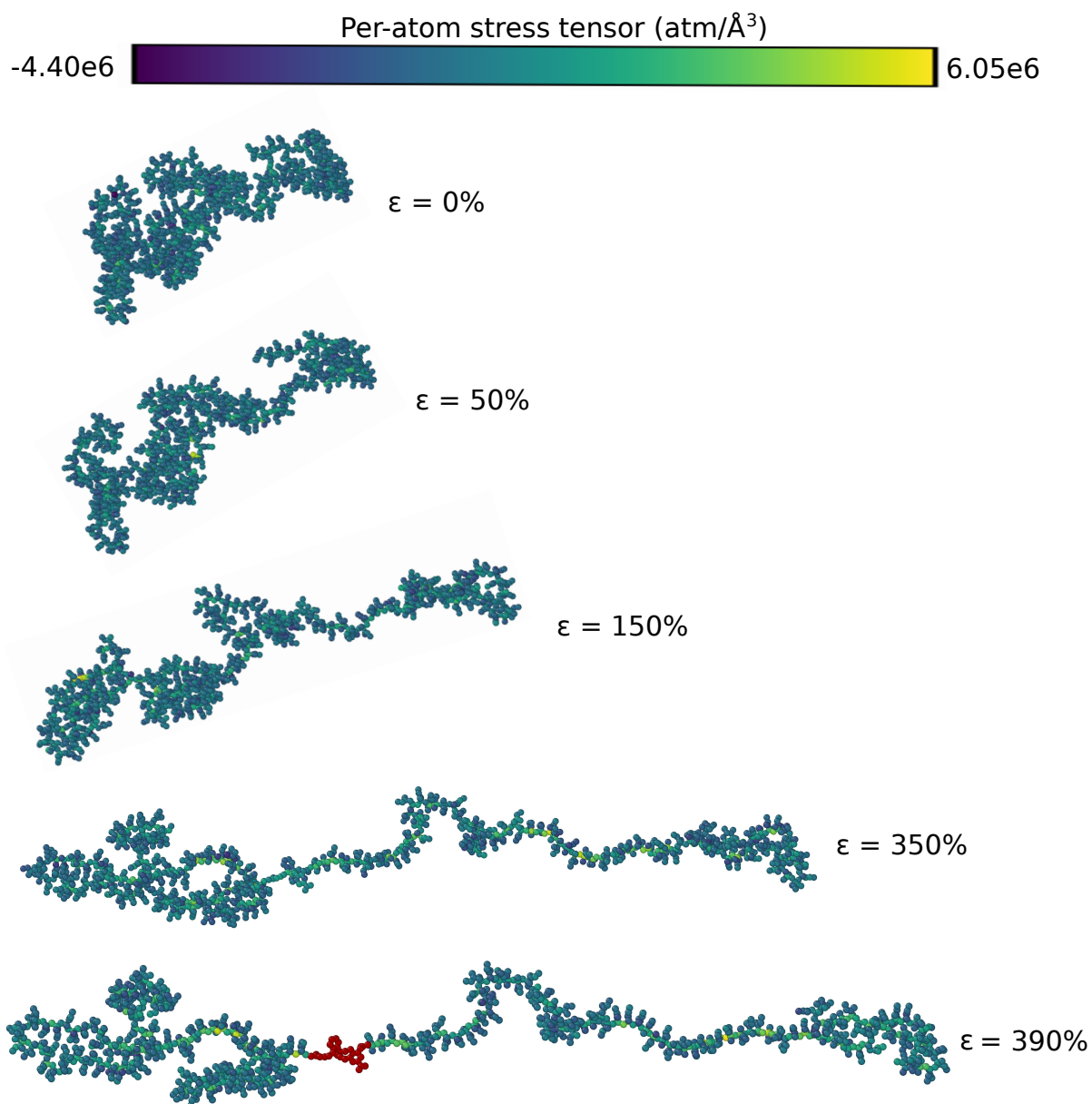


Figure 5.11: The unwrapped coordinates of a particular chain undergoing the first mechanophore activation at 390% of shear stress at a strain rate of $5 \cdot 10^7 \text{s}^{-1}$. The unit highlighted in red at a strain of 390% is the MC form.

Shear plane effect

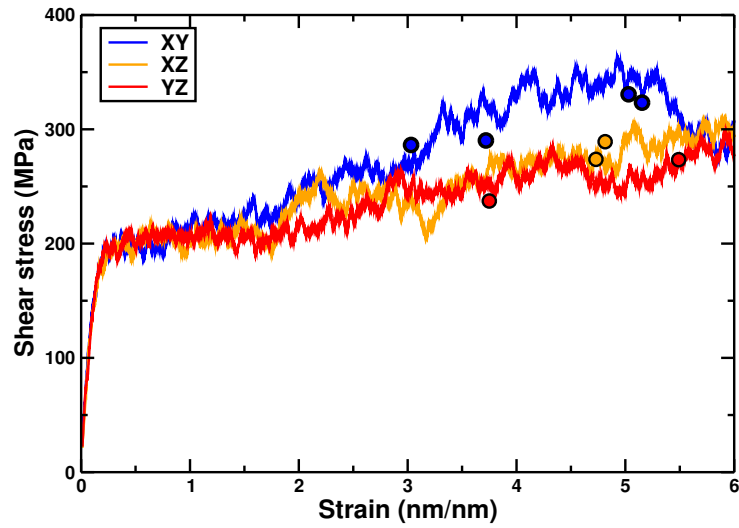


Figure 5.12: Stress-strain curves for shear stress in three different planes. The circles denote mechanophore activation events.

Radius of gyration

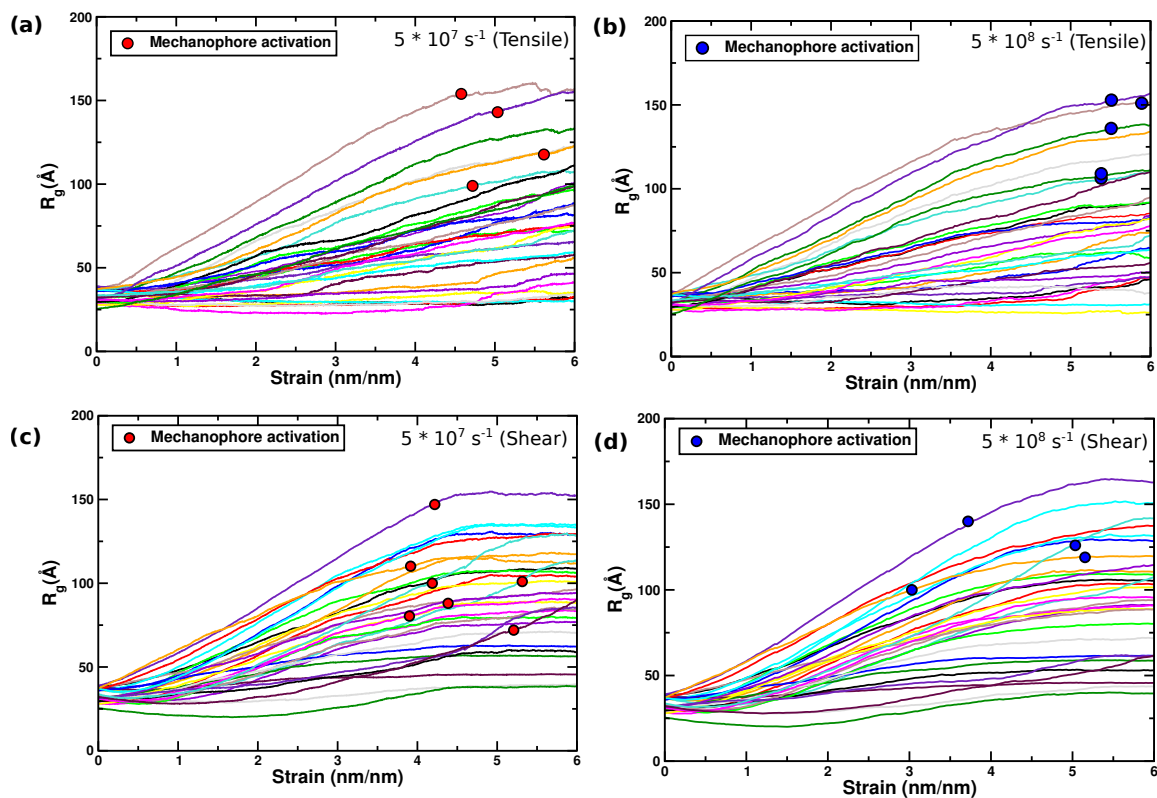


Figure 5.13: Radius of gyration (R_g) for each chain as a function of strain for two different strain rates, i.e., $5 \cdot 10^7 \text{ s}^{-1}$ (a, c) and $5 \cdot 10^8 \text{ s}^{-1}$ (b, d) under tensile (a, b) and shear (c, d) deformation. The red and blue circles represent mechanophore activation.

Chain scission in PMMA

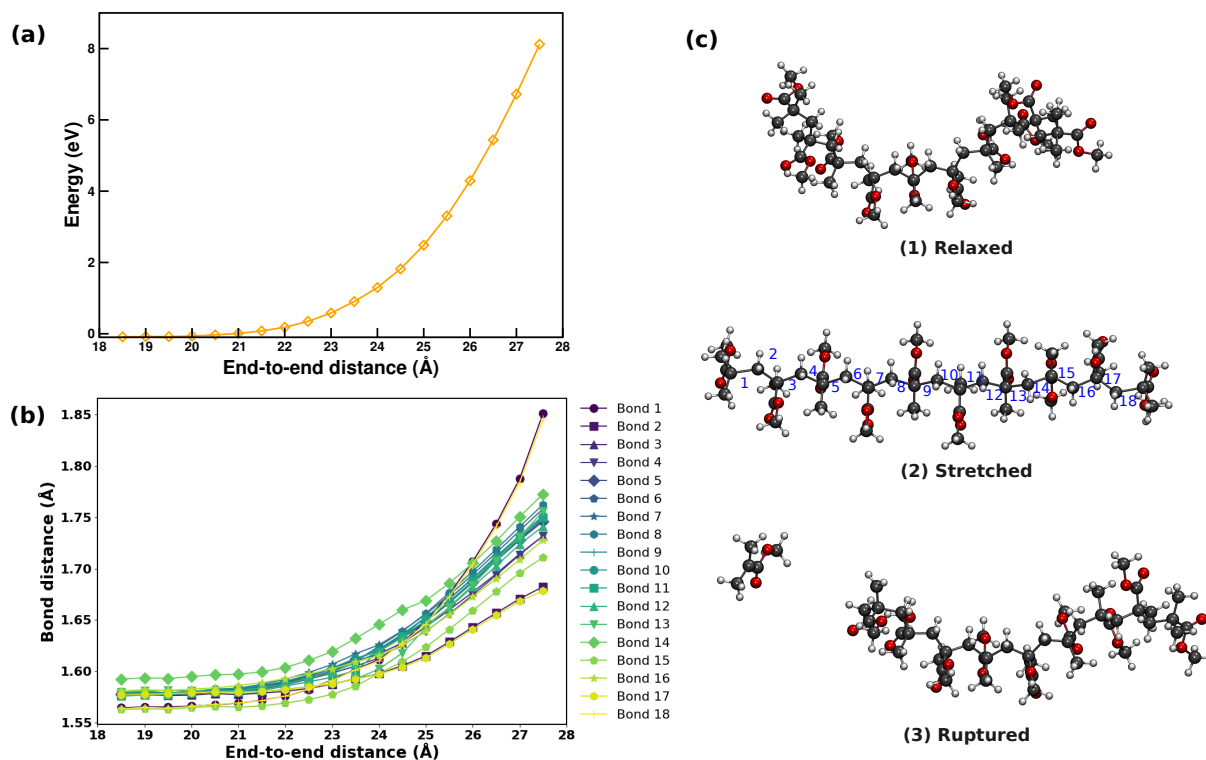


Figure 5.14: (a) Potential energy surface (PES) scan for a SP-free PMMA chain (10 monomers) *via* end-to-end stretching. (b) The backbone's bond length distribution as a function of end-to-end distance.

The SP-free PMMA chain (10 monomer long) stretched from the relaxed stage to full extended form at Density Functional Theory (DFT)^[121,122] at the B3LYP^[100,215]/6-31G(d)^[216] level of theory. The total energy of the system and backbone bonds length as a function of end-to-end distance is shown in Figure 5.14 (a) and (b) respectively. The first bond of the backbone has undergone scission after being stretched up to 1.85 Å length.

System properties at various temperatures

Table 5.2: SP-doped PMMA bulk system density and volume of the simulation box after the last step of the 21-step equilibration process at different temperatures.

Temperature	Density (g/cm ³)	Volume (Å ³)
300	1.10	97.82
350	1.09	98.00
400	1.75	98.75
450	1.06	99.17
480	1.04	99.62
500	1.03	99.86
600	0.99	101.31
750	0.90	104.50

Chapter 6

Summary and outlook

In last two decades, the field of polymer mechanochemistry has undergone significant development. Specifically the concept of mechanophores plays a significant role in expanding the potential application fields. The increasing demand in the field of force sensors, controlled drug release, and autonomous self-healing materials require thoroughly investigations on how mechanophore respond to mechanical forces. In addition, there is still much to be explored regarding the activation efficiency, reversibility, and response time of mechanophores, which are critical factors that impact their performance. Computational investigations are necessary to fulfill these demands in polymer mechanochemistry as they allow for a deeper understanding of the behavior of polymers under mechanical stress, provide insights into the molecular-level mechanisms that govern their response to mechanical forces, and enable the prediction of their properties and behavior under different conditions, all of which may not be feasible or cost-effective to obtain through experiments alone.

The results presented in this thesis have made a substantial contribution to our understanding of the mechanism of mechanophore activation and the influencing factors. Here, the study has provided detailed insights into the impact of mechanical forces,

specifically in terms of pulling or compression, on the activation of mechanophores. Additionally, through the use of molecular dynamics (MD) simulations, we have gained valuable information on the behavior of mechanophore activation under bulk deformations such as shear and tensile stress.

Firstly, we focused on the role of stretching forces on the single molecule level, where we have shown that the activation efficiency of mechanophores very much depends on the pulling coordinates. For flex-activated mechanophores we have demonstrated that the activation of the mechanophore cannot be triggered by mere end-to-end pulling of the main polymer chain. The other two modes (i.e. direct pulling of critical bonds and constraining the bond angle joining the to polymer composition) are found to be more effective to break the labile bond. Based on these results, we suggest utilizing an infrared laser to stimulate specific normal modes that induce either the elongation of the critical bonds or to a bending of the bond angles adjacent to them in the polymer chain. This approach holds great promise for the release of small molecules as it targets the labile bonds.

In case of stretching forces, we have conducted an investigation into the role of linkers, where we have demonstrated that the force required to activate a mechanophore can be modulated by approximately 300% through a chemical composition of the linkers between the mechanophore and the rest of the polymer chain. The eleven different linkers tested throughout the computations revealed a strong dependence of the angle lying between labile bond and linker on the critical force to break the bond. This finding paves the way to precisely adjust the activation rate of mechanophores in polymers when subjected to mechanical stress or ultrasound, offering the ability to enhance mechanophore activation or to suppress it below a threshold force. Computational studies focused on examining the impact of linkers in large-scale simulations offer an encouraging opportunity to gain insights into the role of linkers in polymer materials. Based on the current results one can expect

linkers as a promising choice for improving the state-of-the-art of polymer materials in terms of stress-sensing and material strengthening.

The fourth Chapter discussed the role of mechanical forces that arise from hydrostatic pressure, where in the first section we established a two-step baro-mechanical cycle for repeated activation and deactivation of mechanophores. The possibility to restore force-activated mechanophores to their deactivated form holds great promise for the development of reusable force-responsive materials. Moreover, the color change associated with the barophore conversion paves the way for the use of barophores as internal standards in high-pressure experiments. The results presented in this study are limited to the effects of pressure in an isotropic medium. Hence, over a computational multiscale approach it would be interesting to model such molecular pressure sensors into an anisotropic polymer surrounding. For instance, the response from the barophore under different types of host polymer matrices, such as linear, branched and crosslinked structures, depends on its orientation and interactions with the surrounding polymer network. In addition to this, based on the results from multiscale modelling more baro-mechanical cycles needs to be investigated that can serve and enhance the pressure force sensors efficiency to repeated activation of mechanophores.

In addition to mechanochemical reactions, we conducted quantum chemical calculations and BOMD simulations to investigate the effect of pressure on a [2,3]-sigmatropic rearrangement. Our results demonstrate that the application of hydrostatic pressures between 100 and 150 GPa can effectively "trap" the five-membered cyclic transition state of a model Mislow-Evans rearrangement. Upon decompression, we observed the formation of the rearrangement product, which highlights the potential of hydrostatic pressure to influence chemical reactions. The amount of pressure required is high and difficult to achieve due to limitations in

materials. Therefore, it is necessary to investigate reactions that can be performed at a lower pressure range.

A multiscale mechanochemical model has been developed to govern the activation of the SP mechanophore at the macroscopic scale. To achieve this, the parameterization of SP-MC isomerization has been performed, which serves as a reliable framework to govern the activation at the bulk SP-PMMA system. Furthermore, bulk modeling of the system has revealed that mechanophore activation in linear SP-PMMA chains is only possible when the chain is fully extended, and the stress is aligned along the backbone of the chain. The molecular rearrangements of the chain as a function of strain are responsible for the cavitation and necking of the system. Furthermore, we observed a significant correlation between the type of stress applied and the resulting stress-strain behavior, as well as the subsequent mechanochemical activity. Overall, our results provide a detailed understanding of the force transduction behaviour of bulk scale deformation to govern the mechanophore activation. To gain further insights, the model can be extended to longer chains, consisting of 500 to 2000 monomers per chain. This would allow for a higher degree of entanglements within the system, providing valuable understanding of the role of entanglements in mechanophore activation. In the future, we plan to apply this model to explore more complex polymer networks. SP, as a crosslinker in polymer systems or part of the backbones in crosslinked systems can be helpful in understanding the force transmission behavior in crosslinked systems.

The findings of this thesis have significantly advanced our understanding of mechanophore activation and the factors that influence it. The proposed methods for increasing the efficiency of mechanophore activation hold great promise for the development of force-responsive materials with a wide range of applications. The two-step baromechanical cycle and research findings pertaining to transition states under pressure contribute significantly towards gaining a deeper understanding of

the molecular mechanisms that operate under high pressure. Furthermore, the development of a multiscale mechanochemical model serves as an example for the creation of additional models, thereby enhancing our understanding of force transduction mechanisms at the macroscopic level and advancing the current state-of-the-art in mechanochemical systems.

Bibliography

- [1] L. Takacs, “The historical development of mechanochemistry,” *Chem. Soc. Rev.*, vol. 42, pp. 7649–7659, 2013.
- [2] M. Faraday, “The decomposition of chloride of silver by hydrogen and by zinc,” *Quart. J. Liter. Sci. Arts*, vol. 8, pp. 374–376, 1820.
- [3] M. C. Lea, “Disruption of the silver haloid molecule by mechanical force,” *Philos. Mag.*, vol. 34, no. 206, pp. 46–50, 1892.
- [4] W. Ostwald, *Handbuch der Allgemeinen Chemie*. Leipzig: Akademische Verlagsgesellschaft mbH, 1 ed., 1919.
- [5] J. N. Brantley, C. B. Bailey, K. M. Wiggins, A. T. Keatinge-Clay, and C. W. Bielawski, “Mechanobiochemistry: harnessing biomacromolecules for force-responsive materials,” *Polym. Chem.*, vol. 4, no. 14, pp. 3916–3928, 2013.
- [6] R. Boulatov, *Polymer Mechanochemistry*, vol. 369. Springer, 2015.
- [7] S. L. James, C. J. Adams, C. Bolm, D. Braga, P. Collier, T. Friščić, F. Grepioni, K. D. Harris, G. Hyett, W. Jones, *et al.*, “Mechanochemistry: opportunities for new and cleaner synthesis,” *Chem. Soc. Rev.*, vol. 41, no. 1, pp. 413–447, 2012.

- [8] G. Oster and H. Wang, “Reverse engineering a protein: the mechanochemistry of atp synthase,” *BBA-Bioenergetics*, vol. 1458, no. 2-3, pp. 482–510, 2000.
- [9] P. Lavalle, F. Boulmedais, P. Schaaf, and L. Jierry, “Soft-mechanochemistry: mechanochemistry inspired by nature,” *Langmuir*, vol. 32, no. 29, pp. 7265–7276, 2016.
- [10] J. Yu, J. Moffitt, C. L. Hetherington, C. Bustamante, and G. Oster, “Mechanochemistry of a viral dna packaging motor,” *J. Mol. Biol.*, vol. 400, no. 2, pp. 186–203, 2010.
- [11] C. R. White and J. A. Frangos, “The shear stress of it all: the cell membrane and mechanochemical transduction,” *Philos. Trans. R. Soc. Lond., B, Biol. Sci.*, vol. 362, no. 1484, pp. 1459–1467, 2007.
- [12] D. A. Davis, A. Hamilton, J. Yang, L. D. Cremar, D. V. Gough, S. L. Potisek, M. T. Ong, P. V. Braun, T. J. Martínez, S. R. White, J. S. Moore, and N. R. Sottos, “Force-induced activation of covalent bonds in mechanoresponsive polymeric materials,” *Nature*, vol. 459, pp. 68–72, 5 2009.
- [13] C. M. Kingsbury, P. A. May, D. A. Davis, S. R. White, J. S. Moore, and N. R. Sottos, “Shear activation of mechanophore-crosslinked polymers,” *J. Mater. Chem.*, vol. 21, pp. 8381–8388, 2011.
- [14] X. Meng, G. Qi, X. Li, Z. Wang, K. Wang, B. Zou, and Y. Ma, “Spiropyran-based multi-colored switching tuned by pressure and mechanical grinding,” *J. Mater. Chem. C*, vol. 4, pp. 7584–7588, 2016.
- [15] R. T. O’Neill and R. Boulatov, “The many flavours of mechanochemistry and its plausible conceptual underpinnings,” *Nat. Rev. Chem.*, vol. 5, no. 3, pp. 148–167, 2021.

- [16] A. A. Michalchuk, E. V. Boldyreva, A. M. Belenguer, F. Emmerling, and V. V. Boldyrev, “Tribochemistry, mechanical alloying, mechanochemistry: what is in a name?,” *Front. Chem.*, vol. 9, p. 685789, 2021.
- [17] H. Staudinger and H. F. Bondy, “Über isopren und kautschuk, 19. mittel.: Über die molekülgröße des kautschuks und der balata,” *Ber. Dtsch. Chem. Ges.*, vol. 63, pp. 734–736, 3 1930.
- [18] H. Staudinger and W. Heuer, “Über hochpolymere verbindungen, 93. mittel.: Über das zerreißen der faden-moleküle des poly-styrols,” *Ber. Dtsch. Chem. Ges.*, vol. 67, pp. 1159–1164, 7 1934.
- [19] H. Staudinger and E. O. Leupold, “Über isopren und kautschuk, 18. mittel.: Viscositäts-untersuchungen an balata,” *Ber. Dtsch. Chem. Ges.*, vol. 63, pp. 730–733, 3 1930.
- [20] W. Kauzmann and H. Eyring, “The viscous flow of large molecules,” *J. Am. Chem. Soc.*, vol. 62, pp. 3113–3125, 1940.
- [21] M. Tabata, T. Miyazawa, and J. Sohma, “Direct evidence of main-chain scissions induced by ultrasound irradiation of benzene solutions of polymers,” *Chem. Phys. Lett.*, vol. 73, pp. 178–180, 1980.
- [22] M. V. Encina, E. Lissi, M. Sarasúa, L. Gargallo, and D. Radic, “Ultrasonic degradation of polyvinylpyrrolidone: Effect of peroxide linkages,” *J. Polym. Sci. Polym. Lett. Ed.*, vol. 18, pp. 757–760, 12 1980.
- [23] K. L. Berkowski, S. L. Potisek, C. R. Hickenboth, and J. S. Moore, “Ultrasound-induced site-specific cleavage of azo-functionalized poly (ethylene glycol),” *Macromolecules*, vol. 38, p. 37, 2005.

- [24] C. R. Hickenboth, J. S. Moore, S. R. White, N. R. Sottos, J. Baudry, and S. R. Wilson, "Biasing reaction pathways with mechanical force," *Nature*, vol. 446, pp. 423–427, 3 2007.
- [25] M. Li, Q. Zhang, Y.-N. Zhou, and S. Zhu, "Let spiropyran help polymers feel force!," *Prog. Polym. Sci.*, vol. 79, pp. 26–39, 2018.
- [26] L. Kortekaas and W. R. Browne, "The evolution of spiropyran: fundamentals and progress of an extraordinarily versatile photochrome," *Chem. Soc. Rev.*, vol. 48, no. 12, pp. 3406–3424, 2019.
- [27] J. Li, C. Nagamani, and J. S. Moore, "Polymer mechanochemistry: From destructive to productive," *Acc. Chem. Res.*, vol. 48, pp. 2181–2190, 2015.
- [28] I. M. Klein, C. C. Husic, D. P. Kovács, N. J. Choquette, and M. J. Robb, "Validation of the CoGEF Method as a Predictive Tool for Polymer Mechanochemistry," *J. Am. Chem. Soc.*, vol. 142, pp. 16364–16381, 2020.
- [29] M. Horst, J. Yang, J. Meisner, T. B. Kouznetsova, T. J. Martínez, S. L. Craig, and Y. Xia, "Understanding the mechanochemistry of ladder-type cyclobutane mechanophores by single molecule force spectroscopy," *J. Am. Chem. Soc.*, vol. 143, pp. 12328–12334, 2021.
- [30] M. F. Pill, K. Holz, N. Preußke, F. Berger, H. Clausen-Schaumann, U. Lüning, and M. K. Beyer, "Mechanochemical cycloreversion of cyclobutane observed at the single molecule level," *Chem. Eur. J.*, vol. 22, 2016.
- [31] B. Lee, Z. Niu, J. Wang, C. Slebodnick, and S. L. Craig, "Relative mechanical strengths of weak bonds in sonochemical polymer mechanochemistry," *J. Am. Chem. Soc.*, vol. 137, no. 33, pp. 10826–10832, 2015.

- [32] P. A. May, N. F. Munaretto, M. B. Hamoy, M. J. Robb, and J. S. Moore, “Is molecular weight or degree of polymerization a better descriptor of ultrasound-induced mechanochemical transduction?,” *ACS Macro Lett.*, vol. 5, no. 2, pp. 177–180, 2016.
- [33] T. Frišćić, C. Mottillo, and H. M. Titi, “Mechanochemistry for synthesis,” *Angew. Chem.*, vol. 132, no. 3, pp. 1030–1041, 2020.
- [34] F. Delogu, G. Gorrasi, and A. Sorrentino, “Fabrication of polymer nanocomposites via ball milling: Present status and future perspectives,” *Prog. Mater. Sci.*, vol. 86, pp. 75–126, 2017.
- [35] A. L. Black, J. A. Orlicki, and S. L. Craig, “Mechanochemically triggered bond formation in solid-state polymers,” *J. Mater. Chem.*, vol. 21, no. 23, pp. 8460–8465, 2011.
- [36] Y. Lin, M. H. Barbee, C.-C. Chang, and S. L. Craig, “Regiochemical effects on mechanophore activation in bulk materials,” *J. Am. Chem. Soc.*, vol. 140, no. 46, pp. 15969–15975, 2018.
- [37] M. K. Beyer and H. Clausen-Schaumann, “Mechanochemistry: The mechanical activation of covalent bonds,” *Chem. Rev.*, vol. 105, pp. 2921–2948, 2005.
- [38] K. M. Wiggins, J. N. Brantley, and C. W. Bielawski, “Methods for activating and characterizing mechanically responsive polymers,” *Chem. Soc. Rev.*, vol. 42, pp. 7130–7147, 2013.
- [39] J. Zlatanova, S. M. Lindsay, and S. H. Leuba, “Single molecule force spectroscopy in biology using the atomic force microscope,” *Prog. Biophys. Mol. Biol.*, vol. 74, no. 1-2, pp. 37–61, 2000.

- [40] H. Clausen-Schaumann, M. Seitz, R. Krautbauer, and H. E. Gaub, “Force spectroscopy with single bio-molecules,” *Curr. Opin. Chem. Biol.*, vol. 4, no. 5, pp. 524–530, 2000.
- [41] E. Evans, “Probing the relation between force—lifetime—and chemistry in single molecular bonds,” *Annu. Rev. Bioph. Biom.*, vol. 30, no. 1, pp. 105–128, 2001.
- [42] W. F. Heinz and J. H. Hoh, “Spatially resolved force spectroscopy of biological surfaces using the atomic force microscope,” *Trends Biotechnol.*, vol. 17, no. 4, pp. 143–150, 1999.
- [43] J. Wang, T. B. Kouznetsova, Z. S. Kean, L. Fan, B. D. Mar, T. J. Martínez, and S. L. Craig, “A remote stereochemical lever arm effect in polymer mechanochemistry,” *J. Am. Chem. Soc.*, vol. 136, no. 43, pp. 15162–15165, 2014.
- [44] G. Cravotto, E. C. Gaudino, and P. Cintas, “On the mechanochemical activation by ultrasound,” *Chem. Soc. Rev.*, vol. 42, no. 18, pp. 7521–7534, 2013.
- [45] N. Willis-Fox, E. Rognin, C. Baumann, T. A. Aljohani, R. Göstl, and R. Daly, “Going with the flow: tunable flow-induced polymer mechanochemistry,” *Adv. Funct. Mater.*, vol. 30, no. 27, p. 2002372, 2020.
- [46] P. A. May and J. S. Moore, “Polymer mechanochemistry: techniques to generate molecular force via elongational flows,” *Chem. Soc. Rev.*, vol. 42, pp. 7497–7506, 2013.
- [47] G. I. Peterson, W. Ko, Y.-J. Hwang, and T.-L. Choi, “Mechanochemical degradation of amorphous polymers with ball-mill grinding: Influence of the

- glass transition temperature,” *Macromolecules*, vol. 53, no. 18, pp. 7795–7802, 2020.
- [48] K. Yanada, S. Kato, D. Aoki, K. Mikami, H. Sugita, and H. Otsuka, “Non-symmetric mechanophores prepared from radical-type symmetric mechanophores: Bespoke mechanofunctional polymers,” *Chem. Commun.*, vol. 57, no. 23, pp. 2899–2902, 2021.
- [49] W. Ma, Y. Liu, N. Yu, and K. Yan, “Solvent-free mechanochemical diaza-cope rearrangement,” *ACS Sustain. Chem. Eng.*, vol. 9, no. 48, pp. 16092–16102, 2021.
- [50] M. Bauser and K. Siegert, *Extrusion*. ASM international, 2006.
- [51] N. Willis-Fox, E. Rognin, T. A. Aljohani, and R. Daly, “Polymer mechanochemistry: Manufacturing is now a force to be reckoned with,” *Chem*, vol. 4, pp. 2499–2537, 2018.
- [52] G. I. Peterson, M. B. Larsen, M. A. Ganter, D. W. Storti, and A. J. Boydston, “3d-printed mechanochromic materials,” *ACS Appl. Mater. Interfaces*, vol. 7, no. 1, pp. 577–583, 2015.
- [53] T.-G. Hsu, S. Liu, X. Guan, S. Yoon, J. Zhou, W.-Y. Chen, S. Gaire, J. Seylar, H. Chen, Z. Wang, *et al.*, “Mechanochemically accessing a challenging-to-synthesize depolymerizable polymer,” *Nat. Commun.*, vol. 14, no. 1, p. 225, 2023.
- [54] T. Stoeckel, J. Blasius, and B. Crist, “Chain rupture and tensile deformation of polymers,” *J. Polym. Sci., Polym. Phys. Ed.*, vol. 16, no. 3, pp. 485–500, 1978.

- [55] J. R. Hemmer, C. Rader, B. D. Wilts, C. Weder, and J. A. Berrocal, “Heterolytic bond cleavage in a scissile triarylmethane mechanophore,” *J. Am. Chem. Soc.*, vol. 143, no. 45, pp. 18859–18863, 2021.
- [56] B. A. Beiermann, S. L. Kramer, J. S. Moore, S. R. White, and N. R. Sottos, “Role of mechanophore orientation in mechanochemical reactions,” *ACS Macro Lett.*, vol. 1, no. 1, pp. 163–166, 2012.
- [57] C. L. Brown and S. L. Craig, “Molecular engineering of mechanophore activity for stress-responsive polymeric materials,” *Chem. Sci.*, vol. 6, no. 4, pp. 2158–2165, 2015.
- [58] C. P. Kabb, C. S. O’Bryan, C. D. Morley, T. E. Angelini, and B. S. Sumerlin, “Anthracene-based mechanophores for compression-activated uorescence in polymeric networks†,” *Chem. Sci.*, vol. 10, pp. 7702–7708, 2019.
- [59] B. Cao, N. Boechler, and A. J. Boydston, “Additive manufacturing with a flex activated mechanophore for nondestructive assessment of mechanochemical reactivity in complex object geometries,” *Polymer*, vol. 152, pp. 4–8, 2018.
- [60] M. Naebe, M. M. Abolhasani, H. Khayyam, A. Amini, and B. Fox, “Crack damage in polymers and composites: A review,” *Polym. Rev.*, vol. 56, no. 1, pp. 31–69, 2016.
- [61] T. Stauch and A. Dreuw, “Advances in Quantum Mechanochemistry: Electronic Structure Methods and Force Analysis,” *Chem. Rev.*, vol. 116, pp. 14137–14180, 2016.
- [62] J. Ribas-Arino, M. Shiga, and D. Marx, “Understanding Covalent Mechanochemistry,” *Angew. Chem. Int. Ed.*, vol. 48, pp. 4190–4193, 2009.

- [63] M. K. Beyer, “The mechanical strength of a covalent bond calculated by density functional theory,” *J. Chem. Phys.*, vol. 112, p. 7307, 2000.
- [64] M. T. Ong, J. Leiding, H. Tao, A. M. Virshup, and T. J. Martínez, “First principles dynamics and minimum energy pathways for mechanochemical ring opening of cyclobutene,” *J. Am. Chem. Soc.*, vol. 131, no. 18, pp. 6377–6379, 2009.
- [65] J. Wang, T. B. Kouznetsova, R. Boulatov, and S. L. Craig, “Mechanical gating of a mechanochemical reaction cascade,” *Nat. Commun.*, vol. 7, p. 13433, 2016.
- [66] M. T. Shaw and W. J. MacKnight, *Introduction to polymer viscoelasticity*. John Wiley & Sons, 2018.
- [67] M. Razavi, S. Cheng, D. Huang, S. Zhang, and S.-Q. Wang, “Crazing and yielding in glassy polymers of high molecular weight,” *Polymer*, vol. 197, p. 122445, 2020.
- [68] A. J. Kinloch, *Fracture behaviour of polymers*. Springer Science & Business Media, 2013.
- [69] Y. Li, B. C. Abberton, M. Kröger, and W. K. Liu, “Challenges in multiscale modeling of polymer dynamics,” *Polymers*, vol. 5, no. 2, pp. 751–832, 2013.
- [70] A. Gooneie, S. Schuschnigg, and C. Holzer, “A review of multiscale computational methods in polymeric materials,” *Polymers*, vol. 9, no. 1, p. 16, 2017.
- [71] Q. Zeng, A. Yu, and G. Lu, “Multiscale modeling and simulation of polymer nanocomposites,” *Prog. Mater. Sci.*, vol. 33, no. 2, pp. 191–269, 2008.

- [72] T. E. Gartner III and A. Jayaraman, “Modeling and simulations of polymers: a roadmap,” *Macromolecules*, vol. 52, no. 3, pp. 755–786, 2019.
- [73] A. Karatrantos, N. Clarke, and M. Kröger, “Modeling of polymer structure and conformations in polymer nanocomposites from atomistic to mesoscale: A review,” *Polym. Rev.*, vol. 56, no. 3, pp. 385–428, 2016.
- [74] G. S. Grest, M.-D. Lacasse, K. Kremer, and A. M. Gupta, “Efficient continuum model for simulating polymer blends and copolymers,” *J. Chem. Phys.*, vol. 105, no. 23, pp. 10583–10594, 1996.
- [75] M. N. Silberstein, L. D. Cremar, B. A. Beiermann, S. B. Kramer, T. J. Martinez, S. R. White, and N. R. Sottos, “Modeling mechanophore activation within a viscous rubbery network,” *J. Mech. Phys. Solids*, vol. 63, p. 141–153, 2014.
- [76] B. Koo, A. Chattopadhyay, and L. Dai, “Atomistic modeling framework for a cyclobutane-based mechanophore-embedded nanocomposite for damage precursor detection,” *Comput. Mater. Sci.*, vol. 120, pp. 135–141, 2016.
- [77] T. A. Halgren, “Merck molecular force field. i. basis, form, scope, parameterization, and performance of mmff94,” *J. Comput. Chem.*, vol. 17, no. 5-6, pp. 490–519, 1996.
- [78] A. C. Van Duin, S. Dasgupta, F. Lorant, and W. A. Goddard, “Reaxff: a reactive force field for hydrocarbons,” *J. Phys. Chem. A*, vol. 105, no. 41, pp. 9396–9409, 2001.
- [79] R. F. W. Bader, “Atoms in Molecules,” *Acc. Chem. Res.*, vol. 18, pp. 9–15, 1985.

- [80] P. J. Flory, “Thermodynamics of high polymer solutions,” *J. Chem. Phys.*, vol. 10, no. 1, pp. 51–61, 1942.
- [81] P. J. Flory, “Network structure and the elastic properties of vulcanized rubber,” *Chem. Rev.*, vol. 35, no. 1, pp. 51–75, 1944.
- [82] S. N. Zhurkov, “Kinetic concept of the strength of solids,” *Int. J. Fract. Mech.*, vol. 1, pp. 311–323, 1965.
- [83] G. I. Bell, “Models for the specific adhesion of cells to cells: a theoretical framework for adhesion mediated by reversible bonds between cell surface molecules,” *Science*, vol. 200, no. 4342, pp. 618–627, 1978.
- [84] S. S. M. Konda, J. N. Brantley, C. W. Bielawski, and D. E. Makarov, “Chemical reactions modulated by mechanical stress: Extended bell theory,” *J. Chem. Phys.*, vol. 135, p. 164103, 10 2011.
- [85] J. Ribas-Arino and D. Marx, “Covalent mechanochemistry: Theoretical concepts and computational tools with applications to molecular nanomechanics,” *Chem. Rev.*, vol. 112, pp. 5412–5487, 2012.
- [86] Y. Tian and R. Boulatov, “Comparison of the predictive performance of the bell–evans, taylor-expansion and statistical-mechanics models of mechanochemistry,” *Chem. Comm.*, vol. 49, pp. 4187–4189, 4 2013.
- [87] M. E. McFadden and M. J. Robb, “Force-dependent multicolor mechanochromism from a single mechanophore,” *J. Am. Chem. Soc.*, vol. 141, pp. 11388–11392, 7 2019.
- [88] C. M. Degen, P. A. May, J. S. Moore, S. R. White, and N. R. Sottos, “Time-dependent mechanochemical response of SP-cross-linked PMMA,” *Macromolecules*, vol. 46, no. 22, pp. 8917–8921, 2013.

- [89] G. R. Gossweiler, T. B. Kouznetsova, and S. L. Craig, “Force-rate characterization of two spiropyran-based molecular force probes,” *J. Am. Chem. Soc.*, vol. 137, pp. 6148–6151, 2015.
- [90] Y. Lin, M. H. Barbee, C. C. Chang, and S. L. Craig, “Regiochemical effects on mechanophore activation in bulk materials,” *J. Am. Chem. Soc.*, vol. 140, pp. 15969–15975, 2018.
- [91] H. M. Klukovich, T. B. Kouznetsova, Z. S. Kean, J. M. Lenhardt, and S. L. Craig, “A backbone lever-arm effect enhances polymer mechanochemistry,” *Nat. Chem.*, vol. 5, pp. 110–114, 2013.
- [92] T. Ouchi, W. Wang, B. E. Silverstein, J. A. Johnson, and S. L. Craig, “Effect of strand molecular length on mechanochemical transduction in elastomers probed with uniform force sensors,” *Polym. Chem.*, 2023.
- [93] X. Hu, T. Zeng, C. C. Husic, and M. J. Robb, “Mechanically triggered small molecule release from a masked furfuryl carbonate,” *J. Am. Chem. Soc.*, vol. 141, pp. 15018–15023, 2019.
- [94] H. Hu, Z. Ma, and X. Jia, “Reaction cascades in polymer mechanochemistry,” *Mater. Chem. Front.*, 2020.
- [95] R. Stevenson and G. D. Bo, “Controlling reactivity by geometry in retro-dielsalder reactions under tension,” *J. Am. Chem. Soc.*, vol. 139, p. 16768–16771, 2017.
- [96] J. Yang, M. Horst, J. A. Romaniuk, Z. Jin, L. Cegelski, and Y. Xia, “Benzoladderene mechanophores: Synthesis, polymerization, and mechanochemical transformation,” *J. Am. Chem. Soc.*, vol. 141, pp. 6479–6483, 4 2019.

- [97] Y. Pan, H. Zhang, P. Xu, Y. Tian, C. Wang, S. Xiang, R. Boulatov, and W. Weng, “A mechanochemical reaction cascade for controlling load-strengthening of a mechanochromic polymer,” *Angew. Chem.*, vol. 132, pp. 1–7, 2020.
- [98] J. M. Lenhardt, M. T. Ong, R. Choe, C. R. Evenhuis, T. J. Martinez, and S. L. Craig, “Trapping a diradical transition state by mechanochemical polymer extension,” *Science*, vol. 329, pp. 1057–1060, 2010.
- [99] Y. Liu, S. Holm, J. Meisner, Y. Jia, Q. Wu, T. J. Woods, T. J. Martinez, and J. S. Moore, “Flyby reaction trajectories: Chemical dynamics under extrinsic force,” *Science*, vol. 373, pp. 208–212, 2021.
- [100] A. D. Becke, “Correlation energy of an inhomogeneous electron gas: A coordinate-space model,” *J. Chem. Phys.*, vol. 88, pp. 1053–1062, 1988.
- [101] A. D. Becke, “A new mixing of hartree–fock and local density-functional theories,” *J. Chem. Phys.*, vol. 98, no. 2, pp. 1372–1377, 1993.
- [102] C. Lee, W. Yang, and R. G. Parr, “Development of the colic-salvetti correlation-energy formula into a functional of the electron density,” *Phys. Rev. B*, vol. 37, pp. 785–789, 1988.
- [103] T. H. Dunning, “Gaussian basis sets for use in correlated molecular calculations. I. The atoms boron through neon and hydrogen,” *J. Chem. Phys.*, vol. 90, pp. 1007–1023, 1989.
- [104] S. R. Jezowski, L. Zhu, Y. Wang, A. P. Rice, G. W. Scott, C. J. Bardeen, and E. L. Chronister, “Pressure catalyzed bond dissociation in an anthracene cyclophane photodimer,” *J. Am. Chem. Soc.*, vol. 134, no. 17, pp. 7459–7466, 2012.

- [105] R. Fukuda and K. Nakatani, “Quantum chemical study on the high-pressure effect for [4 + 4] retrocycloaddition of anthracene cyclophane photodimer,” *J. Phys. Chem. C*, vol. 123, p. 44934501, 2019.
- [106] T. Stauch, “Quantum chemical modeling of molecules under pressure,” *Int. J. Quantum Chem.*, vol. 121, pp. 1–8, 2020.
- [107] T. Stauch, R. Chakraborty, and M. Head-Gordon, “Quantum chemical modeling of pressure-induced spin crossover in octahedral metal-ligand complexes,” *ChemPhysChem*, vol. 20, p. 2742–2747, 2019.
- [108] T. Stauch, “A mechanochemical model for the simulation of molecules and molecular crystals under hydrostatic pressure,” *J. Chem. Phys.*, vol. 153, p. 134503, 2020.
- [109] R. W. Nunes, J. R. Martin, and J. F. Johnson, “Influence of molecular weight and molecular weight distribution on mechanical properties of polymers,” *Polym. Eng. Sci.*, vol. 22, no. 4, pp. 205–228, 1982.
- [110] A. Van der Wal, J. Mulder, and R. Gaymans, “Fracture of polypropylene: The effect of crystallinity,” *Polymer*, vol. 39, no. 22, pp. 5477–5481, 1998.
- [111] L. E. Nielsen, “Cross-linking–effect on physical properties of polymers,” *J. Macromol. Sci. Part C*, vol. 3, no. 1, pp. 69–103, 1969.
- [112] H.-Y. Lai, H.-Q. Wang, J.-C. Lai, and C.-H. Li, “A self-healing and shape memory polymer that functions at body temperature,” *Molecules*, vol. 24, no. 18, p. 3224, 2019.
- [113] X. Chen and T. D. Nguyen, “Influence of thermoviscoelastic properties and loading conditions on the recovery performance of shape memory polymers,” *Mech. Mater.*, vol. 43, no. 3, pp. 127–138, 2011.

- [114] T. Stauch and A. Dreuw, “Advances in quantum mechanochemistry: Electronic structure methods and force analysis,” *Chem. Rev.*, vol. 116, p. 1413714180, 2016.
- [115] T. Stauch and A. Dreuw, “Quantum Chemical Strain Analysis For Mechanochemical Processes,” *Acc. Chem. Res.*, vol. 50, pp. 1041–1048, 2017.
- [116] T. Stauch and A. Dreuw, “A quantitative quantum-chemical analysis tool for the distribution of mechanical force in molecules,” *J. Chem. Phys.*, vol. 140, p. 134107, 2014.
- [117] T. Stauch and A. Dreuw, “On the use of different coordinate systems in mechanochemical force analyses,” *J. Chem. Phys.*, vol. 143, p. 074118, 2015.
- [118] T. Stauch and A. Dreuw, “Knots "choke off" polymers upon stretching,” *Angew. Chem. Int. Ed.*, vol. 55, pp. 811–814, 2016.
- [119] T. Stauch, Development and Application of Quantum Chemical Methods for the Description of Molecules Under Mechanical Stress. Dissertation, Ruprecht-Karls-University Heidelberg, 2016.
- [120] J. Schwinger, “The theory of quantized fields. I,” *Phys. Rev.*, vol. 82, no. 6, p. 914, 1951.
- [121] W. Kohn and L. J. Sham, “Self-Consistent Equations Including Exchange and Correlation Effects*,” *Phys. Rev.*, vol. 140, pp. 1133–1138, 1965.
- [122] P. Hohenberg and W. Kohn, “Inhomogeneous Electron Gas,” *Phys. Rev.*, vol. 136, pp. 864–871, 1964.
- [123] S. H. Vosko, L. Wilk, and M. Nusair, “Accurate spin-dependent electron liquid correlation energies for local spin density calculations: a critical analysis,” *Can. J. Phys.*, vol. 58, no. 8, pp. 1200–1211, 1980.

- [124] J. P. Perdew and A. Zunger, “Self-interaction correction to density-functional approximations for many-electron systems,” *Phys. Rev. B*, vol. 23, no. 10, p. 5048, 1981.
- [125] J. P. Perdew and Y. Wang, “Accurate and simple analytic representation of the electron-gas correlation energy,” *Phys. Rev. B*, vol. 45, no. 23, p. 13244, 1992.
- [126] J. P. Perdew, J. A. Chevary, S. H. Vosko, K. A. Jackson, M. R. Pederson, D. J. Singh, and C. Fiolhais, “Atoms, molecules, solids, and surfaces: Applications of the generalized gradient approximation for exchange and correlation,” *Phys. Rev. B*, vol. 46, no. 11, p. 6671, 1992.
- [127] J. P. Perdew, K. Burke, and M. Ernzerhof, “Generalized Gradient Approximation Made Simple,” *Phys. Rev. Lett.*, vol. 77, no. 18, pp. 3865–3868, 1996.
- [128] P. M. Gill, B. G. Johnson, J. A. Pople, and M. J. Frisch, “The performance of the becke—lee—yang—parr (b—lyp) density functional theory with various basis sets,” *Chem. Phys. Lett.*, vol. 197, no. 4-5, pp. 499–505, 1992.
- [129] J. P. Perdew, “Density-functional approximation for the correlation energy of the inhomogeneous electron gas,” *Phys. Rev. B*, vol. 33, no. 12, pp. 8822–8824, 1986.
- [130] J. Sun, B. Xiao, and A. Ruzsinszky, “Communication: Effect of the orbital-overlap dependence in the meta generalized gradient approximation,” *J. Chem. Phys.*, vol. 137, no. 5, p. 051101, 2012.
- [131] J. P. Perdew, K. Burke, and M. Ernzerhof, “Generalized Gradient Approximation Made Simple,” *Phys. Rev. Lett.*, vol. 77, pp. 3865–3868, 1996.

- [132] C. Adamo and V. Barone, "Toward reliable density functional methods without adjustable parameters: The PBE0 model," *J. Chem. Phys.*, vol. 110, pp. 6158–6170, 1999.
- [133] A. D. Becke, "Density-functional thermochemistry. V. Systematic optimization of exchange-correlation functionals," *J. Chem. Phys.*, vol. 107, pp. 8554–8560, 1997.
- [134] Y. Shao, M. Head-Gordon, and A. I. Krylov, "The spin-flip approach within time-dependent density functional theory: Theory and applications to diradicals," *J. Chem. Phys.*, vol. 118, no. 11, pp. 4807–4818, 2003.
- [135] W. L. Jorgensen, D. S. Maxwell, and J. Tirado-Rives, "Development and testing of the opls all-atom force field on conformational energetics and properties of organic liquids," *J. Am. Chem. Soc.*, vol. 118, no. 45, pp. 11225–11236, 1996.
- [136] Y. Gao, J. Liu, J. Shen, Y. Wu, and L. Zhang, "Influence of various nanoparticle shapes on the interfacial chain mobility: a molecular dynamics simulation," *Phys. Chem. Chem. Phys.*, vol. 16, no. 39, pp. 21372–21382, 2014.
- [137] W. Ding, S. Lin, J. Lin, and L. Zhang, "Effect of chain conformational change on micelle structures: experimental studies and molecular dynamics simulations," *J. Phys. Chem. B*, vol. 112, no. 3, pp. 776–783, 2008.
- [138] J. Zhao, L. Wu, C. Zhan, Q. Shao, Z. Guo, and L. Zhang, "Overview of polymer nanocomposites: Computer simulation understanding of physical properties," *Polymer*, vol. 133, pp. 272–287, 2017.
- [139] F. Lin, Y. Xiang, and H.-S. Shen, "Temperature dependent mechanical properties of graphene reinforced polymer nanocomposites—a molecular dynamics simulation," *Compos. B. Eng.*, vol. 111, pp. 261–269, 2017.

- [140] M. Laurien, B. Demir, H. Buttemeyer, A. S. Herrmann, T. R. Walsh, and L. C. Ciacchi, “Atomistic modeling of the formation of a thermoset/thermoplastic interphase during co-curing,” *Macromolecules*, vol. 51, no. 11, pp. 3983–3993, 2018.
- [141] M. N. Silberstein, K. Min, L. D. Cremar, C. M. Degen, T. J. Martinez, N. R. Aluru, S. R. White, and N. R. Sottos, “Modeling mechanophore activation within a crosslinked glassy matrix,” *J. Appl. Phys.*, vol. 114, no. 2, p. 023504, 2013.
- [142] M. S. Manivannan and M. N. Silberstein, “Computational investigation of shear driven mechanophore activation at interfaces,” *Extreme Mech. Lett.*, vol. 8, pp. 6–12, 2016.
- [143] W. C. Swope, H. C. Andersen, P. H. Berens, and K. R. Wilson, “A computer simulation method for the calculation of equilibrium constants for the formation of physical clusters of molecules: Application to small water clusters,” *J. Chem. Phys.*, vol. 76, no. 1, pp. 637–649, 1982.
- [144] C. K. Birdsall and A. B. Langdon, *Plasma physics via computer simulation*. CRC press, 2004.
- [145] M. Stratigaki and R. Göstl, “Methods for exerting and sensing force in polymer materials using mechanophores,” *ChemPlusChem*, vol. 85, pp. 1095–1103, 2020.
- [146] W. H. Binder, “The "labile" chemical bond: A perspective on mechanochemistry in polymers,” *Polymer*, vol. 202, p. 122639, 2020.
- [147] E. Izak-Nau, D. Campagna, C. Baumann, and R. Göstl, “Polymer mechanochemistry-enabled pericyclic reactions,” *Polym. Chem*, vol. 11, pp. 2274–2299, 2020.

- [148] G. D. Bo, “Mechanochemistry of the mechanical bond,” *Chem. sci.*, vol. 9, pp. 15–21, 2018.
- [149] S. Schrettl, D. W. Balkenende, C. Calvino, M. Karman, A. Lavrenova, L. N. Neumann, Y. Sagara, E. Verde-Sesto, M. di Giannantonio, Y. C. Simon, K. M. Fromm, M. Lattuada, and C. Weder, “Functional Polymers Through Mechanochemistry,” 2019.
- [150] W. Qiu, P. A. Gurr, G. D. Silva, and G. G. Qiao, “Insights into the mechanochromism of spiropyran elastomers,” *Polym. Chem.*, vol. 10, pp. 1650–1659, 2019.
- [151] T. Kosuge, X. Zhu, V. M. Lau, D. Aoki, T. J. Martinez, J. S. Moore, and H. Otsuka, “Multicolor mechanochromism of a polymer/silica composite with dual distinct mechanophores,” *J. Am. Chem. Soc.*, vol. 141, no. 5, pp. 1898–1902, 2019.
- [152] R. Göstl, J. M. Clough, and R. P. Sijbesma, “Optical Sensing of Stress in Polymers,” in *Mechanochemistry in Materials* (Y. C. Simon and S. L. Craig, eds.), ch. 3, pp. 53–75, The Royal Society of Chemistry, 2018.
- [153] B. H. Bowser and S. L. Craig, “Empowering mechanochemistry with multi-mechanophore polymer architectures,” *Polymer Chem.*, vol. 9, pp. 3583–3593, 2018.
- [154] C. Calvino, A. Guha, C. Weder, and S. Schrettl, “Self-calibrating mechanochromic fluorescent polymers based on encapsulated excimer-forming dyes,” *Adv. Mater.*, vol. 30, p. 1704603, 2018.
- [155] J. M. Clough, A. Balan, T. L. J. Van Daal, and R. P. Sijbesma, “Probing Force with Mechanobase-Induced Chemiluminescence,” *Angew. Chem. Int. Ed.*, vol. 55, pp. 1445–1449, 2016.

- [156] J. Xu and Z. Chi, *Mechanochromic Fluorescent Materials: Phenomena, Materials and Applications*. Royal Society of Chemistry, 2014.
- [157] F. Ciardelli, G. Ruggeri, and A. Pucci, “Dye-containing polymers: methods for preparation of mechanochromic materials,” *Chem. Soc. Rev.*, vol. 42, pp. 857–870, 2013.
- [158] Y. Chen, A. J. Spiering, S. Karthikeyan, G. W. Peters, E. W. Meijer, and R. P. Sijbesma, “Mechanically induced chemiluminescence from polymers incorporating a 1,2-dioxetane unit in the main chain,” *Nat. Chem.*, vol. 4, pp. 559–562, 2012.
- [159] E. Formoso, J. M. Asua, J. M. Matxain, and F. Ruipérez, “The role of non-covalent interactions in the self-healing mechanism of disulfide-based polymers,” *Phys. Chem. Chem. Phys.*, vol. 19, pp. 18461–18470, 2017.
- [160] X. An, R. H. Aguirresarobe, L. Irusta, F. Ruipérez, J. M. Matxain, X. Pan, N. Aramburu, D. Mecerreyes, H. Sardon, and J. Zhu, “Aromatic diselenide crosslinkers to enhance the reprocessability and self-healing of polyurethane thermosets,” *Polymer Chem.*, vol. 8, pp. 3641–3646, 2017.
- [161] J. M. Matxain, J. M. Asua, and F. Ruipérez, “Design of new disulfide-based organic compounds for the improvement of self-healing materials,” *Phys. Chem. Chem. Phys.*, vol. 18, pp. 1758–1770, 2016.
- [162] R. Groote, R. T. M. Jakobs, and R. P. Sijbesma, “Mechanocatalysis: forcing latent catalysts into action,” *Polym. Chem.*, vol. 4, pp. 4846–4859, 2013.
- [163] P. Michael and W. H. Binder, “A mechanochemically triggered “click” catalyst,” *Angew. Chem.*, vol. 127, pp. 14124–14128, 2015.

- [164] A. Piermattei, S. Karthikeyan, and R. P. Sijbesma, "Activating catalysts with mechanical force," *Nat. Chem.*, vol. 1, pp. 133–137, 2009.
- [165] M. B. Larsen and A. J. Boydston, "Flex-activated" mechanophores: Using polymer mechanochemistry to direct bond bending activation," *J. Am. Chem. Soc.*, vol. 135, no. 22, pp. 8189–8192, 2013.
- [166] M. B. Larsen and A. J. Boydston, "Successive Mechanochemical Activation and Small Molecule Release in an Elastomeric Material," *J. Am. Chem. Soc.*, vol. 136, pp. 1276–1279, 2014.
- [167] H. J. Kulik, "Modeling Mechanochemistry from First Principles," in *Reviews in Computational Chemistry, Vol. 31* (A. L. Parrill and K. B. Lipkowitz, eds.), ch. 6, pp. 265–311, John Wiley & Sons Ltd, 1 ed., 2019.
- [168] G. S. Kochhar, G. S. Heverly-Coulson, and N. J. Mosey, "Theoretical Approaches for Understanding the Interplay Between Stress and Chemical Reactivity," *Top. Curr. Chem.*, vol. 369, pp. 37–96, 2015.
- [169] T. Stauch and A. Dreuw, "Force-induced retro-click reaction of triazoles competes with adjacent single-bond rupture†," *Chem. Sci.*, vol. 8, p. 5567–5575, 2017.
- [170] M. Krupička, P. Dopieralski, and D. Marx, "Unclicking the Click: Metal-Assisted Mechanochemical Cycloreversion of Triazoles is Possible," *Angew. Chem. Int. Ed.*, vol. 56, pp. 7745–7749, 2017.
- [171] M. J. Jacobs, G. Schneider, and K. G. Blank, "Mechanical reversibility of strain-promoted azide–alkyne cycloaddition reactions.," *Angew. Chem. Int. Ed.*, vol. 55, p. 2899–2902, 2016.

- [172] T. Stauch, “Mechanical switching of aromaticity and homoaromaticity in molecular optical force sensors for polymers,” *Chem. Eur. J.*, vol. 24, p. 7340–7344, 2018.
- [173] T. Stauch, M. T. Hoffmann, and A. Dreuw, “Spectroscopic Monitoring of Mechanical Forces during Protein Folding by using Molecular Force Probes,” *ChemPhysChem*, vol. 17, pp. 1486–1492, 2016.
- [174] D. Rivero, M. Á. Fernández-González, and L. M. Frutos, “Tuning molecular excitation energy with external forces,” *Comput. Theor. Chem.*, vol. 1040-1041, pp. 106–111, 2014.
- [175] C. E. Colwell, T. W. Price, T. Stauch, and R. Jasti, “Strain visualization for strained macrocycles,” *Chem. Sci.*, vol. 11, pp. 3923–3930, 2020.
- [176] M. Zhang and G. De Bo, “Mechanical Susceptibility of a Rotaxane,” *J. Am. Chem. Soc.*, vol. 141, pp. 15879–15883, 2019.
- [177] M. T. Ong, J. Leiding, H. Tao, A. M. Virshup, and T. J. Martínez, “First Principles Dynamics and Minimum Energy Pathways for Mechanochemical Ring Opening of Cyclobutene,” *J. Am Chem. Soc.*, vol. 131, pp. 6377–6379, 2009.
- [178] K. Wolinski and J. Baker, “Theoretical predictions of enforced structural changes in molecules,” *Mol. Phys.*, vol. 107, no. 22, pp. 2403–2417, 2009.
- [179] E. A. Nikitina, V. D. Khavryutchenko, E. F. Sheka, H. Barthel, and J. Weis, “Deformation of Poly(dimethylsiloxane) Oligomers under Uniaxial Tension: Quantum Chemical View,” *J. Phys. Chem. A*, vol. 103, pp. 11355–11365, 1999.

- [180] T. Stauch and A. Dreuw, “A quantitative quantum-chemical analysis tool for the distribution of mechanical force in molecules,” *J. Chem. Phys.*, vol. 140, p. 134107, 2014.
- [181] G. Subramanian, N. Mathew, and J. Leiding, “A generalized force-modified potential energy surface for mechanochemical simulations,” *J. Chem. Phys.*, vol. 143, 2015.
- [182] Y. Shao, Z. Gan, E. Epifanovsky, A. T. Gilbert, M. Wormit, J. Kussmann, A. W. Lange, A. Behn, J. Deng, X. Feng, D. Ghosh, M. Goldey, P. R. Horn, L. D. Jacobson, I. Kaliman, R. Z. Khaliullin, T. Kus, A. Landau, J. Liu, E. I. Proynov, Y. M. Rhee, R. M. Richard, M. A. Rohrdanz, R. P. Steele, E. J. Sundstrom, H. L. Woodcock, P. M. Zimmerman, D. Zuev, B. Albrecht, E. Alguire, B. Austin, G. J. Beran, Y. A. Bernard, E. Berquist, K. Brandhorst, K. B. Bravaya, S. T. Brown, D. Casanova, C. M. Chang, Y. Chen, S. H. Chien, K. D. Closser, D. L. Crittenden, M. Diedenhofen, R. A. Distasio, H. Do, A. D. Dutoi, R. G. Edgar, S. Fatehi, L. Fusti-Molnar, A. Ghysels, A. Golubeva-Zadorozhnaya, J. Gomes, M. W. Hanson-Heine, P. H. Harbach, A. W. Hauser, E. G. Hohenstein, Z. C. Holden, T. C. Jagau, H. Ji, B. Kaduk, K. Khistyayev, J. Kim, J. Kim, R. A. King, P. Klunzinger, D. Kosenkov, T. Kowalczyk, C. M. Krauter, K. U. Lao, A. D. Laurent, K. V. Lawler, S. V. Levchenko, C. Y. Lin, F. Liu, E. Livshits, R. C. Lochan, A. Luenser, P. Manohar, S. F. Manzer, S. P. Mao, N. Mardirossian, A. V. Marenich, S. A. Maurer, N. J. Mayhall, E. Neuscamman, C. M. Oana, R. Olivares-Amaya, D. P. O'Neill, J. A. Parkhill, T. M. Perrine, R. Peverati, A. Prociuk, D. R. Rehn, E. Rosta, N. J. Russ, S. M. Sharada, S. Sharma, D. W. Small, A. Sodt, T. Stein, D. Stück, Y. C. Su, A. J. Thom, T. Tsuchimochi, V. Vanovschi, L. Vogt, O. Vydrov, T. Wang, M. A. Watson, J. Wenzel, A. White, C. F. Williams, J. Yang, S. Yeganeh,

- S. R. Yost, Z. Q. You, I. Y. Zhang, X. Zhang, Y. Zhao, B. R. Brooks, G. K. Chan, D. M. Chipman, C. J. Cramer, W. A. Goddard, M. S. Gordon, W. J. Hehre, A. Klamt, H. F. Schaefer, M. W. Schmidt, C. D. Sherrill, D. G. Truhlar, A. Warshel, X. Xu, A. Aspuru-Guzik, R. Baer, A. T. Bell, N. A. Besley, J. D. Chai, A. Dreuw, B. D. Dunietz, T. R. Furlani, S. R. Gwaltney, C. P. Hsu, Y. Jung, J. Kong, D. S. Lambrecht, W. Liang, C. Ochsenfeld, V. A. Rassolov, L. V. Slipchenko, J. E. Subotnik, T. V. Voorhis, J. M. Herbert, A. I. Krylov, P. M. Gill, and M. Head-Gordon, "Advances in molecular quantum chemistry contained in the q-chem 4 program package," *Mol. Phys.*, vol. 113, pp. 184–215, 2014.
- [183] W. Humphrey, A. Dalke, and K. Schulten, "VMD: Visual Molecular Dynamics," *J. Mol. Graphics*, vol. 14, pp. 33–38, 1996.
- [184] T. Lu and F. Chen, "Multiwfn: A Multifunctional Wavefunction Analyzer," *J. Comput. Chem.*, vol. 33, pp. 580–592, 2012.
- [185] A. D. Becke, "Density-functional exchange-energy approximation with correct asymptotic behavior," *Phys. Rev. A*, vol. 38, pp. 3098–3100, Sep 1988.
- [186] S. Garcia-Manyes and A. E. M. Beedle, "Steering chemical reactions with force," *Nature Rev. Chem.*, vol. 1, p. 0083, 2017.
- [187] P. Cintas, G. Cravotto, A. Barge, and K. Martina, "Interplay Between Mechanochemistry and Sonochemistry," *Top. Curr. Chem.*, vol. 369, pp. 239–284, 2015.
- [188] H. M. Klukovich, Z. S. Kean, A. L. B. Ramirez, J. M. Lenhardt, J. Lin, X. Hu, and S. L. Craig, "Tension trapping of carbonyl ylides facilitated by a change in polymer backbone," *J. Am. Chem. Soc.*, vol. 134, p. 9577–9580, 2012.

- [189] J. Ribas-Arino, M. Shiga, and D. Marx, “Mechanochemical transduction of externally applied forces to mechanophores,” *J. Am. Chem. Soc.*, vol. 132, p. 10609–10614, 2010.
- [190] P. Dopieralski, P. Anjukandi, M. Rückert, M. Shiga, J. Ribas-Arino, and D. Marx, “On the role of polymer chains in transducing external mechanical forces to benzocyclobutene mechanophores,” *J. Mater. Chem.*, vol. 21, no. 23, pp. 8309–8316, 2011.
- [191] Y. Tian, X. Cao, X. Li, H. Zhang, C.-L. Sun, Y. Xu, W. Weng, W. Zhang, and R. Boulatov, “A polymer with mechanochemically active hidden length,” *J. Am. Chem. Soc.*, vol. 142, no. 43, pp. 18687–18697, 2020.
- [192] S. K. Jha, K. Brown, G. Todde, and G. Subramanian, “A mechanochemical study of the effects of compression on a diels-alder reaction,” *J. Chem. Phys.*, vol. 145, no. 7, p. 074307, 2016.
- [193] R. Cammi, V. Verdolino, B. Mennucci, and J. Tomasi, “Towards the elaboration of a QM method to describe molecular solutes under the effect of a very high pressure,” *Chem. Phys.*, vol. 344, no. 1-2, pp. 135–141, 2008.
- [194] R. Cammi, “A new extension of the polarizable continuum model: Toward a quantum chemical description of chemical reactions at extreme high pressure,” *J. Comput. Chem.*, vol. 36, no. 30, pp. 2246–2259, 2015.
- [195] B. Chen, R. Hoffmann, and R. Cammi, “The effect of pressure on organic reactions in fluids—a new theoretical perspective,” *Angew. Chem. Int. Ed.*, vol. 56, no. 37, pp. 11126–11142, 2017.
- [196] T. Stauch, “A mechanochemical model for the simulation of molecules and molecular crystals under hydrostatic pressure,” *J. Chem. Phys.*, vol. 153, no. 13, p. 134503, 2020.

- [197] M. Scheurer, A. Dreuw, E. Epifanovsky, M. Head-Gordon, and T. Stauch, “Modeling Molecules under Pressure with Gaussian Potentials,” *J. Chem. Theory Comput.*, vol. 17, pp. 583–597, 2021.
- [198] K. Nagura, S. Saito, H. Yusa, H. Yamawaki, H. Fujihisa, H. Sato, Y. Shimoikeda, and S. Yamaguchi, “Distinct responses to mechanical grinding and hydrostatic pressure in luminescent chromism of tetrathiazolylthiophene,” *J. Am. Chem. Soc.*, vol. 135, pp. 10322–10325, 2013.
- [199] H. Yan, F. Yang, D. Pan, Y. Lin, J. N. Hohman, D. Solis-Ibarra, F. H. Li, J. E. P. Dahl, R. M. K. Carlson, B. A. Tkachenko, A. A. Fokin, P. R. Schreiner, G. Galli, and W. L. Mao, “Sterically controlled mechanochemistry under hydrostatic pressure,” *Nature*, vol. 554, pp. 505–510, 2018.
- [200] F. G. Klärner, V. Ruster, B. Zimny, and D. Hochstrate, “The effect of pressure on pericyclic reactions,” *High Press. Res.*, vol. 7, pp. 133–135, 1991.
- [201] R. V. Eldik, T. Asano, and W. J. L. Noble, “Activation and reaction volumes in solution. 2,” *Chem. Rev.*, vol. 89, pp. 549–688, 1989.
- [202] S. L. James, C. J. Adams, C. Bolm, D. Braga, P. Collier, T. Friščić, F. Grepioni, K. D. Harris, G. Hyett, W. Jones, A. Krebs, J. Mack, L. Maini, A. G. Orpen, I. P. Parkin, W. C. Shearouse, J. W. Steed, and D. C. Waddell, “Mechanochemistry: opportunities for new and cleaner synthesis,” *Chem. Soc. Rev.*, vol. 41, pp. 413–447, 2012.
- [203] K. J. Ardila-Fierro and J. G. Hernández, “Sustainability assessment of mechanochemistry by using the twelve principles of green chemistry,” *ChemSusChem*, vol. 14, pp. 2145–2162, 2021.
- [204] G. De Bo, “Polymer Mechanochemistry and the Emergence of the Mechanophore Concept,” *Macromolecules*, vol. 53, pp. 7615–7617, 2020.

- [205] C. E. Diesendruck, “Mechanophores for Chemical Function,” in *Mechanochemistry in Materials* (Y. C. Simon and S. L. Craig, eds.), ch. 2, pp. 36–52, The Royal Society of Chemistry, 2018.
- [206] H. Traeger, D. J. Kiebala, C. Weder, and S. Schrettl, “From Molecules to Polymers - Harnessing Inter- and Intramolecular Interactions to Create Mechanochromic Materials,” *Macromol. Rapid Commun.*, vol. 42, p. 2000573, 2021.
- [207] Z. Chen, X. Zhu, J. Yang, J. A. Mercer, N. Z. Burns, T. J. Martinez, and Y. Xia, “The cascade unzipping of ladderane reveals dynamic effects in mechanochemistry,” *Nat. Chem.*, vol. 12, pp. 302–309, 2020.
- [208] L. J. Mier, G. Adam, S. Kumar, and T. Stauch, “The Mechanism of Flex-Activation in Mechanophores Revealed By Quantum Chemistry,” *ChemPhysChem*, vol. 21, pp. 2402–2406, 2020.
- [209] M. B. Larsen and A. J. Boydston, “"Flex-activated" mechanophores: Using polymer mechanochemistry to direct bond bending activation,” *J. Am. Chem. Soc.*, vol. 135, no. 22, pp. 8189–8192, 2013.
- [210] M. Ghani, A. Heiskanen, J. Kajtez, B. Rezaei, N. B. Larsen, P. Thomsen, A. Kristensen, A. Žukauskas, M. Alm, and J. Emnéus, “On-demand reversible uv-triggered interpenetrating polymer network-based drug delivery system using the spiropyran-merocyanine hydrophobicity switch,” *ACS Appl. Mater. Interfaces*, vol. 13, pp. 3591–3604, 2021.
- [211] T. Yamaguchi, K. J. Imwiset, and M. Ogawa, “Efficient negative photochromism by the photoinduced migration of photochromic merocyanine/spiropyran in the solid state,” *Langmuir*, vol. 37, pp. 3702–3708, 2021.

- [212] Z. Cao, “Highly stretchable tough elastomers crosslinked by spiropyran mechanophores for strain-induced colorimetric sensing,” *Macromol. Chem. Phys.*, vol. 221, pp. 1–7, 2020.
- [213] M. Li, L. Lei, Q. Zhang, and S. Zhu, “CO₂-breathing induced reversible activation of mechanophore within microgels,” *Macromol. Rapid Commun.*, vol. 37, pp. 957–962, 2016.
- [214] J. D. Steen, D. R. Duijnste, A. S. Sardjan, J. Martinelli, L. Kortekaas, D. Jacquemin, and W. R. Browne, “Electrochemical ring-opening and -closing of a spiropyran,” *J. Phys. Chem. A*, vol. 125, pp. 3355–3361, 2021.
- [215] A. D. Becke, “A new mixing of hartree-fock and local density-functional theories,” *J. Chem. Phys.*, vol. 98, pp. 1372–1377, 1993.
- [216] W. J. Hehre, R. Ditchfield, and J. A. Pople, “Self — consistent molecular orbital methods . xii . further extensions of gaussian — type basis sets for use in molecular orbital studies of organic molecules,” *J. Chem. Phys.*, vol. 56, pp. 2257–2261, 1972.
- [217] E. Epifanovsky, A. T. B. Gilbert, X. Feng, J. Lee, Y. Mao, N. Mardirossian, P. Pokhilko, A. F. White, M. P. Coons, A. L. Dempwolff, Z. Gan, D. Hait, P. R. Horn, L. D. Jacobson, I. Kaliman, J. Kussmann, A. W. Lange, K. U. Lao, D. S. Levine, J. Liu, S. C. McKenzie, A. F. Morrison, K. D. Nanda, F. Plasser, D. R. Rehn, M. L. Vidal, Z.-Q. You, Y. Zhu, B. Alam, B. J. Albrecht, A. Aldossary, E. Alguire, J. H. Andersen, V. Athavale, D. Barton, K. Begam, A. Behn, N. Bellonzi, Y. A. Bernard, E. J. Berquist, H. G. A. Burton, A. Carreras, K. Carter-Fenk, R. Chakraborty, A. D. Chien, K. D. Closser, V. Cofer-Shabica, S. Dasgupta, M. de Wergifosse, J. Deng, M. Diedenhofen, H. Do, S. Ehlert, P.-T. Fang, S. Fatehi, Q. Feng, T. Friedhoff, J. Gayvert, Q. Ge, G. Gid-

ofalvi, M. Goldey, J. Gomes, C. E. González-Espinoza, S. Gulania, A. O. Gunina, M. W. D. Hanson-Heine, P. H. P. Harbach, A. Hauser, M. F. Herbst, M. Hernández Vera, M. Hodecker, Z. C. Holden, S. Houck, X. Huang, K. Hui, B. C. Huynh, M. Ivanov, Á. Jász, H. Ji, H. Jiang, B. Kaduk, S. Kähler, K. Khistyayev, J. Kim, G. Kis, P. Klunzinger, Z. Koczor-Benda, J. H. Koh, D. Kosenkov, L. Koulias, T. Kowalczyk, C. M. Krauter, K. Kue, A. Kunitsa, T. Kus, I. Ladjászki, A. Landau, K. V. Lawler, D. Lefrancois, S. Lehtola, R. R. Li, Y.-P. Li, J. Liang, M. Liebenthal, H.-H. Lin, Y.-S. Lin, F. Liu, K.-Y. Liu, M. Loipersberger, A. Luenser, A. Manjanath, P. Manohar, E. Mansoor, S. F. Manzer, S.-P. Mao, A. V. Marenich, T. Markovich, S. Mason, S. A. Maurer, P. F. McLaughlin, M. F. S. J. Menger, J.-M. Mewes, S. A. Mewes, P. Morgante, J. W. Mullinax, K. J. Oosterbaan, G. Paran, A. C. Paul, S. K. Paul, F. Pavošević, Z. Pei, S. Prager, E. I. Proynov, Á. Rák, E. Ramos-Cordoba, B. Rana, A. E. Rask, A. Rettig, R. M. Richard, F. Rob, E. Rossomme, T. Scheele, M. Scheurer, M. Schneider, N. Sergueev, S. M. Sharada, W. Skomorowski, D. W. Small, C. J. Stein, Y.-C. Su, E. J. Sundstrom, Z. Tao, J. Thirman, G. J. Tornai, T. Tsuchimochi, N. M. Tubman, S. P. Veccham, O. Vydrov, J. Wenzel, J. Witte, A. Yamada, K. Yao, S. Yeganeh, S. R. Yost, A. Zech, I. Y. Zhang, X. Zhang, Y. Zhang, D. Zuev, A. Aspuru-Guzik, A. T. Bell, N. A. Besley, K. B. Bravaya, B. R. Brooks, D. Casanova, J.-D. Chai, S. Coriani, C. J. Cramer, G. Cserey, A. E. DePrince, R. A. DiStasio, A. Dreuw, B. D. Dunietz, T. R. Furlani, W. A. Goddard, S. Hammes-Schiffer, T. Head-Gordon, W. J. Hehre, C.-P. Hsu, T.-C. Jagau, Y. Jung, A. Klamt, J. Kong, D. S. Lambrecht, W. Liang, N. J. Mayhall, C. W. McCurdy, J. B. Neaton, C. Ochsenfeld, J. A. Parkhill, R. Peverati, V. A. Rassolov, Y. Shao, L. V. Slipchenko, T. Stauch, R. P. Steele, J. E. Subotnik, A. J. W. Thom, A. Tkatchenko, D. G. Truhlar, T. Van Voorhis, T. A. Wesolowski, K. B. Whaley, H. L. Woodcock, P. M.

- Zimmerman, S. Faraji, P. M. W. Gill, M. Head-Gordon, J. M. Herbert, and A. I. Krylov, “Software for the frontiers of quantum chemistry: An overview of developments in the Q-Chem 5 package,” *J. Chem. Phys.*, vol. 155, p. 084801, 2021.
- [218] X. Meng, G. Qi, C. Zhang, K. Wang, B. Zou, and Y. Ma, “Visible mechanochromic responses of spiropyrans in crystals via pressure-induced isomerization,” *Chem. Commun.*, vol. 51, pp. 9320–9323, 2015.
- [219] S. Kumar and T. Stauch, “Trapping the Transition State in a [2, 3]-Sigmatropic Rearrangement by Applying Pressure,” *ChemRxiv*, pp. DOI: 10.33774/chemrxiv-2021-7d2r7.
- [220] B. Chen, R. Hoffmann, and R. Cammi, “The effect of pressure on organic reactions in fluids—a new theoretical perspective,” *Angew. Chem. Int. Ed.*, vol. 56, pp. 11126–11142, 2017.
- [221] R. Bauernschmitt and R. Ahlrichs, “Treatment of electronic excitations within the adiabatic approximation of time dependent density functional theory,” *Chem. Phys. Lett.*, vol. 256, pp. 454–464, 1996.
- [222] M. Reggelin, “[2, 3]-sigmatropic rearrangements of allylic sulfur compounds,” *Sulfur-Mediated Rearrangements II*, pp. 1–65, 2007.
- [223] F. Tang, Y. Yao, Y. Xu, and C. Lu, “Diastereoselective aza-mislow–evans rearrangement of N-acyl tert-butanefulfonamides into α -sulfenyloxy carboxamides,” *Angew. Chem.*, vol. 130, no. 47, pp. 15809–15812, 2018.
- [224] I. Colomer, M. Velado, R. Ferna, D. Pradilla, and A. Viso, “From allylic sulfoxides to allylic sulfenates : Fifty years of a never- ending [2 , 3] -sigmatropic rearrangement,” *Chem. Rev.*, vol. 117, pp. 14201–14243, 2017.

- [225] D. R. Rayner, E. G. Miller, P. Bickart, A. J. Gordon, and K. Mislow, "Mechanisms of thermal racemization of sulfoxides," *J. Am. Chem. Soc.*, vol. 88, pp. 3138–3139, 1966.
- [226] E. G. Miller, D. R. Rayner, and K. Mislow, "Thermal rearrangement of sulfenates to sulfoxides¹," *J. Am. Chem. Soc.*, vol. 88, pp. 3139–3140, 1966.
- [227] P. Bickart, F. W. Carson, J. Jacobus, E. G. Miller, and K. Mislow, "The thermal racemization of allylic sulfoxides and the interconversion of allylic sulfoxides and sulfenates. mechanism and stereochemistry^{1,2}," *J. Am. Chem. Soc.*, vol. 90, pp. 4869–4876, 5 1968.
- [228] D. A. Evans, G. C. Andrews, and C. L. Sims, "Reversible 1,3 transposition of sulfoxide and alcohol functions. potential synthetic utility," *J. Am. Chem. Soc.*, vol. 93, pp. 4956–4957, 1971.
- [229] D. A. Evans and G. C. Andrews, "Nucleophilic cleavage of allylic sulfenate esters. mechanistic observations," *J. Am. Chem. Soc.*, vol. 94, pp. 3672–3674, 1972.
- [230] D. A. Evans, G. Andrews, T. T. Fujimoto, and D. Wells, "Stereoselective synthesis of trisubstituted olefins," *Tetrahedron Lett.*, vol. 16, pp. 1389–1392, 1973.
- [231] D. A. Evans, G. C. Andrews, T. T. Fujimoto, and D. Wells, "The application of allylic sulfoxide anions as vinyl anion equivalents. a general synthesis of allylic alcohols.," *Tetrahedron Lett.*, vol. 16, pp. 1385–1388, 1973.
- [232] R. Tang and K. Mislow, "Rates and equilibria in the interconversion of allylic sulfoxides and sulfenates¹," *J. Am. Chem. Soc.*, vol. 92, pp. 2100–2104, 1970.

- [233] Y. Masaki, K. Hashirnoto, K. Sakuma, and K. Kaji, "Facile regio- and stereo-specific allylic oxidation of gem-dimethyl olefins via addition of benzenesulphenyl chloride. synthesis of allylic oxygenated terpenes," *J. Chem. Soc., Perkin trans.*, vol. 1, pp. 1289–1295, 1984.
- [234] H. Iio, M. Isobe, T. Kawai, and T. Goto, "Total synthesis of vernolepin. 2.1 stereocontrolled synthesis of (\pm)-vernolepin," *J. Am Chem. Soc.*, vol. 101, pp. 6076–6081, 1979.
- [235] F. Zutterman, H. D. Wilde, R. Mungheer, P. D. Clercq, and M. Vandewalle, "A total synthesis of (\pm)-vernolepin," *Tetrahedron*, vol. 35, pp. 2389–2396, 1979.
- [236] J. de Vicente, J. R. Huckins, and S. D. Rychnovsky, "Synthesis of the c31–c67 fragment of amphidinol 3," *Angew. Chem.*, vol. 118, pp. 7416–7420, 2006.
- [237] K. M. Engstrom, M. R. Mendoza, M. Navarro-villalobos, and D. Y. Gin, "Total synthesis of (+) -pyrenolide d **," *Angew. Chem. Int. Ed.*, vol. 40, pp. 1128–1130, 2001.
- [238] R. W. Hoffmann, "Stereochemistry of [2,3]sigmatropic rearrangements," *Angew. Chem. Int. Ed. Engl.*, vol. 18, pp. 563–640, 1979.
- [239] D. K. Jones-hertzog and W. L. Jorgensen, "Elucidation of transition structures and solvent effects for the mislow — evans rearrangement of allylic sulfoxides," *J. Am Chem. Soc.*, pp. 9077–9078, 1995.
- [240] F. Freeman, R. M. Bathala, J. E. Cavillo, A. C. Huang, T. K. Jackson, A. Z. Lopez-Mercado, S. Phung, J. Suh, and J. D. O. Valencia, "[2,3]-sigmatropic rearrangements of hydrogen and alkyl 3-propenyl sulfoxides: A computational study," *Int. J. Quantum Chem.*, vol. 106, pp. 2390–2397, 2006.

- [241] B. Li, C. Ji, W. Yang, J. Wang, K. Yang, R. Xu, W. Liu, Z. Cai, J. Chen, and H. kwang Mao, “Diamond anvil cell behavior up to 4 mbar,” *Proc. Natl. Acad. Sci.*, vol. 115, pp. 1713–1717, 2018.
- [242] H. Takaya, Y. Taniguchi, P. Wong, and E. Whalley, “Effect of pressure on molecular conformations. iii. internal rotation angle in gauche-1, 2-dichloroethane and gauche-1, 2-dibromoethane,” *J. Chem. Phys.*, vol. 75, no. 10, pp. 4823–4828, 1981.
- [243] I. Mayer, “Charge, bond order and valence in the ab initio SCF theory,” *Chem. Phys. Lett.*, vol. 97, no. 3, pp. 270–274, 1983.
- [244] I. Mayer, “On Bond Orders and Valences in the Ab initio Quantum Chemical Theory,” *Int. J. Quantum Chem.*, vol. 29, no. 1, pp. 73–84, 1986.
- [245] S. Kumar and T. Stauch, “The activation efficiency of mechanophores can be modulated by adjacent polymer composition,” *RSC Adv.*, vol. 11, no. 13, pp. 7391–7396, 2021.
- [246] N. Mardirossian and M. Head-Gordon, “Mapping the genome of meta-generalized gradient approximation density functionals: The search for b97m-v,” *J. Chem. Phys.*, vol. 142, no. 7, p. 074111, 2015.
- [247] C. Lee, W. Yang, and R. G. Parr, “Development of the colle-salvetti correlation-energy formula into a functional of the electron density,” *Phys. Rev. B*, vol. 37, pp. 785–789, Jan 1988.
- [248] Y. Zhao and D. G. Truhlar, “A new local density functional for main-group thermochemistry, transition metal bonding, thermochemical kinetics, and noncovalent interactions,” *J. Chem. Phys.*, vol. 125, no. 19, p. 194101, 2006.

- [249] V. N. Staroverov, G. E. Scuseria, J. Tao, and J. P. Perdew, “Comparative assessment of a new nonempirical density functional: Molecules and hydrogen-bonded complexes,” *J. Chem. Phys.*, vol. 119, no. 23, pp. 12129–12137, 2003.
- [250] J.-D. Chai and M. Head-Gordon, “Long-range corrected hybrid density functionals with damped atom–atom dispersion corrections,” *Phys. Chem. Chem. Phys.*, vol. 10, no. 44, pp. 6615–6620, 2008.
- [251] J. P. Perdew, K. Burke, and M. Ernzerhof, “Generalized gradient approximation made simple,” *Phys. Rev. Lett.*, vol. 77, pp. 3865–3868, Oct 1996.
- [252] C. Adamo and V. Barone, “Toward reliable density functional methods without adjustable parameters: The pbe0 model,” *J. Phys. Chem.*, vol. 110, no. 13, pp. 6158–6170, 1999.
- [253] T. H. Dunning Jr, “Gaussian basis sets for use in correlated molecular calculations. i. the atoms boron through neon and hydrogen,” *J. Chem. Phys.*, vol. 90, no. 2, pp. 1007–1023, 1989.
- [254] S. L. Potisek, D. A. Davis, N. R. Sottos, S. R. White, and J. S. Moore, “Mechanophore-linked addition polymers,” *J. Am. Chem. Soc.*, vol. 129, pp. 13808–13809, 2007.
- [255] J. N. Brantley, K. M. Wiggins, and C. W. Bielawski, “Polymer mechanochemistry: the design and study of mechanophores,” *Polym. Int.*, vol. 62, no. 1, pp. 2–12, 2013.
- [256] N. Deneke, M. L. Rencheck, and C. S. Davis, “An engineer’s introduction to mechanophores,” *Soft Matter*, vol. 16, pp. 6230–6252, 2020.

- [257] M. K. Beyer and H. Clausen-Schaumann, “Mechanochemistry: the mechanical activation of covalent bonds,” *Chem. Rev.*, vol. 105, no. 8, pp. 2921–2948, 2005.
- [258] J. Li, C. Nagamani, and J. S. Moore, “Polymer mechanochemistry: from destructive to productive,” *Acc. Chem. Res.*, vol. 48, no. 8, pp. 2181–2190, 2015.
- [259] E. Izak-Nau, D. Campagna, C. Baumann, and R. Göstl, “Polymer mechanochemistry-enabled pericyclic reactions,” *Polym. Chem.*, vol. 11, no. 13, pp. 2274–2299, 2020.
- [260] N. Willis-Fox, E. Watchorn-Rokutan, E. Rognin, and R. Daly, “Technology pull: scale-up of polymeric mechanochemical force sensors,” *Trends Chem.*, 2023.
- [261] D. A. Davis, A. Hamilton, J. Yang, L. D. Cremar, D. Van Gough, S. L. Potisek, M. T. Ong, P. V. Braun, T. J. Martínez, S. R. White, *et al.*, “Force-induced activation of covalent bonds in mechanoresponsive polymeric materials,” *Nature*, vol. 459, no. 7243, pp. 68–72, 2009.
- [262] M. L. Rencheck, B. T. Mackey, Y.-Y. Hu, C.-C. Chang, M. D. Sangid, and C. S. Davis, “Identifying internal stresses during mechanophore activation,” *Adv. Eng. Mater.*, vol. 24, no. 4, p. 2101080, 2022.
- [263] H. Hu, X. Cheng, Z. Ma, R. P. Sijbesma, and Z. Ma, “Polymer mechanochromism from force-tuned excited-state intramolecular proton transfer,” *J. Am. Chem. Soc.*, vol. 144, no. 22, pp. 9971–9979, 2022.
- [264] T. Watabe and H. Otsuka, “Swelling-induced mechanochromism in multinet-work polymers,” *Angew. Chem.*, vol. 135, no. 9, p. e202216469, 2023.

- [265] M. A. Ghanem, A. Basu, R. Behrou, N. Boechler, A. J. Boydston, S. L. Craig, Y. Lin, B. E. Lynde, A. Nelson, H. Shen, and D. W. Storti, “The role of polymer mechanochemistry in responsive materials and additive manufacturing,” *Nat. Rev. Mater.*, vol. 6, pp. 84–98, 2021.
- [266] M. F. Pillay, K. Holz, N. Preußke, Florian Berger, Hauke Clausen-Schaumann, U. Lining, and M. K. Beyer, “Mechanochemical cycloreversion of cyclobutane observed at the single molecule level,” *Chem. Eur. J.*, vol. 22, p. 12034 – 12039, 2016.
- [267] H. Shen, M. B. Larsen, A. G. Roessler, P. M. Zimmerman, and A. J. Boydston, “Mechanochemical release of n-heterocyclic carbenes from flex-activated mechanophores,” *Angew. Chem.*, vol. 133, no. 24, pp. 13671–13675, 2021.
- [268] P. A. May and J. S. Moore, “Polymer mechanochemistry: techniques to generate molecular force via elongational flows,” *Chem. Soc. Rev.*, vol. 42, no. 18, pp. 7497–7506, 2013.
- [269] S. Akbulatov and R. Boulatov, “Experimental polymer mechanochemistry and its interpretational frameworks,” *ChemPhysChem*, vol. 18, p. 1422–1450, 2017.
- [270] C. Baumann, N. Willis-Fox, D. Campagna, E. Rognin, P. Marten, R. Daly, and R. Göstl, “Regiochemical effects for the mechanochemical activation of 9- π -extended anthracene-maleimide diels–alder adducts,” *J. Polym. Sci.*, vol. 60, no. 22, pp. 3128–3133, 2022.
- [271] S. J. Bailey, C. W. Barney, N. J. Sinha, S. V. Pangali, C. J. Hawker, M. E. Helgeson, M. T. Valentine, and J. R. de Alaniz, “Rational mechanochemical design of diels–alder crosslinked biocompatible hydrogels with enhanced properties,” *Mater. Horiz.*, vol. 9, no. 7, pp. 1947–1953, 2022.

- [272] R. Stevenson and G. De Bo, “Controlling reactivity by geometry in retro-diels–alder reactions under tension,” *J. Am. Chem. Soc.*, vol. 139, no. 46, pp. 16768–16771, 2017.
- [273] J. M. Lenhardt, M. T. Ong, R. Choe, C. R. Evenhuis, T. J. Martinez, and S. L. Craig, “Trapping a diradical transition state by mechanochemical polymer extension,” *Science*, vol. 329, no. 5995, pp. 1057–1060, 2010.
- [274] Q. Wang, G. R. Gossweiler, S. L. Craig, and X. Zhao, “Mechanics of mechanochemically responsive elastomers,” *J. Mech. Phys. Solids*, vol. 82, pp. 320–344, 2015.
- [275] L. S. Dodda, I. Cabeza de Vaca, J. Tirado-Rives, and W. L. Jorgensen, “Ligpargen web server: an automatic opls-aa parameter generator for organic ligands,” *Nucleic Acids Res.*, vol. 45, no. W1, pp. W331–W336, 2017.
- [276] A. P. Thompson, H. M. Aktulga, R. Berger, D. S. Bolintineanu, W. M. Brown, P. S. Crozier, P. J. in ’t Veld, A. Kohlmeyer, S. G. Moore, T. D. Nguyen, R. Shan, M. J. Stevens, J. Tranchida, C. Trott, and S. J. Plimpton, “LAMMPS - a flexible simulation tool for particle-based materials modeling at the atomic, meso, and continuum scales,” *Comp. Phys. Comm.*, vol. 271, p. 108171, 2022.
- [277] Y. K. Choi, S.-J. Park, S. Park, S. Kim, N. R. Kern, J. Lee, and W. Im, “Charmm-gui polymer builder for modeling and simulation of synthetic polymers,” *J. Chem. Theory Comput.*, vol. 17, no. 4, pp. 2431–2443, 2021.
- [278] A. I. Jewett, D. Stelter, J. Lambert, S. M. Saladi, O. M. Roscioni, M. Ricci, L. Autin, M. Maritan, S. M. Bashusqeh, T. Keyes, *et al.*, “Moltemplate: A tool for coarse-grained modeling of complex biological matter and soft condensed matter physics,” *J. Mol. Biol.*, vol. 433, no. 11, p. 166841, 2021.

- [279] L. J. Abbott, K. E. Hart, and C. M. Colina, “Polymatic: a generalized simulated polymerization algorithm for amorphous polymers,” *Theor. Chem. Acc.*, vol. 132, pp. 1–19, 2013.
- [280] W. Gall and N. McCrum, “Internal friction in stereoregular polymethyl methacrylate,” *J. Polym. Sci.*, vol. 50, no. 154, pp. 489–495, 1961.
- [281] P. J. Flory and M. Volkenstein, “Statistical mechanics of chain molecules,” 1969.
- [282] L. Fetters, D. Lohse, and R. Colby, “Chain dimensions and entanglement spacings,” *Physical properties of polymers handbook*, pp. 447–454, 2007.
- [283] A. Van der Lee, L. Hamon, Y. Holl, and Y. Grohens, “Density profiles in thin pmma supported films investigated by x-ray reflectometry,” *Langmuir*, vol. 17, no. 24, pp. 7664–7669, 2001.
- [284] B. A. Beiermann, D. A. Davis, S. L. Kramer, J. S. Moore, N. R. Sottos, and S. R. White, “Environmental effects on mechanochemical activation of spiropyran in linear pmma,” *J. Mater. Chem.*, vol. 21, no. 23, pp. 8443–8447, 2011.
- [285] A. Soldera, “Comparison between the glass transition temperatures of the two pmma tacticities: A molecular dynamics simulation point of view,” in *Macromol. Symp.*, vol. 133, pp. 21–32, 1998.
- [286] B. Demir and T. R. Walsh, “A robust and reproducible procedure for cross-linking thermoset polymers using molecular simulation,” *Soft matter*, vol. 12, no. 8, pp. 2453–2464, 2016.
- [287] I. Gilmour, A. Trainor, and R. Haward, “Elastic moduli of glassy polymers at low strains,” *J. Appl. Polym. Sci.*, vol. 23, no. 10, pp. 3129–3138, 1979.

- [288] C. M. Kingsbury, P. A. May, D. A. Davis, S. R. White, J. S. Moore, and N. R. Sottos, “Shear activation of mechanophore-crosslinked polymers,” *J. Mater. Chem.*, vol. 21, no. 23, pp. 8381–8388, 2011.
- [289] M. J. Buehler, “Atomistic and continuum modeling of mechanical properties of collagen: elasticity, fracture, and self-assembly,” *J. Mater. Res.*, vol. 21, no. 8, pp. 1947–1961, 2006.
- [290] S. Kumar, F. Zeller, and T. Stauch, “A two-step baromechanical cycle for repeated activation and deactivation of mechanophores,” *J. Phys. Chem. Lett.*, vol. 12, no. 39, pp. 9470–9474, 2021.
- [291] B. Hamilton and A. Strachan, “Many-body mechanochemistry: Intra-molecular strain in condensed matter chemistry,” *chemRxiv*, DOI: 10.26434/chemrxiv-2022-bvdmp, 2022.

Appendices

SP-MC isomerization

```

1 # This is a LAMMPS input file, used to perform the SP-MC conversion
2 # during the end-to-end constraints
3
4 clear
5 units      real
6 boundary   p p p
7 atom_style full
8
9 bond_style harmonic
10 angle_style harmonic
11 dihedral_style opls
12 improper_style cvff
13
14 pair_style lj/cut/coul/long 13.0
15 pair_modify mix geometric
16 kspace_style pppm 1.0e-4
17 special_bonds lj/coul 0.0 0.0 0.5
18
19 read_data  SP.lmp
20 log        log.log
21
22
23 neighbor   2.0 multi
24 neigh_modify cluster yes every 1 delay 0 check yes one 50000 page 500000
25 comm_style brick
26 comm_modify mode single vel yes
27 thermo_style custom etotal ke temp pe step
28 thermo_modify line multi format float %g
29 thermo 5000
30
31
32 #Generate trajectory
33 dump 2 all custom 100 SP-MC.lampstrj id mol type mass q xu yu zu ix iy iz vx vy vz
34 dump_modify 2 sort id
35
36
37
38 #---- Set end-to-end constraint ----
39 variable end2end equal 15.0
40 bond_coeff 61 85 ${end2end} # "61" is the additional topology (bond)
41 # added in SP.data to define the end-to-end
42 # constraints (an alternative is "add_force"
43
44     command)
45
46 #-----Fire Minimization-----
47 thermo 1000
48 timestep 1.0
49 min_style fire
50 minimize 0 1e-8 5000 5000
51 min_modify dmax 0.1
52
53 #----- Ruptre process -----
54 if "${end2end} > 14.6" then "include MC.settings" # MC.settings include the MC FF
55 # parameters.
56 # MC.settings first involve the following lines to delete the previous
57 # topology related to the C-O bond present in the SP molecule:
58 # delete_bonds all bond 60 remove
59 # delete_bonds all angle 102 remove

```



```
60 # delete_bonds all angle 103 remove
61 # delete_bonds all angle 104 remove
62 # delete_bonds all angle 105 remove
63 # delete_bonds all dihedral 139 remove
64 # delete_bonds all dihedral 140 remove
65 # delete_bonds all dihedral 141 remove
66 # delete_bonds all dihedral 142 remove
67 # delete_bonds all dihedral 143 remove
68 # delete_bonds all dihedral 144 remove
69 # delete_bonds all dihedral 145 remove
70 # delete_bonds all dihedral 146 remove
71 # delete_bonds all dihedral 147 remove
72 # delete_bonds all dihedral 148 remove
73 # delete_bonds all dihedral 149 remove
74 # delete_bonds all dihedral 150 remove
75 # delete_bonds all improper 34 remove
76
77 # Further, full force-field file of MC molecule is included in MC.settings file.
78 #-----
79
80 #----- Fire Minimization ----- # in bulk scale, no minimization is performed.
81 thermo 1000
82 timestep 1.0
83 min_style fire
84 minimize 0 1e-8 5000 5000
85 min_modify dmax 0.1
86
87
88 write_data geom- $\{end2end\}$ .data # writes constrained file
89
90
91 undump 2
92
93 # Additional notes
94 # (a) No extra topology/stretching coordinates is defined for being stretched
95 # during the bulk deformations.
96 #
97 # (b) For bulk simulations, the end-to-end distance is manually calculated for
98 # SP molecule and further used for the rupture process.
99 #
100 # (c) No minimization is carried out during the deformation process after the
101 # SP to MC conversion.
102 #
```

Spiropyran geometry

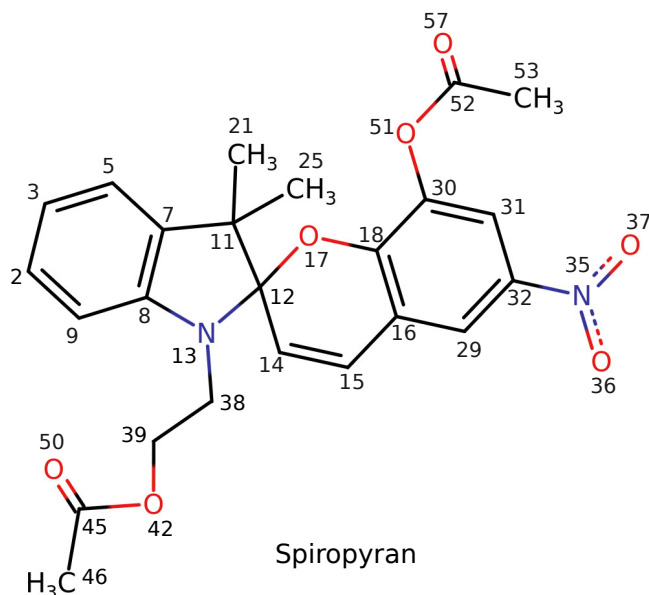


Figure 1: Labels (index-wise) of SP molecule. Labels were not added for hydrogen atoms. Same labels (index-wise) followed for the MC molecule (activated via force).

Table 1: Spiropyran molecule's index and XYZ coordinates.

1	H	4.7468373468	1.4594419224	-3.0518338747
2	C	4.0181952689	1.6960020617	-2.2809353138
3	C	3.6641345824	3.0243556001	-2.0478390177
4	H	4.1160635420	3.8184881095	-2.6349637641
5	C	2.7253455409	3.3380415741	-1.0521175954
6	H	2.4492596243	4.3733337786	-0.8675683038
7	C	2.1541659473	2.3137467515	-0.3142159813
8	C	2.5128893966	0.9800529528	-0.5622972807
9	C	3.4476791355	0.6507908155	-1.5406917999
10	H	3.7307816595	-0.3791006877	-1.7360195977
11	C	1.1851352447	2.3488486462	0.8577007414
12	C	0.6773527025	0.8487005491	0.8490634489
13	N	1.8039031242	0.1226784542	0.2998397765
14	C	0.2239023889	0.3109804366	2.1738683890
15	C	-1.0083641859	-0.1669103224	2.4006269084
16	C	-2.0022129241	-0.2374899138	1.3420119770
17	O	-0.4097495912	0.7769944808	-0.1645804084

continues on the next page

continues from the previous page

18	C	-1.6114525288	0.2293360463	0.0703523252
19	H	0.9674315387	0.3220127555	2.9627152694
20	H	-1.2815499232	-0.5389807716	3.3848623702
21	C	1.9911217635	2.6348078629	2.1489163716
22	H	2.7777507030	1.8904648234	2.3091766010
23	H	1.3393055342	2.6566257343	3.0295745495
24	H	2.4704549068	3.6148022568	2.0614663321
25	C	0.0422955598	3.3647031247	0.7410668153
26	H	-0.5218739628	3.2596695949	-0.1863896011
27	H	0.4488132273	4.3813885308	0.7867961550
28	H	-0.6527386627	3.2539422422	1.5817107834
29	C	-3.2766171575	-0.7801685220	1.5152285012
30	C	-2.4995593889	0.1169078675	-1.0167037412
31	C	-3.7627364224	-0.4195198271	-0.8442297012
32	C	-4.1393314294	-0.8611667016	0.4272007167
33	H	-3.6001657913	-1.1464361280	2.4824333492
34	H	-4.4468451953	-0.5013659387	-1.6790729870
35	N	-5.4725988326	-1.4312236286	0.6125069676
36	O	-5.7824435521	-1.8086814871	1.7445978624
37	O	-6.2092400521	-1.5025973594	-0.3729785071
38	C	1.7183548994	-1.3103597059	0.0564607717
39	C	2.8311668253	-2.0587898216	0.7866379851
40	H	1.7673710114	-1.5227718906	-1.0196251040
41	H	0.7505225275	-1.6746503971	0.4121885444
42	O	2.6842157770	-3.4499897378	0.4448278405
43	H	2.7485425976	-1.9314079093	1.8699313813
44	H	3.8241316985	-1.7089231968	0.4854175522
45	C	3.5236277742	-4.3052034476	1.0814494544
46	C	3.2729280357	-5.7285632890	0.6436752922
47	H	3.4251814075	-5.8223809729	-0.4366302318
48	H	2.2357974489	-6.0113510884	0.8522436681
49	H	3.9534739244	-6.3958198996	1.1732937746
50	O	4.3524008449	-3.9463772370	1.8872292729
51	O	-2.0711477054	0.4640775329	-2.2907725883
52	C	-1.9381106886	1.8042710573	-2.5848404667
53	C	-1.2901113925	1.9725895934	-3.9332601602
54	H	-0.2159022279	1.7768463472	-3.8354475106
55	H	-1.4371907076	2.9958080380	-4.2806207133
56	H	-1.6952725110	1.2584715967	-4.6549765885
57	O	-2.2899278299	2.6829954850	-1.8401339866

Parameterized Force Fields for SP and MC

Table 2: Partial atomic charges in SP and MC.

	Partial atomic charges	
	Spiropyran	Merocyanine
1	0.15060000	0.33960000
2	-0.11180000	-0.18530000
3	-0.18340000	-0.05660000
4	0.15410000	0.17230000
5	-0.08800000	-0.13460000
6	0.15570000	0.17550000
7	-0.13560000	-0.04420000
8	0.19740000	0.05600000
9	-0.18480000	0.04580000
10	0.15960000	0.20410000
11	0.01450000	-0.01170000
12	0.42500000	0.35610000
13	-0.68530000	-0.58590000
14	-0.21990000	-0.33880000
15	-0.08510000	0.19750000
16	-0.17390000	-0.26860000
17	-0.32920000	-0.48090000
18	0.23390000	0.05670000
19	0.18110000	0.13780000
20	0.16910000	0.10730000
21	-0.22800000	-0.21680000
22	0.09680000	0.11150000
23	0.09680000	0.11150000
24	0.09680000	0.11150000
25	-0.22540000	-0.22720000
26	0.10180000	0.11360000
27	0.10180000	0.11360000
28	0.10180000	0.11360000
29	-0.00400000	-0.03720000
30	0.03920000	-0.00290000
31	-0.02460000	-0.09820000
32	-0.21810000	-0.22160000
33	0.19780000	0.17010000
34	0.20980000	0.19060000
35	0.86350000	0.85800000

continues on the next page

continues from the previous page

	Partial atomic charges	
	Spiropyran	Merocyanine
36	-0.50920000	-0.51970000
37	-0.50920000	-0.51970000
38	0.08270000	0.08630000
39	0.00090000	0.00040000
40	0.11500000	0.12560000
41	0.11500000	0.12560000
42	-0.38020000	-0.39760000
43	0.11370000	0.13080000
44	0.11370000	0.13080000
45	0.44420000	0.42910000
46	-0.25450000	-0.21430000
47	0.12850000	0.12730000
48	0.12850000	0.12730000
49	0.12850000	0.12730000
50	-0.44290000	-0.43690000
51	-0.31410000	-0.31650000
52	0.45750000	0.42380000
53	-0.25240000	-0.22050000
54	0.13360000	0.12600000
55	0.13360000	0.12600000
56	0.13360000	0.12600000
57	-0.41640000	-0.41950000

Table 3: Force field parameters for bonds used in SP and MC, where K_b and r_o is the force constant and equilibrium distance.

		FF style: harmonic			
		Spiropyran		Merocyanine	
		(K_b)	(r_o)	(K_b)	(r_o)
1	2–1	367.0000	1.0800	367.0000	1.0800
2	3–2	469.0000	1.4000	469.0000	1.4000
3	4–3	367.0000	1.0800	367.0000	1.0800
4	5–3	469.0000	1.4000	469.0000	1.4000
5	6–5	367.0000	1.0800	367.0000	1.0800
6	7–5	469.0000	1.4000	469.0000	1.4000
7	8–7	469.0000	1.4040	469.0000	1.4040
8	9–2	469.0000	1.4000	469.0000	1.4000
9	10–9	367.0000	1.0800	367.0000	1.0800
10	11–7	317.0000	1.5100	317.0000	1.5100
11	12–11	268.0000	1.5290	317.0000	1.5100
12	13–8	317.0000	1.5100	436.0000	1.3740
13	14–12	317.0000	1.5100	549.0000	1.3400
14	15–14	549.0000	1.3400	385.0000	1.4600
15	16–15	427.0000	1.4330	427.0000	1.4330
16	17–18	750.0000	1.3300	570.0000	1.2290
17	18–16	469.0000	1.4040	410.0000	1.4440
18	19–14	367.0000	1.0800	340.0000	1.0800
19	20–15	374.4600	1.1200	340.0000	1.0800
20	21–11	268.0000	1.5290	268.0000	1.5290
21	22–21	340.0000	1.0900	340.0000	1.0900
22	23–21	340.0000	1.0900	340.0000	1.0900
23	24–21	340.0000	1.0900	340.0000	1.0900
24	25–11	268.0000	1.5290	268.0000	1.5290
25	26–25	340.0000	1.0900	340.0000	1.0900
26	27–25	340.0000	1.0900	340.0000	1.0900
27	28–25	340.0000	1.0900	340.0000	1.0900
28	29–16	469.0000	1.4040	549.0000	1.3400
29	30–18	469.0000	1.4000	410.0000	1.4440

continues on the next page

continues from the previous page

		FF style: harmonic			
		Spiropyran		Merocyanine	
		(K_b)	(r_o)	(K_b)	(r_o)
30	31–30	469.0000	1.4000	427.0000	1.4330
31	32–29	469.0000	1.4000	427.0000	1.4330
32	33–29	367.0000	1.0800	412.5200	1.0500
33	34–31	367.0000	1.0800	367.0000	1.0800
34	35–32	400.0000	1.4600	400.0000	1.4600
35	36–35	550.0000	1.2250	550.0000	1.2250
36	37–35	550.0000	1.2250	550.0000	1.2250
37	38–13	382.0000	1.4480	337.0000	1.4750
38	39–38	268.0000	1.5290	268.0000	1.5290
39	40–38	340.0000	1.0900	340.0000	1.0900
40	41–38	340.0000	1.0900	340.0000	1.0900
41	42–39	320.0000	1.4100	320.0000	1.4100
42	43–39	340.0000	1.0900	340.0000	1.0900
43	44–39	340.0000	1.0900	340.0000	1.0900
44	45–42	214.0000	1.3270	214.0000	1.3270
45	46–45	317.0000	1.5220	317.0000	1.5220
46	47–46	340.0000	1.0900	340.0000	1.0900
47	48–46	340.0000	1.0900	340.0000	1.0900
48	49–46	340.0000	1.0900	340.0000	1.0900
49	50–45	570.0000	1.2290	570.0000	1.2290
50	51–30	450.0000	1.3640	450.0000	1.3640
51	52–51	214.0000	1.3270	214.0000	1.3270
52	53–52	317.0000	1.5220	317.0000	1.5220
53	54–53	340.0000	1.0900	340.0000	1.0900
54	55–53	340.0000	1.0900	340.0000	1.0900
55	56–53	340.0000	1.0900	340.0000	1.0900
56	57–52	570.0000	1.2290	570.0000	1.2290
57	9–8	469.0000	1.4040	469.0000	1.4040
58	13–12	700.0000	1.4200	700.0000	1.4200
59	32–31	469.0000	1.4000	469.0000	1.4000
60	17–12	120.0000	1.4800	–	–

Table 4: Force field parameters for angles used in SP and MC, where K_θ and θ_o is the force constant and equilibrium angle.

		FF style: harmonic			
		Spiropyran		Merocyanine	
		(K_θ)	(θ_o)	(K_θ)	(θ_o)
1	1–2–3	35.000	120.000	35.000	120.000
2	2–3–4	35.000	120.000	35.000	120.000
3	2–3–5	63.000	120.000	63.000	120.000
4	3–5–6	35.000	120.000	35.000	120.000
5	3–5–7	63.000	120.000	63.000	120.000
6	5–7–8	63.000	120.000	63.000	120.000
7	1–2–9	35.000	120.000	35.000	120.000
8	2–9–10	35.000	120.000	35.000	120.000
9	5–7–11	70.000	120.000	70.000	120.000
10	7–11–12	63.000	114.000	40.000	109.500
11	7–8–13	70.000	120.000	70.000	108.700
12	11–12–14	70.000	124.000	35.000	132.000
13	12–14–15	70.000	124.000	30.000	145.000
14	14–15–16	85.000	117.000	30.000	135.000
15	27–25–28	33.000	107.800	33.000	107.800
16	15–16–18	70.000	124.000	30.000	145.000
17	12–14–19	60.430	118.760	35.000	120.000
18	14–15–20	45.740	115.690	35.000	120.000
19	7–11–21	63.000	114.000	63.000	114.000
20	11–21–22	37.500	110.700	37.500	110.700
21	11–21–23	37.500	110.700	37.500	110.700
22	11–21–24	37.500	110.700	37.500	110.700
23	7–11–25	63.000	114.000	63.000	114.000
24	11–25–26	37.500	110.700	37.500	110.700
25	11–25–27	37.500	110.700	37.500	110.700
26	11–25–28	37.500	110.700	37.500	110.700
27	15–16–29	70.000	124.000	60.430	118.760
28	16–18–30	63.000	120.000	69.900	118.180
29	18–30–31	63.000	120.000	85.000	120.700
30	16–29–32	63.000	120.000	85.000	117.000
31	16–29–33	35.000	120.000	60.000	122.260
32	30–31–34	35.000	120.000	60.430	118.760
33	29–32–35	85.000	120.000	64.510	118.990
34	32–35–36	80.000	117.500	80.000	117.500
35	32–35–37	80.000	117.500	80.000	117.500
36	8–13–38	50.000	116.000	70.000	125.800

continues on the next page

continues from the previous page

		FF style: harmonic			
		Spiropyran		Merocyanine	
		(K_θ)	(θ_o)	(K_θ)	(θ_o)
37	13–38–39	56.200	109.470	51.650	110.580
38	13–38–40	35.000	109.500	35.000	109.500
39	13–38–41	35.000	109.500	35.000	109.500
40	38–39–42	50.000	109.500	50.000	109.500
41	38–39–43	37.500	110.700	37.500	110.700
42	38–39–44	37.500	110.700	37.500	110.700
43	39–42–45	83.000	116.900	83.000	116.900
44	42–45–46	81.000	111.400	81.000	111.400
45	45–46–47	35.000	109.500	35.000	109.500
46	45–46–48	35.000	109.500	35.000	109.500
47	45–46–49	35.000	109.500	35.000	109.500
48	42–45–50	83.000	123.400	83.000	123.400
49	18–30–51	70.000	120.000	60.000	122.260
50	30–51–52	83.000	116.900	69.510	114.540
51	51–52–53	81.000	111.400	81.000	111.400
52	52–53–54	35.000	109.500	35.000	109.500
53	52–53–55	35.000	109.500	35.000	109.500
54	52–53–56	35.000	109.500	35.000	109.500
55	51–52–57	83.000	123.400	83.000	123.400
56	16–15–20	45.740	115.690	35.000	123.300
57	8–13–12	50.000	116.000	70.000	125.200
58	13–12–14	63.000	111.100	70.000	121.200
59	12–11–21	58.350	112.700	63.000	111.100
60	32–29–33	35.000	120.000	60.000	122.260
61	26–25–28	33.000	107.800	33.000	107.800
62	21–11–25	58.350	112.700	58.350	112.700
63	39–38–41	37.500	110.700	37.500	110.700
64	18–16–29	85.000	134.900	85.000	120.700
65	31–32–35	85.000	120.000	85.000	120.000
66	29–32–31	63.000	120.000	70.000	124.000
67	32–31–34	35.000	120.000	35.000	120.000
68	15–14–19	60.430	118.760	35.000	120.000
69	53–52–57	80.000	120.400	80.000	120.400
70	47–46–49	33.000	107.800	33.000	107.800
71	12–13–38	51.800	107.200	63.000	112.400
72	42–39–43	35.000	109.500	35.000	109.500
73	12–11–25	58.350	112.700	63.000	111.100
74	31–30–51	70.000	120.000	70.000	123.000

continues on the next page

continues from the previous page

		FF style: harmonic			
		Spiropyran		Merocyanine	
		(K_θ)	(θ_o)	(K_θ)	(θ_o)
75	26–25–27	33.000	107.800	33.000	107.800
76	16–18–17	70.000	120.000	80.000	125.300
77	4–3–5	35.000	120.000	35.000	120.000
78	40–38–41	33.000	107.800	33.000	107.800
79	7–8–9	85.000	134.900	85.000	134.900
80	30–31–32	63.000	120.000	85.000	117.000
81	6–5–7	35.000	120.000	35.000	120.000
82	2–9–8	63.000	120.000	63.000	120.000
83	46–45–50	80.000	120.400	80.000	120.400
84	39–38–40	37.500	110.700	37.500	110.700
85	22–21–24	33.000	107.800	33.000	107.800
86	55–53–56	33.000	107.800	33.000	107.800
87	8–7–11	70.000	128.600	70.000	128.600
88	17–18–30	70.000	120.000	80.000	125.300
89	11–12–13	56.200	109.470	70.000	120.000
90	48–46–49	33.000	107.800	33.000	107.800
91	54–53–56	33.000	107.800	33.000	107.800
92	23–21–24	33.000	107.800	33.000	107.800
93	54–53–55	33.000	107.800	33.000	107.800
94	36–35–37	80.000	125.000	80.000	125.000
95	3–2–9	63.000	120.000	63.000	120.000
96	43–39–44	33.000	107.800	33.000	107.800
97	8–9–10	35.000	120.000	35.000	120.000
98	22–21–23	33.000	107.800	33.000	107.800
99	9–8–13	70.000	120.000	70.000	108.700
100	47–46–48	33.000	107.800	33.000	107.800
101	42–39–44	35.000	109.500	35.000	109.500
102	11–12–17	50.000	109.500	–	–
103	13–12–17	50.000	109.500	–	–
104	14–12–17	50.000	109.500	–	–
105	12–17–18	75.000	111.000	–	–

Table 5: Force field parameters for dihedrals used in SP and MC, where K_{ϕ_1} , K_{ϕ_2} , K_{ϕ_3} and K_{ϕ_4} are the force constants.

		FF style: Optimized potentials for liquid simulations (OPLS)							
		Spiropyran				Merocyanine			
		K_{ϕ_1}	K_{ϕ_2}	K_{ϕ_3}	K_{ϕ_4}	K_{ϕ_1}	K_{ϕ_2}	K_{ϕ_3}	K_{ϕ_4}
1	4–3–2–1	0.000	7.250	0.000	0.000	0.000	7.250	0.000	0.000
2	6–5–3–2	0.000	7.250	0.000	0.000	0.000	7.250	0.000	0.000
3	8–7–5–3	0.000	7.250	0.000	0.000	0.000	7.250	0.000	0.000
4	12–11–7–5	0.000	0.000	0.000	0.000	0.000	0.000	0.000	0.000
5	15–14–12–11	0.000	14.000	-2.300	0.000	-2.300	10.50	14.000	0.000
6	16–15–14–12	0.000	0.000	-0.372	0.000	1.000	-7.000	12.000	0.000
7	18–16–15–14	1.241	3.353	-0.286	0.000	0.000	0.000	14.000	0.000
8	22–21–11–7	0.000	0.000	0.462	0.000	0.000	0.000	0.462	0.000
9	26–25–11–7	0.000	0.000	0.462	0.000	0.000	0.000	0.462	0.000
10	31–30–18–16	0.000	7.250	0.000	0.000	0.000	0.000	-0.372	0.000
11	32–29–16–15	0.000	7.000	0.000	0.000	0.000	14.000	0.000	0.000
12	36–35–32–29	0.000	1.150	0.000	0.000	0.000	1.150	0.000	0.000
13	39–38–13–8	0.416	-0.128	0.695	0.000	1.000	-0.350	0.000	0.000
14	42–39–38–13	8.000	0.000	0.000	0.000	8.000	0.000	0.000	0.000
15	45–42–39–38	-1.220	-0.126	0.422	0.000	-1.220	-0.126	0.422	0.000
16	46–45–42–39	4.669	5.124	0.000	0.000	4.669	5.124	0.000	0.000
17	47–46–45–42	0.000	0.000	0.132	0.000	0.000	0.000	0.132	0.000
18	52–51–30–18	0.000	2.500	0.000	0.000	-1.220	-0.126	0.422	0.000
19	53–52–51–30	1.500	5.000	0.000	0.000	4.669	5.124	0.000	0.000
20	54–53–52–51	0.000	0.000	0.132	0.000	0.000	0.000	0.132	0.000
21	43–39–38–40	0.000	0.000	0.300	0.000	0.000	0.000	0.300	0.000
22	42–39–38–41	0.000	0.000	0.468	0.000	0.000	0.000	0.468	0.000
23	8–9–2–3	0.000	7.250	0.000	0.000	0.000	7.250	0.000	0.000
24	10–9–2–1	0.000	7.250	0.000	0.000	0.000	7.250	0.000	0.000
25	21–11–7–5	0.000	0.000	0.000	0.000	0.000	0.000	0.000	0.000
26	25–11–12–13	2.392	-0.674	0.550	0.000	2.366	-0.262	0.505	0.000
27	14–12–13–8	0.416	-0.128	0.695	0.000	0.000	14.000	0.000	0.000
28	55–53–52–51	0.000	0.000	0.132	0.000	0.000	0.000	0.132	0.000
29	56–53–52–51	0.000	0.000	0.132	0.000	0.000	0.000	0.132	0.000
30	38–13–8–9	-7.582	3.431	3.198	0.000	0.000	7.250	0.000	0.000
31	41–38–13–8	0.000	0.000	0.560	0.000	0.000	0.000	0.000	0.000
32	10–9–8–7	0.000	7.250	0.000	0.000	0.000	7.250	0.000	0.000
33	30–31–32–29	0.000	7.250	0.000	0.000	1.241	3.353	-0.286	0.000
34	44–39–38–40	0.000	0.000	0.300	0.000	0.000	0.000	0.300	0.000
35	13–8–9–10	0.000	7.250	0.000	0.000	0.000	7.250	0.000	0.000
36	9–2–3–4	0.000	7.250	0.000	0.000	0.000	7.250	0.000	0.000

continues on the next page

continues from the previous page

		FF style: Optimized potentials for liquid simulations (OPLS)							
		Spiropyran				Merocyanine			
		K_{ϕ_1}	K_{ϕ_2}	K_{ϕ_3}	K_{ϕ_4}	K_{ϕ_1}	K_{ϕ_2}	K_{ϕ_3}	K_{ϕ_4}
37	43–39–38–41	0.000	0.000	0.300	0.000	0.000	0.000	0.300	0.000
38	25–11–21–24	0.000	0.000	0.300	0.000	0.000	0.000	0.300	0.000
39	14–12–11–7	-1.697	-0.456	0.585	0.000	0.000	14.000	3.000	0.000
40	37–35–32–31	0.000	1.150	0.000	0.000	0.000	1.150	0.000	0.000
41	32–31–30–18	0.000	7.250	0.000	0.000	1.241	3.353	-0.286	0.000
42	21–11–7–8	0.000	0.000	0.000	0.000	0.000	0.000	0.000	0.000
43	33–29–16–15	0.000	7.250	0.000	0.000	0.000	14.000	0.000	0.000
44	35–32–31–34	0.000	7.250	0.000	0.000	0.000	0.000	-0.372	0.000
45	34–31–30–18	0.000	7.250	0.000	0.000	0.000	14.000	0.000	0.000
46	51–30–18–17	-0.750	1.500	0.000	0.000	-0.750	1.500	0.000	0.000
47	51–30–18–16	0.000	7.250	0.000	0.000	0.000	1.500	0.000	0.000
48	28–25–11–7	0.000	0.000	0.462	0.000	0.000	0.000	0.462	0.000
49	50–45–42–39	0.000	5.124	0.000	0.000	0.000	5.124	0.000	0.000
50	30–18–16–29	0.000	7.000	0.000	0.000	0.000	14.000	0.000	0.000
51	25–11–12–14	1.300	-0.200	0.200	0.000	0.346	0.405	-0.904	0.000
52	36–35–32–31	0.000	1.150	0.000	0.000	0.000	1.150	0.000	0.000
53	19–14–15–16	0.000	14.000	0.000	0.000	0.000	0.000	0.300	0.000
54	29–16–15–20	0.000	7.250	0.000	0.000	0.000	14.000	0.000	0.000
55	42–39–38–40	0.000	0.000	0.468	0.000	0.000	0.000	0.468	0.000
56	25–11–21–23	0.000	0.000	0.300	0.000	0.000	0.000	0.300	0.000
57	34–31–32–29	0.000	7.250	0.000	0.000	0.000	0.000	-0.372	0.000
58	28–25–11–12	0.000	0.000	0.300	0.000	0.000	0.000	0.366	0.000
59	9–8–7–5	0.000	7.000	0.000	0.000	0.000	7.000	0.000	0.000
60	8–9–2–1	0.000	7.250	0.000	0.000	0.000	7.250	0.000	0.000
61	11–12–13–8	0.650	-0.250	0.670	0.000	0.650	-0.250	0.670	0.000
62	50–45–46–48	0.000	0.000	0.000	0.000	0.000	0.000	0.000	0.000
63	6–5–3–4	0.000	7.250	0.000	0.000	0.000	7.250	0.000	0.000
64	48–46–45–42	0.000	0.000	0.132	0.000	0.000	0.000	0.132	0.000
65	39–38–13–12	0.416	-0.128	0.695	0.000	1.000	-0.350	0.000	0.000
66	25–11–7–8	0.000	0.000	0.000	0.000	0.000	0.000	0.000	0.000
67	38–13–12–14	0.416	-0.128	14.695	0.000	3.416	-2.100	7.250	0.000
68	41–38–13–12	0.000	0.000	0.560	0.000	0.000	0.000	0.000	0.000
69	40–38–13–12	0.000	0.000	0.560	0.000	0.000	0.000	0.000	0.000
70	57–52–53–56	0.000	0.000	0.000	0.000	0.000	0.000	0.000	0.000
71	35–32–31–30	0.000	7.250	0.000	0.000	0.000	7.000	0.000	0.000
72	29–16–15–14	1.241	3.353	-0.286	0.000	0.000	14.000	0.000	0.000
73	33–29–16–18	0.000	7.250	0.000	0.000	0.000	14.000	0.000	0.000
74	35–32–29–16	0.000	7.250	0.000	0.000	0.000	7.000	0.000	0.000

continues on the next page

continues from the previous page

		FF style: Optimized potentials for liquid simulations (OPLS)							
		Spiropyran				Merocyanine			
		K_{ϕ_1}	K_{ϕ_2}	K_{ϕ_3}	K_{ϕ_4}	K_{ϕ_1}	K_{ϕ_2}	K_{ϕ_3}	K_{ϕ_4}
75	43–39–38–13	-1.013	-0.709	0.473	0.000	-1.013	-0.709	0.473	0.000
76	13–8–7–5	0.000	7.000	0.000	0.000	0.000	7.000	0.000	0.000
77	21–11–12–13	2.392	-0.674	0.550	0.000	2.366	-0.262	0.505	0.000
78	23–21–11–7	0.000	0.000	0.462	0.000	0.000	0.000	0.462	0.000
79	20–15–14–12	0.000	14.000	0.000	0.000	0.000	-3.000	7.500	0.000
80	20–15–16–18	0.000	7.250	0.000	0.000	0.000	14.000	0.000	0.000
81	7–5–3–4	0.000	7.250	0.000	0.000	0.000	7.250	0.000	0.000
82	23–21–11–12	0.000	0.000	0.300	0.000	0.000	0.000	0.366	0.000
83	57–52–53–55	0.000	0.000	0.000	0.000	0.000	0.000	0.000	0.000
84	28–25–11–21	0.000	0.000	0.300	0.000	0.000	0.000	0.300	0.000
85	12–13–8–7	-7.582	3.431	3.198	0.000	0.000	7.250	0.000	0.000
86	33–29–32–31	0.000	7.250	0.000	0.000	0.000	0.000	-0.372	0.000
87	24–21–11–7	0.000	0.000	0.462	0.000	0.000	0.000	0.462	0.000
88	51–30–31–32	0.000	7.250	0.000	0.000	0.000	14.000	0.000	0.000
89	38–13–12–11	0.416	-0.128	0.695	0.000	0.650	-0.250	0.670	0.000
90	12–11–7–8	0.000	0.000	0.000	0.000	0.000	0.000	0.000	0.000
91	10–9–2–3	0.000	7.250	0.000	0.000	0.000	7.250	0.000	0.000
92	27–25–11–7	0.000	0.000	0.462	0.000	0.000	0.000	0.462	0.000
93	26–25–11–21	0.000	0.000	0.300	0.000	0.000	0.000	0.300	0.000
94	19–14–12–13	0.000	7.250	0.000	0.000	0.000	0.000	-0.372	0.000
95	29–16–18–17	0.000	7.250	0.000	0.000	2.500	6.000	0.000	0.000
96	31–30–18–17	0.000	7.250	0.000	0.000	2.500	6.000	0.000	0.000
97	7–5–3–2	0.000	7.250	0.000	0.000	0.000	7.250	0.000	0.000
98	13–8–7–11	0.000	7.000	0.000	0.000	0.000	7.000	0.000	0.000
99	50–45–46–49	0.000	0.000	0.000	0.000	0.000	0.000	0.000	0.000
100	20–15–14–19	0.000	14.000	0.000	0.000	1.500	18.00	-3.500	0.000
101	7–8–9–2	0.000	7.000	0.000	0.000	0.000	7.000	0.000	0.000
102	31–32–29–16	0.000	7.250	0.000	0.000	1.241	3.353	-0.286	0.000
103	19–14–12–11	0.000	-8.000	0.000	0.000	0.000	14.000	0.000	0.000
104	44–39–38–13	-1.013	-0.709	0.473	0.000	-1.013	-0.709	0.473	0.000
105	11–7–5–6	0.000	7.250	0.000	0.000	0.000	7.250	0.000	0.000
106	25–11–7–5	0.000	0.000	0.000	0.000	0.000	0.000	0.000	0.000
107	24–21–11–12	0.000	0.000	0.300	0.000	0.000	0.000	0.366	0.000
108	49–46–45–42	0.000	0.000	0.132	0.000	0.000	0.000	0.132	0.000
109	25–11–21–22	0.000	0.000	0.300	0.000	0.000	0.000	0.300	0.000
110	5–3–2–1	0.000	7.250	0.000	0.000	0.000	7.250	0.000	0.000
111	32–29–16–18	0.000	7.000	0.000	0.000	0.000	2.170	0.000	0.000
112	11–7–8–9	0.000	7.000	0.000	0.000	0.000	7.000	0.000	0.000

continues on the next page

continues from the previous page

		FF style: Optimized potentials for liquid simulations (OPLS)							
		Spiropyran				Merocyanine			
		K_{ϕ_1}	K_{ϕ_2}	K_{ϕ_3}	K_{ϕ_4}	K_{ϕ_1}	K_{ϕ_2}	K_{ϕ_3}	K_{ϕ_4}
113	27–25–11–21	0.000	0.000	0.300	0.000	0.000	0.000	0.300	0.000
114	45–42–39–43	0.000	0.000	0.198	0.000	0.000	0.000	0.198	0.000
115	35–32–29–33	0.000	7.250	0.000	0.000	0.000	0.000	0.198	0.000
116	17–18–16–15	0.000	7.000	0.000	0.000	2.500	6.000	0.000	0.000
117	45–42–39–44	0.000	0.000	0.198	0.000	0.000	7.250	0.000	0.000
118	57–52–53–54	0.000	0.000	0.000	0.000	0.000	0.000	0.000	0.000
119	8–7–5–6	0.000	7.250	0.000	0.000	0.000	7.250	0.000	0.000
120	11–7–5–3	0.000	7.250	0.000	0.000	0.000	7.250	0.000	0.000
121	13–12–11–7	-0.800	0.000	0.000	0.000	0.845	-0.962	0.713	0.000
122	37–35–32–29	0.000	1.150	0.000	0.000	0.000	1.150	0.000	0.000
123	27–25–11–12	0.000	0.000	0.300	0.000	0.000	0.000	0.366	0.000
124	26–25–11–12	0.000	0.000	0.300	0.000	0.000	0.000	0.366	0.000
125	50–45–46–47	0.000	0.000	0.000	0.000	0.000	0.000	0.000	0.000
126	21–11–12–14	1.300	-0.200	0.200	0.000	0.346	0.405	-0.904	0.000
127	44–39–38–41	0.000	0.000	0.300	0.000	0.000	0.000	0.300	0.000
128	12–13–8–9	-7.582	3.431	3.198	0.000	0.000	7.250	0.000	0.000
129	57–52–51–30	0.000	14.00	0.000	0.000	0.000	5.124	0.000	0.000
130	38–13–8–7	-7.582	3.431	3.198	0.000	0.000	7.250	0.000	0.000
131	52–51–30–31	0.000	2.500	0.000	0.000	-1.220	-0.126	0.422	0.000
132	13–8–9–2	0.000	7.000	0.000	0.000	0.000	7.000	0.000	0.000
133	40–38–13–8	0.000	0.000	0.560	0.000	0.000	0.000	0.000	0.000
134	30–18–16–15	0.000	7.000	0.000	0.000	0.000	14.000	0.000	0.000
135	9–2–3–5	0.000	7.250	0.000	0.000	0.000	7.250	0.000	0.000
136	51–30–31–34	0.000	7.250	0.000	0.000	0.000	14.000	0.000	0.000
137	22–21–11–12	0.000	0.000	0.300	0.000	0.000	0.000	0.366	0.000
138	15–14–12–13	0.000	0.000	7.250	0.000	0.000	14.000	0.000	0.000
139	17–12–11–7	1.711	-0.500	0.663	0.000	–	–	–	–
140	21–11–12–17	1.711	-0.500	0.663	0.000	–	–	–	–
141	17–12–13–8	1.500	-1.500	0.000	0.000	–	–	–	–
142	38–13–12–17	1.500	-1.500	0.000	0.000	–	–	–	–
143	19–14–12–17	0.000	0.000	0.468	0.000	–	–	–	–
144	18–17–12–14	0.000	5.000	0.000	0.000	–	–	–	–
145	25–11–12–17	1.711	-0.500	0.663	0.000	–	–	–	–
146	30–18–17–12	0.000	3.000	0.000	0.000	–	–	–	–
147	16–18–17–12	0.000	3.000	0.000	0.000	–	–	–	–
148	17–12–14–15	0.500	0.000	0.000	0.000	–	–	–	–
149	18–17–12–11	0.650	-0.250	0.670	0.000	–	–	–	–
150	18–17–12–13	-0.500	14.500	1.000	0.000	–	–	–	–

Table 6: Force field parameters for impropers used in SP and MC, where i , j and k are the force constants.

		FF style: Consistent-valence force field (CVFF)					
		Spiropyran			Merocyanine		
		i	j	k	i	j	k
1	3-2-4-5	2.500	-1	2	2.500	-1	2
2	5-3-6-7	2.500	-1	2	2.500	-1	2
3	2-9-3-1	2.500	-1	2	2.500	-1	2
4	9-10-8-2	2.500	-1	2	2.500	-1	2
5	7-11-5-8	2.500	-1	2	2.500	-1	2
6	8-9-13-7	2.500	-1	2	2.500	-1	2
7	12-11-13-14	0.000	-1	2	2.500	-1	2
8	14-19-12-15	2.500	-1	2	2.500	-1	2
9	15-20-14-16	2.500	-1	2	2.500	-1	2
10	11-12-21-7	0.000	-1	2	0.000	-1	2
11	21-11-22-23	0.000	-1	2	0.000	-1	2
12	21-11-22-24	0.000	-1	2	0.000	-1	2
13	11-25-12-7	0.000	-1	2	0.000	-1	2
14	25-26-27-11	0.000	-1	2	0.000	-1	2
15	25-26-11-28	0.000	-1	2	0.000	-1	2
16	16-18-29-15	2.500	-1	2	2.500	-1	2
17	18-17-30-16	2.500	-1	2	10.500	-1	2
18	29-33-32-16	2.500	-1	2	2.500	-1	2
19	31-34-30-32	2.500	-1	2	2.500	-1	2
20	32-35-29-31	2.500	-1	2	2.500	-1	2
21	35-36-37-32	2.500	-1	2	2.500	-1	2
22	13-12-38-8	0.000	-1	2	0.000	-1	2
23	38-13-39-40	0.000	-1	2	0.000	-1	2
24	38-41-13-39	0.000	-1	2	0.000	-1	2
25	39-42-43-38	0.000	-1	2	0.000	-1	2
26	39-42-44-38	0.000	-1	2	0.000	-1	2
27	46-45-47-48	0.000	-1	2	0.000	-1	2
28	46-49-45-47	0.000	-1	2	0.000	-1	2
29	45-50-46-42	10.500	-1	2	10.500	-1	2
30	30-18-51-31	2.500	-1	2	2.500	-1	2
31	53-52-54-55	0.000	-1	2	0.000	-1	2
32	53-52-54-56	0.000	-1	2	0.000	-1	2
33	52-57-51-53	10.500	-1	2	10.500	-1	2
34	12-17-11-13	0.000	-1	2	–	–	–

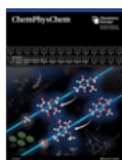
Permission & Licence

Permissions and licenses of Section 3.1



?
Help ▾

Live Chat



The Mechanism of Flex-Activation in Mechanophores Revealed By Quantum Chemistry

Author: Tim Stauch, Sourabh Kumar, Gheorghe Adam, et al

Publication: ChemPhysChem

Publisher: John Wiley and Sons

Date: Oct 7, 2020

© 2020 The Authors. Published by Wiley-VCH GmbH

Open Access Article

This is an open access article distributed under the terms of the [Creative Commons CC BY](#) license, which permits unrestricted use, distribution, and reproduction in any medium, provided the original work is properly cited.

You are not required to obtain permission to reuse this article.

For an understanding of what is meant by the terms of the Creative Commons License, please refer to [Wiley's Open Access Terms and Conditions](#).

Permission is not required for this type of reuse.

Wiley offers a professional reprint service for high quality reproduction of articles from over 1400 scientific and medical journals. Wiley's reprint service offers:

- Peer reviewed research or reviews
- Tailored collections of articles
- A professional high quality finish
- Glossy journal style color covers
- Company or brand customisation
- Language translations
- Prompt turnaround times and delivery directly to your office, warehouse or congress.

Please contact our Reprints department for a quotation. Email corporatesaleseurope@wiley.com or corporatesalesusa@wiley.com or corporatesalesDE@wiley.com.

Permissions and licenses of Section 3.2


The activation efficiency of mechanophores can be modulated by adjacent polymer composition


S. Kumar and T. Stauch, *RSC Adv.*, 2021, **11**, 7391

DOI: 10.1039/D0RA09834E

This article is licensed under a [Creative Commons Attribution 3.0 Unported Licence](#). You can use material from this article in other publications without requesting further permissions from the RSC, provided that the correct acknowledgement is given.

Permissions and licenses of Section 4.1

HomeHelp ▾Live ChatSign inCreate Account



A Two-Step Baromechanical Cycle for Repeated Activation and Deactivation of Mechanophores
Author: Sourabh Kumar, Felix Zeller, Tim Stauch
Publication: Journal of Physical Chemistry Letters
Publisher: American Chemical Society
Date: Oct 1, 2021
Copyright © 2021, American Chemical Society

PERMISSION/LICENSE IS GRANTED FOR YOUR ORDER AT NO CHARGE

This type of permission/license, instead of the standard Terms and Conditions, is sent to you because no fee is being charged for your order. Please note the following:

- Permission is granted for your request in both print and electronic formats, and translations.
- If figures and/or tables were requested, they may be adapted or used in part.
- Please print this page for your records and send a copy of it to your publisher/graduate school.
- Appropriate credit for the requested material should be given as follows: "Reprinted (adapted) with permission from {COMPLETE REFERENCE CITATION}. Copyright {YEAR} American Chemical Society." Insert appropriate information in place of the capitalized words.
- One-time permission is granted only for the use specified in your RightsLink request. No additional uses are granted (such as derivative works or other editions). For any uses, please submit a new request.

If credit is given to another source for the material you requested from RightsLink, permission must be obtained from that source.

BACK **CLOSE WINDOW**

© 2023 Copyright - All Rights Reserved | [Copyright Clearance Center, Inc.](#) | [Privacy statement](#) | [Data Security and Privacy](#)
| [For California Residents](#) | [Terms and Conditions](#)Comments? We would like to hear from you. E-mail us at customer@copyright.com

List of Publications

1. **S. Kumar**, F. Zeller, T. Stauch, “A-two-step baromechanical cycle for repeated activation and deactivation of mechanophores,” *J. Phys. Chem. Lett.*, **2021**, 12, 9470–9474.
2. **S. Kumar**, F. Zeller, R. Weiß, T. Neudecker, “Trapping the transition state in a [2,3]-sigmatropic rearrangement by applying pressure”, *ACS Omega*, **2022**, 7, 45208-45214.
3. **S. Kumar**, T. Stauch, “The activation efficiency of mechanophores can be modulated by adjacent polymer composition”, *RSC Adv.*, **2021**, 11, 7391-7396.
4. L. J. Mier, G. Adam, **S. Kumar**, T. Stauch, “The mechanism of flex-activation in mechanophores revealed by quantum chemistry”, *ChemPhysChem*, **2020**, 21, 2402-2406.

